Modélisation mathématique de l'allongement de l'axe antéro-postérieur de l'embryon vertébré

Michèle Romanos

THÈSE

En vue de l'obtention du

DOCTORAT DE L'UNIVERSITÉ DE TOULOUSE

Délivré par : *l'Université Toulouse 3 Paul Sabatier (UT3 Paul Sabatier)*

Présentée et soutenue le *17 octobre 2022* **par :**

Michèle Romanos

Modélisation mathématique de l'allongement de l'axe antéro-postérieur de l'embryon vertébré

JURY

Ruth Baker	University of Oxford	Rapporteuse
Bertrand Bénazéraf	Université Paul Sabatier	Co-directeur de thèse
Raluca Eftimie	Université de Franche-Comté	Rapporteuse
Pierre-François Lenne	Aix-Marseille Université	Examinateur
Magali Ribot	Université d'Orléans	Examinatrice
Magali Suzanne	Université Paul Sabatier	Présidente du jury
Ariane Trescases	Université Paul Sabatier	Co-directrice de thèse

---

École doctorale et spécialité :
BSB : Biologie du développement

Unité de Recherche :
Institut de Mathématiques de Toulouse (UMR 5219) et Centre de Biologie Intégrative (UMR 5547)

Directeur(s) de Thèse :
Bertrand Bénazéraf et *Ariane Trescases*

Rapporteuses :
Ruth Baker et *Raluca Eftimie*

To Carine,

"Hit me with your best shot".

Acknowledgments

My first words of gratitude go to my advisors Bertrand Bénazéraf and Ariane Trescases for giving me the opportunity to do a PhD under their supervision and with their guidance. You have given me the chance and the means to do Science through the lenses of Mathematics and of Biology. You made me the scientist I am today. Throughout these four years, your kindness, support, energy, and encouragement were immaculate and indispensable. Bertrand, you taught me how to be a biologist, how to work with one, and how to drive Science forward as a team. Ariane, you encouraged me to visit labs and attend conferences around the world. Thanks to you, I can now say I did Mathematics around the globe. Your inspiring support, patience, care, and subtlety have helped me grow and have given me the freedom to explore Mathematics without fear of making mistakes.

I sincerely thank Pierre Degond, who led the train of this thesis and who started this collaboration between mathematicians and biologists. Your wisdom and brilliant ideas made this work happen. Your guidance throughout this PhD was truly outstanding.

I would like to thank Ruth Baker and Raluca Eftimie who accepted to review my manuscript, and did so with great attention, and brought insightful ideas to it. I would also like to thank Pierre-François Lenne, Magali Ribot and Magali Suzanne for accepting to be members of my jury. It is an honor to have you all here today.

I've had the chance to work with Sophie Hecht who hosted me in London then in Paris, your methods and enthusiasm in our fruitful discussions taught me a lot.

I thank Madame Marie Ajjoub, who made me love Math, and who made me swear never to stop before getting my PhD.

I have spent four years in the walls of the Mathematics Institute of Toulouse, and they have been a real pleasure thanks to the presence of the PhD students. I thank my first office mates, Walter and Moctar, your precious advice gave me a big push in the beginning of my PhD. I thank Clément and Lucas, who always asked me what was wrong when I stormed into the office and listened to me complain just about everything. Your friendship and your support for the crazy decorating ideas mean a lot to me. Also, I am sorry you had to live with the mess I made in the office. I also thank Samuel, who in the few days I've known him, has made his mark, I hope you

become the scientist you aspire to be. I cannot forget the previous occupants of the office 302. Alexis, Joachim, Mathias and Baptiste. Alexis, you have always given me the best advice, and I knew I could always count on you. Joachim, your sense of humor made every day better. Mathias, our late-night therapy sessions in my office are priceless to me, and yes, I am still climbing the ladder... Your friendship has given me so much. Finally, a una persona indimenticabile, Baptiste, your loving support along the years grew stronger, thank you for the person that you are. I have had the privilege of seeing you all become PhDs, I thank you all for being here today. As to the current occupants of the office 302, I am grateful to have met Louis, the most humble person I know and a true friend, you helped me in so many ways. Also thanks to you I met Anaelle whose deep care (and cooking recipes) I will never forget. I thank Etienne, who listens, cares, and whose sense of humor cracks me up. I am so happy to have met you. Viviana, your kindness, laughter, and good vibes are the motors of this office, thank you for being you. Diego, gracias por su apoyo y por todas las clases de español y por su paciencia porque hablo español muy lentamente. To the first occupants of the office 201: Joe, the first day we met I was looking for the building of the doctoral school, without you, I would still be looking for it. Thank you for all the times (every, single, year) you gave me your TD notes, and all your coffee. But more seriously, you are the most precious friend I have in Toulouse. A special thank you here is a must to the Lebanese community in Toulouse who made home feel a little closer. I also thank Kuntal, François and Hoang Phuong, we had so much fun, I hope you are all now quadrilingual. As always, now there is Alexandre the great, Anthony and Nicolas taking over the journey, you are the engines of the PhDs' social life, and also, the Biergarten should have a statue of you guys. Do you hear them laugh? that's the famous trio Corentin, Paola and Perla. You guys are a pleasure to hang out with every day. Your laughter is contagious! A thought to Anthony Mur who made me laugh every day and always had a story to tell about one of his never-ending travels. Minming and Alex (nerd) you guys are the best, in the little time we've known each other you grew on me. A special thank you goes out to Denis who has saved me from 9 years of computations with Mathematica, and Alain who I have never seen not smiling, ever. To my fellow probabilists, Laetitia your friendship means a lot to me, you have been nothing but kind and caring to the PhD students in your responsibility as representative in the doctoral school council. I also thank Eva with whom I had the opportunity to share the responsibility of representing the PhD students in the lab council, alongside Louis, Clément, Florian and Baptiste. Clément I hope you don't freeze in Canada. To Maylis, Xavi, Alberto and Fu-Hsuan who spread joy in the lab, Fabien with his famous role playing games, Mehdi our favourite soccer player, the iconic duo Nicolas and Sophia your dynamic is hilarious, Mahmoud who has the best subtle dark humor, Luca whospeakssofastnotimeforspacing, Virgile the coolest person I know, and Fanny who has the purest heart. To my fellow algebrists, Florian fellow council member, the most patient person I know! J-M, Dominique, William, Dmitri and Solène I hope our paths cross again. To all the PhD students and Drs, thank you for making these four years unforgettable.

I cannot forget to thank permanent members of the institute with whom I have had the chance to discuss about Science and Life, Sépideh Mirrahimi you are a role model for women and men in Science, Philippe Laurençot, your jokes and encouragements throughout the years meant a lot to me, Grégory Faye who always made sure the PDE team remained vibrant, Franck Boyer's hilarious sense of humour, Franck Barthe and Vincent Guedj who presided the council so articulately, Sébastien Déjean (or should I say Benzema?) who animated the institute with the winning football team, Marie-Laure, Delphine, Janani, Marie-Line and Nicole for your amazing work and advice.

I have had the great opportunity of working alongside biologists in the Centre of Integrative Biology, led by a remarkable scientist Fabienne Pituello, who welcomed me as one of their own, and then trained me to be one of their own. Here again, I've lived some of the best moments with Sofiane (whom I've stressed with all my deadlines), Delphine, Vincent and Sulov, thank you for all the coffee breaks complemented with some Biology courses. I also thank Damien, Clair, Marie and Maha (most quite laugh ever right?) for your positive vibes and support. I had the chance to share this experience with the amazing Bénazéraf team: Guillaume, who skillfully coupled Biology, engineering, and Image processing. Nathalie, Myriam (I am still not quitting Krav Maga!), and Cathy your deep care, scientific and moral support mean a lot to me, you made my time in the team an amazing experience, and I believe that I am a better scientist for having known you. I also thank Cathy D for her encouragement, and for reading my proposals over and over again, Julie whose random endorsements when passing through the halls made me smile and pushed me to go further, Eric T a scientist I look up to, Denis' support and kindness, Sophie V for her work and endorsement for women in Science, Anne for her sweet words I hope your new life in Nantes is good to you, Eric A for making everyone laugh with the newest jokes, Sophie T whose laughter fills the halls, Mélanie (Méla-night)for always being so nice and supportive, François M for his friendliness, Marion I am so grateful for your help, Valérie for accepting to be in my thesis comity alongside Franck Plouraboué. To all the scientists in the CBI, I am forever grateful for the great years I've spent among you.

I want to thank all the master and PhD students and PhDs whom I've had the chance to encounter throughout my university years. A special thank you goes out to Florence Hubert for her support and kindness, to Martin Burger for hosting me in Erlangen on several occasions. I am also very happy to have shared 6 weeks in the CEMRACS with the brightest people, we call ourselves myxo dream team: Jean-Baptiste, Benoit, and Hélène, I've learned so much from all of you, and I hope our collaborations will continue. I want to thank especially Vincent Calvez who formed this team, and with whom I will have the chance to work during my post-doc, I am sure I have a lot to learn from you. I thank all my CEMRACS fellows for an awesome summer spent alongside

all of you, a special thought goes out to my CEMRACS roommate Averil, to Hélène Hivert who managed everything, and to Claire, Léo and Nathan for making it particularly fun. A special thank you goes out to my friends with whom i did my masters degree, my sweet Salma, my long-distance friend José, Torres who taught me all the Spanish I know, Franck whose support was indispensable through some tough times, and of course my dear friend Lois.

My next thank you goes out to my friends in Lebanon, who gave me international support, especially my childhood friends, Adib, Ray, Joanna, Charbel B, Joe, Mira, and Charbel M, with whom I was raised. Your kindness and friendship is a blessing. To my friends Sirine and Olivier who welcomed me into their home in Paris, your continuous encouragement fuels me.

To my best friends, Joanne, Karine and Paola, with whom I shared my life, secrets, pain and happy moments. You have been there for me since day one. Thank you for everything.

To Carine, who left us but remains in my heart and memory, to whom this manuscript is dedicated, I know you would have been proud today. To my dear friend Louna, with whom I've shared a life in Lyon alongside Carine as the third roommate, and with whom I will live in Lyon, I hope this chapter is the beginning of new adventures for both of us. You both give me strength to continue.

And last, my biggest thank you goes out to my family: my grandmother Teta who lit a candle for me for every big event, who prayed for me to succeed. To my brother who supported me in the biggest ways, to my sister, the army behind my back, to my mom and dad, without whom today would not have been possible. I hope I make you all proud today. And finally, to our source of joy, love and happiness, Sherlock.

Contents

List of Figures

List of abbreviations

- Bra: Brachyury
- DAPI: 4',6-Dimidino-2-Phenylindole
- EdU: 5-Ethynyl-2'-Deoxyuridine
- ESVM: Enforced Segregation Viscous Model
- FGF: Fibroblast Growth Factor
- HH: Hamburger-Hamilton
- L-ESVM: Limit-ESVM (ESVM at the incompressible limit)
- L-VM: Limit-VM (VM at the incompressible limit)
- MET: Meseynchymal-to-Epithelial Transition
- NMP: Neuro-Mesodermal Progenitor
- NT: Neural Tube
- ODE: Ordinary Differential Equation
- PDE: Partial Differential Equation
- PME: Porous Medium Equation
- PSM: Pre-Somitic Mesoderm
- PZ: Progenitor Zone
- Sox2: SRY-Box Transcription Factor 2
- VM: Viscous Model
- WT: Wild-Type

Chapter 1

Introduction

1.1 Mathematical modelling

Mathematical modelling is the art of translating real life phenomena into equations. It is the process by which one can make complex phenomena more intelligible and accessible to analysis by means of mathematical tools. A mathematical model represents an idealistic representation of the real phenomena and can be manipulated to gain insight on phenomena, which are often unattainable by means of physical or experimental analysis (as in biology, physics or chemistry). Before constructing the model, specifying its objectives is a fundamental step (Figure 1.1). For that matter, one needs to answer a few questions beforehand:

1. What is the real-world phenomena to model ?
2. What are the main questions which the model has to answer ?
3. What are the observable variables ?
4. What is the model going to be compared to (other models, data)?
5. What is the best mathematical setting or formalism to use?
6. How do we analyze and use the results of the model to draw conclusions on the original phenomena ?

All these questions need to be clarified and answered to optimize the modelling process, which can be broken down into the following steps:

1. Create the model consisting in describing one or several aspects of the studied real-world system and the relations between them by means of an adequate mathematical formalism
2. Calibrate and evaluate the mathematical model against real data
3. Analyze and quantify the studied aspects and/or use the model to predict the real-world system's behavior
4. Verify the accuracy of the mathematical model's results by comparing them to existing data and, when needed and possible, refine the model

Modelling is a broad and multidisciplinary field that attracts the interest of scientists from diverse backgrounds. In recent years, mathematical modelling has been used across all branches of Science. It allows to identify specific behaviors, patterns and collective kinematics with rigour and

thoroughness, and can provide predictions and a deeper understanding of the underlying processes. And all that, without expenditure of valuable financial resources (such as the cost of physical and experimental analysis). In engineering and technology, it provides an analytical basis for design and control. In the field of fluid mechanics, it is an essential tool for studying turbulent motions, and in medicine it plays a key role in assisting radiation and chemotherapy. Thanks to the modelling of neural networks, we have a more complete understanding of the functioning of the brain of certain living beings. Mathematical models are increasingly used to describe living systems, population dynamics, human behavior, pattern formation in nature... It is also widely used in the interpretation of bio medical data. It is worth noting that despite all the advances in technology and in the techniques of problem solving, answer predicting and computational support, the **human intelligence, experience, and human intuition** still play the key role in mathematical modelling.

In this thesis, we are interested in the morphogenesis of vertebrate embryos, which is the process by which tissues and organs develop, grow in contact, and shape during embryo development. Throughout the growth, the embryo acquires an axis of development: the antero-posterior axis, which is defined by the head-to-tail directionality of the embryo. The tissues' development extends this axis through the stages of embryonic growth. A natural question to ask is: **what are the mechanisms that explain and govern axis elongation ?** We can consider for example three possibilities: A) Can growth alone (volume gain) explain the elongation of the embryonic tissues ? B) Is elongation a consequence of chemical signals leading tissue growth ? C) Is there a complex mechanical dynamics leading the inter-cellular and inter-tissue interactions ? Interestingly, all three paradigms hold. Evidence of dominant growth, and of chemical and mechanical interplay was identified in literature. For each one of these paradigms, one can construct a different model that reproduces axis elongation. In this thesis we will focus on the third paradigm, that is, we will opt for the multi-scale mechanical approach on axis elongation. Multiple tissues, tissue types and cell types are involved in axis elongation. One could think of muscle tissues, nerve tissues, bone tissues, stem cells, skin cells to grasp the variety of cell and tissue types that appear in the vertebrate body. In addition, these cells are incredibly numerous. When these cells are of the same type and when they can be considered indistinguishable, we will consider, in our mechanical approach, systems of multi-agents interacting. Advanced Mathematics is needed to build and study such systems. There are several model architectures to choose from, and we choose to focus on two of them: the so-called **microscopic architecture** which consists in a model that represents and describes every component of the system and the way these components are related to each other, at a very small scale, if not the smallest. In our modelling context, this corresponds to describing cell behavior in terms of position, motility, protein synthesis, for each one of the cells of the system. The **macroscopic architecture** consists in a representation on a larger scale of the whole system. This corresponds to modelling the elongating tissues (constituted by a very large number of cells)

in our context. This macroscopic description can include organs, systems and organisms. In either case, the microscopic or the macroscopic approach, the components to be modeled are chosen based on the questions asked about the system, the scales at which we wish to study the system, and the complexity we wish to represent. The mathematical implementation (formalism, choice of model) depends heavily on the available computing power, the sample size, and the scale at which we want to represent the dynamics of each component. In this manuscript, we focus on microscopic and macroscopic multi-agent systems. The necessity for both types of models comes from the multi-scale aspect of the phenomena occurring in the embryo, i.e cellular processes are underlying tissue formation. It is also important to understand the link between these two scales. From a mathematical and a biological point of view it is interesting to confront and link the models on the microscopic and macroscopic scale. Some cellular models lead to a tissue description, which can be derived using an asymptotic limit -that is, a change of scale. This makes the transition from microscopic to macroscopic point of view quite natural. An active mathematical field of study is deriving macroscopic models from microscopic ones. Kinetic theory builds a bridge between these scales, and raises fundamental questions as to the theoretical framework in which such bridges can be built. Kinetic theory, which was originally developed in the context of statistical physics, is now being developed in all fields of modelling of natural phenomena. In what follows, we will discuss the derivation of fundamental microscopic and macroscopic models, as well as some consequent mathematical results on these models and their application fields.

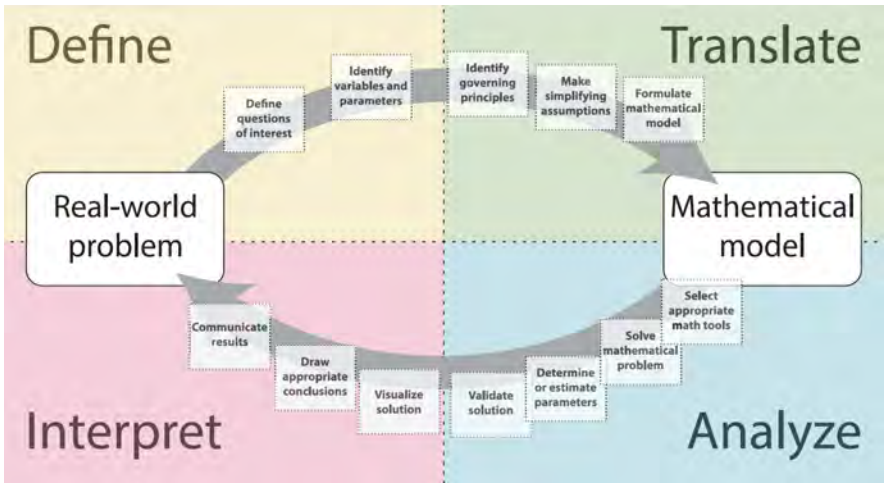

Figure 1.1 – Taken from [162]. Schematic representation of the mathematical modelling process.

1.1.1 Microscopic models

Discrete models or agent-based models are used to describe phenomena taking place at the microscopic scale, i.e. the variable of interest is the agent itself (its position, speed, etc). In this type of model, each agent individually evaluates its situation and makes decisions based on a set of rules. When multiple agents are involved, and when they correlate their respective movements with that of others, the emerging phenomena is a collective dynamics. Typically one can think of herds, flocks, embryonic cell populations, bacteria, cancer cells, immune cells, etc. Agent-based modelling is one of the famous approaches when it comes to collective dynamics in populations. In the case of cell populations, this approach includes single and multi-site cellular automata (Cellular Potts) [77, 52], or a spherical or ellipsoidal description of cells [122, 55], or even a description of cell boundaries as a deformable one - voronoi tessellations model or vertex model- [133] (Figure 1.2).

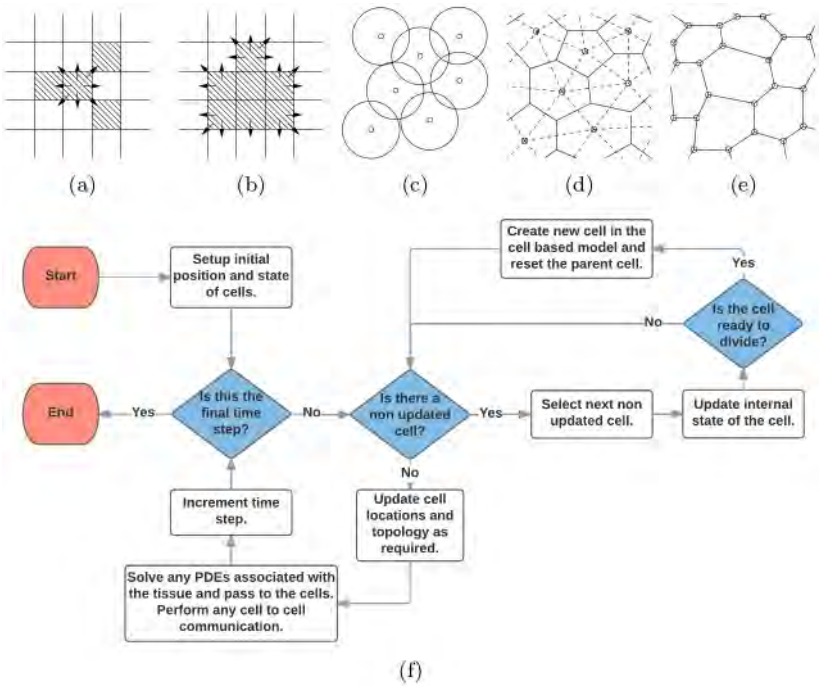

Figure 1.2 – Figure taken from [120]. Caption adapted from [120]. Schematics of some cell-based models considered here. (a) Cellular automaton (CA). (b) Cellular Potts (CP) model. (c) Overlapping spheres (OS) model. (d) Voronoi tessellation (VT) model. (e) Vertex model (VM). (f) Example of a flow chart of a cell-based simulation algorithm.

An important feature of multi-agent discrete modelling is the precision of the interactions between agents, and the ability to describe chaotic behaviors, which is difficult with ordinary differential equations (ODE) or partial differential equations (PDE). The advantage of this type of modelling is that it is conceptually simple, and is essentially used to capture more precise information about the system studied. This is especially true when the variable of interest is fluctuating,

since ODEs and PDEs tend to smooth out the fluctuations. Agent-based models are also used when individual behavior is governed by if-then rules, by transition probabilities, or by randomness (stochasticity). This type of modelling is commonly adopted given its ability to capture inter-agent heterogeneities. Stochasticity is a very important notion in discrete models, as some variables -like position, behavior, variations of a quantity- do not always follow a specific deterministic set of rules, but are rather governed by chaos. One of the most famous examples of such chaotic events is the Brownian motion of a particle [113]. During its movement, the particle is undergoing random small fluctuations in its position. The Brownian motion can be considered as the process by which a particle diffuses microscopically. In Figure 1.3 we illustrate a moving particle with a Brownian (random) motion.

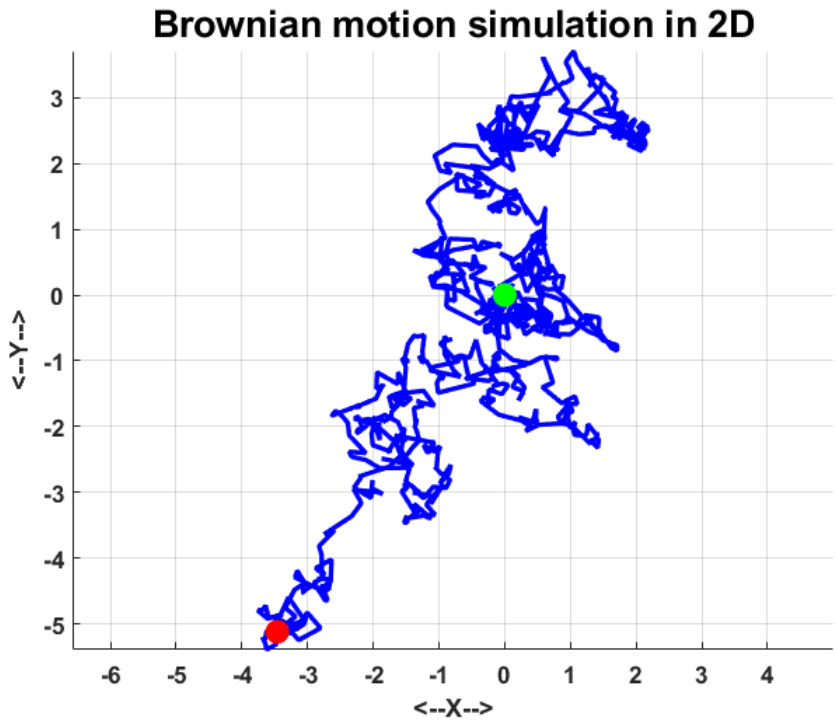

Figure 1.3 – Numerical simulation (Matlab R2021a) of a Brownian motion in 2D, 1000 steps. Particle trajectory in blue, green dot represents the particle's position at time $t = 0$, and the red dot is the particle's position at time $t = 1000$.

Agent-based models are applicable to various domains such as the study of traffic and crowd movements in panic situations. Agent-based models are well suited to provide valuable information on evacuation mechanisms, and on strategies to minimize the harmful consequences of such an event [86]. On the other hand, in the context of biology, discrete models have proven useful in capturing certain phenomena such as the evolution of a population of bacteria (growth, division, biofilm formation...) [54, 73], angiogenesis [13], cancer biology [107], and cell biology [121, 116],

etc.

Although agent-based models entail many advantages when it comes to precision, their limitations motivate alternative approaches. In fact, agent-based models provide precisions at the microscopic scale at a computationally high cost. They lack analytical methods thus strongly depending on computations, which become cumbersome very fast as the population size becomes large. This motivates another type of models called macroscopic models, which allows to circumvent this difficulty by thinking "larger". We present this type of model in what follows.

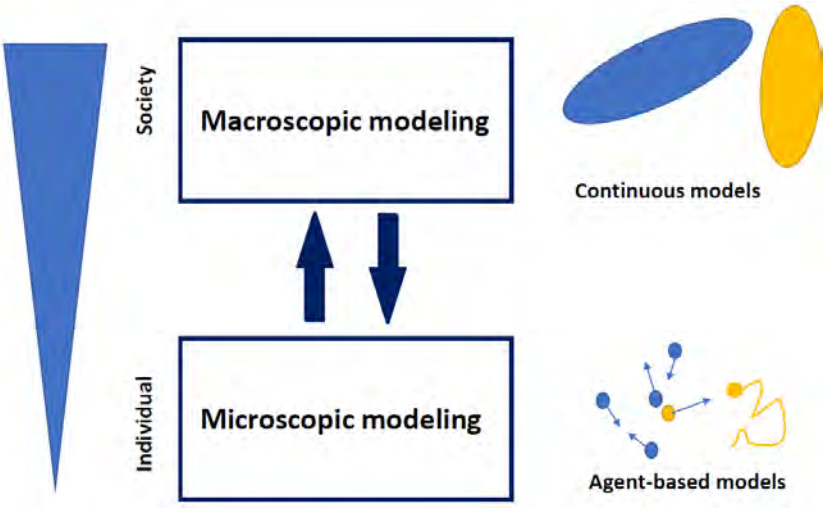

Figure 1.4 – Representation of the differences of multi-scale mathematical modelling. Arrows schematize the direction of blue and yellow cells which obey a specific set of rules.

1.1.2 Macroscopic models

The alternative approach to microscopic models uses continuous models. When the number of individuals becomes very large, discrete models fail. The computational cost becomes enormous, and above all, the precision involved can mask certain emergent behaviors at the macroscopic scale. In this case, we resort to continuous models. These models consider local averages of some quantity we want to describe as functions of space and time, such as the cell density, the pressure, the velocity... This is particularly feasible as in continuum models, individuals are considered indistinguishable, which circumvents the need to describe each individual, but rather an average description of a group of individuals. The most common continuous models that allow the study of complex systems are based on ODEs or PDEs. ODE and PDE based continuum models have their merit owed to the fact that well posed continuous problems have unique solutions for given initial data. They also enjoy many analytical methods developed from classical theories, which provides valuable information on the solution's behavior (positivity, long time asymptotics, numerical behavior).

Diffusion in PDEs. Diffusion is a concept that is omnipresent around us. We cite for example the diffusion of particles, fluids, species, people, ideas, trees, news... The main idea is the same for all these examples: a diffusing quantity will spread from its current position where the concentration of that quantity is high. Diffusion in PDEs was introduced to account for the random migration or spontaneous dispersal of individuals in their environment. Microscopically, the diffusion of a particle can be described by a Brownian motion. The latter describes how microscopic particles undergo small fluctuations in their position, and can eventually invade the space. Macroscopically, the concept of diffusion led to the active and growing field of reaction-diffusion systems commonly written in terms of PDEs. PDEs are used to describe phenomena occurring at the macroscopic scale which in practice translates to the study of local averages of individuals/agents. One of the most famous equations in PDEs is the diffusion equation. This equation shows how a global population's migration can be explained as a result of individuals moving randomly (Brownian motion). In dimension 1 the diffusion (or heat) equation writes,

$$\underbrace{\partial_t n(t,x)}_{\text{Time derivative/variation}} = \underbrace{D\partial_{xx}^2 n(t,x)}_{\text{Diffusion}}, \tag{1.1}$$

with the mass diffusivity D taken as a constant. We note that the heat equation is a special case of a more general type of diffusion, the Fickian diffusion, where the diffusivity D can depend on the space variable.

Boundary conditions. Let us consider the heat equation in a closed room. It is important to specify whether the room is sealed shut (no inflow or outflow of the quantity) or whether the doors

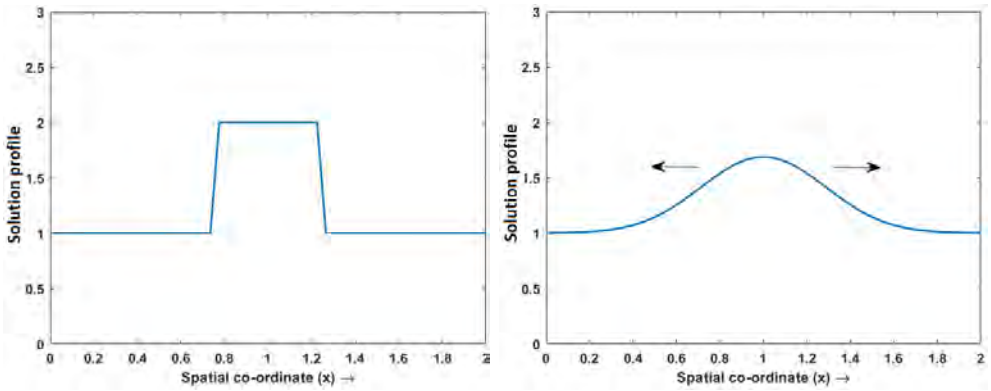

Figure 1.5 – Numerical simulation (Matlab R2021a) of the solution of the diffusion equation (1.1) with D=0.01 and homogeneous Dirichlet boundary conditions. Left: initial condition ($t = 0$). Right: at time $t = 0.5$, the solution diffused (right and left black arrows).

are permeable. This is known as the boundary conditions, which are crucial to close the system, and to hope for existence and uniqueness of the solution of (1.1) (with suitable initial data, i.e by prescribing the heat at time 0). Boundary conditions come in different types, we cite a few useful ones for this manuscript: the Neumann boundary conditions prescribe the variation of some quantity across the boundary. For example, going back to our analogy of the closed room, this is the case when heat transfer through doors is known or prescribed. Another known boundary condition is the Dirichlet boundary conditions, which, in our analogy, can correspond to a wall held at a fixed temperature. The Robin boundary conditions are a mix of the Neumann and of the Dirichlet type.

Reaction-diffusion equations. When dealing with species that spread and evolve in their number of individuals due to reproduction or death, the heat equation (1.1) fails to reproduce both phenomena. This gave rise to the somewhat revolutionary reaction-diffusion equations, which account for the evolution of the population size by adding a reaction term (growth/death) as follows,

$$\partial_t n \underbrace{- D\Delta n}_{\text{Diffusion}} = \underbrace{R(n)}_{\text{Reaction}}, \tag{1.2}$$

with $R(n)$ the reaction term, which can take various forms. For example, an exponential growth is used to describe rapidly expanding populations,

$$R(n) = an, \tag{1.3}$$

with a the growth rate. This type of growth is typical for a population of *E. Coli*. Other growth types were later introduced such as the logistic growth which entails a carrying capacity limiting

the population expansion,

$$R(n) = an\left(1 - \frac{n}{n^*}\right), \tag{1.4}$$

with n^* the maximal number of individuals the population can have (either due to lack of nutriments, or lack of space, etc.). An example of such logistic growth is the evolution of the number of fungus in bread or alcohol. In particular, when the source term is as in (1.4), the equation is known as the Fisher-Kolmogorov-Petrovsky-Piskunov equation (Fisher-KPP) [98]. This equation enjoys a wide literature on its properties and on the behavior of its solution (well-posedness, existence of wave fronts, appropriate numerical schemes, long time behavior...). Variants of reaction-diffusion equations have been developed and applied in many fields including local (in space) and non-local (long range/short range) effects [69]. A straightforward example of a non-local effect is the ability of the species to sense how many individuals are present in their entire environment and not only in their immediate vicinity, and then behave accordingly. When modelling tissues, a natural assumption is to consider them as fluids which grow thanks to cell division and shrink with cell death. This allows us to use PDEs (such as reaction-diffusion equations) to describe tissue kinetics. More so, tissue kinetics require a low accuracy at the cellular level, and only an averaged description of the evolution of some macroscopic quantities related to the tissue such as density, concentration, velocity, pressure, etc. We now discuss a few variants of the reaction-diffusion equations.

The reaction-diffusion-advection equation. A distinguishable feature of diffusion is that it is directly related to the random motion of the particle which yields mass transport, without requiring directed bulk motion. Bulk motion, is the characteristic of advection. The concept of advection originates from fluid mechanics. In a few words, it describes how a particle density submerged in a fluid is transported by the fluid's velocity. It can also model an environmental flow, or an active navigation by individuals. This gave rise to a variant of (1.2) including advection called the reaction-diffusion-advection equation, see for example,

$$\partial_t n - \underbrace{D\Delta n}_{\text{diffusion}} + \underbrace{\nabla\cdot(vn)}_{\text{advection}} = \underbrace{R(n)}_{\text{reaction}}, \tag{1.5}$$

In the context of biology, advection can be due to possible chemotactic effects (Keller-Segel equations [92]) from the presence of pheromones or nutrients for example. Chemotaxis entails a driven motion towards or against a gradient of some signal, i.e $v = W\nabla c$, with c the concentration of some chemo-attractant/chemo-repellent and W a certain function. One could think of cells following a gradient of nutrients, or bacteria following a gradient of oxygen.

The notion of pressure and viscosity: the Navier-Stokes equations and their descendants. When considered in the context of living systems, we rapidly realize that the mathematical

elements in (1.5) are insufficient to fully grasp the complexity of growing tissues. The most important notion which is absent in this equation is the pressure, which governs the growth of living systems. When cells sense high pressured environments they tend to move away from them. Furthermore, when the pressure is too high cells can stop their growth or undergo apoptosis (suicide). The pressure is then a key element controlling both growth and cell velocity. The necessity to include this pressure dependent velocity resulted in more biologically pertinent forms of the velocity v in (1.5). For example, let's consider Darcy's law,

$$v = -\nabla p(n), \tag{1.6}$$

with p the pressure. In (1.6), a clear link is made between the pressure sensed by the species and the velocity responding to that pressure. Darcy's law follows a simple principle, that individuals move against the pressure gradient, i.e, favor low pressured environments. The pressure in (1.6) is taken as an increasing function of the population density which translates the fact that more individuals result in a higher pressure. Darcy's law is widely used in literature as it is both mathematically useful and translates an agreed-upon biological phenomenon. This led to the use of the reaction-diffusion-advection equation in the modelling of various biological processes [65, 101]. The origins of Darcy's law goes back to the Navier-Stokes equations which describe the motion of viscous fluids [155]. The Navier-Stokes equations are fundamental equations in fluid mechanics which see their applications in a very large variety of fields such as engineering and oceanography, to cite a few. They are also quite the mathematical challenge, as we still do not know whether they admit smooth solutions in 3D. The challenge is so interestingly hard that the Clay Mathematics Institute classified this problem as one of the 7 Millenium Prize Problems, offering 1 Million dollars to the solver. Let us now take a look at the compressible Navier-Stokes equations based on the conservation of mass and momentum,

$$\underbrace{\partial_t(nv) + \nabla\cdot(nv\otimes v)}_{\text{Inertia}} = \underbrace{-\nabla p}_{\text{Pressure forces}} + \underbrace{\nabla\cdot(\mu\psi(v))}_{\text{Divergence of stress}} + \underbrace{F}_{\text{External forces}}, \tag{1.7}$$

$$\partial_t n + \nabla\cdot(nv) = 0. \tag{1.8}$$

In the first equation (1.7), n, v and p represent respectively the fluid density, velocity, and the pressure, and μ is the dynamic fluid viscosity. The term ψ is the stress tensor which takes the following form,

$$\psi(v) = \nabla v + (\nabla v)^T - \frac{2}{d}(\nabla\cdot v)Id,$$

with Id the identity matrix, and d the space dimension. The second equation (1.8) is non other than the continuity equation. To formally derive Darcy's law, we neglect inertial and external

forces, and consider that the viscous resisting force is linear to the velocity. In 2D this yields,

$$v = -\kappa \nabla p, \tag{1.9}$$

with $\kappa > 0$ the hydraulic conductivity.
Darcy's law, entails biological meaning, but is not useful when the viscous forces of the fluid are significant. For that reason, Brinkman [21] modified Darcy's law to consider these viscous forces and give rise to the so-called Brinkman law (or Brinkman-Darcy law) which takes the form of an elliptic equation for the fluid velocity v,

$$-\mu \Delta v + \frac{1}{\kappa} v = -\nabla p. \tag{1.10}$$

A straightforward observation shows that for $\mu = 0$, (1.10) gives Darcy's law. It is also possible to derive Brinkman's law for the velocity from the Navier-Stokes equations. In fact, neglecting the inertial and external forces, the viscous forces (term in Δv) arise from the divergence of the stress tensor. A useful property of the Brinkman law is that, if considered in a bounded domain in $\mathbb{R}^d, d > 1$, with suitable boundary conditions, the velocity can exhibit swirling motion, see Figure 1.6.

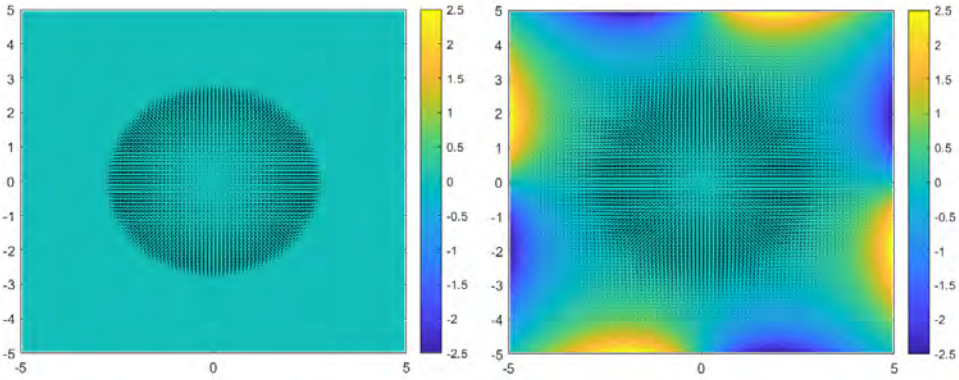

Figure 1.6 – Curl v (colorbar) overlapped with the vector v (arrows in black). Left: Darcy's law with $\kappa = 1$. Right: Brinkman's law with $\mu = \kappa = 1$ and Dirichlet boundary conditions. The pressure is taken as : $p(x, y) = 10^3 e^{-1/(1-(x/3)^2-(y/3)^2)} \chi_{(x/3)^2+(y/3)^2 \leq 1}$, with χ the indicator function.

This will be of interest to us in this manuscript, as the Brinkman equation (1.10) is able to reproduce and explain swirling motions observed *in vivo* in the vertebrate embryo [24].

Multi-species. With the developing field of the mathematical tools in macroscopic PDE models, these models see their applications expand to the context of tumor growth [6, 14, 36, 99, 124, 153], ecology, epidemiology, neuroscience, chemical reactions, pattern formation in nature and in species, and behavioral sciences [114]. When dealing with multiple interacting species, macroscopic models

were also developed to incorporate such interspecific interactions. One could think of a cancerous tissue and a healthy tissue cohabitating, or a prey-predator relationship between animals. The first and simplest model was developed by Lotka and Volterra [104, 150] where an ODE coupled system describes the evolution of two species where one is the predator of the other,

$$\frac{d}{dt}n_1(t) = b_1 n_1(t) - d_1 n_1(t) n_2(t), \tag{1.11}$$

$$\frac{d}{dt}n_2(t) = b_2 n_1(t) n_2(t) - d_2 n_2(t). \tag{1.12}$$

In the system (1.11)-(1.12), the total number of the preys is represented by n_1, and of the predators by n_2. The preys grow at rate b_1. The terms $-d_1 n_1 n_2$ and $b_2 n_1 n_2$ model respectively the proportional ($d_1 > 0$) decay of the preys due to the presence of n_2 predators, and the proportional ($b_2 > 0$) increase of predators by consuming n_1 preys. Finally, in the absence of preys ($n_1 = 0$), the predators die at rate d_2. In the absence of predators ($n_2 = 0$), the size of the prey population grows exponentially.

With this model it became relatively clear how competing/interacting species affect the dynamics of each population size. When integrating the spatial variable to the equations, the resulting PDEs exhibit very interesting phenomena. To account for the spatial dynamics, the coupling of the equations can not only happen through the reaction term (as in (1.11)-(1.12)) but also through the diffusive term. This is known as cross-diffusion, which models how the migration of one species is altered by the presence of the other. An intuitive example to consider is an invasion-evasion situation, i.e, one species flees as the other approaches. We cite an example of such cross-diffusion models found in the works [18] which writes,

$$\partial_t n_1 + \nabla \cdot (n_1 q_1) = 0, \quad \text{with} \quad q_1 = -\kappa_1 \nabla (n_1 + n_2), \tag{1.13}$$

$$\partial_t n_2 + \nabla \cdot (n_2 q_2) = 0, \quad \text{with} \quad q_2 = -\kappa_2 \nabla (n_1 + n_2). \tag{1.14}$$

In (1.13)-(1.14), n_1 and n_2 denote the interacting species, with $\kappa_1, \kappa_2 > 0$. The dispersal of the two species is driven by the quantities q_1 and q_2, which model the species' response to the total pressure (the sum of both densities). This example shows how cross diffusion can drive the species to change their spatial dynamics in response to the presence of the other. This type of models, where the diffusive part is dependent of both species exhibits an interesting property known as phase separation or emerging segregation effects [18, 34, 50, 63, 105]. This means that initially segregated populations remain segregated at all times. This property will be useful in this manuscript, as embryonic tissues, once fully differentiated and attributed different functions, never mix. This type of model can help understand why. We also note here that nonlinear diffusion such as in (1.13)-(1.14) are commonly used in literature to induce a volume filling effect (for example to avoid overcrowding and aggregation). Other types of spatial interactions exist and can be integrated

in the macroscopic PDE based models such as non-local attractive/repulsive terms between the species [22, 23], other authors considered one species moving along the gradient of the other one [34, 51].

Free boundary problems. When the quantity of interest is no longer the fluid density, but is the evolution of the domain it occupies, we can refer to this description as a geometric one. Macroscopic models include geometric models under the form of free boundary problems. Obtaining a free boundary problem can be done for example by considering the tissue density to be constant, and in the presence of growth terms, the pressure inside the tissue will induce its movement and deformation. It then suffices to describe the shape and velocity of the moving domain the tissue occupies. An example of a free boundary problem is the following,

$$n = 1, \quad \text{in} \quad \Omega(t), \tag{1.15}$$

$$-\Delta p = G(p) \quad \text{in} \quad \Omega(t), \tag{1.16}$$

$$v = (-\nabla p \cdot \vec{\nu})\vec{\nu} \quad \text{on} \quad \partial\Omega(t), \tag{1.17}$$

where n is the density, G a growth function, p the pressure and v the velocity of the moving domain $\Omega(t)$, see Figure 1.7.

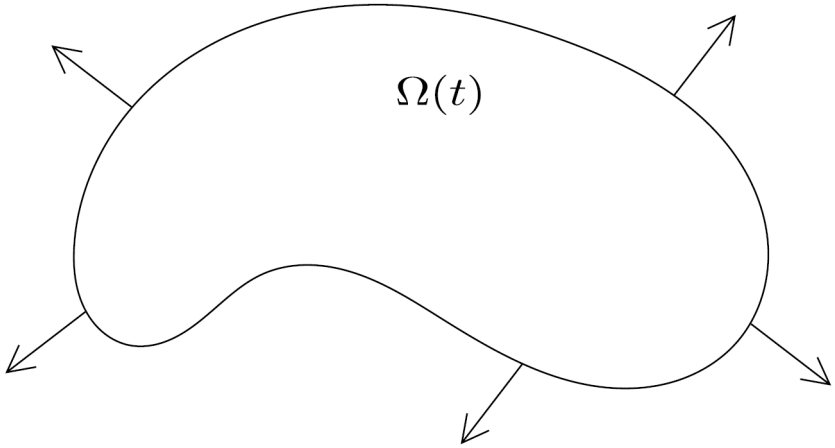

Figure 1.7 – The moving domain $\Omega(t)$. The arrows represent the velocity vector defined by $v = (-\nabla p \cdot \vec{\nu})\vec{\nu}$ on $\partial\Omega(t)$.

This description has many advantages, as it reduces the number of equations and the number of parameters to estimate/fit. In the context of tissue growth, this description is deemed very useful [17, 96, 125, 11]. In literature, many authors propose a free boundary approach to model vertebrate embryo development [129, 112, 11]. Their derivation of the model is a phenomenological one, i.e it is based on the observation of the phenomena and on the data at hand, leaving behind the density description. Our approach is different, as we aim to give both descriptions (density and geomet-

ric), and to link them. More precisely, we start with the derivation of a macroscopic model which describes the evolution of the embryonic tissues as fluid densities. From that model, we derive its **corresponding** free boundary problem through a mathematical tool called the **incompressible limit**. This mathematical link first guarantees the right geometric description consistent with the density model. Second, it allows us to compare our model to the works in literature based on phenomenological approaches. Third, with this new point of view on embryonic growth, where tissue density and tissue shape descriptions are linked, we can have more information on the macroscopic density model via its simplified version, and vice versa.

In the next section, we perform some formal computations to highlight the link between the models presented previously. Namely, we exhibit the link between the Brownian motion and diffusion in PDEs as well as some examples of free boundary systems which can be derived via the incompressible limit of hydrodynamic models.

1.1.3 Link between the models

Link between a Brownian motion and diffusion in PDEs. The diffusion equation (1.1), which describes a macroscopic random dispersal of individuals, can be derived from a Brownian motion of randomly moving particles. We note here that there are many ways to derive the diffusion equation from random processes [114], however we focus on the Brownian derivation for the sake of simplicity. Here, we will perform some formal computations to show the link between a Brownian motion and a diffusion process, which was first achieved by Einstein [62].
Assume some Brownian particles evolve in space $x \in \mathbb{R}$ and time $t \geq 0$. The particle density of these particles defined as $n(t,x)$ describes their distribution for a given time in a given position. Assuming conservation of particles, we expand the particle density at time $t+\Delta t$ as a Taylor series,

$$\begin{aligned} n(t+\Delta t, x) &= n(t,x) + \Delta t \partial_t n(t,x) + o(\Delta t) \\ &= \int_{-\infty}^{+\infty} n(t, x+\Delta x)\mu(\Delta x) d\Delta x. \end{aligned} \tag{1.18}$$

The second equality comes from the assumption that a particle can move by Δx to $x+\Delta x$ at time $t+\Delta t$ if it was previously in position x at time t, with a probability density $\mu(\Delta x)$.

Writing the Taylor series in (1.18) yields,

$$\begin{aligned} n(t+\Delta t,x) &= n(t,x)+\Delta t\partial_t n(t,x)+o(\Delta t) \\ &= \int_{-\infty}^{+\infty} n(t,x+\Delta x)\mu(\Delta x)d\Delta x \\ &= \int_{-\infty}^{+\infty}\left(n(t,x)+\Delta x\partial_x n(t,x)+\frac{\Delta x^2}{2}\partial_{xx}^2 n(t,x)+o(\Delta x^2)\right)\mu(\Delta x)d\Delta x \end{aligned} \quad (1.19)$$

By space symmetry we have,

$$\int_{-\infty}^{+\infty}\Delta x\mu(\Delta x)d\Delta x = 0, \quad (1.20)$$

and by definition of the probability μ we have,

$$\int_{-\infty}^{+\infty}\mu(\Delta x)d\Delta x = 1. \quad (1.21)$$

Considering only the highest order terms in (1.19) we obtain,

$$\Delta t\partial_t n(t,x)+o(\Delta t) = \int_{-\infty}^{+\infty}\left(\frac{\Delta x^2}{2}\partial_{xx}^2 n(t,x)+o(\Delta x^2)\right)\mu(\Delta x)d\Delta x.$$

This gives rise to the diffusion equation (or heat equation),

$$\underbrace{\partial_t n(t,x)}_{\text{Time derivative/variation}} = \underbrace{D\partial_{xx}^2 n(t,x)}_{\text{Diffusion}}, \quad (1.22)$$

with the mass diffusivity D defined as,

$$D = \int_{-\infty}^{+\infty}\frac{\Delta x^2}{2\Delta t}\mu(\Delta x)d\Delta x.$$

This derivation explicitly shows how diffusion on the microscopic scale and on the macroscopic scale are linked.

Link between hydrodynamic models and free boundary problems. The derivation of free boundary problems from hydrodynamic systems via the incompressible limit is an active mathematical field. This limit consists in considering the hydrodynamic model in its asymptotic regime. A first example in which the incompressible limit was computed is with the porous medium equation (PME) which reads,

$$\partial_t n-\Delta n^m = 0, \quad m>0, \quad (1.23)$$

where n is a density, m a positive parameter. We can directly see that the heat equation (1.1) is the simplest form of the nonlinear equation (1.23), when $m = 1$. The PME is used in the description of fluid flow, heat transfer, diffusion of an isotropic gas through a porous medium etc. It is widely studied in mathematics as its non-linearity conveys its solutions interesting properties and challenging analysis techniques [149]. The incompressible limit was studied in the case of the PME (1.23), that is when $m \to +\infty$, [27]. In the absence of growth, as in this case, the limit is stationary. When one considers a source term, interesting properties arise. To give an example of the incompressible limit with growth, we introduce the parabolic-hyperbolic system in [125] which considers the evolution of a single tissue, with Darcy's law for the velocity,

$$\partial_t n - \nabla \cdot (n \nabla p) = nG(p), \qquad \text{with} \quad p(n) = \frac{\gamma}{\gamma - 1} n^\gamma, \tag{1.24}$$

where n is the tissue density, γ a positive constant, and G a decreasing growth function of the pressure. As previously explained, the pressure is a very important notion to consider when modelling living tissues. This motivates taking a growth function that is pressure dependent to decrease and stop cell division when the pressure is too high. The pressure is taken naturally as an increasing function of the density, i.e, more cells yields more pressure. Power pressure laws are commonly used in literature, but other forms inhibiting cell overlap [50, 85, 39] were investigated. In this example, when γ (the pressure parameter) becomes very large, the pressure becomes asymptotically stiff, that is, when $0 < n < 1$, the pressure is null, and when n approaches 1, the pressure becomes strictly positive. This motivates the definition of a moving domain $\Omega(t)$ where $n = 1$ and $p > 0$ (Figure 1.7). Then, we can compute the incompressible limit as $\gamma \to +\infty$, and derive the corresponding free boundary problem which yields,

$$n = 1, \quad \text{in} \quad \Omega(t), \tag{1.25}$$

$$-\Delta p = G(p) \quad \text{in} \quad \Omega(t), \tag{1.26}$$

$$v = (-\nabla p \cdot \vec{\nu})\vec{\nu} \quad \text{on} \quad \partial\Omega(t), \tag{1.27}$$

The elliptic equation on the pressure, called the complementary relation, drives the growth of the moving domain $\Omega(t)$. The velocity of the domain boundary is given by the gradient of the pressure taken in the normal direction $\vec{\nu}$ to the boundary. Many free boundary problems actually derive from hydrodynamic models through the incompressible limit. It was computed for the reaction diffusion equation [27, 28, 74, 94, 96, 125], with active motion, or nutrients in the case of tumor growth [45, 46, 96, 125, 126], and for the Navier-Stokes equations with growth terms [148]. The incompressible limit builds a bridge between two descriptions of the same problem. In this manuscript, we are particularly interested in finding the link between a density description of the embryonic tissues and a geometric one, through the incompressible limit.

In this section we have presented the main pillars and tools we are going to use in our modelling approach to model morphogenesis in vertebrate embryo. In what follows, we explain the process of morphogenesis in more detail. We present the cell behavior and the tissue kinetics involved to have a clear view of the biological phenomena to model.

1.2 Morphogenesis

Morphogenesis: a vital multi-scale process. Morphogenesis is the biological process by which tissues and organs form, develop and grow to give rise to the future adult. During this process, patterns emerge and tissues acquire their shapes and functions. This process relies on local cell activities, which divide, migrate, adhere, detach or die to eventually reorganize into a structure. These events are controlled by a combination of short and long range chemical signals received from other cells, or by the mechanical pressure from cells in neighboring tissues or by tension. The cells' response to these forces, tensions and signals affects their fate and behavior which in turn influences tissue structure. This multi-scale interplay is common to all vertebrates, and is essential to form a complete being.

In this manuscript we use mathematical modelling in the context of developmental biology which is the study of how living systems go through morphogenesis, and grow and develop to become fully-formed adults. Taking the example of a human being's development, it is rapidly clear how long and complex the process of morphogenesis is. In approximately nine month starting fertilization, the embryo goes from a flat disk shape, to a fully grown and complete human, with arms, legs, a head, and a beating heart (Figure 1.8). However, this process is not always perfect. Many defects can occur during early stages of development leading to congenital diseases. This very complex choreography where a dysfunction or a delay in one event can induce a cascade of malfunctions in the body formation requires an exhaustive study and exploration. Therefore, studying these processes as individual ones and as a collective dynamic, on the cell and on the tissue scale can bring a better understanding on the foundations of life, and help apprehend congenital diseases. Research on morphogenesis has also proven useful outside the scope of the growing embryo. It is known that many types of cancers exhibit similar behavior as to those of the developing embryo. Indeed tumor cells develop at a very high rate, similarly to some embryonic cells. They also share the same process to provide nutriments to these growing cells. This process is called angiogenesis, which consists in the formation of new blood vessels to allow nutriments to enter cells. In the case of cancers, the tumor undergoes this process to continue its development, and uses it to trigger metastasis. Tumor cells, similarly to embryonic cells, can then migrate and colonize other tissues. It is therefore crucial to study cell and tissue behavior during morphogenesis to understand the underlying cellular processes behind these diseases and to prevent them.

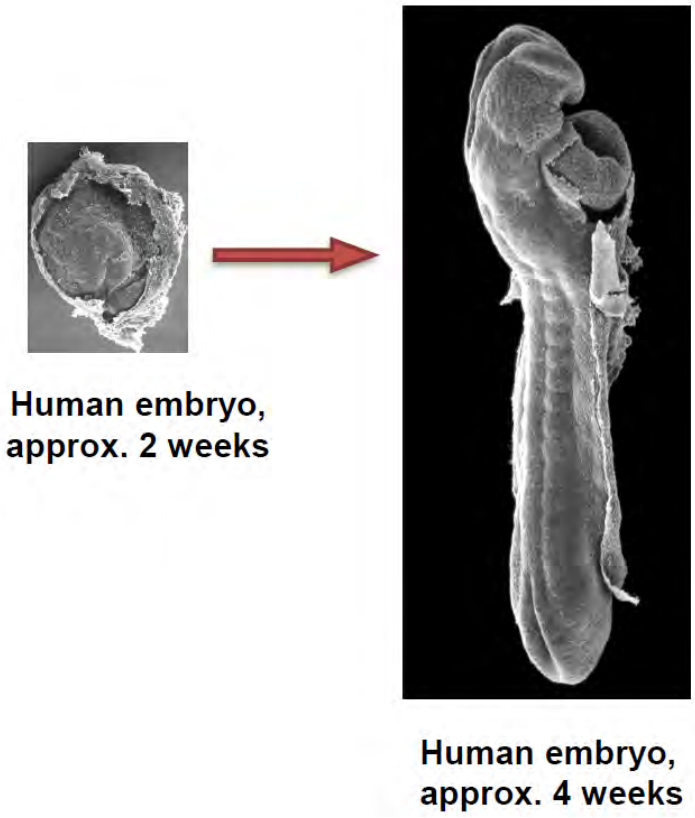

Figure 1.8 – Left: human embryo approximately two weeks old. Right: human embryo approximately four weeks old. Taken from UNSW, embryology, Hill, M.A, SulikK.,Vekemans, Attié-Bitach T, Embryology Human embryo.

1.2.1 Formation of the vertebrate body

During vertebrate embryo development, morphogenesis translates into a series of cell and tissue changes, which starts as a group of a few cells forming a round shaped structure. The next stage consists in the formation of the three germ layers (ectoderm -future skin and nerve tissue, epidermis, mesoderm -future skeletal system and muscles, endoderm -future internal organs), it is known as the gastrulation stage. During this phase, the embryo adopts a head-to-tail axis along which it elongates. The extension of the body is accompanied by the gradual formation of embryonic structures starting from the head, and ending with the tail. Some of these structures originate from the caudal region of the embryo. The body is driven towards the posterior of the embryo, by means of formation and elongation of posterior tissues which are spatially organized in a very stereotypical manner: the neural tube (NT) and the notochord are located axially. The NT is the future nervous system and is a central and dorsal structure. The notochord is a structure in the form of a rod that develops ventrally to the neural tube. It is formed during gastrulation and induces the formation of the neural plate (neurulation). The presomitic mesoderm (PSM), future muscles and skeletal system, is located on either side of the NT. On the lateral edges of the PSM, we find the lateral plate (or lateral plate mesoderm), which constitutes the future heart and cardiovascular system. It condenses into two lateral tissues on either sides of the PSM, see Figure 1.9. Anterior to the PSM, the somites form. Somites are solid dense structures of mesoderm which form in pairs, and are located on either side of the body's axis of symmetry. They correspond to the future vertebrae. Periodically, these somites start appearing by pairs and contribute to the formation of the embryo. The NT, the PSM and the notochord are confined by epithelial tissues, namely the ectoderm on the dorsal side and the endoderm on the ventral side, see Figure 1.9. At the most posterior tip of the embryo, we find the progenitor zone, which contains a group of stem cells and which becomes the tail bud during the latest stages of development, see Figure 1.9. During the formation of the vertebrate body, cell dynamics are governed by proliferation and migration which depend on their nature and location in the posterior body. These stages of posterior development are vital to form the essential organs and attribute their functions. In what follows, we detail the organization of the posterior region.

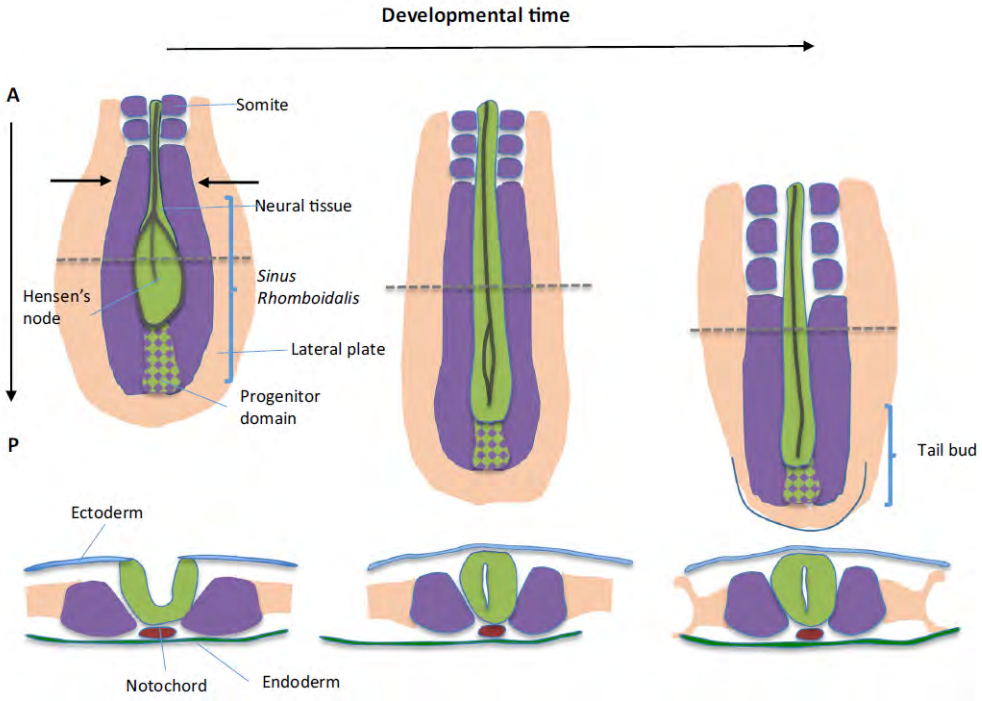

Figure 1.9 – Taken from [12]. Schema of posterior tissue morphologies and organization during posterior elongation. Dorsal view (top) and transverse sections (bottom) of the posterior part of higher vertebrate embryo during different times of axis elongation (from left to right: equivalent to stage 9HH, 11HH, and 15HH in chicken embryo). Paraxial mesoderm is in purple, neural tissue in green, notochord in red, lateral mesoderm in pink, ectoderm in blue, and endoderm in dark green, progenitor domain in purple and green. Ectoderm is not represented on the dorsal views. Note that tissues have a higher width posteriorly than anteriorly in the early phase (black arrows), whereas they are becoming more straight during later phases. General tissue organization remains conserved throughout the stages (transverse section); A anterior, P Posterior.

1.2.2 Organization of the posterior growth region

Posteriorly, the body is organized in a very specific manner: the NT is located axially, flanked with two stripes of PSM laterally. The PSM, is a mesenchymal tissue, where cells diffuse extensively, and proliferate. Some cells migrate towards the anterior to form the somites and others towards the posterior in the direction of the elongation of the embryo. The somites originate from the PSM which densifies and solidifies anteriorly. This is known as Mesenchymal-to-Epithelial Transition (MET) which occurs in a posterior to anterior manner in the PSM. The NT is a very dense epithelial tissue, where cells proliferate and adhere to each other, see Figure 1.10. The NT and the PSM grow in contact with each other and they maintain their segregation throughout their development. The extra-cellular matrix defines clear boundaries between the tissues along the antero-posterior axis. Their growth is due to cell proliferation and migration [24], but also thanks to newly added cells originating from the PZ. The PZ is a mesenchymal tissue located in the posterior tip of the embryo. Progenitors, also called neuro-mesodermal progenitors (NMPs), are a population of stem-like undifferentiated cells and are known to be bi-potent [147] (more details on NMPs in the next paragraph). Bi-potency is the ability of a stem cell to differentiate and give rise to two different cell fates. Indeed NMPs can give rise to either neural cells which will colonize the NT, or to mesodermal cells, which will migrate and enter the PSM. A portion of these NMPs remains in the PZ to regenerate (by cell division) the pool of progenitors continuously [33, 147, 131] (Figure 1.11). The PZ can be thought of as a mixing region between the NT and the PSM, as it contains cells of both fates. By means of live imaging and biological experiments on bird embryos, the role of each of the PZ, the PSM and the NT in the elongation process was highlighted in recent years [24, 25], giving some insight on the mechanisms of axis elongation.

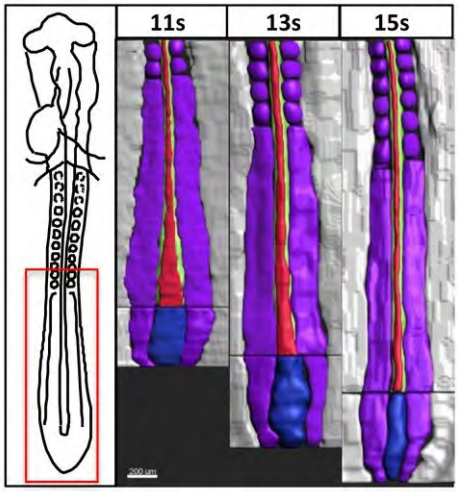

Figure 1.10 – Taken from [24]. 3D representation/drawing of different tissues forming the posterior part of quail embryo during axis extension (area of interest is shown in the red rectangle of the scheme on the left, ventral view; anterior side is at the top). The samples are: a representative 11 pairs of somites embryo (left), a 13 pairs of somites embryo (middle), a 15 pairs of somites embryo (right). The progenitor zone is in blue, the paraxial mesoderm is in purple, the notochord is in red and the neural tube is in green.

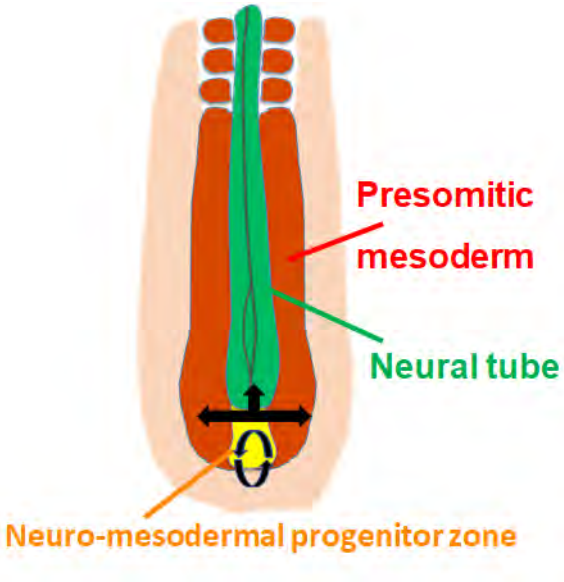

Figure 1.11 – Sketch of the tissues in the posterior growth zone. Straight black arrows represent the exit of NMPs into the NT and the PSM. Curved black arrows represents the self-renewal of NMPs.

1.2.3 Neuromesodermal progenitors

Progenitors are located at the most posterior end of the tailbud, in a zone called the progenitor zone. These progenitors constitute a good model to study how a group of undifferentiated cells can generate different tissues and organs. These progenitors were first studied in bird and mouse embryos. They were tracked using fluorescent markers which revealed that progenitors contribute to the formation of the PSM and of the NT [134, 156]. These works also demonstrated that a portion of these cells remains undifferentiated and self-renews in the PZ to provide progeny, while others colonize the PSM and the NT [32, 33]. Interestingly, this heterogeneous cell behavior within the PZ was further founded by single cell experiments in the mouse embryo. These experiments consist in following one progenitor cell and its descendants, which confirmed the bi-potency of progenitors, as a single cell gives rise to both neural and mesodermal cells. These cells are known as the neuro-mesodermal progenitors and were also documented in avian embryos and zebrafish [147, 131, 143]. These studies highlight the importance of progenitor balance between providing new cells to the NT and the PSM, and remain resident and proliferate to generate more progeny. How this balance is achieved remains an open question which we address in this manuscript.
On the protein level, two transcription factors Sox2 (SRY sex-determining region Y-box 2) and Bra (Brachyury) were identified in their role in the specification of respectively neural cells forming the NT [15] and mesodermal cells forming the PSM [87]. Indeed, a study showed that a high expression of Sox2 in undifferentiated NMPs is enough to induce their neural specification [146]. In contrast, Bra plays a key role in mesoderm formation. In [156], authors show that Bra mutant mouse embryos are unable to produce a posterior mesoderm. Interestingly, these transcription factors were found to be co-expressed in progenitor cells, prior to their exit from the PZ and colonization of the PSM and NT [159, 119], see Figure 1.12. The presence of both proteins supports the bi-potent nature (mixed identity) of NMPS. Unsurprisingly, these two proteins showed a significant effect on cell fate coupled with spatial sorting by fate: high Sox2 cell regions and high Bra cell regions were more prone to becoming respectively neural and mesodermal cells [159]. Finally, Sox2 and Bra are thought to have antagonistic activities on the neural and the mesodermal gene expressions, thus influencing the cell choice of becoming neural or mesodermal.
It is an active field to understand the relative contribution of the addition of new cells from the PZ into the posterior tissues versus the proliferation of each tissue to the axis elongation. Also, little is known about NMP movements within the PZ and their migration into the tissues, and how the protein expression of Sox2 and Bra affects these phenomena. We address these questions in this manuscript by combining mathematical modelling, numerical and biological experiments.

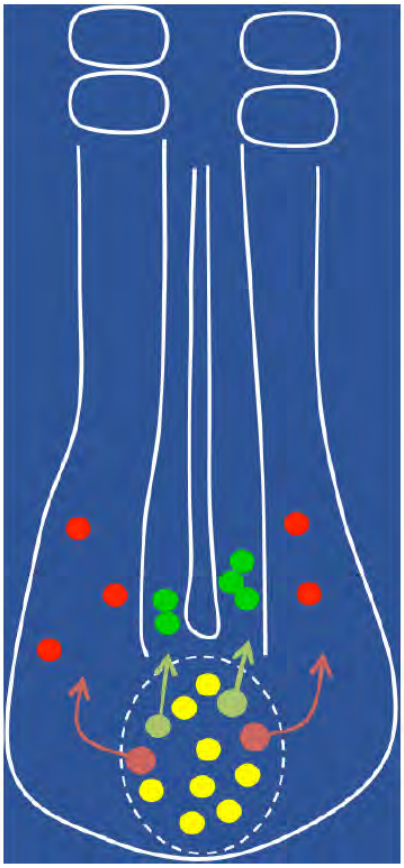

Figure 1.12 – Progenitor cells (in yellow and shades of yellow) give rise to mesodermal cells (red) that enter the PSM (red arrows in the lateral tissue expressing the Bra gene) and to neural cells (green cells expressing the Sox2 gene) that enter the NT (green arrows in the axial tissue).

1.2.4 Mechanisms of axis elongation

During vertebrate embryo development, thousands of cells self-organize following a very precise and complex choreography to form the tissues of the posterior region. Tissue formation comes hand in hand with the elongation of the embryo along its antero-posterior axis. In this section, we will lay out an outline of the known mechanisms of axis elongation. We rely primarily on the pioneering papers [25, 24] for the cell and tissue dynamics and exhibit the main results in what follows. The main biological motivations of this manuscript arose from these two papers [25, 24].

1.2.4.1 The biological models

The organization of the vertebrate body is reproduceable across vertebrates which display a striking anatomical resemblance at early developmental stages. In fact, these similarities gave rise to the famous hourglass model conjecture: at the very first stages of development species exhibit distinguishable features, they then converge to a common phenotype before diverging again and adopting specific traits per species [57]. To understand morphogenesis on a multi-scale level, bird embryos, but also zebrafish, frog (*Xenopus*) and mouse embryos are commonly used in literature to perform biological experiments. They constitute a great model to analyze cell and tissue behavior owing to their striking resemblance to human embryos at early developmental stages. More so, their availability, easy culture and accessibility to transgenic lines make them an efficient model. Biological experiments on these vertebrate embryos are also quite accessible, namely immunodetection and electroporation techniques. Finally, they are a suitable model since their development can be observed and quantified using live imaging, which is enhanced by the transparency of their bodies. Live imaging is especially used on these models as the same phenomenon that lasts for up to several weeks in humans, can last for only hours in bird embryos. This particular feature allows a faster study and analysis of morphogenesis.
In this manuscript we will often rely on studies involving bird embryos across their development. For that reason, it is useful to have in mind the staging classification of these embryos. The Hamburger-Hamilton (HH) staging [81], is a unified classification of embryos by age, commonly adopted in literature. The HH stages are determined by the number of embryonic structures called somites. Somites develop sequentially in time along the antero-posterior axis at a rate of one pair of somites per hour and a half. They can therefore provide a temporal marker for the stages of development. Each stage is characterized by an interval of three formed somites (Figure 1.13). In this thesis, we will use the same notations and staging criteria when describing bird embryos.

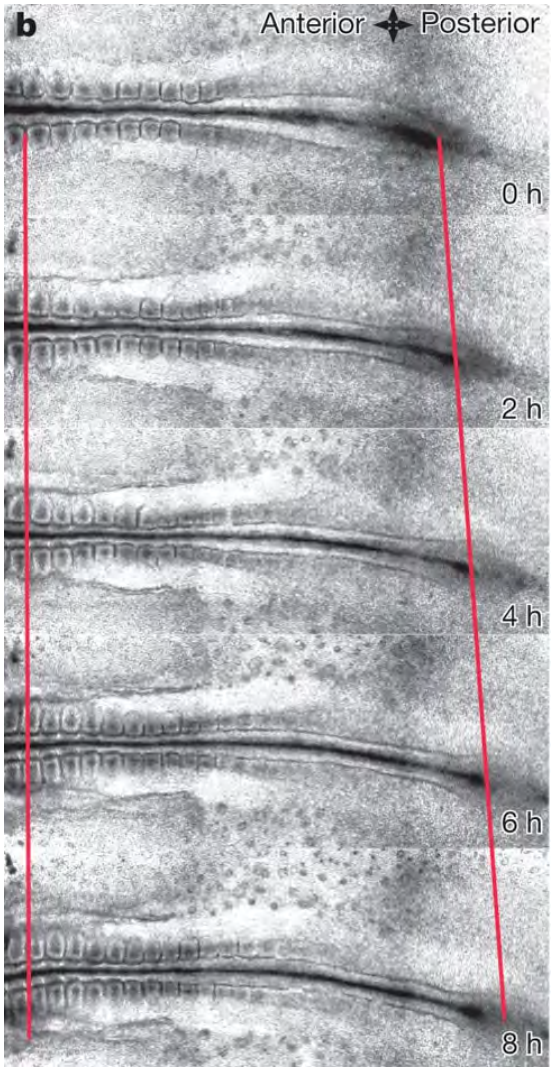

Figure 1.13 – Taken from [25]. Snapshot of different time points (during an 8-hour time period) showing elongation (red lines) of a wild type (WT) embryo starting at stage HH11. The left red line denotes the level of somite 3, while the right red line denotes the level of Hensen's node.

1.2.4.2 Convergence-extension

Historically, the origins of embryonic axis elongation was first explained in seminal papers [135, 93, 136] on frog embryos (*Xebopus laevis*) as the result of the convergence-extension phenomenon. Since then, it has been widely studied and described in literature on other vertebrates such as in zebrafish [154]. These works showed that the convergence-extension mechanism is crucial to form the anterior part of the axis. "Convergence" refers to patterned cell rearrangements during development. In fact, by intercalating medio-laterally, cells form a narrower and longer array. This behavior is thought to be the result of cell traction, which would first elongate the cells, then using a pushing force, rearranges them between one another. The intercalation must be oriented perpendicularly to the axial tissues and parallel to the medio-lateral axes. The consequence of cell convergence is the narrowing of the tissue followed by its elongation, this is referred to as "extension". The convergent extension phenomena can be either an active process as a result of cell intercalation, or a passive one driven by forces from interactions of multiple neighboring tissues (e.g extension by compression).

The narrowing and consequent lengthening of the tissue plays a key role in axis elongation as it can morph a wide and short tissue into a thin and long one [26, 111], but can also cause long range forces leading to the extension of the axis. If this convergence-extension mechanism explains how the NT and the notochord elongate, it does not explain the extension of the PSM along the antero-posterior axis, as it shows little to no convergence [25]. This is coherent with the findings that PSM cells move randomly. In fact, convergence-extension constitutes only the first phase of axis elongation. The second phase is primarily governed by the growth of the caudal region, with little change in the width of the axis. It is interesting to note here that axis elongation does not occur exclusively via the growth (volume gain) of the caudal region. If this is true in bird embryos, it is not for zebrafish. In fact, the zebrafish tailbud showed a smaller proportion of proliferating cells compared to the rest of the antero-posterior axis [142]. More so, it was shown that a down-regulation of cell division is necessary to form the paraxial mesoderm [19].

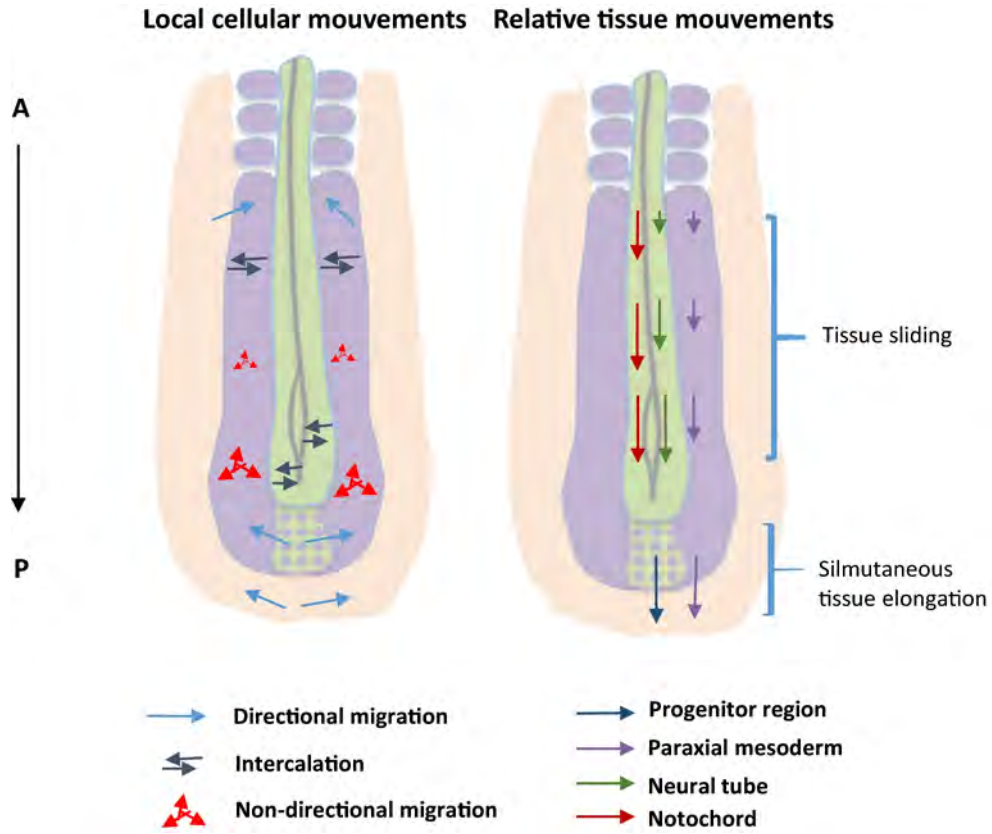

Figure 1.14 – Taken from [12]. Schema of the main cell and tissue movements during posterior elongation. Dorsal view of a schematized vertebrate embryo during posterior axial elongation. Local cellular movements on the left schema, relative tissue movements on the right schema. Note that tissue movements are shown relative to the last formed somite. Note that for a matter of simplicity, the elongation phase represented is a transition phase in which early and late phase movements are both present (equivalent of stage 10–11HH in chicken embryo).

1.2.4.3 The contribution of the PSM to axial elongation

Although convergence-extension is generally thought to be behind embryonic axis elongation, scientists found evidence that the way posterior tissues are spatially organized conveys them with certain mechanical and chemical properties which contribute to axis elongation. For instance, in [25], authors conduct a study on the role of the PSM during axis elongation and on its contribution to the posterior growth zone. Chicken embryos were used at stages 10-11 HH for the biological experiments. By performing laser ablation of several regions in the posterior part of the embryo they could identify the main structures controlling the posterior growth. Their first observation was that posterior PSM ablation had a significant effect on the elongation speed of the embryo whereas anterior PSM ablations had little effect. This allowed the authors to conclude that the posterior PSM plays a paramount role in axis elongation. A thorough analysis of cell movements in the PSM demonstrated a clear decreasing posterior to anterior motility gradient. Posteriorly cell motility reaches $1um/min$ whereas anterior cells move with a velocity of approximately $0.2um/min$. Strikingly, and although a global posterior movement is observed during axis elongation, the cell net movements were random, that is, no directional bias was observed in cell motility within the PSM. This observation was further supported by computations of the mean square displacement which showed a random walk like diffusive behavior. To sum up, all PSM cells move randomly, but posterior cells move more than anterior ones (Figure 1.15). This graded cell motility is supported by the discovery of an FGF8 (Fibroblast Growth Factor) decreasing posterior to anterior gradient in the PSM of chick, zebrafish and mouse embryos [58]. Studies showed the implication of FGF signaling pathways in the elongation process of the vertebrate embryo [91], by controlling cell motility. To confirm this control on motility in chick embryos, authors in [25] blocked the expression of FGF in the PSM cells and observed a clear decay in cell motility and in the elongation rate. Complementarily, the over-expression of FGF induced a random motion in the PSM even in the anterior region, which disrupted the graded motility profile. This suggests that FGF signaling pathway is responsible for the gradient of random cell motility. More so, their results also show that FGF controls cell density, which displays an opposite gradient to that of the motility. The motility and density gradients are consistent with the fact that PSM cells will regroup anteriorly to form the somites, thus the need to reduce their velocity and increase the cell density anteriorly. A posterior to anterior MET is then observed (Figure 1.14). This graded cell density was not accompanied by a gradient of proliferation of PSM cells. When proliferation was inhibited, no apparent effect was observed on the elongation rate for short times. This raises many questions on which biological factor (proliferation, density, cell migration) plays the key role in the elongation process. The authors end on an interesting note stating the importance of developing an accurate mathematical model that incorporates the antero-posterior forces responsible for elongation. The work in this manuscript addresses the mechanism of elongation by proposing multi-tissue mathematical models

which can determine the share of each biological factor in axis elongation.

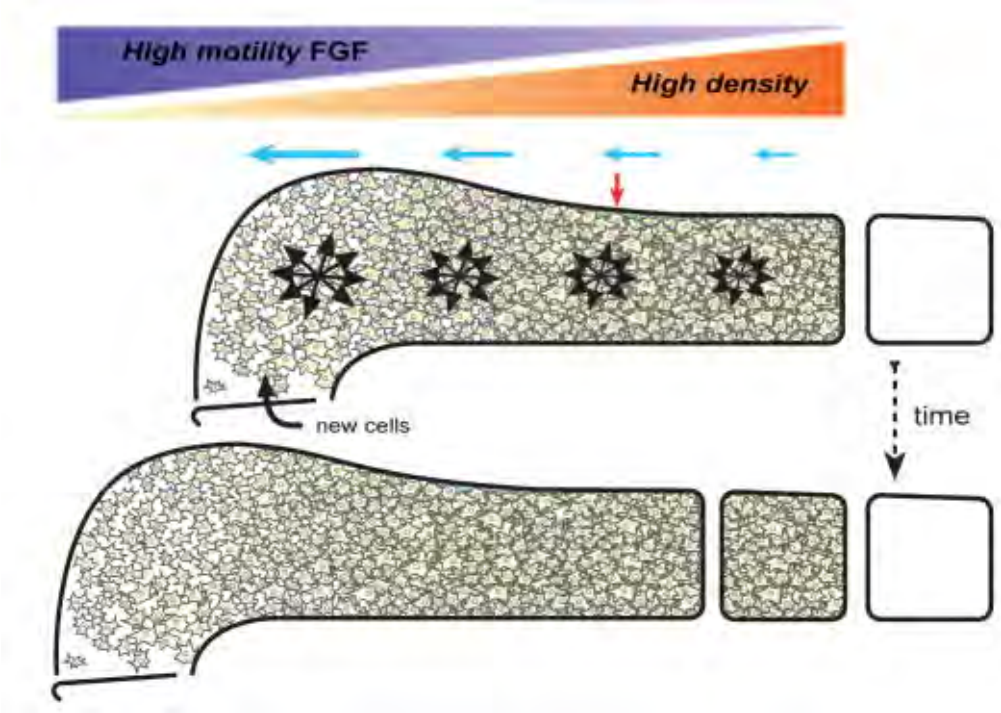

Figure 1.15 – Adapted from [25]. Model of the control of elongation by a gradient of random cellular motion in the PSM. Dorsal view of a schematic representation of the left PSM at two consecutive stages of embryo elongation. While new cells are entering the PSM, the gradient of random motility (lavender gradient; black arrow clusters) opposed to the gradient of cellular density (orange gradient) creates a directional bias in elongation (blue arrows) toward the posterior part of the tissue. This posterior expansion induces the convergence of the PSM tissue (red arrow).

1.2.4.4 Multi-tissue dynamics

Although the PSM displayed an important role in driving elongation, this process remains a complex combination of several tissues and different cell types in a collective dynamics. The emergence of new tools, algorithms and technologies allows to track these cells within the tissues and brings us a step closer to grasp the complexity of morphogenesis. Cell tracking revealed in the tailbud of the zebrafish embryos that extensive collective migration is behind its elongation [100]. More so, it was shown that interfering with cell-cell or cell-fibronectin interactions impairs the multi-tissue dynamics of axis elongation [56]. These works highlight the critical role of large-scale collective migration and multi-tissue mechanics on axis elongation in fish embryos. These results were also retrieved in bird embryos using an H2B-Cherry line of transgenic quails. Developing a line of transgenic models allowed to study the 3D multi-tissue kinetics in live time as all cells' nuclei are visible [88]. A more recent study [24] aimed at understanding this multi-tissue choreography on multiple scales by measuring and quantifying the contribution of each tissue (PSM, NT, PZ, notochord) in the elongation process. The main focus of the work in [24] was the multi-tissue dynamics during embryo elongation where authors analyze the tissues forming the posterior part of the vertebrate embryo by using as a biological model transgenic quails. The authors first investigated the variation in volumes during elongation. Using tissue specific markers allowed the delimitation of each tissue and the computation of the volume gain throughout embryo development. The results show that the PSM and the NT grow primarily in the antero-posterior direction (i.e. in length more than in width and thickness) during axis extension, but that the volume gain was not at all identical across the tissues. The PSM appeared to gain the most in volume, gaining up to $3 \times 10^6 \mu m^3/h$ followed by the NT with a volume expansion of $1 \times 10^6 \mu m^3/h$. The PZ showed no volume gain across HH stages. The authors then exhibited density measurements in the posterior region. Using DAPI staining (nuclear labeling) followed by segmentation algorithms, they generated a map of the densities in the posterior part of the embryo. This map shows a clear differential density between the tissues. The NT is the most dense tissue with a density reaching 2388 cells per 100 μm^3. It is followed by the PZ with a medium density between 1382 and 2388 cells per 100 μm^3. Finally, the PSM displays an antero-posterior density gradient along the axis, with a very high density anteriorly (close to the somites), comparable to that of the NT, and a low density posteriorly with less than 1382 cells per $100 \mu m^3$. These density patterns were compared across developmental stages and appeared to be conserved. The authors then looked at the proliferation rates of these tissues. By EdU labeling, they determined the cell cycle duration in each tissue. They found that these durations differ across posterior tissues. In fact, the notochord has the longest cell cycle (28 hours) followed by NT cells which divide with a cycle of 10.83 hours, and finally the PSM with a cell cycle duration of 8.75 hours. These discrepancies in the proliferation rates can very well explain the differential volume gains. By computing the elongation speed of

each tissue, the authors highlighted an even more apparent differential behavior. The elongation rates were computed by taking the last formed somite as a reference point. It was found that the NT elongates the most rapidly to the posterior with a growing antero-posterior velocity varying from $5um/h$ to $35um/h$ in the most posterior region. As for the PSM, it displays two different velocity profiles. Anteriorly, the velocities are negative, suggesting that cells move up towards the last formed somite, where they pack and solidify into a somite. Posteriorly, cell velocity reaches $25um/h$. The PSM and the NT join the PZ velocity posteriorly reaching $45um/h$. Finally, authors analyzed tissue deformations, namely the compression/expansion movements inside the tissues as well as the swirling cell motions. This analysis, made possible by 3D cell tracking, demonstrated a clear contraction anteriorly, corresponding to the closing of the NT and tissue expansion posteriorly was observed especially in the PSM. The swirling cell motions were observed and quantified inside the PSM: in the posterior region, clear medio-lateral vortices were seen, which may correspond to cell entry from the PZ. Anteriorly, dominant latero-medial vortices were observed. A closer look to the 3D images shows some adjacent anterior regions with opposite vortices appearing. To summarize, this comprehensive study of tissue dynamics during embryo elongation allowed the authors to propose that these dynamics are accompanied by inter-tissue sliding (Figure 1.14). This hypothesis was supported by a computational model. The causes of this sliding appear to be directly related to the differential bio-physical properties of these tissues. However, it is still unclear as to which mechanism, or combination of mechanisms (differential proliferation, entry of new cells from the PZ, differential cell motility...) plays the key role in this choreography of axial elongation [111]. One of the main goals of this manuscript is to bring answers to this question by means of mathematical modelling.

Altogether, the extensive literature on the mechanisms of axis elongation shows the extent of complexity of this process and the need to understand how these mechanisms are tuned to ensure the right extension.

After having introduced the biological system to model, and having evoked some of the main questions that arise during axis elongation, we will go into detail of the objectives of this thesis.

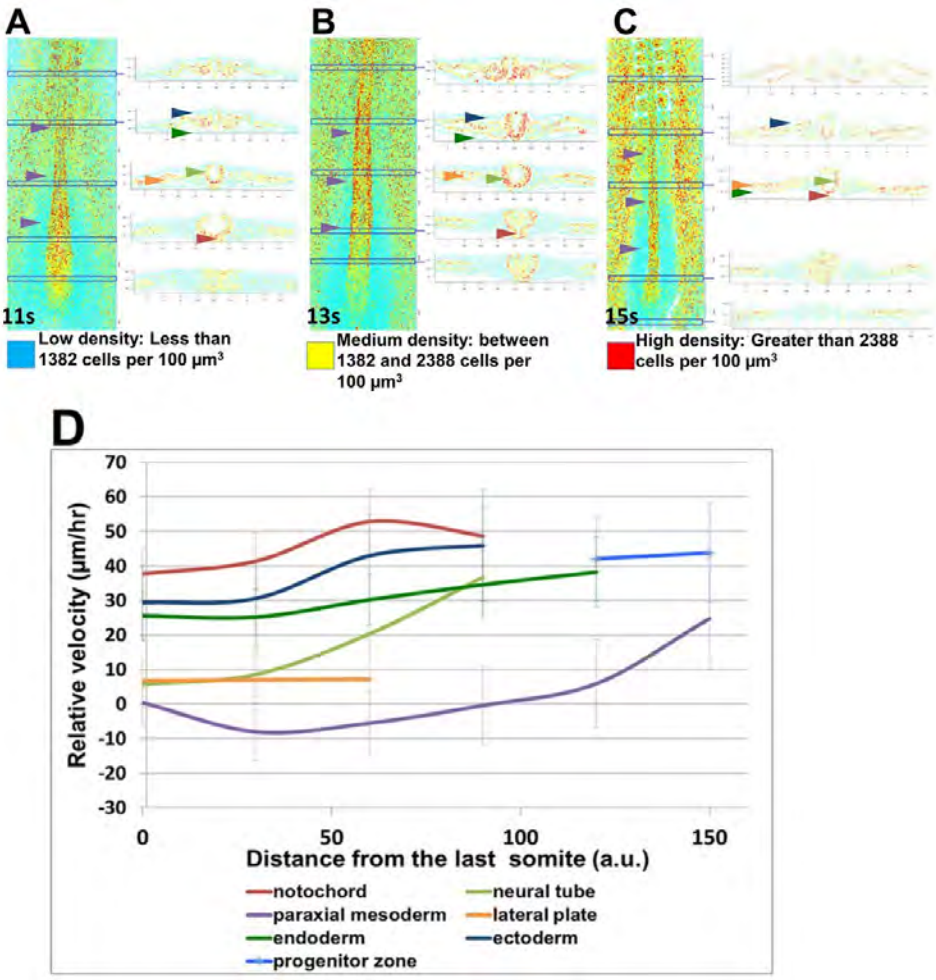

Figure 1.16 – Adapted from [24]. (A-C) Cell density in the elongating embryo. 3D density map (dorsal view) and associated transverse sections of representative embryos at different stages. 11 pairs of somites (A), 13 pairs of somites (B), 15 pairs of somites (C). Colors represent average cell densities: cyan codes for density lower than 1382 cells/100 μm^3, yellow codes for density between 1382 and 2388 cells/μm^3, red codes for density higher than 2388 cells/μm^3. The cell densities for PSM, endoderm and ectoderm are low (purple, green, blue arrowheads, respectively), cell densities for the notochord, neural tube and lateral plate are medium to high (red, light green and orange arrowheads, respectively); note that within the paraxial mesoderm there is a caudal-to-rostral increasing gradient of cell density (purple arrowheads). (D) Averaged differential tissue motilities along the A/P axis. Zones of interest along the antero-posterior axis were tracked, and their motilities were calculated compared with the last-formed somite. Error bars represent standard error of the mean. Distances from the last-formed somite to the end of the notochord were normalized. a.u., arbitrary units.

1.3 Objectives

In this manuscript, we are interested in the multi-tissue dynamics occurring during vertebrate embryo development. These dynamics are very complex and sometimes seem to obey certain biological rules, while other times they seem to be governed by pure randomness. In the previous section we evoked some interesting phenomena observed during embryo development. Our goal is to understand and explain their origins. We recall the striking phenomena we observe:

- The segregation of the PSM and of the NT along the antero-posterior axis and across all stages of development. This separation is not present in the PZ, which we can consider as a zone of mixing as it contains cells of both fates.
- The PSM exhibits swirling motions along the antero-posterior axis which seem to have an effect on tissue dynamics.
- Altogether the known results on axis elongation seem to suggest multiple mechanisms driving the elongation, namely cell proliferation, addition of new cells migrating from the PZ, biophysical properties intrinsic to each tissue, and tissues' differential velocities.
- Finally, while NT cells and PSM cells show mostly an expression of the Sox2 protein and the Bra protein respectively, the PZ displays a co-expression of Sox2 and Bra which appears to be involved in cell behavior.

Based on these observations, we set three goals:

1. **Objective 1. Develop macroscopic PDE models exhibiting segregated solutions and swirling motions.** We develop hydrodynamic mechanical multi-species PDE models as the behavior of interest relates to collective dynamics on the tissue scale. In these models, the tissues are considered as viscous fluids, and the observables are the evolution in time and space of the tissues' density, velocity and pressure. For this objective, we are concerned in selecting the most adequate mechanical forces which will segregate the model's solution and in the most adequate physical laws which allow to observe swirling motions. We aim to link these models to their free boundary formulations via the incompressible limit, and focus on the theoretical study of the geometric models. We seek to extract properties from these models regarding the solution's behavior, which yields meaningful physical properties on the biological model. Finally, we apply these models to embryonic development. We test different hypotheses as to the types of segregations, namely active or passive, which can explain how the PSM and the NT grow segregated and remain segregated throughout the development. We propose some biological tests to validate the emerging biophysical hypotheses from the models.
2. **Objective 2. Determine the share of each morphogenetic mechanism on axis**

elongation. Although the models in Objective 1 emulate well the elongation of the embryo and the inter-tissue kinetics observed *in vivo*, they can be complexified and completed to incorporate more physical mechanisms involved in elongation. Therefore, our second goal is to include in these models most of the possible mechanical mechanisms known to take part in vertebrate development. Namely this new model includes cell proliferation and cell addition from the PZ as drivers of growth. It also accounts for the differential biophysical properties such as tissue viscosity and friction. An important step is to calibrate this model using existing parameters in literature and by doing biological experiments and image analysis. We seek to use this model to test different morphogenetic combinations of these mechanisms *in silico*. This approach determines the right set of parameters that emulates best the elongation of the vertebrate embryo. It also assesses the share of each morphogenetic mechanism on axis elongation and on the sliding between the tissues. Finally, it highlights the governing mechanisms or combination of mechanisms driving elongation.

3. **Objective 3. Investigate the role of the two proteins Sox2 and Bra on the population of progenitors.** Bi-potency conveys progenitors the ability to differentiate and to colonize the NT and the PSM. This process is accompanied by either a decrease or an increase in protein concentration in Sox2 and Bra. Moreover, some cells remain resident in the PZ and self renew. Sustaining this balance between differentiation and migration plays a key role in the formation of the posterior body. In this project, the main goal is to understand how NMPs' balance is maintained between providing new cells to the tissues and keeping the pool of progenitors alive in the caudal region of the embryo. We focus on the gene expression Sox2 and Bra inside the progenitors to highlight their role in PZ maintenance. By using immunodetection and electroporation techniques, we aim at determining and quantifying the effect of Sox2 and Bra expression in progenitors on cell motility, cell fate, and on the spatial cell distribution inside the PZ. Driven by biological experiments, we develop a microscopic stochastic agent-based model linking protein expression and cell behavior. We explore this model numerically and test different spatial cell distributions within the PZ. The objective of this model is to improve our understanding of the contribution of spatial cell patterning on tissue formation.

To achieve these goals, we will exhibit in what follows our modelling approach and compare it to the existing models in literature.

1.4 Modelling of morphogenesis: state of the art

During morphogenesis, embryonic cells migrate and divide extensively. Cell migration allows tissue formation and reshaping whereas cell division enables growth. Cell migration plays a critical role in biology (embryonic growth, cancer development, medicine, wound healing, tissue regeneration). It is known that most of the cell motion occurs in a collective manner. Cells migrate in groups using inter-cellular interactions or cell and tissue interactions or interactions with their environment. Morphogenesis is a direct consequence of collective cell migration, growth and of interactions ranging from the cell to the tissue scale. Understanding this process on the cellular level requires agent-based models that are able to capture the complexity of the cell, and the inter-cellular interactions. These models are able to capture discontinuous cell behavior, and can capture heterogeneities. In heterogeneous cell populations where gene expression is variable from cell to cell as well as cell motion, genotype and phenotype, the extent of the role of heterogeneity on collective migration is still an active field. To comprehend morphogenesis on the tissue level, we find in literature PDE models that are commonly used to capture long range forces being transmitted across the tissue, or between the tissues. The aim of this manuscript is to contribute to the active field of mathematical modelling, in PDE/ODE and agent based models, which can reproduce and explain the origins of morphogenesis. To this end, we will now exhibit some existing agent-based models and PDE/ODE models on axis elongation, cell migration and specification and compare them to our modelling approach.

1.4.1 Models for axis elongation

Our modelling approach consists in considering complex systems of the macroscopic type and of the microscopic type. For Objectives 1 and 2, as they both pertain to the tissue scale, our approach entails macroscopic PDE models and their techniques, by considering tissues as viscous fluids. These model are of the **hydrodynamic type**, where the observables are the evolution in time and space of the density, pressure and velocity of the tissues. We consider the **fully mechanical** point of view to explain axis elongation, i.e, we will not consider chemically induced elongation (such as signaling pathways or chemotactism). The mechanical phenomena we consider are:

- Tissue proliferation
- The addition of new cells from the PZ
- Biophysical properties: tissue viscosity and friction
- Inter and intra tissue pressure

More specifically, our models are in **2D** (in space), as the vertebrate embryo is very flat, and because the biological data at hand is most often in 2D. To account for the different segregated tissue types

involved (PSM and NT) and their development in contact, our models are **multi-species**. They allow to consider the inter and intra tissue mechanics (congestion, repulsion) which we use to explain tissue segregation. Our mechanical point of view distinguishes our work from some models in literature, which consider chemical signals to explain elongation. In [129], a first 2D agent-based model is developed to account for FGF8 signaling and its effect on cell motility in the PSM. It incorporates cell size and diffusivity, and the temporal degradation of FGF8. Their approach is geometric, as they model the elongating posterior boundary of the PSM as an elastic spring that elongates as a response to pressure from the cells in the PSM. This model is a great paradigm to test different sets of cell parameters, such as cell diffusivity and velocity on PSM elongation. However, it only considers one cell type (that of the PSM), which is not aligned with our objectives. In the same paper [129], authors develop a mechanico-chemical PDE model of the free boundary type to describe the evolution of the PSM. The driving mechanism of elongation considered is cell ingression from the PZ. The model accounts for the FGF8 signaling gradient within the PSM controlling cell motility, and for the viscous frictions through the Brinkman law. This model suggests that cell ingression accompanied with PSM confinement by the lateral plate can explain axis elongation. Although this model emulates well axis elongation and allows parameter fitting (viscosity and friction within the PSM), it does not include proliferation as a possible mechanism, and it cannot explain the multi-tissue dynamics occurring during development as it is mono-species. In our approach, as our goal is to understand the multi-tissue dynamics during axis elongation, we intend to address this modelling aspect by considering multi-species models with proliferation in the reaction terms of the equations. A similarity we have with [129] is considering the tissues as viscous fluids. We also make use of the Brinkman law for the velocities of the PSM and the NT, which allows to consider different viscosity coefficients for each tissue. We use the parameters estimated in [129] (and in [108]) for the PSM and NT's viscosities and for the friction terms.

Finally, our approach has the additional advantage of offering two descriptions: a density description and a free boundary description, and ensures the mathematical link between them. Other chemical models were based on FGF8 signaling to regulate the regression and patterning of the posterior region in the developing embryo [82, 10]. In these works, the formation of gradients of FGF8 and their regulation along the antero-posterior axis are investigated. Authors in [82] develop a 1D continuum model to study the concentration of FGF8. They postulate that the FGF8 secretion induces a chemotactic like behavior and could underlie the migration towards the posterior - via the study of traveling wave solutions. Our point of view does not consider the chemical interplay between signaling pathways and cell behavior but rather considers the effect of signaling pathways on the density. Precisely, the 2D model developed in Objective 2 accounts for the density gradient -induced by the FGF8 gradient- in the PSM in the initial condition and is maintained throughout the development. ODE models were developed to focus on the volume gain of the different tissues during elongation. We cite the model in [24] where only cell proliferation is considered to drive

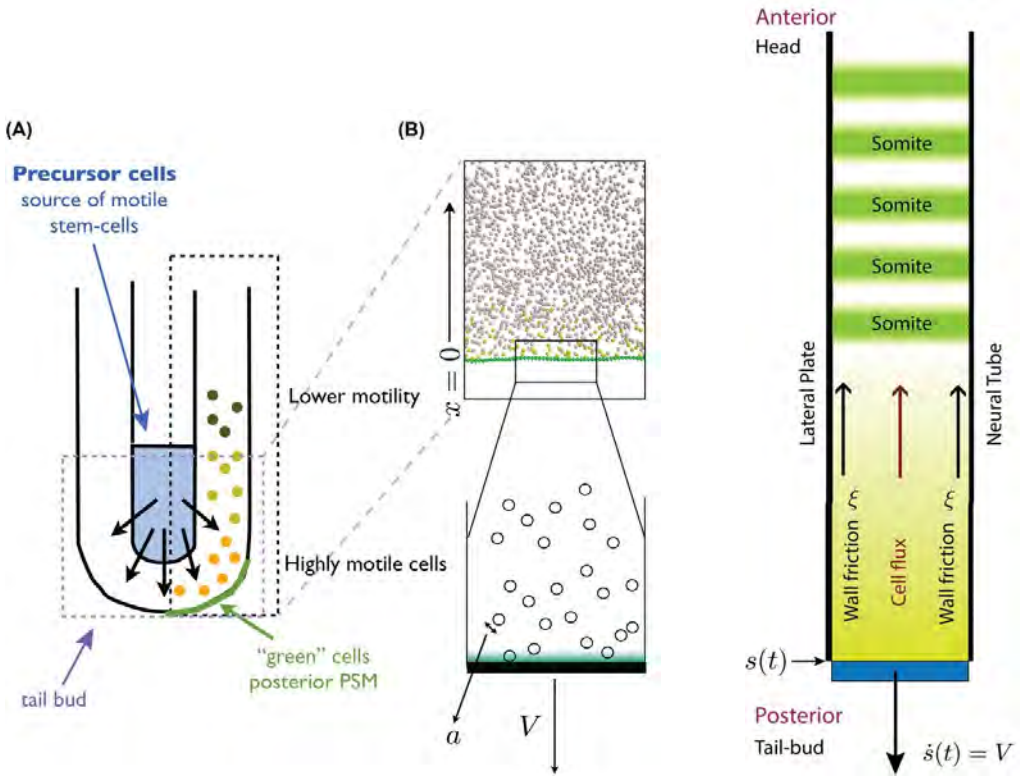

Figure 1.17 – Adapted from [129]. Left: Microscopic cell-based simulation: (A) Schematic view of the presomitic mesoderm used as a basis for a cellular simulation. (B) Yellow and grey spheres represent motile and immobile cells respectively. The green spheres form a connected wall which represents the tailbud and can move in response to pressure applied by the motile cells. The wall velocity is V and the size of the cell is a. Right: Macroscopic continuum model. Schematic showing half of the PSM in the neighborhood of the tailbud whose position is $s(t)$.

elongation (in length). This model incorporates four posterior tissues: the NT, the PSM, the PZ and the notochord. The model simulation shows that all four tissues have elongated after a few hours of development, using only proliferation as a driving force. Interestingly, this model suggests a possible sliding between the tissues, but fails to explain inter-tissue kinetics as there is no tissue coupling in the model. Moreover, the addition of new cells from the PZ into the PSM and NT is not taken into account. This is yet another divergence with our approach. As our goal (Objective 2) is to evaluate the contribution of the addition of new cells from the PZ into the PSM and the NT versus cell division, it is crucial in our modelling approach to incorporate cell injection in the PSM and in the NT, and cell proliferation to account for (almost) all the possible mechanism behind tissue growth.

Finally, we find an exhaustive literature on multi-species PDE models exhibiting segregated solutions (tissue separation). The segregation is a consequence of the coupling of the species' equations through a nonlinear cross diffusion, typically modelling volume exclusion, repulsion or

differential adhesion between cell types [18, 34, 50, 63, 105, 22, 23, 51]. These models propagate segregation from initial data, i.e initially segregated tissues remain segregated. In the case of the growing embryo, the PZ is the origin of the formation of the PSM and the NT. It is a mixed region where both cell types coexist. We seek to understand how these initially mixed cells segregate into different tissues, which is different than propagating segregation. In our approach, we want to test the hypothesis of an enforced segregation via a repulsion pressure. Our model will then ensure tissue segregation, and its persistence throughout the development.

We now discuss the different modelling approaches involved in modelling cell specification and cell migration.

1.4.2 Models for cell specification and cell migration

Microscopy techniques and their advancements allow researchers to observe cell-specific properties such as cell shape and size, and filopodia extensions for environment exploration. This level of detail is incorporated in agent-based models, which are often stochastic. These models confer the cell with the ability to evolve as an individual entity and to interact with other cells according to a set of rules inspired by known biological properties. These properties can include: cell-cell attraction, contact inhibition [1], repulsive interactions, chemotaxis... Interesting dynamics arise when coupling migration and specification. For example, pattern formation can emerge in colonies, see Figure 1.18. This pattern can be due to several mechanisms. Indeed, consider a colony of cells

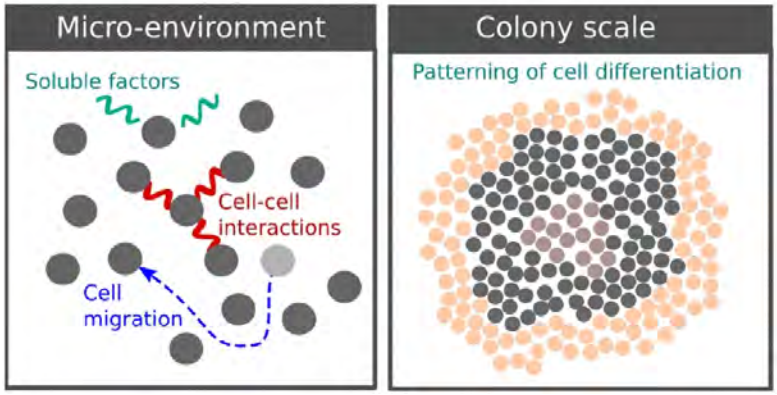

Figure 1.18 – Taken from [152]. Left: Cell micro-environment e.g., interaction with other cells, the medium and substrate. Right: Colony-scale phenomena e.g., patterning of differentiated cells.

which do not move extensively (do not mix nor change neighbours, or the time scales of their movement is very small compared to the pattern formation scale). In this case, graded cell differentiation is the mechanism that confers them this patterned shape. This is known as the french flag model. Gradients of signals convey a specific identity to each cell depending on its position with respect to the gradient, see Figure 1.19).

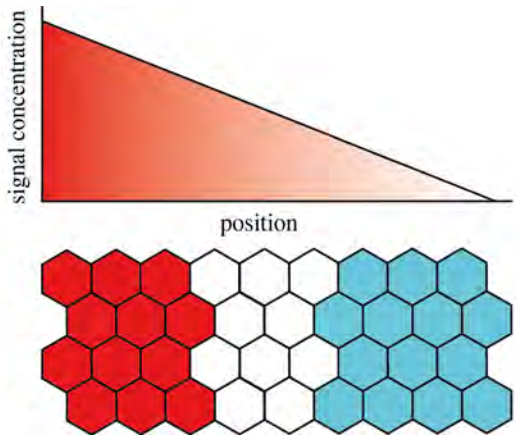

Figure 1.19 – Taken from [144]. The french flag model. Cells sense the signal gradient and differentiate spatially according their position with respect to the gradient.

In Objective 3, we are interested in how progenitors balance their proliferation and their colonization of the PSM and the NT. The interplay between proliferation, cell specification and migration into the tissues is crucial to maintain the pool of progenitors and to add new cells to the tissues to ensure their growth. The protein expression Sox2 and Bra within PZ cells seems to play a key role in their bi-potency. Moreover, we are concerned with the effect of Sox2 and Bra on the spatial distribution of cells in the PZ. We want to investigate the consequent pattern formation in the PZ with respect to this distribution and the properties it confers to the formation of the posterior body.

In consequence, as the scale of interest is the cell, we adopt an agent-based modelling approach. Our approach consists in constructing 2D stochastic models to depict cell motility, and protein concentration (in Sox2 and Bra). The latter determines their differentiation stage. The model is multi-species, as it accounts for the progenitors, and the surrounding PSM and NT cells. The model comprises two equations: one for the time evolution of the cells' positions (in 2D) and the other for protein time evolution. At each time step we numerically solve each equation for each cell. It is interesting to mention that a variety of agent-based models are based on the minimization of a free energy which governs the system [66]. The latter formulation allows to integrate different viscous and mechanical forces that are transmitted to the cells and which add up to the system's energy. In our approach, the agents (cells) are moving 2D points in a bounded domain which allows us to ignore cell size and shape in our model. Usually, cell shape is taken into account when modelling an epithelium (such as the NT) [70, 106]. In our case, as we are modelling different tissue types (the PSM is mesenchymal), we do not consider cell shape. For cell displacement, we use a classic Brownian motion, with a protein-dependent velocity. The use of stochasticity is not a novel feature, in fact many models incorporate it in cell positions, cell fate, or cell proliferation to model heterogeneities within the population [106]. All the cells in our agent-based models are

conferred with the ability to proliferate. We also consider local forces with short range effects, i.e we use congestion dependent rules where cells evaluate their local surrounding density and move accordingly. In many models, cells have the ability to sense their environment and adapt their behavior accordingly. The cell-cell interactions we consider are protein-dependent adhesion rules. These rules are translated as a modified cell displacement (when cells adhere they move less in the opposite direction). This is in contrast with other models where cell-cell attractions are modeled as strings (one-dimensional or two-dimensional) [115, 129, 106] which make use of Hooke's law. Interestingly, cell-matrix interactions can also be incorporated to account for cells sensing not only the presence of other neighboring cells, but also for their affinity with their ambient environment [70]. As for the evolution of the cells' protein concentration, very few is known about its fluctuations. Therefore, we include Brownian variables to depict the evolution of protein concentration. Our approach has the advantage of bringing out possible pattern formations as in Figure 1.18, as we consider cell-cell interactions, differentiation and migration as driving forces of PZ dynamics. To sum up, we take into account the following properties in our agent-based models:

- Cell movement in 2D (random motion)
- Protein concentration (Sox2/Bra)
- Cell division for all cell types
- Local cell-cell attractions
- Local non-mixing rules

With these ingredients, we use this model to highlight that the collective migration of cells in the direction of the posterior region (elongation) emerges as result of the cell-cell interactions encoded in our model. This property was also found in the migration of neural crest cells [158]. Finally, our simplistic modelling approach challenges the french flag model and demonstrates the role of cell distribution in the PZ (depending on protein expression) by having the advantage of testing distinct patterns.
In what follows, we exhibit the main results in this manuscript per chapter.

Chapter 2

Main results

In this section, the main results of this manuscript are exhibited. We divide this section in three parts. The first part deals with our contribution on continuum models for tissue growth (Objective 1). In the second part we present a mathematical model for axis elongation and confront it to the biological data (Objective 2). Lastly in the third part we present biological experiments on quail embryos and agent-based models for cell specification and migration (Objective 3).

In what follows, we exhibit in detail the main results in each chapter.

2.1 Multi-species viscous models for tissue growth: incompressible limit and qualitative behaviour.

As per Objective 1, we aim to understand the origins of tissue segregation and of swirling motions. For that reason, we develop two mechanical multi-species 2D models incorporating the Brinkman law for the velocity, which allows the appearance of swirling motions in the right setting. We test two types of segregations: in the first model, segregation is solely propagated from initial data, i.e, if the solution is initially segregated it remains segregated. In the second model, we encode a segregation pressure which actively segregates the solution in finite time, if initially mixed. We study the two models numerically and find that both models reproduce well axis elongation. Interestingly, only the model with active segregation reproduces the exact swirling motions observed in the embryo. This analysis led to an exciting biological hypothesis which suggests that an active force may be at play to segregate tissues throughout the development of the embryo. We compute the incompressible limit of each model and derive their corresponding geometric formulations. Considering the geometric models at their stationary states, we exhibit well-posedness and regularity results on the velocity-pressure system. We show that the pressure exhibits jumps on the tissues' geometric boundaries. This work is exhibited in Chapter 4.

In this chapter we aim to understand how tissue segregation occurs and is maintained during embryonic growth, and explain the origins of observed swirling motions. In Figure 2.1, we schematize the observed rotations in cell movements in [24]. For example, within the left PSM, posterior rotations are clockwise and are related to cell exit from the PZ. Anteriorly, a global counter-clockwise

rotation is observed. However, live imaging showed small regions of alternating rotations. We aim at capturing and understanding these complex dynamics via mathematical modelling.

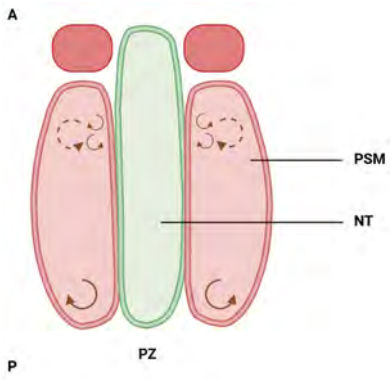

Figure 2.1 – Sketch of the cell rotations inside the PSM. As anterior cell movements are less obvious compared to the posterior ones, the arrows representing the global vortices are dashed. Small vortices of opposite directions are also observed in the anterior region. The notations A and P respectively denote the anterior and the posterior parts of the embryo.

Modelling tissue segregation and swirling motions. We have presented in Chapter 1 the main ingredients which we will use to construct models for tissue segregation and swirling motions. Having two interacting species to model (the NT and the PSM), we are clearly in the context of multi-species systems. By considering the NT and the PSM as viscous fluids, we develop variants of equations (1.13)-(1.14) on the population densities, taking into consideration only their mechanical interactions, but also the growth of each tissue due to cell proliferation and cell death via reaction terms of the type (1.3). We use the Brinkman law presented in (1.10) to allow the appearance of swirling motions in the form of nontrivial curls. We consider different viscosity coefficients for the tissues as one is epithelial and the other is mesenchymal. Mechanical interactions entail, similarly to (1.13)-(1.14), mechanical pressures as functions of the two densities thus generating a non-linearity in the equations. This non-linearity is an interesting addition to the system, as it is responsible for possible segregation phenomena.

Strategy: the VM and the ESVM. We construct two models: the Viscous Model (VM) and the Enforced Segregation Viscous Model (ESVM). They both entail the ingredients described previously, i.e evolution equations on the population densities, the Brinkman law for the velocities to observe swirling motions, mechanical pressures in terms of the two densities. We use these models to test two different types of segregations: a passive segregation, and an active one. In the VM, segregation is passive, i.e propagated from initial data. That is, if initially segregated, the densities

remain segregated for all times. In the ESVM, we actively enforce segregation using a mechanical repulsion pressure which penalizes the presence of both densities in the same region. The ESVM allows to consider initially mixed densities which segregate in finite time except for a small interface. In what follows, we introduce the two models, and compare them to identify the most suitable one that emulates best the observations *in vivo*.

We now construct the VM.

Model 1: The Viscous Model (VM). We consider two cell population densities $n_1(t,x)$ (representing the NT) and $n_2(t,x)$ (representing the PSM) evolving in space and time. We consider both tissues as viscous ones, and confer them with viscosity parameters, respectively β_1 and β_2, and use the Brinkman law to govern the velocities v_1 and v_2 of each tissue. The model equations are as follows. For all $(t,x) \in [0;+\infty) \times \mathbb{R}^d$,

$$\partial_t n_1 + \nabla \cdot (n_1 v_1) = n_1 G_1(p_\epsilon), \tag{2.1}$$

$$\partial_t n_2 + \nabla \cdot (n_2 v_2) = n_2 G_2(p_\epsilon), \tag{2.2}$$

$$-\beta_1 \Delta v_1 + v_1 = -\nabla p_\epsilon, \tag{2.3}$$

$$-\beta_2 \Delta v_2 + v_2 = -\nabla p_\epsilon, \tag{2.4}$$

$$p_\epsilon = \epsilon \frac{n}{1-n}, \qquad n = n_1 + n_2. \tag{2.5}$$

The evolution equations on the densities (2.1)-(2.2) can be seen as variants of the equations (1.13)-(1.14) where we replaced Darcy's law with Brinkman law for the velocities' as it allows the appearance of nontrivial curls. The evolution equations also consider cell proliferation in each tissue through a reaction term (on the right hand side) which is another difference with (1.13)-(1.14). Cell division and death rates are encoded in each tissue i by the functions $G_i, i = 1, 2$. They are typically taken as decreasing functions of the pressure. The congestion pressure p_ϵ in (2.5) is a function of the total density $n = n_1 + n_2$, and controlled by $\epsilon > 0$. The pressure is taken singular in $n = 1$ (chosen as the maximal density) to inhibit cell overlap. Commonly in literature we find a power pressure law of the form,

$$p(n) = \frac{\gamma}{\gamma - 1} n^\gamma, \tag{2.6}$$

with γ a positive parameter and $n = n_1 + n_2$ the total density. However, this law does not insure the non-overlap constraint.

The VM is a variation of the model in [47]. The latter model is in itself a natural generalization to the two-species case of the model used in the case of tumor growth in [125] for a single species (presented in Chapter 1). The main difference between the model (2.1)-(2.5) and the one in [47], is that the Brinkman law in [47] considers the velocity in the form of a gradient, and in the whole

space ($\mathbb{R}^d$). However, this setting does not allow the appearance of swirling motions, and this is not in accordance with our Objective 1. For that reason, in the VM, we do not make any assumption on the form of the velocity, and formulate our problem in a **bounded domain in $\mathbb{R}^2$, with homogeneous Dirichlet boundary conditions on the velocity**.
Interestingly, by taking the pressure as a function of the total density, we recover a similar segregation phenomena as the one we observed in equations (1.13)-(1.14). More precisely, if we consider the tissues' viscosities to be equal ($\beta_1 = \beta_2$), we can formally show that if the densities are initially segregated then they remain segregated for all times. We will call this statement the *segregation property* which is stated in the following proposition.

Proposition 2.1.1. *(Formal) [Segregation property, VM] Let n_1, n_2 solve (2.1)–(2.5) and suppose $\beta_1 = \beta_2$. If the initial densities are fully segregated, that is, $n_1^{ini} n_2^{ini} = 0$ on $\mathbb{R}^d$, then the densities remain segregated for all times:*

$$n_1 n_2(t,x) = 0, \ \forall (t,x) \in [0;+\infty) \times \mathbb{R}^d. \tag{2.7}$$

We numerically observe that the segregation property is verified also in the case $\beta_1 \neq \beta_2$. We refer the reader to Chapter 4 for more details.

Numerical illustration. Let us now take a closer look at the swirling motions in the VM. We perform numerical simulations of the VM in Figure 2.2 Panels (c)–(d) with the initial densities taken as ${n_1}^{ini} = 0.9\chi_{[-2/3;2/3]\times[-1;0]}$ and ${n_2}^{ini} = 0.9\chi_{([-1;-2/3]\cup[[2/3;1])\times[-1;0]}$ with χ the indicator function. The densities (left panels) emulate very well axis elongation and tissue growth and shape. The swirling motions (right panels) are also consistent with the general curls observed in the PSM. Indeed, we notice in the left PSM clockwise rotations in the posterior, and counter clockwise rotations in the anterior region of the PSM. However, we do not observe the anterior regions of alternating curls. This suggests that another phenomena may be at play to replicate these swirling motions. We investigate this hypothesis in what follows.

We now construct the second model (the ESVM) which differs from the VM in the way segregation is encoded. In the ESVM, we enforce tissue segregation by including a mechanical segregation pressure we call q_m. This model allows to consider initially mixed densities which will segregate in finite time, except for a small interface. Using the same notations as the ones in the VM, the model is as follows.

Model 2: The Enforced Segregation Viscous Model (ESVM). For all $(t,x) \in [0;+\infty)\times \mathbb{R}^d$,

$$\partial_t n_1 + \nabla \cdot (n_1 v_1) + \alpha \nabla \cdot (n_1 \nabla(\Delta n_1)) = n_1 G_1(p_1), \tag{2.8}$$

$$\partial_t n_2 + \nabla \cdot (n_2 v_2) + \alpha \nabla \cdot (n_2 \nabla(\Delta n_2)) = n_2 G_2(p_2), \tag{2.9}$$

$$-\beta_1 \Delta v_1 + v_1 = -\nabla p_1, \tag{2.10}$$

$$-\beta_2 \Delta v_2 + v_2 = -\nabla p_2, \tag{2.11}$$

$$p_1 = p_\epsilon(n_1 + n_2) + n_2 q_m(n_1 n_2), \tag{2.12}$$

$$p_2 = p_\epsilon(n_1 + n_2) + n_1 q_m(n_1 n_2), \tag{2.13}$$

$$q_m(r) = \frac{m}{m-1}((1+r)^{m-1} - 1),\ r = n_1 n_2, \tag{2.14}$$

$$p_\epsilon(n) = \epsilon \frac{n}{1-n},\ n = n_1 + n_2. \tag{2.15}$$

The ESVM, similarly to the VM, considers evolution equations on the population densities n_1 and n_2, with reaction terms modelling cell proliferation and cell death via the functions G_i. The Brinkman law is also used for the velocities v_1 and v_2, but we note the difference in the pressures p_1, p_2 in the right hand side of the equations (2.10)-(2.11). The total pressures p_1 in (2.12) and p_2 in (2.13) in each tissue are the sum of the congestion pressure p_ϵ and the segregation pressure q_m. The congestion pressure p_ϵ is a function of the total density $n = n_1 + n_2$, and q_m a power function of the product $r = n_1 n_2$ which is null whenever n_1 and n_2 are not in contact. The fourth order term in $\alpha > 0$ in the evolution equations enforces stability on the ESVM induced by the segregation pressure q_m. Indeed, when considering the system with $\alpha = 0$, initially mixed densities tend to segregate by forming multiple patches of each density, this is known as the *bubble effect*. Adding the fourth order term controlled by the parameter α promotes the cohesion of the densities, that is, two initially mixed densities will segregate in bulks, minimizing the appearance of multiple patches. Finally, the parameters $m > 0$ and $\epsilon > 0$ control respectively the repulsion pressure q_m, and the congestion pressure p_ϵ.

This model is inspired by the two-species model in [39] where it was applied to study tissue segregation in Drosophilia, with Darcy's law for the velocity. We modified the model in [39] to account for the viscous forces through the Brinkman law.

Remark 2.1.2. ***[On fourth order models and their applications].*** *Models of fourth order arise in the modelling of many biological phenomena. These models are generally used when describing biophysical processes involving surface tensions and topological changes. In this context, using lubrication theory, fourth order fluid-dynamical models were developed and widely studied to describe the slow motion of a small flat and viscous droplet, see [16] and references therein. Analogies have been made between a cell spreading on a substrate and an oil droplet moving on a surface*

based on studies and observations found in [20, 123, 35]. Furthermore, seminal papers have reported that inter-facial tensions are involved in cell motility (Carter in 1967 [35]) and in tissue organization (Steinberg in 1963 [141]), which is why these types of fourth-order models can extend to the study of cell motility on substrates and of tissue dynamics, which initiated with Greenspan in 1977 [78]. These models are particularly useful when describing the life cycle of a normal cell cultured on a substrate (in contrast with a cancerous one) which is characterized by several changes in its shape. In order to spread, the cell adopts a flat shape which helps in its spreading on the substrate, during mitosis, the cell rounds up to be able to divide. In this example, inter-facial tensions between membranes play a key role in the physical changes in cell shape. A famous example of fourth order equations is the Cahn-Hilliard equation [29, 31, 30], initially developed in 1958 in the context of phase separation of fluid components, and on which huge literature exists. The Cahn-Hilliard equation was first introduced to model the so-called spinodal decomposition of binary alloys in a rapid cooling process, assuming isotropy of the material. It depicts the process of phase separation where one phase occupies a single domain and excludes the other [110]. It now sees its applications in different domains in biology particularly in the description of living tissues. In developmental biology, the ESVM, which can be perceived as a (multi-species) variant of the Cahn-Hilliard equation, was applied to study the imaginal disc of Drosophila where two tissues of different nature share an interface [39]. In the context of this thesis, and similarly to the Cahn-Hilliard equation, we use the ESVM to reproduce and explain the segregation of two embryonic tissues (considered as two fluids), with a diffuse interface where cell mixing can occur. This interface can undergo topological changes as well, as it responds to the various pressures from the tissues: it can deform, bend, become thinner or wider. In oncology, the Cahn-Hilliard equation and its variants bring answers as to the physical principles governing the self-organized architectures of tumor cell populations composed of cancerous and healthy cells with different proliferation rates. In fact, the tumor and the surrounding host tissue occupy areas of a domain and are subject to a variety of forces and biological processes. It is intuitive to represent the healthy and the cancerous tissues as two domains (shapes) in contact and sharing an interface of zero thickness. This mathematical representation provides a precise description of the interface that differentiates the tumor from the surrounding host tissue. Nevertheless, the mathematical analysis of such accurate interface models is challenging and can fail when the interface undergoes a topological change. An example of such change is when metastasis occurs. In such a case, the interface can no longer be considered as a mathematical surface, and thus the net interface models are not valid when the tumor metastasizes. For that reason, the use of diffuse interface models became popular as they consider the interface between tumor and the healthy tissue as a thin layer where cancerous and healthy cells are mixed [53]. This novel representation of the interface yields more suitable model equations for mathematical analysis, and the mathematical description holds true even when the tumor undergoes topological changes. Therefore, many recent efforts in mathematical modeling of tumor growth have been devoted to diffuse interface models and

to their numerical simulations, which demonstrate both complex changes in tumor morphologies due to mechanical stress and chemical interactions such as with nutrients or toxic pathogens. The interaction between multiple cell types (tumor, healthy, heterogeneous cancerous cells, extra-cellular matrix) is therefore often described using mixture models or multi-phase models which are typically of fourth order. We cite the works on glioblastoma [3], melanoma [40, 38], multi-species tumour growth and invasion [68, 2, 83, 157, 67, 42, 37, 117, 5, 71, 60, 61] and chemotaxis [72].

We now look at the density profiles and the swirling motions in the ESVM, and compare them to those of the VM.

Comparison of the ESVM and of the VM via numerical simulations. We compare the VM and the ESVM numerically. We represent in Figure 2.2 the densities (left panels) and the curl of the velocity of the PSM (right panels). Our initial data are ${n_1}^{ini} = 0.9\chi_{[-2/3;2/3]\times[-1;0]}$ and ${n_2}^{ini} = 0.9\chi_{([-1;-2/3]\cup[[2/3;1])\times[-1;0]}$ with χ the indicator function. Our first observation is that the two models, the ESVM depicted in Figures 2.2a-2.2b and the VM depicted in Figures 2.2c-2.2d, maintain tissue segregation and emulate the swirling motions in the PSM. However, only the ESVM captures the small anterior regions of alternating rotations. This suggests that the repulsion pressure in the ESVM plays an important role in tissue dynamics.
We refer the reader to Chapter 4 for the complete set of numerical simulations, where we also compare our model with that of [47] where the velocity is under a gradient form, preventing the appearance of swirling motions.

Remark 2.1.3. ***[Link with Objective 1: biological hypotheses].*** *Using the VM and the ESVM we have tested different types of mechanical segregations which could be responsible for the observed maintenance of segregation between the NT and the PSM. As seen in the simulations of the ESVM, the repulsion pressure is involved in creating the observed anterior regions of alternating in the embryo. The emerging biological hypothesis is that an active force may be at play to maintain the tissues segregated throughout the growth. This segregation, modeled in the ESVM as a repulsion pressure, can be a chemical repulsion which translates into a driven cell motion away from each other when in contact, or it can be an active mechanical force from cell surface tension. In either case, this biological hypothesis can be tested by creating a protocol where cells of the PSM and of the NT are mixed in the same environment. Filming cell motion and analyzing the consequent images will then tell us more about the cell-cell interactions at play.*
Furthermore, the parameter α is responsible for the cohesion of the species in the model, which ensures the stability of the system. Namely, it is necessary to prevent the formation of alternating densities. This parameter can be perceived as a self-adhesion force, i.e tissues of the same type adhere in the form of bulks (cohesion). Once again, testing this biological hypothesis by filming the behavior of different cell types in contact will validate this hypothesis in the vertebrate embryo.

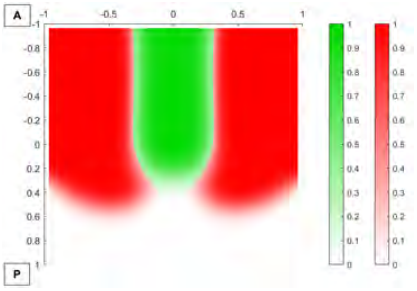

(a) PSM and NT densities in the ESVM.

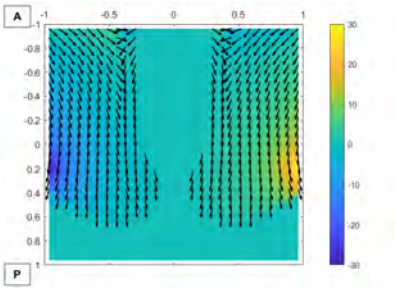

(b) PSM velocity and curl in the ESVM.

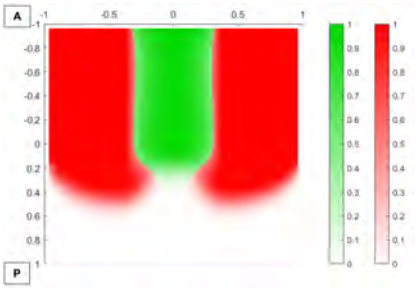

(c) PSM and NT densities in the VM.

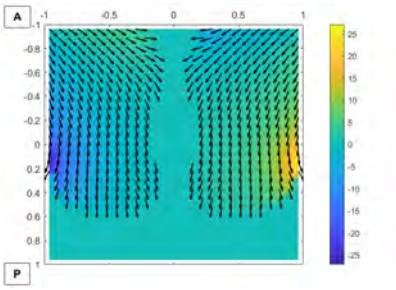

(d) PSM velocity and curl in the VM.

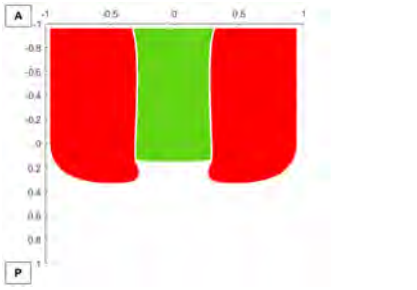

(e) PSM and NT densities in the L-VM.

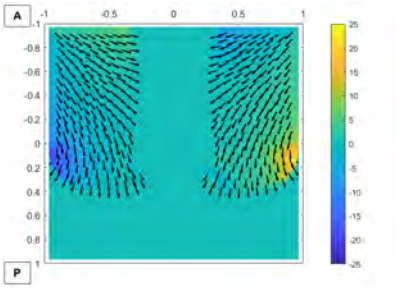

(f) PSM velocity and curl in the L-VM.

Figure 2.2 – Numerical simulations. The left panels illustrate the NT density n_1 (in green) and the PSM density n_2 (in red) and the right panels illustrate curl v_2 (heat map) overlayed by the vector $\frac{v_2}{\|v_2\|}$ (black arrows) at time $t = 0.1$ in respectively the ESVM, with $\epsilon = 0.1, m = 30, \alpha = 0.001$ (Panel (a)–(b)), the VM (Panel (c)–(d)) and the L-VM (Panel (e)–(f)). The velocity vector $\frac{v_2}{\|v_2\|}$ is represented only in the regions where the density of the PSM is above a threshold equal to 0.1.

A geometric description of the PSM and the NT. To reduce the system's complexity, we no longer consider the temporal evolution of the densities of the PSM and of the NT, but rather the geometric domains the tissues occupy. Ideally, we could consider the densities to be constant inside a certain growing domain (the tissue's domain), and we would only need to have access to the domain's velocity and to the pressure inside to have a complete description. This changes the type of model we should consider, as neither the VM nor the ESVM gives this geometric description. However, in our numerical simulations in Figure 2.2, we see that the tissues' densities are approximately equal to 1 in the domain they occupy and equal to zero elsewhere. This strongly suggests that when the parameter ϵ for the VM and the parameters (ϵ, α, m) for the ESVM are in their asymptotic regime (taken either very large or very small), a geometric description is possible. For that reason, we investigate a free boundary formulation of the VM and of the ESVM. We seek to keep the link between the hydrodynamic models and their free boundary formulations, which can be achieved by computing the incompressible limit of the VM and of the ESVM. In the VM it corresponds to taking $\epsilon \to 0$ and in the ESVM to $(\epsilon, \alpha, m) \to (0, 0, +\infty)$. We first present the incompressible limit of the VM then of the ESVM in a simplified case where the densities are constant in the domains they occupy and zero elsewhere. We then exhibit in Theorem 2.1.8 the incompressible limit of the VM and in Theorem 2.1.10 that of the ESVM in the general case.

The incompressible limit of the VM: a simplified case. The incompressible limit of the VM is formally obtained by taking $\epsilon \to 0$. We denote the quantities at the limit with a superscript "∞". Then by taking $\epsilon \to 0$ in the VM we obtain for all $(t, x) \in [0; +\infty) \times \mathbb{R}^d$, two evolution equations on the densities at the limit n_1^∞, n_2^∞, as well as two elliptic equations on the velocities v_1^∞, v_2^∞, which are detailed in Theorem 2.1.8 and not shown here. Moreover, we obtain the following relation on the pressure and the total density,

$$p^\infty(1 - n^\infty) = 0, \text{ where } n^\infty = n_1^\infty + n_2^\infty. \tag{2.16}$$

This relation directly derives from taking $\epsilon \to 0$ in the expression of the pressure (2.5). This relation allows us to define the moving domain (the free boundary) as the following set,

$$\Omega(t) \coloneqq \{x |\ p^\infty(t, x) > 0\} = \{x |\ n^\infty(t, x) = 1\},\ a.e. \tag{2.17}$$

This implies that inside the moving domain the total density is equal to 1 and the pressure is strictly positive. Outside $\Omega(t)$, the pressure is null and the density is strictly less than 1, see Figure 2.3. We will now exhibit a simplified case where the density is null outside $\Omega(t)$.

As the total density $n^\infty = n_1^\infty + n_2^\infty$ is equal to 1 in the moving domain, we can consider the simplified case where we define the subdomain $\Omega_1(t) \subset \Omega(t)$ a moving subdomain occupied by n_1^∞ and where $n_1^\infty(t, x) = 1$ and $n_2^\infty(t, x) = 0$ and $\Omega_2(t) \subset \Omega(t)$ the moving subdomain occupied by

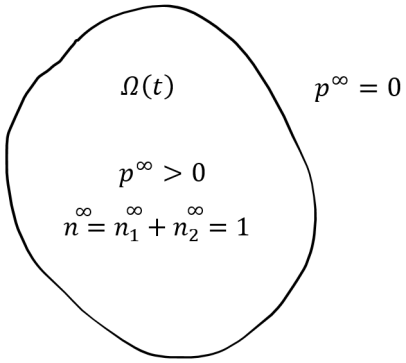

Figure 2.3 – The free boundary defined by the relation (2.17).

$n_2^\infty(t,x)$ and where $n_2^\infty(t,x) = 1$ and $n_1^\infty(t,x) = 0$, and such that $\Omega_1(t), \Omega_2(t)$ are segregated and remain segregated for all times. More precisely we have,

$$\Omega_1(t) = \{x|\ n_1^\infty = 1\} \cap \Omega(t) \ \text{ and } \ \Omega_2(t) = \{x|\ n_2^\infty = 1\} \cap \Omega(t),$$

with,

$$\Omega_1(t) \cap \Omega_2(t) = \varnothing \text{ and } \Omega_1(t) \cup \Omega_2(t) = \Omega(t).$$

This decomposition of $\Omega(t)$ into two subdomains $\Omega_1(t)$ and $\Omega_2(t)$ fully occupied by either density is depicted in Figure 2.4 in the case of two concentric species.

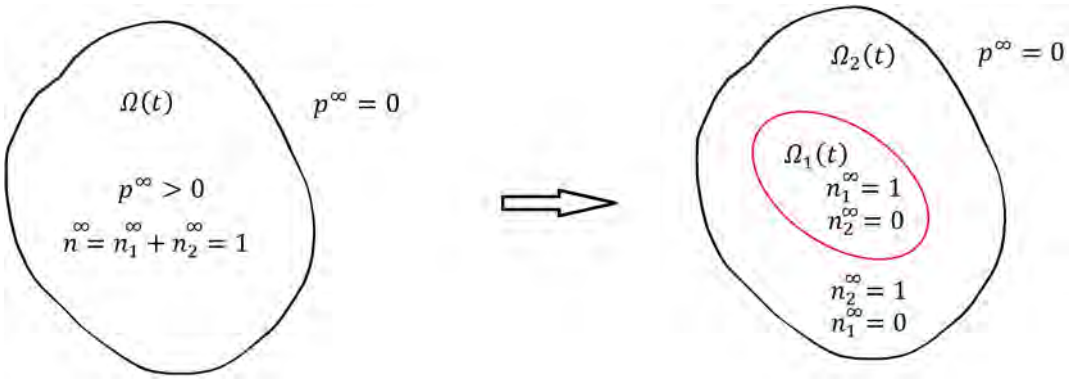

Figure 2.4 – Decomposition of $\Omega(t)$.

We note here that this type of solution verifies the equations of the densities at the incompressible limit (2.25)-(2.26) in Theorem 2.1.8.

We now exhibit the limit equations prescribing the pressure in $\Omega_1(t)$ and $\Omega_2(t)$. Indeed, by deriving an equation on p_ϵ in the VM, then taking $\epsilon \to 0$, we have,

$$\nabla \cdot v_1^\infty \ = \ G_1(p^\infty), \quad \text{in } \ \Omega_1(t), \tag{2.18}$$

$$\nabla \cdot v_2^\infty = G_2(p^\infty), \quad \text{in } \Omega_2(t). \tag{2.19}$$

Finally, to fully describe the free boundary, we need to define its velocity on all the boundaries. We can show that the exterior boundaries of $\Omega_1(t)$ and $\Omega_2(t)$ evolve with respective velocities given by (see Figure 2.5),

$$V_{\partial\Omega_1(t)\cap\partial\Omega(t)} = v_1^\infty \cdot \vec{\nu}, \quad V_{\partial\Omega_2(t)\cap\partial\Omega(t)} = v_2^\infty \cdot \vec{\mu}, \tag{2.20}$$

with $\vec{\nu}$ the outward normal vector to $\Omega_1(t)$ and $\vec{\mu}$ the outward normal vector to $\Omega_2(t)$, and with v_1^∞, v_2^∞ the velocities at the incompressible limit (which we define more precisely in the Theorem 2.1.8). Finally, we define the interface between these two domains as,

$$\Gamma(t) = \partial\Omega_1(t) \cup \partial\Omega_2(t).$$

Then the interface $\Gamma(t)$ evolves with the following velocity,

$$V_{\Gamma(t)} = v_1^\infty \cdot \vec{\nu} = v_2^\infty \cdot \vec{\nu}, \tag{2.21}$$

meaning that the velocities are continuous on the interface.

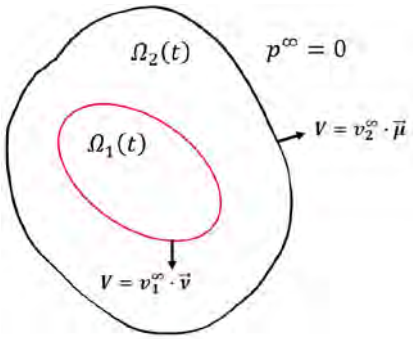

Figure 2.5 – Velocities of the free boundaries.

We call the resulting model at the limit the L-VM.

Remark 2.1.4. ***[On the segregation in the L-VM].*** *Similarly to the VM, we can formally show that the L-VM is endowed with the segregation property in the case $\beta_1 = \beta_2$. In the general case where $\beta_1 \neq \beta_2$, we present arguments, similar to those of the VM in Chapter 4 which advocate for the segregation property in the L-VM. This justifies the use of segregated indicator functions in the simplified case presented above for the L-VM.*

Numerical illustration. In Figures 2.2e-2.2f, we exhibit numerical simulations (in FreeFem++) of the L-VM in the case of the vertebrate embryo. We first notice the striking resemblance of the density profiles between the L-VM and the VM in its asymptotic regime, i.e for small ϵ, in Figure 2.2c. The L-VM reproduces axis elongation, and maintains the segregation of the densities. Furthermore, we see that the swirling motions in the L-VM are qualitatively identical to those of the VM in its asymptotic regime. The resemblance between these two models advocates for the incompressible limit. Altogether, we deduce that the L-VM reproduces well the observed phenomena in the embryo.

Remark 2.1.5. ***[Link with Objective 1].*** *We have presented a geometric description (the L-VM) of the NT and the PSM via the incompressible limit. This mathematical tool allowed us to build a bridge between the hydrodynamic description of the densities (the VM) and its corresponding geometric description (the L-VM). In the simplified case detailed above, where the densities are constant inside the domains they occupy, the model is less complex, as we do not need to simulate the equations of the densities at the limit. We only need the velocities of the domains' boundaries and interfaces as well as the equations prescribing the pressure (2.18)-(2.19) inside each domain. This description also reduces the parameters in the model (as now ϵ is 0). Our numerical simulations show that this new geometric description is a great model to study vertebrate axis elongation as it reproduces tissue elongation and segregation, as well as the general swirling motions in the PSM.*

In what follows, we will exhibit the incompressible limit of the ESVM in the same simplified case as for the L-VM, that is, taking the densities constant in the domain they occupy and zero elsewhere.

The incompressible limit of the ESVM: a simplified case. The incompressible limit of the ESVM is formally obtained by taking the parameters $(\epsilon, \alpha, m) \to (0, 0, +\infty)$. We use the same notation for the quantities at the limit with a superscript "∞". Then at the incompressible limit we obtain for all $(t, x) \in [0; +\infty) \times \mathbb{R}^d$, two evolution equations on the densities at the limit n_1^∞, n_2^∞, and two elliptic equations on the velocities v_1^∞, v_2^∞, detailed in Theorem 2.1.10.

The main difference with the L-VM is that we also recover an evolution equation for the segregation pressure q^∞. The equation is detailed in Theorem 2.1.10.

We obtain the same relation (2.16) linking the pressure and the total density, and we can define the set $\Omega(t)$ as in (2.17).

Moreover, by taking $m \to +\infty$ in the expression of q_m in the ESVM, we obtain the **full**

segregation of the densities at the limit, that is,

$$n_1^\infty n_2^\infty = 0. \tag{2.22}$$

This is another difference with the L-VM, as the L-ESVM always ensures segregation at the limit for any (mixed) initial data.

Motivated by the segregation at the limit (2.22), we consider the segregated moving subdomains $\Omega_1(t) \subset \Omega(t)$ and $\Omega_2(t) \subset \Omega(t)$ respectively occupied by n_1^∞ and n_2^∞. Then we have $n_1^\infty(t,x) = 1$ and $n_2^\infty(t,x) = 0$ on $\Omega_1(t)$ and $n_2^\infty(t,x) = 1$ and $n_1^\infty(t,x) = 0$ on $\Omega_2(t)$. We recover the case depicted in Figure 2.4. We can also show that this type of solution verifies the equations of the densities at the incompressible limit (2.31)-(2.32) in Theorem 2.1.10.
The limit equations prescribing the pressure in $\Omega_1(t)$ and $\Omega_2(t)$ for the L-ESVM are the same as (2.18)-(2.19), and we recover the velocities at the domains' exterior boundaries given by (2.20), and the interface given by (2.21), as depicted in Figure 2.5. We call the resulting model at the limit the L-ESVM.

Remark 2.1.6. ***[Link with Objective 1 : the ghost effect, a biological hypothesis].*** *Unintuitively, and although we achieve full segregation of the tissues at the incompressible limit as shown in (2.22), the segregation pressure q^∞ does not vanish at the limit but is given by evolution equations (detailed in Theorem 2.1.10 in equations (2.40)-(2.41)). The persistence of q^∞ can be seen as a ghost effect. This terminology was first used in kinetic theory for gas dynamics when performing a continuum limit (taking the Knudsen number to zero) on the Boltzmann equation. As certain flows vanish at the continuum limit, they still produce a finite effect on the solution behavior at the limit [137, 139]. In our case, q^∞ is involved in the tissue dynamics through the Brinkman law for the velocities. This shows that q^∞ cannot be neglected at the incompressible and actually plays a role on the dynamics. We notice that the L-ESVM, simulated in the case where $q^\infty = 0$ (which yields the L-VM) in Figures 2.2e-2.2f, recovers well the swirling motions in the PSM. However, we note the absence of the anterior regions of alternating rotations, compared to the simulations of the ESVM in its asymptotic regime in Figures 2.2a-2.2b. The simulations of the ESVM in its asymptotic regime give us an idea about the dynamics occurring in the L-ESVM with $q^\infty \neq 0$. This suggests, as noted previously in Remark 2.1.3, that the segregation pressure, even at the incompressible limit, appears to be responsible for the appearance of the anterior regions of alternating curls in the PSM, which yields the observed swirling motions in vivo. This further highlights the role of the segregation pressure q^∞ as an active force segregating the tissues, maintaining their segregation, and giving rise to the swirling motions observed in vivo.*

Remark 2.1.7. ***[Link between the ESVM, VM, L-ESVM and L-VM].*** *The four models at hand, ESVM, VM, L-ESVM, and L-VM, reproduce embryonic growth. The ESVM and the VM*

give a density description of the tissues, and coincide when initial data are segregated, and when $\alpha = 0$ *in the ESVM. At the incompressible limit the L-ESVM and the L-VM differ fundamentally as the former encompasses a segregation force (the segregation pressure* q^∞*) that still produces a finite effect at the limit on the dynamics and that yields the strict segregation of the densities even if initially mixed. The L-VM only propagates tissue segregation if imposed on the initial data. The two models at the limit then coincide under two conditions: 1) if the segregation pressure* q^∞ *is taken initially null 2) if the initial data are initially segregated. The link between the models is illustrated in Figure 2.6.*

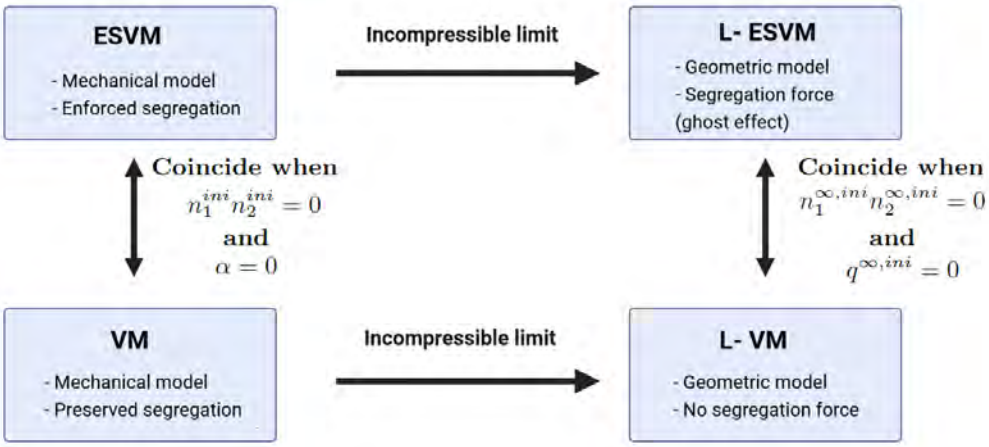

Figure 2.6 – Links between the models: ESVM, VM, L-ESVM, and L-VM.

In what follows we exhibit the main theorems of the incompressible limit first for the VM then for the ESVM. We first denote,

$$\forall x \in \mathbb{R}^d, \quad n_1(t=0,x) = n_1^{ini}(x), \quad n_2(t=0,x) = n_2^{ini}(x), \tag{2.23}$$

on which we assume the following conditions,

$$\forall x \in \mathbb{R}^d, \quad n_1^{ini}(x) \geq 0, \quad n_2^{ini}(x) \geq 0, \quad \text{and} \quad n^{ini}(x) := n_1^{ini}(x) + n_2^{ini}(x) < 1. \tag{2.24}$$

We now exhibit a formal theorem on the incompressible limit of the VM.

Theorem 2.1.8. *(Formal)[Incompressible limit of the VM] Let* n_1^{ini}, n_2^{ini} *satisfy the conditions* (2.23)-(2.24) *and let* n_1, n_2, v_1, v_2, p_ϵ *solve the viscous two-species model* (2.1)-(2.5)*. Assume that at the incompressible limit, that is, when* ϵ *goes to zero, the quantities* n_1, n_2, v_1, v_2, p_1, p_2, $q_m(n_1 n_2)$ *converge (in a sufficiently strong sense) towards, respectively,* n_1^∞, n_2^∞, v_1^∞, v_2^∞, p^∞.

Then, these quantities satisfy the following system of equations for all $(t,x) \in [0;+\infty) \times \mathbb{R}^d$,

$$\partial_t n_1^\infty + \nabla \cdot (n_1^\infty v_1^\infty) = n_1^\infty G_1(p^\infty), \tag{2.25}$$

$$\partial_t n_2^\infty + \nabla \cdot (n_2^\infty v_2^\infty) = n_2^\infty G_2(p^\infty), \tag{2.26}$$

$$-\beta_1 \Delta v_1^\infty + v_1^\infty = -\nabla p^\infty, \tag{2.27}$$

$$-\beta_2 \Delta v_2^\infty + v_2^\infty = -\nabla p^\infty, \tag{2.28}$$

and the following relation holds

$$p^\infty(1-n^\infty) = 0, \text{ where } n^\infty = n_1^\infty + n_2^\infty. \tag{2.29}$$

The complementary relation prescribing the dynamics of the pressure due to congestion at the limit reads

$$p^{\infty^2}\Big(n_1^\infty \nabla \cdot v_1^\infty + n_2^\infty \nabla \cdot v_2^\infty\Big) \quad = \quad p^{\infty^2}\Big(n_1^\infty G_1(p^\infty) + n_2^\infty G_2(p^\infty)\Big). \tag{2.30}$$

Remark 2.1.9. *When* $n_i^\infty = \chi_{\Omega_i(t)}, i = 1,2$, *with* χ *the indicator function, we find the simplified case of the L-VM described previously.*

We now exhibit a formal theorem on the incompressible limit of the ESVM.

Theorem 2.1.10. *(Formal)[Incompressible limit of the ESVM] Let* n_1^{ini}, n_2^{ini} *satisfy the conditions* (2.23)-(2.24) *and let* n_1, n_2, v_1, v_2, p_1, p_2 *solve the viscous two-species model* (2.8)-(2.13) *with* (2.14)–(2.15). *Assume that at the incompressible limit, that is, when* ϵ *and* α *go to zero and* m *goes to infinity, the quantities* n_1, n_2, v_1, v_2, p_1, p_2, $q_m(n_1 n_2)$ *converge (in a sufficiently strong sense) towards, respectively,* n_1^∞, n_2^∞, v_1^∞, v_2^∞, p_1^∞, p_2^∞, q^∞. *Then, these quantities satisfy the following system of equations for all* $(t,x) \in [0;+\infty) \times \mathbb{R}^d$,

$$\partial_t n_1^\infty + \nabla \cdot (n_1^\infty v_1^\infty) = n_1^\infty G_1(p_1^\infty), \tag{2.31}$$

$$\partial_t n_2^\infty + \nabla \cdot (n_2^\infty v_2^\infty) = n_2^\infty G_2(p_2^\infty), \tag{2.32}$$

$$-\beta_1 \Delta v_1^\infty + v_1^\infty = -\nabla p_1^\infty, \tag{2.33}$$

$$-\beta_2 \Delta v_2^\infty + v_2^\infty = -\nabla p_2^\infty, \tag{2.34}$$

$$p_1^\infty = p^\infty + n_2^\infty q^\infty, \tag{2.35}$$

$$p_2^\infty = p^\infty + n_1^\infty q^\infty, \tag{2.36}$$

and the following relation holds,

$$p^\infty(1-n^\infty)=0, \text{ where } n^\infty=n_1^\infty+n_2^\infty. \tag{2.37}$$

Moreover, we obtain full segregation of the two-species at the limit,

$$n_1^\infty n_2^\infty=0. \tag{2.38}$$

The complementary relation prescribing the dynamics of the pressures inside the two tissues at the limit reads,

$$p^{\infty^2}\Big(\nabla\cdot(n_1^\infty v_1^\infty)+\nabla\cdot(n_2^\infty v_2^\infty)\Big) \;=\; p^{\infty^2}\Big(n_1^\infty G_1(p_1^\infty)+n_2^\infty G_2(p_2^\infty)\Big). \tag{2.39}$$

Finally, defining $K_1^\infty=n_1^\infty q^\infty$ and $K_2^\infty=n_2^\infty q^\infty$, the equations prescribing the dynamics of the pressure due to repulsion at the limit read,

$$\begin{aligned}\partial_t K_1^\infty &+ (q^\infty+1)\log(q^\infty+1)\nabla\cdot(n_1^\infty v_1^\infty)+(q^\infty+1)\log(q^\infty+1)n_1^\infty\nabla\cdot v_2^\infty\\ &+ n_1^\infty v_2^\infty\cdot\nabla q^\infty-(q^\infty+1)\log(q^\infty+1)\nabla n_1^\infty\cdot v_2^\infty+q^\infty\nabla\cdot(n_1^\infty v_1^\infty)\\ &= (q^\infty+1)\log(q^\infty+1)n_1^\infty(G_1(p_1^\infty)+G_2(p_2^\infty))+q^\infty n_1^\infty G_1(p_1^\infty),\end{aligned} \tag{2.40}$$

$$\begin{aligned}\partial_t K_2^\infty &+ (q^\infty+1)\log(q^\infty+1)\nabla\cdot(n_2^\infty v_2^\infty)+(q^\infty+1)\log(q^\infty+1)n_2^\infty\nabla\cdot v_1^\infty\\ &+ n_2^\infty v_1^\infty\cdot\nabla q^\infty-(q^\infty+1)\log(q^\infty+1)\nabla n_2^\infty\cdot v_1^\infty+q^\infty\nabla\cdot(n_2^\infty v_2^\infty)\\ &= (q^\infty+1)\log(q^\infty+1)n_2^\infty(G_1(p_1^\infty)+G_2(p_2^\infty))+q^\infty n_2^\infty G_2(p_2^\infty).\end{aligned} \tag{2.41}$$

We call L-ESVM the limiting system (2.31)–(2.41) thus obtained.

Remark 2.1.11. *When $n_i^\infty=\chi_{\Omega_i(t)}, i=1,2$, with χ the indicator function, we find the simplified case of the L-ESVM described previously.*

We now aim to study the mathematical properties of the solution's behavior of the L-ESVM and of the L-VM. More precisely, we are interested in determining whether the solution of the stationary L-ESVM exists. When the solution exists, we want to determine its regularity. This theoretical study allows us to extract biophysical properties on the biological system as we discuss in Remark 2.1.16.

Our framework. At the incompressible limit, we are interested in the study of the stationary velocity-pressure system. We call Ω_1 the stationary subdomain occupied by the density n_1^∞ (the

NT) and by Ω_2 that of the n_2^∞ (the PSM). We work in a bounded domain $\Theta \subset \mathbb{R}^2$, and suppose that Θ, Ω_1 and Ω_2 are as follows,

$$\Theta \text{ a smooth bounded domain in } \mathbb{R}^2, \Omega,\ \Omega_1,\ \Omega_2 \text{ subdomains of } \Theta \text{ such that} \tag{2.42}$$

$$\Omega_1 \cap \Omega_2 \text{ is empty, } \Gamma := \overline{\Omega_1} \cap \overline{\Omega_2} \text{ is non-empty,} \tag{2.43}$$

$$\Omega = \Omega_1 \cup \Omega_2 \text{ and } \overline{\Omega} \subset \Theta, \tag{2.44}$$

$$\text{and, defining } \Omega^c := \Theta \backslash \overline{\Omega},\ \text{the boundaries } \Gamma,\ \Gamma_1 := \overline{\Omega_1} \cap \overline{\Omega^c},\ \Gamma_2 = \overline{\Omega_2} \cap \overline{\Omega^c} \text{ are } \mathcal{C}^\infty. \tag{2.45}$$

Our analysis is conducted in a simplified framework, where we drop the equations (2.40) and (2.41) and consider instead that q is a given function on Ω. We assume,

$$q^\infty \in L^2(\Omega). \tag{2.46}$$

For simplicity, we suppose that the growth function is linear (and decreasing), that is,

$$G_1(s) = g_1(p_1^* - s), \quad G_2(s) = g_2(p_2^* - s), \tag{2.47}$$

for some g_1, g_2, p_1^*, $p_2^* > 0$.

The stationary system. With the framework defined above above, we now exhibit the resulting stationary velocity-pressure system. The system (2.31)–(2.39) at equilibrium and complemented with homogeneous Dirichlet boundary conditions becomes the following elliptic system on (v_1^∞, v_2^∞), for q^∞ given as in (2.46),

$$(S_2) \quad \begin{cases} -\beta_1 \Delta v_1^\infty + v_1^\infty = -\nabla[(p_1^* - \frac{1}{g_1}\nabla \cdot v_1^\infty)\chi_{\Omega_1} + (p_2^* - \frac{1}{g_2}\nabla \cdot v_2^\infty + q^\infty)\chi_{\Omega_2}] & \text{on } \Theta, \\ -\beta_2 \Delta v_2^\infty + v_2^\infty = -\nabla[(p_2^* - \frac{1}{g_2}\nabla \cdot v_2^\infty)\chi_{\Omega_2} + (p_1^* - \frac{1}{g_1}\nabla \cdot v_1^\infty + q^\infty)\chi_{\Omega_1}] & \text{on } \Theta, \\ v_1^\infty = v_2^\infty = 0 & \text{on } \partial\Theta, \end{cases}$$

For the existence theory and the elliptic regularity, we assume that the model parameters satisfy the following condition,

$$\beta_1 g_2 > \frac{1}{4}, \qquad \text{and} \qquad \beta_2 g_1 > \frac{1}{4}. \tag{2.48}$$

Analysis of stationary solutions at the limit: well-posedness and regularity results. We now exhibit our well-posedness and regularity results on the solution (v_1^∞, v_2^∞) of system (S_2).

0. **Notations.** Let $U \subset \mathbb{R}^2$ be a bounded domain. For $k \geq 0$, we use the notation $\mathcal{C}^k(\overline{U})$, or equivalently write " $\mathcal{C}^k$ up to the boundary of U", in the classical sense, see [64]:

$$\mathcal{C}^k(\overline{U}) = \{u \in \mathcal{C}^k(U) | D^\alpha u \text{ is uniformly continuous on } U \text{ for all } |\alpha| \leq k\}.$$

Theorem 2.1.12. *[Well-posedness and regularity, stationary L-ESVM] Let Θ, Ω_1 and Ω_2 be bounded domains as in (2.42)-(2.45), and let $\beta_1, \beta_2, g_1, g_2 > 0$ satisfy the condition (2.48). Let q^∞ as in (2.46). Then, there exists a unique solution $(v_1^\infty, v_2^\infty) \in H_0^1(\Theta)^2 \times H_0^1(\Theta)^2$ to system (S_2). Note in particular that (v_1^∞, v_2^∞) is continuous across the interfaces $\Gamma_1, \Gamma_2, \Gamma$.*

Furthermore, if $q^\infty \in \mathcal{C}^{0,\mu}(\overline{\Omega_1}) \cap \mathcal{C}^{0,\mu}(\overline{\Omega_2})$ for some $\mu \in (0,1)$, then the solution (v_1^∞, v_2^∞) to system (S_2) lies in $\mathcal{C}^{1,\alpha'}(\overline{\Omega_1}) \cap \mathcal{C}^{1,\alpha'}(\overline{\Omega_2}) \cap \mathcal{C}^{1,\alpha'}(\overline{\Omega^c})$, with $0 < \alpha' \leq \min(\mu, \frac{1}{4})$.

Finally, under the following additional condition on the domains,

$$\partial\Omega \text{ is smooth } (\mathcal{C}^\infty). \tag{2.49}$$

and if $q^\infty \in \mathcal{C}^\infty(\overline{\Omega_1}) \cap \mathcal{C}^\infty(\overline{\Omega_2})$, then the solution (v_1, v_2) to system (S_2) lies in $\mathcal{C}^\infty(\overline{\Omega_1}) \cap \mathcal{C}^\infty(\overline{\Omega_2}) \cap \mathcal{C}^\infty(\overline{\Omega^c})$.

The additional condition (2.49) is met when the tissues are concentric as depicted in Figure 2.4 (right).

To show the well-posedness, we rely on the Lax-Milgram Theorem. Regularity is shown via known results in classical elliptic theory.

The transmission problem. The couple (v_1^∞, v_2^∞) is a solution to the elliptic system with discontinuous coefficients (S_2). Depending on which subdomain we consider, Ω_1, Ω_2 or Ω^c, the solution changes its behavior as it verifies a different equation than the one in its neighboring subdomain. The dynamics in each subdomain are however very co-dependent as the information is transferred from one to the other through their interfaces. For that reason, we formulate the system (S_2) as a transmission problem. This new formulation consists in describing the solution in every subdomain through the PDE it verifies, and in defining the transmission conditions on every interface and boundary, see Figure 2.7 in the case of the vertebrate embryo.

Proposition 2.1.13 (Transmission problem, stationary L-ESVM)**.** *Assume (2.42)-(2.45), (2.48), and $q \in \mathcal{C}^{0,\mu}(\overline{\Omega_1}) \cap \mathcal{C}^{0,\mu}(\overline{\Omega_2})$ for some $\mu \in (0,1)$. Then the solution of system (S_2) solves the following transmission problem (T_2) considered on Θ and coupled with homogeneous Dirichlet boundary*

Thus if $u \in \mathcal{C}^k(\overline{U})$, then $D^\alpha u$ can be continuously extended to $\overline{U}$ for each multi-index α, with $|\alpha| \leq k$.

For $\mu \in (0,1)$, we use the notation $\mathcal{C}^{0,\mu}(\overline{U})$ for (uniformly) Hölder continuous functions on U with exponent μ. Thus, such functions can be extended into a (uniformly) Hölder continuous functions on $\overline{U}$ with the same exponent μ.

Finally, for $k \geq 0$ and $\mu \in (0,1)$, we write,

$$\mathcal{C}^{k,\mu}(\overline{U}) = \{u \in \mathcal{C}^k(U) | D^\alpha u \ \in \mathcal{C}^{0,\mu}(\overline{U}) \text{ for all } |\alpha| \leq k\}.$$

conditions on $\partial\Theta$,

$$(T_{2,\Omega_1})\begin{cases} -\beta_1\Delta v_1 + v_1 - \frac{1}{g_1}\nabla\nabla\cdot v_1 = 0 & \text{in } \Omega_1,\\ -\beta_2\Delta v_2 + v_2 - \frac{1}{g_1}\nabla\nabla\cdot v_1 = -\nabla q & \text{in } \Omega_1.\end{cases}$$

$$(T_{2,\Omega_2})\begin{cases} -\beta_1\Delta v_1 + v_1 - \frac{1}{g_2}\nabla\nabla\cdot v_2 = -\nabla q & \text{in } \Omega_2,\\ -\beta_2\Delta v_2 + v_2 - \frac{1}{g_2}\nabla\nabla\cdot v_2 = 0 & \text{in } \Omega_2.\end{cases}$$

$$(T_{2,\Omega^c})\begin{cases} -\beta_1\Delta v_1 + v_1 = 0 & \text{in } \Omega^c,\\ -\beta_2\Delta v_2 + v_2 = 0 & \text{in } \Omega^c.\end{cases}$$

$$(T_{2,\Gamma_1})\begin{cases} \beta_1[(\nabla v_1)_{\Omega_1} - (\nabla v_1)_{\Omega^c}]\cdot\vec{\nu} = [p_1^* - \frac{1}{g_1}(\nabla\cdot v_1)_{\Omega_1}]\vec{\nu} & \text{on } \Gamma_1,\\ \beta_2[(\nabla v_2)_{\Omega_1} - (\nabla v_2)_{\Omega^c}]\cdot\vec{\nu} = [p_1^* + (q)_{\Omega_1} - \frac{1}{g_1}(\nabla\cdot v_1)_{\Omega_1}]\vec{\nu} & \text{on } \Gamma_1,\\ (v_1)_{\Omega_1} = (v_1)_{\Omega^c}, \quad (v_2)_{\Omega_1} = (v_2)_{\Omega^c} & \text{on } \Gamma_1.\end{cases}$$

$$(T_{2,\Gamma_2})\begin{cases} \beta_1[(\nabla v_1)_{\Omega_2} - (\nabla v_1)_{\Omega^c}]\cdot\vec{\mu} = [p_2^* + (q)_{\Omega_2} - \frac{1}{g_2}(\nabla\cdot v_2)_{\Omega_2}]\vec{\mu} & \text{on } \Gamma_2,\\ \beta_2[(\nabla v_2)_{\Omega_2} - (\nabla v_2)_{\Omega^c}]\cdot\vec{\mu} = [p_2^* - \frac{1}{g_2}(\nabla\cdot v_2)_{\Omega_2}]\vec{\mu} & \text{on } \Gamma_2,\\ (v_1)_{\Omega_2} = (v_1)_{\Omega^c}, \quad (v_2)_{\Omega_2} = (v_2)_{\Omega^c} & \text{on } \Gamma_2.\end{cases}$$

$$(T_{2,\Gamma})\begin{cases} \beta_1[(\nabla v_1)_{\Omega_1} - (\nabla v_1)_{\Omega_2}]\cdot\vec{\nu} = [(p_1^* - p_2^*) - (q)_{\Omega_2} + \frac{1}{g_2}(\nabla\cdot v_2)_{\Omega_2} - \frac{1}{g_1}(\nabla\cdot v_1)_{\Omega_1}]\vec{\nu} & \text{on } \Gamma,\\ \beta_2[(\nabla v_2)_{\Omega_1} - (\nabla v_2)_{\Omega_2}]\cdot\vec{\nu} = [(p_1^* - p_2^*) + (q)_{\Omega_1} + \frac{1}{g_2}(\nabla\cdot v_2)_{\Omega_2} - \frac{1}{g_1}(\nabla\cdot v_1)_{\Omega_1}]\vec{\nu} & \text{on } \Gamma,\\ (v_1)_{\Omega_1} = (v_1)_{\Omega_2}, \quad (v_2)_{\Omega_1} = (v_2)_{\Omega_2}, \quad v_1\cdot\vec{\nu} = v_2\cdot\vec{\nu} & \text{on } \Gamma.\end{cases}$$

Remark 2.1.14. ***[The transmission problem applied to the vertebrate embryo].*** *In Figure 2.7, we show how this transmission problem is applied to the vertebrate embryo. We see that* T_{2,Ω_1} *is verified in the NT (green tissue) and that* T_{2,Ω_2} *is verified in the PSM (red tissue on the left and right of the NT). The two tissues communicate through their interface* Γ*, on which the normal velocities are equal according to* $T_{2,\Gamma}$*. The PSM and the NT communicate with* Ω^c *through their exterior boundaries* Γ_1, Γ_2 *which can be interpreted as the extra-cellular matrix. Here again, there is a transmission of forces according to the transmission conditions* T_{2,Γ_1} *and* T_{2,Γ_2}*. Interestingly, the transmission conditions show that the velocity gradient has a jump. In what follows, we show that it is related to the pressure jump across the interfaces of the tissues, and to our choice of velocity law: the Brinkman law.*

Existence of pressure jumps. We show a striking feature of the stationary L-VM (equivalently the stationary L-ESVM with $q^\infty = 0$). The system exhibits a pressure jump at the tissue bound-

0. **Notations.** For D a domain of $\mathbb{R}^2$ and h a continuous function on D that can be continuously extended on $\overline{D}$, then, for $x \in \partial D$, we note

$$(h)_D(x) \coloneqq \lim_{\substack{y\in D,\\ y\to x}} h(y). \tag{2.50}$$

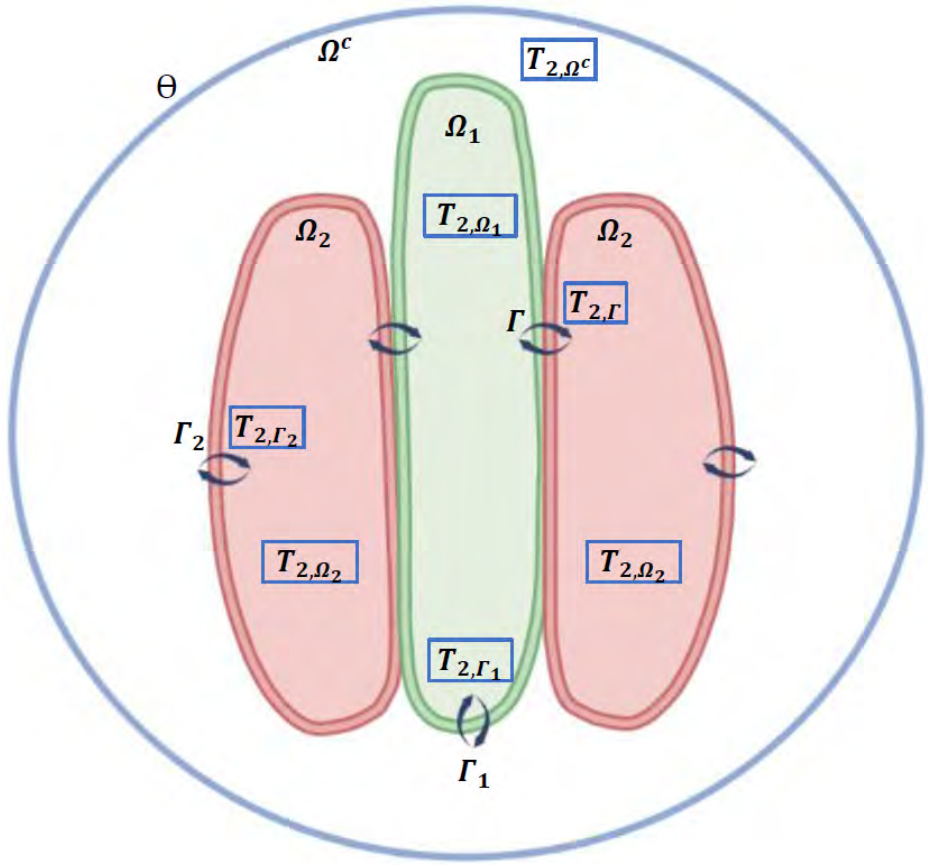

Figure 2.7 – The PSM occupies the domain Ω_2 where the solution (v_1^∞, v_2^∞) verifies (T_{2,Ω_2}). The NT occupies Ω_1 where the solution (v_1^∞, v_2^∞) verifies (T_{2,Ω_1}). Outside $\Omega_1 \cup \Omega_2$, (T_{2,Ω^c}) holds. The arrows represent the transmission conditions across the interfaces Γ_1, Γ_2 and Γ, which are respectively (T_{2,Γ_1}), (T_{2,Γ_2}) and $(T_{2,\Gamma})$.

aries and interfaces. This result is obtained thanks to the transmission problem formulation in Proposition 2.1.13. Interestingly, this pressure jump is not present when Darcy's law is used, and particularly the pressure jump is not present on the interface Γ when $\beta_1 = \beta_2$, but only on the exterior boundaries. This suggests that it is induced by the differential viscosities. The result is stated in the following proposition.

Proposition 2.1.15 (Pressure jump, stationary L-VM). *Suppose (2.42)-(2.45), (2.48) and (2.49). Let $q^\infty = 0$ and let $(v_1^\infty, v_2^\infty) \in H_0^1(\Theta)^2 \times H_0^1(\Theta)^2$ be the solution of (S_2) given by Theorem 2.1.12. Then, the pressure p^∞ of the L-VM is discontinuous across the interfaces $\Gamma_1 \cup \Gamma_2 \cup \Gamma$, and the*

pressure jumps are given by the following expression,

$$p^\infty = \begin{cases} p_1^* - \frac{1}{g_1}(\nabla \cdot v_1^\infty)_{\Omega_1} & \text{on } \Omega_1, \\ p_2^* - \frac{1}{g_2}(\nabla \cdot v_2^\infty)_{\Omega_2} & \text{on } \Omega_2, \\ 0 & \text{on } \Omega^c. \end{cases} \tag{2.51}$$

To prove this proposition, we showed that the velocities $v_1^\infty, v_2^\infty \notin H^2(\Theta)^2$.

Remark 2.1.16. ***[Link with Objective 1: biophysical properties].*** *We have shown in Proposition 2.1.15 that the pressure exhibits discontinuities at the tissues' interfaces and boundaries. This biophysical property can be tested in vivo by measuring the pressure on the interfaces of the tissues. As the pressure jump is expressed in terms of the growth functions G_i, that is, $p^\infty = G_1^{-1}(\nabla \cdot v_1^\infty)$ in Ω_1, and as cell proliferation is known in the embryonic tissues thanks to [24], it would be interesting to see if this relation between the pressure and the growth holds in vivo.*

In conclusion, the ESVM, VM, L-ESVM, and L-VM reproduce and explain embryonic tissue segregation and the general swirling motions within the PSM. However, only the ESVM (and the L-ESVM with $q^\infty \neq 0$) reproduce the correct observed swirling motions within the PSM, thanks to the segregation pressure. The models suggest that an active force might be at play to segregate embryonic tissues, to maintain their segregation and to emulate the observed swirling motions *in vivo*. At their incompressible limit, the models exhibit a viscosity-induced pressure jump, and the persistence of the segregation pressure. The latter is reminiscent of the *ghost effect* in kinetic theory. An open question remains: can other forms of segregation pressures emulate the same swirling motions ? This question still requires to be fully explored numerically and compared to experimental data. We elaborate on this question in Chapter 7.

2.2 A multi-tissue viscous model for long-term effects of mechanisms of axis elongation in the vertebrate embryo.

In Chapter 5, we develop a variant of the VM developed in Chapter 4, which describes the time and space evolution of the PSM and the NT. We bring this new model as close as possible to the biological data of the vertebrate embryo. For that reason, we complexify the model to incorporate two sources of growth: one reaction term accounting for cell proliferation, and a source term accounting for cell addition from the PZ into the PSM and the NT. Thus the PZ is not considered as a third tissue, but its role can be modeled as an incoming flux of cells. We also include inter-tissue friction in our model. After an exhaustive literature exploration, and some biological experiments followed by image analysis and quantification, we calibrate the model parameters. We explore the model numerically by simulating first a wild type embryo *in silico*, and by looking at the inter-tissue sliding, and the differential tissue velocities. We perform *in silico* experiments by changing the values of some parameters such as proliferation, and the incoming flux of new cells from the PZ. It allows to understand the role of differential proliferation as well as differential addition of new cells. It also permits to determine the contribution of each of these phenomena on the inter-tissue sliding, on tissue velocity, and on the overall axis elongation. This work is presented in Chapter 5 and brings answers to Objective 2.

Strategy: the VMI. In this Chapter, we bring answers to Objective 2. We construct a variant of the VM (introduced in Chapter 4) which we call the VMI (Viscous Model with cell Injection) and which takes into account cell proliferation and cell injection from the PZ as main drivers of tissue growth. We calibrate the new model and validate it by comparing it to the biological data at hand. We then conduct *in silico* experiments to test different biological hypotheses.

The new model: the VM with cell Injection (VMI). Using the same notations as for the VM, the new model which we call the VMI reads, for all $(t,x) \in [0;+\infty) \times \mathbb{R}^2$,

$$\partial_t n_1 + \nabla \cdot (n_1 v_1) = n_1 g_1 + \frac{\kappa_{NT}}{\delta} \chi_{PZ^\delta \cap PSM}, \tag{2.52}$$

$$\partial_t n_2 + \nabla \cdot (n_2 v_2) = n_2 g_2 + \frac{\kappa_{PSM}}{\delta} \chi_{PZ^\delta \cap PSM} \tag{2.53}$$

$$-\beta_1 \Delta v_1 + \mu v_1 = -\nabla p_\epsilon, \tag{2.54}$$

$$-\beta_2 \Delta v_2 + \mu v_2 = -\nabla p_\epsilon, \tag{2.55}$$

$$p_\epsilon = \epsilon \frac{n}{n_{max} - n}, \qquad n = n_1 + n_2. \tag{2.56}$$

As our aim in Objective 2 is to test differential proliferation within the tissues, and the contribu-

tion of the incoming cells from the PZ into the PSM and the NT, we introduce a source term in the evolution equations for the densities (2.52) (for the NT) -(2.53) (for the PSM). This additional term accounts for the entry of new cells with flux κ_{NT} and κ_{PSM} in respectively the NT and the PSM. Cell injection from the PZ into the PSM and NT occurs at the most posterior tip of each tissue in a region denoted $PZ^{\delta} \cap NT$ for the region of entry of new cells in the NT and $PZ^{\delta} \cap PSM$ for that of the PSM. The width of the entry zone is denoted by δ. In the Brinkman law for the velocities (2.54)-(2.55) the parameter μ represents the friction between the tissue and its surroundings. In the theoretical study of the VM (Chapter 4), we set several constants to 1 for simplicity such as tissue friction and the maximal density (here denoted by n_{max} in the pressure law (2.56)). As the VMI serves as a model as close as possible to the biological model, we use specific values measured in literature for each parameter. Finally, for simplicity, the growth functions formerly referred to as G_i in the VM, and as they are close to being constant [24], are taken as constants determined in [24].

Model assumptions. To complete our description of the VMI, we made three assumptions:

1. Our model is in 2D: we represent a projection of the 3D embryo onto a 2D plane as most of our biological data at hand are in 2D and as tissue width ($50\mu m$) is very small compared to the length scales we want to model.
2. The friction coefficient of the PSM and of the NT are both equal to μ: to our knowledge, the friction coefficient of the NT is not a known parameter in literature.
3. The PZ being attached to the posterior end of the NT whose density is denoted by n_1, we first define the posterior tip y_0 as,

$$y_0 = \inf_{y \in \mathbb{R}} \left\{ n_1(t, y) > \frac{1000\, cells}{100\, \mu m^2} \right\}.$$

Then the evolution of the set PZ^{δ} is determined by the following,

$$PZ^{\delta}(t) \cap NT = [a_1; b_1] \times [y_0 - \frac{\delta}{2}; y_0 + \frac{\delta}{2}],$$

with $[a_1; b_1]$ the width of the NT, Figure 2.8a and similarly we can define,

$$PZ^{\delta}(t) \cap PSM = [a_2; b_2] \cup [a_3; b_3] \times [y_0 - \frac{\delta}{2}; y_0 + \frac{\delta}{2}],$$

with $[a_2; b_2]$ the width of the left PSM and $[a_3; b_3]$ the width of the right PSM, see Figure 2.8a.

0. In equations (2.52)-(2.53) χ is the indicator function.

Model Calibration. In what follows, we present a table with a list of all the parameters in the VMI (for calibration). We indicate their source (reference in literature) as well as their value and their unit. We note here that the parameters κ_{NT} and κ_{PSM} are not known parameter in literature and were measured in the Bénazéraf lab. The method we used is detailed in Chapter 5.

Parameter	Literature source	Measurement technique	Value	Unit
β_1	[108]	Aspiration technique	$10^4 - 10^5 > \beta_2$	$Pa \cdot s$
β_2	[108, 129]	Aspiration technique	$10^4 - 10^5 < \beta_1$	$Pa \cdot s$
μ	[129, 108]	Estimated	$10^{12} - 10^{13}$	$Pa \cdot s/m^2$
ϵ	Numerical estimation	Free parameter set to obtain the correct elongation rate	10	Pa
κ_{NT}	Measured in the Bénazéraf lab	Image analysis on quail embryos	3.4	$\frac{cells}{hour \cdot \mu m}$
κ_{PSM}	Measured in the Bénazéraf lab	Image analysis on quail embryos	5	$\frac{cells}{hour \cdot \mu m}$
g_1	[24]	EdU staining on quail embryos	$\frac{1}{10.83}$	$hour^{-1}$
g_2	[24]	EdU staining on quail embryos	$\frac{1}{8.75}$	$hour^{-1}$
n_{max}	[24]	Image analysis on quail embryos	2800	$cells/100\mu m^3$

The wild-type embryo *in silico*. Using the list of parameters above, we simulated the equivalent of a wild-type (WT) embryo *in silico* for 12 hours of biological time. Initially, the densities are taken as segregated indicator functions, see Figure 2.8a. At $t = 12$ hours, we observe that tissues have elongated, and have densified, see Figure 2.8b. The model reproduces the density gradients along the antero-posterior as well as the gradients of cell motility in both tissues (see Chapter 5).

We quantified the inter-tissue sliding in the anterior and in the posterior region of the tissues, see Figure 2.9, by taking two sets of reference points. The first couple is of mid-anterior reference points: one in the PSM at $(35\mu m, 964\mu m)$ and one in the NT at $(135\mu m, 964\mu m)$, whereas the second couple is of mid-posterior points one in the PSM at $(35\mu m, 1392\mu m)$ and one in the NT at $(135\mu m, 1392\mu m)$. The model proposes that sliding mainly occurs in the anterior region of the tissues, with the NT sliding past the PSM.

The contribution of proliferation, injection, and the effect of differential proliferation and injection on tissue formation, axis elongation and inter-tissue sliding. To test these

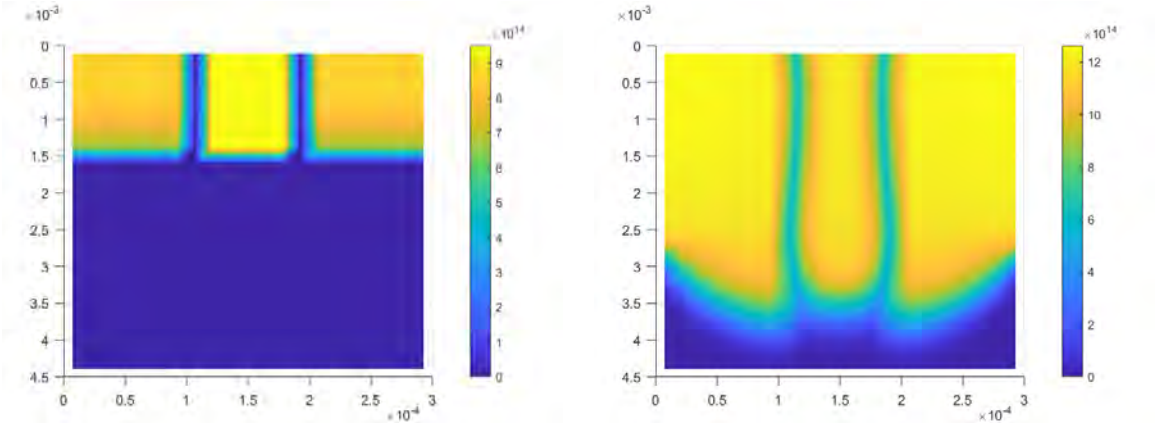

(a) Initial condition. The NT is the middle tissue and the PSM on its right and left.

(b) The tissues (PSM and NT) at $t = 12$ hours.

Figure 2.8 – Numerical simulations of the VMI in the case of the wild-type embryo. The left panel (a) is the initial conditions of the densities. The right panel (b) is the density profiles at the final time $t = 12$ hours. The axis are in the meter unit. Anterior is up.

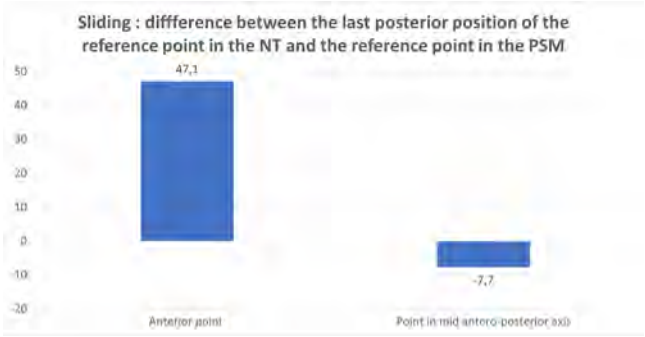

Figure 2.9 – Difference between the last posterior location of the reference point in the NT and the reference point in the PSM when the points are at $y = 964\mu m$ (left) and $y = 1392\mu m$ (right).

effects, we performed 8 simulations with only the following parameter values changing and the other parameters remained unchanged:

1. Simulation 1: $g_1 = g_2 = 1/8.75$: to test the effect of differential cell proliferation.
2. Simulation 2: $g_1 = g_2 = 1/10.83$: to test the effect of differential cell proliferation .
3. Simulation 3: $\kappa_{PSM} = \kappa_{NT} = 3.4$: to test the effect of differential cell injection.
4. Simulation 4: $\kappa_{PSM} = \kappa_{NT} = 5$: to test the effect of differential cell injection.
5. Simulation 5: $\kappa_{PSM} = \kappa_{NT} = 0$: to test the contribution of cell injection.
6. Simulation 6: $g_1 = 0$: to test the contribution of cell proliferation in the NT.
7. Simulation 7: $g_2 = 0$: to test the contribution of cell proliferation in the PSM.
8. Simulation 8: $g_1 = g_2 = 0$: to test if cell injection is sufficient to sustain elongation.

Comparison of density profiles. We compared the density profiles in these sets of simulations with the WT case in figure 2.8. We represent the densities in Figure 2.10. The first observation is that when injection rates in both tissues are taken equal to that of the PSM (Figure 2.10b) or taken equal to 0 (Figure 2.10d), the density profiles resemblance very much those in the WT case, suggesting that injection has little effect on tissue formation and on axis elongation. However, cell proliferation seems to play a key role. In fact, when cell proliferation in the PSM was decreased (taken equal to that of the NT), we see in Figure 2.10a that the tissues are shorter, thus the elongation rate is smaller, and observed that the NT is much wider compared to the WT case. When cell proliferation is equal to that of the PSM (Figure 2.10c), the tissues are longer, with a higher elongation rate, and the NT is also wider than that of the WT case. Finally, when we set cell proliferation to zero in the PSM (Figure 2.10e), the PSM is not formed properly and we observe a clear expansion of the NT in the lateral direction instead of in the axial one. This expansion does not seem sufficient to push the posterior boundary downwards. Finally, setting the NT proliferation to zero, we observe a striking phenomena (Figure 2.10f): elongation still occurs as a result of lateral compression of the PSM on the NT. The NT however does not form properly, and the PSM is much larger compared to the WT case.
The remaining simulations (along with the velocity profiles) are detailed and commented in Chapter 5.

Comparison of inter-tissue sliding. We compared the density and velocity profiles of all the simulations cited above as well as the shape of the tissues, the elongation rate and the inter-tissue sliding. To quantify the sliding between the tissues we first computed the central velocities in each tissue (velocities along the antero-posterior axis inside reach tissue, details in Chapter 5). We then took two reference points one in the PSM at $(35\mu m, 964\mu m)$ and one in the NT at $(135\mu m, 964\mu m)$

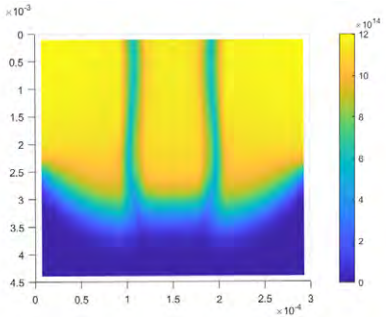

(a) Final time: proliferation rates equal to that of the NT.

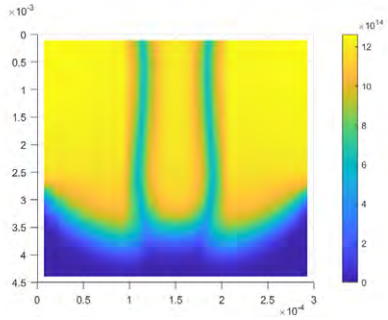

(b) Final time: injection rates equal to that of the PSM.

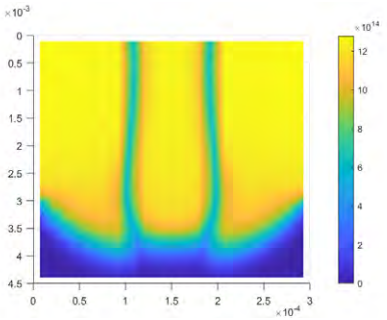

(c) Final time: proliferation rates equal to that of the PSM.

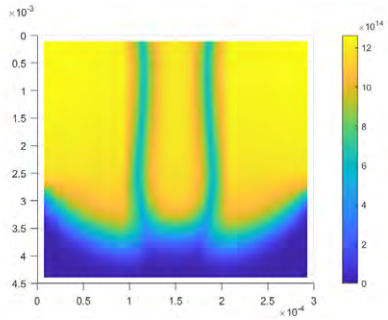

(d) Final time: injection rates equal to 0.

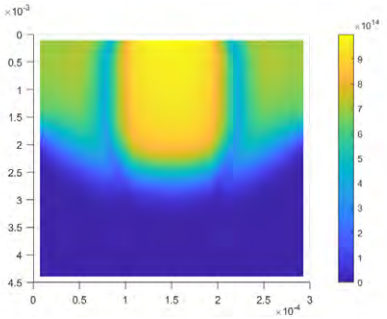

(e) Final time: PSM proliferation rate equal to 0.

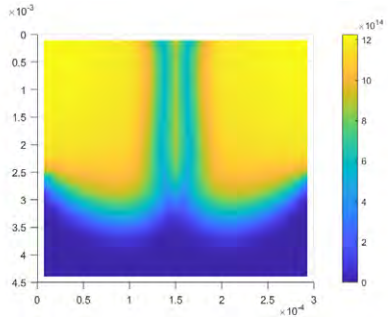

(f) Final time: NT proliferation rate equal to 0.

Figure 2.10 – Density profiles in the case when proliferation rates are equal to that of the NT (Panel (a)), when injection rates are equal to that of the PSM (Panel (b)), when proliferation rates are equal to that of the PSM (Panel (c)), when injection rates are equal to 0 in the PSM and NT (Panel (d)), when PSM proliferation rate is equal to 0 (Panel (e)) and when NT proliferation rate is equal to 0 (Panel (f)).

and using the central velocities in each tissue, we computed their trajectories (in the y-component) along the posterior axis. We show their final posterior position in Figure 2.11 for each simulation.

We first observe that cell proliferation in the PSM and in the NT greatly affects the poste-

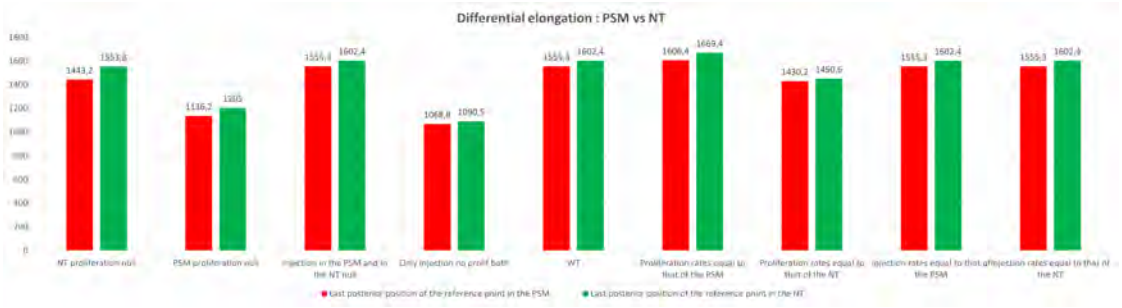

Figure 2.11 – Comparison of of differential elongation: last posterior position of the reference point in the PSM (red) and in the NT (green) in all the simulations.

rior movement of the reference points. We also see that cell injection does not seem to affect the differential elongation. In Chapter 5, we quantified the inter-tissue sliding by computing the difference between these two reference points in each simulation. We observed that when proliferation is reduced in the PSM (taken equal to that of the NT), the sliding was reduced by 50%. When proliferation is increased in the NT (equal to that of the PSM) the inter-tissue sliding increased by 50%. We also noticed that when cell proliferation is null in the PSM, the points travel much less to the posterior and the sliding increases. Interestingly, when cell proliferation in the NT was equal to zero, the sliding also increased significantly.

Summary of the results. We compared the numerical results by focusing on the density and the velocity profiles, the elongation rate, and the inter-tissue sliding. We exhibited some of the simulations in this section and we refer the reader to Chapter 5 for the complete set of simulations and analyses. We now summarize the numerical results and model predictions:

- PSM cell proliferation is essential to sustain long-term tissue formation and axis elongation.
- PSM tissue growth produces an important lateral-to-medial compression on the NT which promotes the NT extension.
- The PSM and the NT must both grow to maintain normal tissue formation and elongation.
- NT cell proliferation in the absence of PSM proliferation does not generate enough force to push the PZ boundary posteriorly.
- Differential cell injection and cell injection have little effect on tissue formation, axis elongation and inter-tissue sliding compared to cell proliferation.
- Cell injection in the absence of cell proliferation is not enough to sustain long-term tissue formation and axis elongation.
- When cell proliferation rates of both tissues are equal to that of the NT the model predicts a

shortening of the tissues, a wider NT, a smaller elongation rate, lower velocities in the PSM and in the NT, less posterior movement of both reference points in the anterior, 50% less sliding.

- When the cell proliferation rates of both tissues are equal to that of the PSM the model predicts a longer tissues, a wider NT, a bigger elongation rate, higher velocities in the PSM and in the NT, more posterior movement of both reference points in the anterior, 50% more sliding.

Comparison with the biological data. We compared our results first to known biological data. We see that the density, velocity and pressure profiles in the *in silico* WT case quantitatively match the ones measured *in vivo* [24, 108]. The model prediction that cell injection has little effect on elongation is supported by PZ ablations [25] where authors noted very little difference in elongation compared to the WT embryo. The importance of PSM lateral compression predicted by the VMI also supports the posterior PSM ablation experiments in [25] which drastically affected axis elongation. Our simulations of PSM cell proliferation rate reduction (taken equal to that of the NT) predicted that the NT becomes much wider than the WT case. We acquired live movies of transgenic quail embryos and tested this prediction in treated embryos with P27 (a cell cycle inhibitor) electroporated in the PSM. We measured the width of the NT and compared it to that of the WT embryo and found that it had indeed significantly increased in width, see Figure 2.12.

Figure 2.12 – Averaged NT width over three antero-posterior locations: at the last formed somite, $250\mu m$ lower, and $500\mu m$ lower, in the wild-type embryo (blue) and in the P27 in the PSM treated embryos (in orange). Stars indicate the significance of the t-test (p-value<0.05, $N = 7$ embryos).

This confirms the model hypothesis. In an ongoing work, we aim to test the rest of the model

hypotheses in the quail embryo.

In conclusion, the VMI we developed reproduces very well tissue formation and axis elongation. Using the VMI, we quantified the sliding between the tissues and performed multiple *in silico* experiments to test various hypotheses. The model predictions were compared to the biological data and prove to hold in the vertebrate embryo. We also used this model to test the dynamics of the PSM and the notochord (see Chapter 5). This shows that the VMI is a multi-functional and polyvalent model which provides insight and a new perspective as to the long-term mechanisms governing axis elongation.

2.3 Cell-to-cell heterogeneity in Sox2 and Bra expression guides progenitor motility and destiny

In Chapter 6, we take a closer look at the PZ using functional experiments on quail embryos, as well as live imaging, image analysis and mathematical modelling. Progenitors co-express the transcription factors Sox2 and Bra which are involved in respectively neural and mesodermal cell fates. We investigate the protein expression by immunodetection techniques and discover that it is heterogeneous across NMPs. We also notice that the cell spatial distribution with respect to their protein expression is heterogeneous as well. We first look at the cell properties in the wild type embryo. We observe that cells move in a random manner in the three tissues PZ, PSM and NT. However, these cells do not have the same motility, as NT cells move slower than PSM and PZ cells, whose motilities are comparable. Using functional experiments (by electroporation techniques), we can over express or down-regulate the genes within these cells to study the resulting biological system with this new gene expression. We study the effect of Sox2 and Bra on cell fate, by comparing the functional experiments to the wild type embryo. We find that Sox2 promotes cell exit from the PZ and into the NT, whereas Bra promotes cell exit into the PSM. We study the role of Sox2 and Bra on cell motility and show that Sox2 inhibits cell motility whereas Bra promotes it. These results exhibit the role of these two genes in progenitor behavior. The spatial heterogeneity in the PZ was unexpected and surprising, as it does not comply with the french flag model. For that reason, we pursue the goal of understanding the role of this heterogeneity by developing an agent-based model that allows to test different spatial cell distributions in the PZ. The model highlights a surprising paradox: chaos (heterogeneity) can sustain an apparently very ordered process (axis elongation).
In what follows we summarize the results in Chapter 6.

Sox2 and Bra are spatially heterogeneously expressed in the PZ. We carefully examined the levels of expression of Sox2 and Bra using immunodetection techniques, in quail embryos at stages 10-11HH. Our analysis showed extensive cell-to-cell heterogeneity in protein expression in the PZ, Figure 2.13.

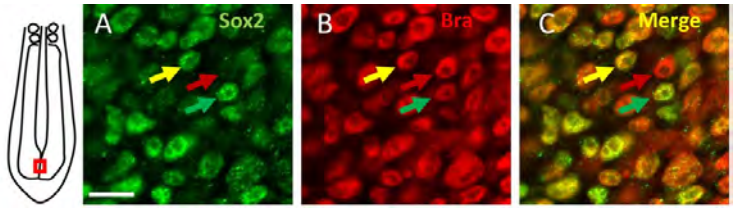

Figure 2.13 – Immunodetection of Sox2 (A - green) and Bra (B -red) analyzed at the cellular scale in the caudal part of stage HH11 quail embryo in the PZ (C - merge).

By analyzing protein expression in transverse sections of the PZ, we notice the presence of a zone in mid-PZ where cells express heterogeneous levels of Sox2 and Bra, and in a spatially heterogeneous manner. That is, there is no apparent order in cell location with respect to its protein concentration. Interestingly, a global antero-posterior Sox2-to-Bra gradient was detected in the PZ, with cells expressing more Sox2 in the anterior-dorsal part of the PZ and cells with more Bra in the most posterior part, Figure 2.14. This variability is lost as cells migrate into the tissues, by respectively decreasing Sox2 when entering the PSM and decreasing Bra when entering the NT.

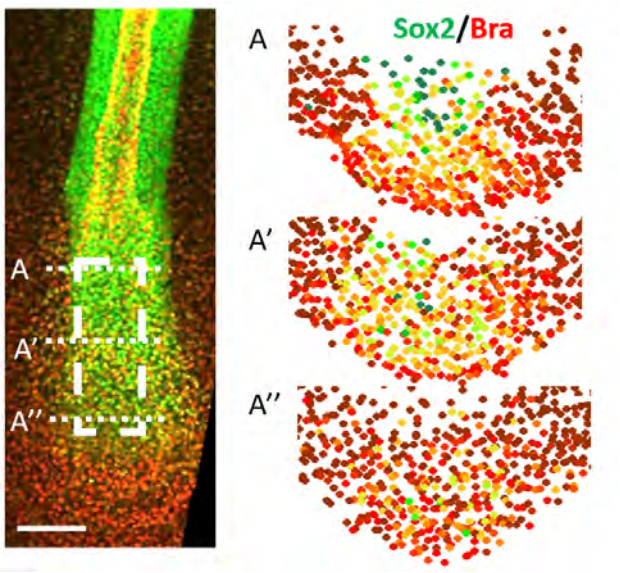

Figure 2.14 – Representation of the Sox2-to-Bra ratio (green to red) in digital transversal sections A,A',A" (40 um) made in the PZ. (A,A',A"): dashed lines in the double immunodetection image - left.

The effect of Sox2 and Bra on tissue distribution. As Sox2 is a neural marker, and Bra is a mesodermal marker, a natural question to ask is whether cells displaying high levels of Sox2 are going to enter the NT and those with high levels of Bra are going to the PSM. To study the influence of Sox2 and Bra on cell distribution in posterior tissues, we conducted functional experiments using electroporation techniques. This technique consists in transfecting the embryos (namely the PZ) with expression vectors or morpholinos and analyze the distribution of the targeted cells in the posterior tissues. We first studied the distribution in the wild-type embryo. Approximately 22% of the targeted (fluorescent) cells from the PZ were found in the PSM, with 60% in the NT, and 18%

0. **Immunodetection** is a technique consisting in fixing the embryos at a certain stage of their development in formaldehyde 4% in phosphate-buffered saline (PBS). The embryos are then incubated with primary antibodies for Sox2 or Bra overnight. After a wash, the embryos undergo a second overnight incubation with antibodies coupled with a fluorescent substance. This technique allows to observe protein levels using fluorescence.

of the cells remained in the PZ, Figure 2.15.

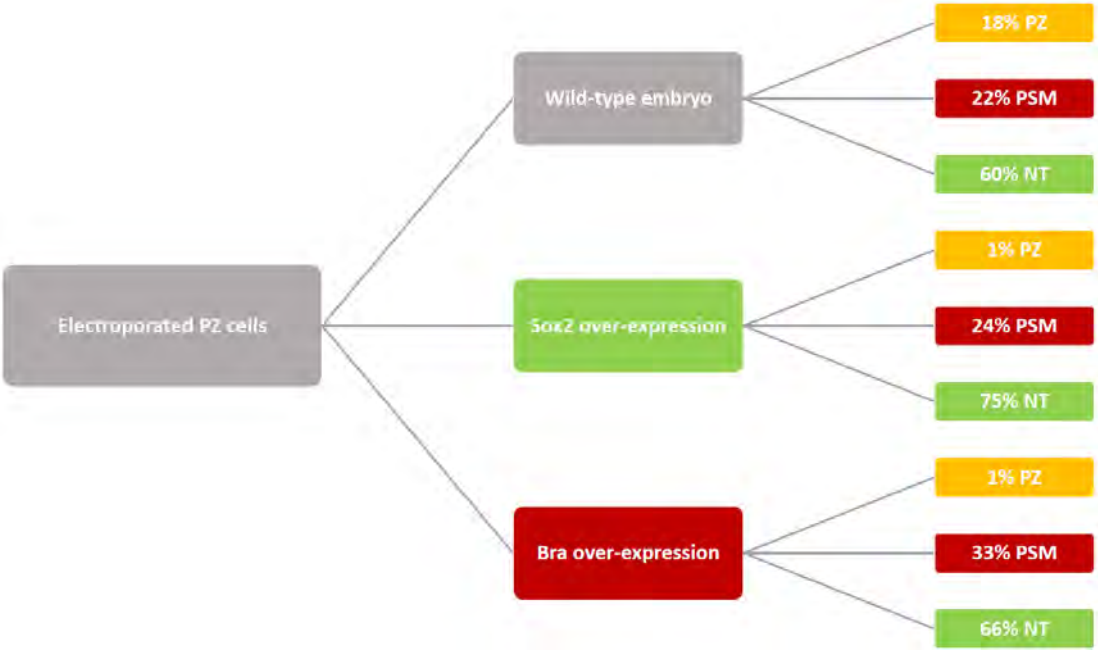

Figure 2.15 – Graph summarizing the results of cell distribution post-electroporation in the wild-type embryo (upper branch), Sox2 over-expression (middle branch) and Bra over-expression (lower branch). The secondary branches indicate the final destination of the electroporated PZ cells (which amount to 100%) in either the PZ, the PSM or the NT.

When Sox2 was over-expressed in the progenitors, the cell distribution was significantly different: cells exited the PZ and favored their entry into the NT. When Bra was over-expressed, cells exited the PZ in favor of the PSM. In Figure 2.15 we summarize the results hereby discussed as well as the results of the morpholinos (down-regulation of Sox2 and Bra).

These results show that a Sox2/Bra deregulation triggers cell exit from the PZ. They also show the influence of the Sox2/Bra concentration on the final destination of cells in the posterior tissues, with cells with high Sox2 levels entering the NT, and with high Bra levels entering the PSM.

Cell behavior in the PZ: the case of the wild-type embryo. Cells exiting the PZ and entering specific tissues suggests a relationship between Sox2/Bra expression and cell motility. For that reason, we examine in the wild-type embryo the cell behavior in the PZ, the PSM and the NT. Namely, we look at three properties:

0. **Electroporation** is a technique used on live embryos. After harvesting the embryos at stages 4-6HH, they are micro-injected at the anterior region of the primitive streak with a solution containing expression vectors or morpholinos. The embryos are then subjected to a pulse -of 5.2V with a duration of 50ms on a time interval of 200ms-, by positioning electrodes on either side of the embryo. The embryos are incubated overnight and left to develop. We can then observe the cell distribution based on the fluorescence in the tissues.

- Cell velocity
- Trajectory angles
- Diffusivity (mean square displacement)

Using live imaging followed by thorough quantification of the data, we tracked electroporated cells in each tissue. We found that NT cells have the slowest velocity of all three tissues. As for the PSM and the PZ cells, they display a comparable average velocity. Interestingly, the PZ contained cells with velocities as low as those of the NT and as fast as those of the PSM, see Figure 2.16. This resurfaces the heterogeneous nature of the PZ. Furthermore, by analyzing cell trajectory angles, we found that cell motion was non-directional, i.e, the cell trajectories did not display any apparent bias towards the posterior in all three tissues, and cells move in a random manner. Finally, the mean square displacements were measured in the three tissues. We observed that the mean square displacements of the PSM and of the PZ cells were significantly higher than that of the NT, and were linear in lag-time. This exhibits the diffusive behavior of progenitors.

These results highlight the highly motile nature of the NMPs, and the randomness and heterogeneity of their behavior. In what follows we conduct functional experiments and compare them to the wild-type embryo.

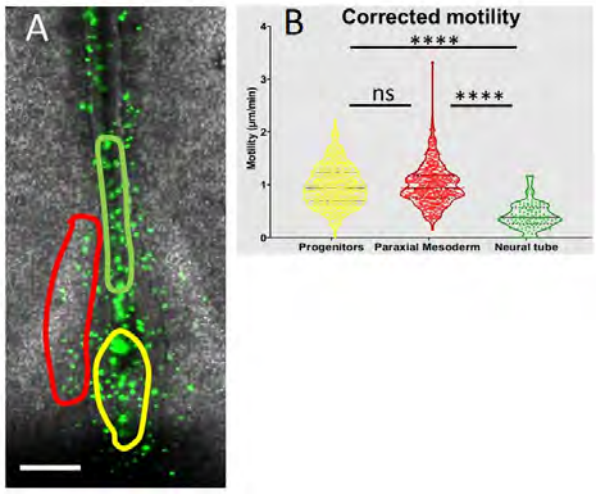

Figure 2.16 – In Panel A we show an electroporated quail embryo with three drawn zones: the NT (green), the PSM (red) and the PZ (yellow) where cell behavior analysis was conducted. In Panel B we represent violin plots showing the velocity distribution in each tissue.

The effect of Sox2 and Bra on NMP motility. Now that we have gathered data on cell behavior in the wild-type embryo, we compare these data to functional experiments where Sox2

and Bra are deregulated, to understand their effect on cell motility in the PZ. We observed that over-expressing Bra induced a higher cell motility in the PZ, and did not affect cell directionality (trajectory angles). When Sox2 was over-expressed, we noted a sharp decrease in cell motility, coupled with an anterior bias in trajectory angles suggesting their entry to the NT (Figure 2.17). These results strongly suggest that Bra promotes cell motility and Sox2 inhibits it. Experiments on morpholinos also confirm this hypothesis.

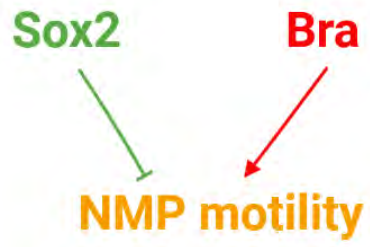

Figure 2.17 – Graphical representation of the effect of Sox2 and Bra on NMP motility. Sox2 inhibits PZ cell motility, and Bra promotes it.

Modelling the role of spatial heterogeneity. The role of Sox2 and Bra having been identified, there still remains one interesting observation which we wanted to address: the spatial heterogeneity in NMPs. As we previously explained, the presence of this zone where spatial heterogeneities exist defies the french flag model. Within this zone, cells are not obeying a specific gradient that confers them a particular function and a protein concentration. Cells rather move randomly, with heterogeneous concentrations. This begs the question: **what is the role of spatial heterogeneity in this zone ?** In the spirit of the functional experiments, to study the role of spatial heterogeneity we would need to study a system where it is absent. In the vertebrate embryo, it is feasible to disorder an ordered system. However, it is inconceivable to organize a system governed by disorder (as in the PZ) and to keep it organized. For that reason, we turn to *in silico* experiments. We introduce an agent-based model to study different spatial cell distributions inside the PZ and extract the properties of spatial heterogeneity. We consider three cell populations: the PZ, the PSM and the NT cells. We are interested in the cell position in 2D, as well as its concentration in Sox2 and Bra. Each cell i is then endowed with two variables $X_i(t) = (x_i(t), y_i(t))$ and $R_i(t)$ denoting respectively its position and its ratio of Sox2 and Bra. Cell ratio is considered as the variable $R_i = \dfrac{Sox2}{Bra + Sox2}$ ranging between 0 and 1, with $R_i = 0$ corresponding to a PSM cell and $R_i = 1$ to a neural cell. Cells with ratio $0 < R_i < 1$ are progenitors. The dynamics of the

ratio R_i are given by the following equation,

$$dR_i(t) = \left(100\,(R_i(t)-0.2)\,(R_i(t)-0.5)\,(R_i(t)-0.8)\,dt + k_r dB_i^R(t)\right)\chi_{R_i(t)\in(0,1)}, \tag{2.57}$$

with χ the indicator function. The deterministic function (taken with the indicator) has 5 equilibriums: $\{0, 0.2, 0.5, 0.8, 1\}$. The stable equilibriums are $\{0, 0.5, 1\}$ and $R_i = 0.2, 0.8$ are unstable. Taking this form allows to account for the fact that cells with very high (or very low) ratios are already engaged in a certain fate and will not go back to being NMPs, see Figure 2.18.

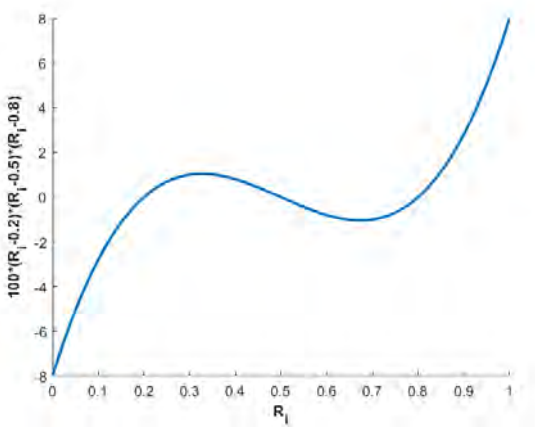

Figure 2.18 – The function $100\,(R_i - 0.2)\,(R_i - 0.5)\,(R_i(t) - 0.8)$ with respect to $R_i \in [0, 1]$.

This form also considers that differentiated cells ($R_i = 0$ or $R_i = 1$) cannot de-differentiate and become progenitors. This is in accordance with a classical theory on pluripotent stem cells called the Waddington commitment landscape [151].

Remark 2.3.1. ***[The Waddington commitment landscape.]*** *Waddington compared the differentiation journey of a cell to a ball traveling downwards along valleys. Once it reaches its final destination (full differentiation), it cannot return to its original state (de-differentiated), and can hardly cross valleys, see Figure 2.19.*

The noise dB_i^R, with intensity k_r represents the various signals that cells receive during their differentiation, which guide their fate and final destination in the tissues. The noise intensity k_r is uniform among progenitors.

Furthermore, in our model all cells proliferate with their division rates given in [24]. Cell motion follows a diffusion process (Brownian motion) as suggested by our biological experiments. The equations for cell position $X = (x, y)$ are,

$$dx_i(t) = k_x dB_i^x(t) \times \mathcal{V}(R_i(t)), \tag{2.58}$$

$$dy_i(t) = k_y dB_i^y(t) \times \mathcal{V}(R_i(t)), \tag{2.59}$$

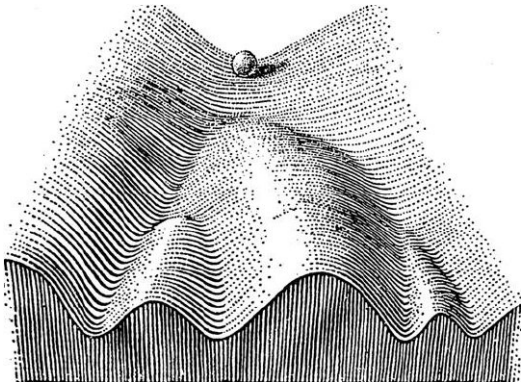

Figure 2.19 – Waddington's landscape [151].

with dB_i^x, dB_i^y the increment of the Brownian motion, with k_x and k_y their respective intensities. The cell velocity $\mathcal{V}(R_i(t))$ depends on the cell protein ratio as suggested by our biological experiments, i.e cells with high levels of Sox2 are slow, and cells with high levels of Bra are fast. The velocity function takes the following form,

$$\mathcal{V}(R_i(t)) = \begin{cases} 1 + a_1 \left(\tilde{R} - R_i(t)\right)^2 & \text{if } 0 \leq R_i(t) \leq \tilde{R} \\ 1 & \text{if } \tilde{R} \leq R_i(t) \leq R^* \\ 1 - a_2 \left(R^* - R_i(t)\right)^2 & \text{if } R^* \leq R_i(t) \leq 1 \end{cases}$$

with $a_1, a_2 > 0$, and $R^* = 0.8$ is the threshold above which progenitor cells change their dynamics (slow down) and commit to their pre-neural fate. Similarly, under the threshold $\tilde{R} = 0.2$, cells adopt a pre-mesodermal fate and migrate faster. Progenitors with ratio between these two thresholds have intermediate speed.

Remark 2.3.2. ***[Calibration of the noise intensities*** k_r, k_x, k_y***]*** *The intensity of the ratio's noise k_r in (2.57) controls cell differentiation into NT or mesodermal cells. Therefore, to calibrate this parameter, we ensured that the total number of cells in the PZ remained constant, as per in vivo observations [24]. This ensured a balanced between cell proliferation and differentiation.*
For the position noise intensities k_x and k_y in (2.58)-(2.59), we calibrated them based on their ability to qualitatively reproduce cell dynamics (velocity, angles, elongation), noting that $k_x = k_y$. An ongoing project (in collaboration with Gabrielle Roullet, a Master 1 internship student in Applied Mathematics from Marseille University) aims at confronting these noises with biological data to calibrate the model more accurately.

The biophysical properties and the cell-cell interactions follow specific rules, which are encoded directly in the numerical algorithm:

1. All cells cannot exit the left and right boundary of the PSM. The boundaries represent the lateral plate which is a rather stiff wall.

2. All cells cannot exit the anterior wall as it represents the last formed somite, which is a hard structure.
3. Cells with high ratios R_i (close to 1) search for the nearest group of cells of the same type.
4. Cells re-direct their movement in the opposite direction of groups of cells of different types.

We specify that in the list of interactions above, item 3 is related to the assumption that cells with high levels of Sox2 adhere, therefore, NT cells adhere the most. This assumption is done as the NT is an epithelium with densely packed cells. Concerning item 4, we have added this local non-mixing property, i.e cells move away from foreign high densities, as we noticed that this condition guarantees the maintenance of the boundaries between the tissues *in silico*.

Strategy: the random, the gradient, and the mixed models. To understand the role of heterogeneity, we created three models: a) the random model, b) the gradient model, c) the mixed model. The three models incorporate the same equations on the ratio and the position. They differ in their global implemented structure (random, gradient, mixed). More precisely, for each model, we implement a different structure by choosing a different initial condition which will be maintained thanks to a biased noise (dB_i^R in (2.57)). We assume that this noise represents numerous signals that cells receive during their migration and differentiation, and which are responsible of cells' final fate. The initial conditions and the choice of noise are as follows.

We consider the embryo to be at a stage where a portion of the NT and the PSM have already been formed (anteriorly), for example at stage HH8. We consider neural cells (green) forming a portion of the NT , and PSM cells (red) from either side of the NT. For each model, we organize the progenitors (shades of yellow) in the PZ in a specific spatial distribution, depending on the model considered, which will be conserved throughout the simulation thanks to our choice of biased noise:

- In the random model, cells are attributed a random ratio between $R_i = 0.15$ and $R_i = 0.85$ and randomly distributed in the PZ, see Figure 2.20 (left). The noise dB_i^R in (2.57) is random for all PZ cells.
- In the gradient model, cells are attributed an initial ratio between $R_i = 0.15$ and $R_i = 0.85$ linearly depending on their position on the antero-posterior axis (only the y-coordinates are considered). The initial ratio distribution is of the form,

$$R_i(t = 0) = -\alpha y_i(t = 0) + \beta, \tag{2.60}$$

with $\alpha, \beta > 0$, see Figure 2.20 (right). In this model, all cells are subjected to a biased noise depending on their position on the antero-posterior axis of the PZ. Anterior cells are subjected to a biased noise dB_i^R promoting neural differentiation. Moving posteriorly in the

PZ, this noise gradually switches to become a mesodermal promoter in the most posterior part of the PZ. Such noise allows to maintain the gradient structure.

- In the mixed model, we divide the PZ into subregions. In the first anterior subregion, cells are attributed a random initial ratio $0.5 < R_i < 0.85$, clearly indicating a pre-destination towards a neural fate ($R_i = 1$). In the last posterior subregion, cells are attributed a random initial ratio $0.15 < R_i < 0.5$, clearly indicating a pre-destination towards a mesodermal fate ($R_i = 0$). In the middle subregions, random initial ratios are given $0.15 < R_i < 0.85$, see Figure 2.20 (middle). In this model, only the anterior subregion (promoting neural fate) and the posterior one (promoting mesodermal fate) are subjected to a biased noise dB_i^R. Cells between these two regions (mid PZ) are subjected to an unbiased random noise dB_i^R. Such noise allows to maintain the mixed structure.

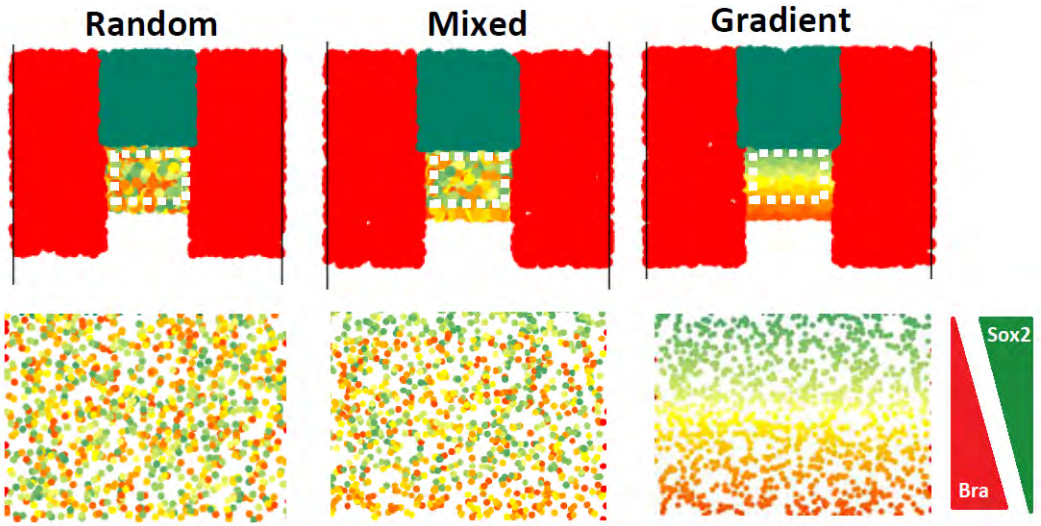

Figure 2.20 – The initial conditions of the random (left), the mixed (middle) and the gradient models (right).

Remark 2.3.3. *Considering progenitors with initial ratios higher than the threshold $R^* = 0.8$ (respectively lower than the threshold $\tilde{R} = 0.2$) is justified by our analysis of cell ratios in the PZ where we noticed the presence of cells with ratios as high as the PSM cells and as low as the NT cells.*

The mixed model: wild-type embryo *in silico*. The model that is the closest to the wild-type embryo is the mixed model, as it displays two features observed in the biological experiments: the global antero-posterior Sox2-to-Bra gradient in the PZ, and the zone of spatial heterogeneity in mid PZ. The random and the gradient models are two extreme *in silico* cases which we use to understand the role of spatial heterogeneity. For that reason, we first made sure that the mixed

model reproduces the qualitative behavior of the wild-type embryo. We computed *in silico* the cell trajectory angles, which we found were random, see Figure 2.21. We computed the cell velocities in each tissue and with no surprise [as it is encoded in the velocity function $\mathcal{V}(R_i(t))$] obtained a slower velocity for NT cells, and a faster one for PZ and PSM cells. The model reproduces elongation with progenitors gradually differentiating and migrating into the corresponding tissue according to their fate (by pure migration led by the prescribed cell-cell interactions). The PZ is driven to the posterior, and the NT and PSM also elongate towards the posterior, see Figure 2.21. This leads to an increase in the total cell number in the NT population, and in the PSM population, thanks to cell addition and cell division. The number of progenitor cells remains constant as we calibrated the noise intensity (controlling differentiation) to balance cell proliferation. We analyzed cell trajectory angles and found them to be random in all three tissues, see Figure 2.21. We also simulated the case of Sox2 over-expression and the case of Bra over-expression and found comparable qualitative results with the biological experiments: cells exit the PZ (decrease in cell number) and favor their entry to the NT (Sox2 over-expression) or PSM (Bra over-expression). We refer the reader to Chapter 6 for more details on these results. All in all, using the lateral confinement and local interaction rules, the mixed model depicts well the cell dynamics during axis elongation, and exhibits self-organizing phenomena, with physical boundaries maintained between the tissues.

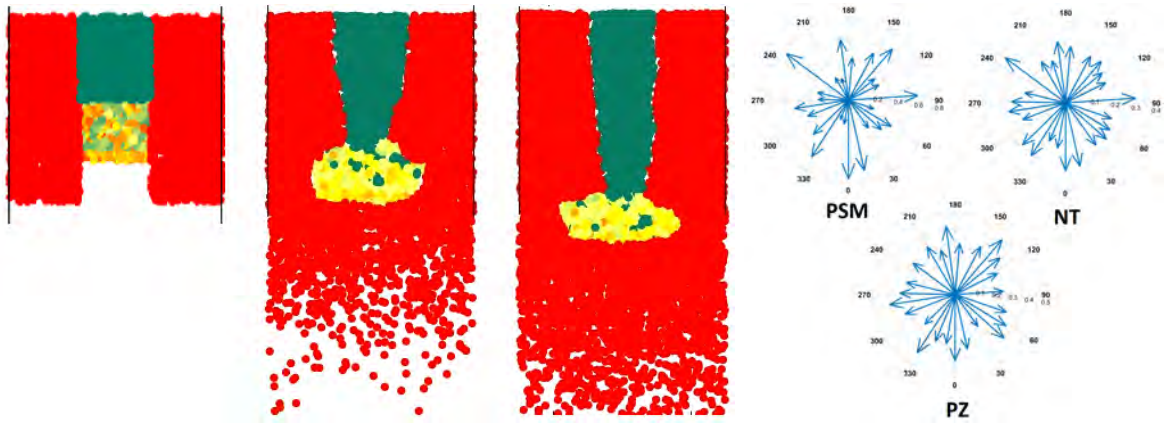

Figure 2.21 – Left: three snapshots of the numerical simulation of the mixed model at time $t = 0$ hours, $t = 5$ hours and $t = 10$ hours of development of the mixed model. The NT (green cells) is flanked with two stripes of PSM (red cells). The PZ spatial cell distribution is depicted in zoom in Figure 2.20. Right: Trajectory angles for the PSM, the NT and the PZ in the mixed model.

The role of spatial heterogeneity: comparison of the three models. Comparing the three models, we observe that all three of them reproduce axis elongation by maintaining the PZ posteriorly and by elongating the axial and lateral tissues, see Figure 2.22. This suggests that randomness and a gradient pattern might both be at play in this system. To capture the role of heterogeneity and its effect on tissue formation, we distinguished specific aspects to quantify, which

differed greatly between the models:

- Elongation rate
- Cell diffusivity (mean square displacement)
- Average distance traveled towards the posterior by resident progenitors
- Tissue shape conservation

Our analysis showed that the random model elongates faster compared to the mixed and gradient model. The elongation rate of the mixed model falls between the random and the gradient one, Figure 2.22. We tested the average posterior distance traveled by resident progenitor cells and found that in the random model progenitors reach more posterior positions compared to the other models. This indicates that spatial heterogeneity is more efficient in imposing a posterior movement than the graded patterning.

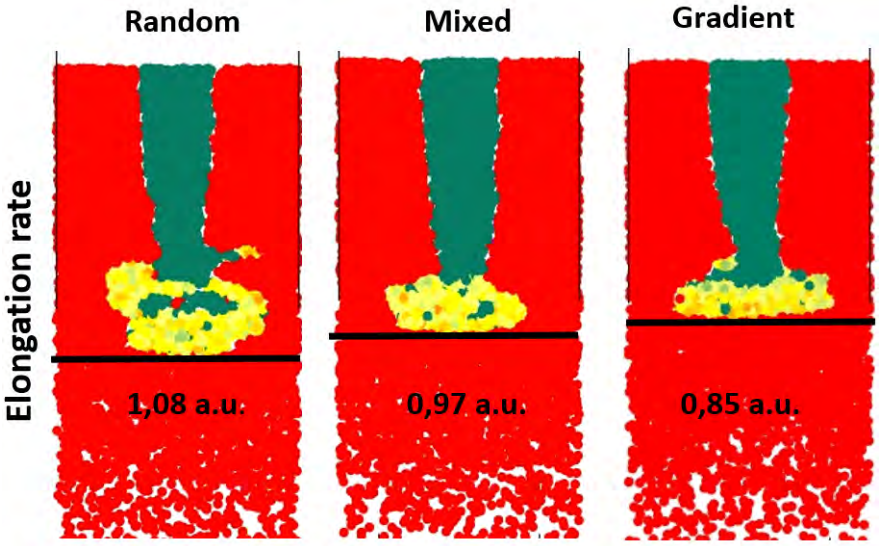

Figure 2.22 – The elongation rates (in arbitrary units (a.u))of the three models, snapshots taken at final time $t = 10$ hours of development.

In Figure 2.22, we notice that the shape of the PZ at final time is not the same in all three models. In fact, we measured the shape proportions of the PZ at $t = 10$ hours and compared it to its initial shape proportion in each model. Interestingly, in the random model, these proportions were much more conserved (up to 74%) than in the gradient (37%) and mixed (53%) models, Figure 2.23 (left). In the gradient model the PZ shape became flat (shorter and larger). Finally, the mean square displacements were compared in all three models. Our results showed that the random model has the highest mean square displacement, followed by the mixed then the gradient model. This suggests that spatial heterogeneity enhances the diffusive behavior of progenitors, see Figure 2.23

(right), which confers tissue fluidity and allows deformation and remodelling. This observation is supported by the auto-corrective cell behavior extensively present in the random model, compared to a more stable elongation -very little local deformations- in the gradient model.

In conclusion, the mathematical models strongly suggest that spatial heterogeneity in the PZ promotes cell rearrangements, tissue fluidity, posterior elongation and long-term conservation of tissue shape.

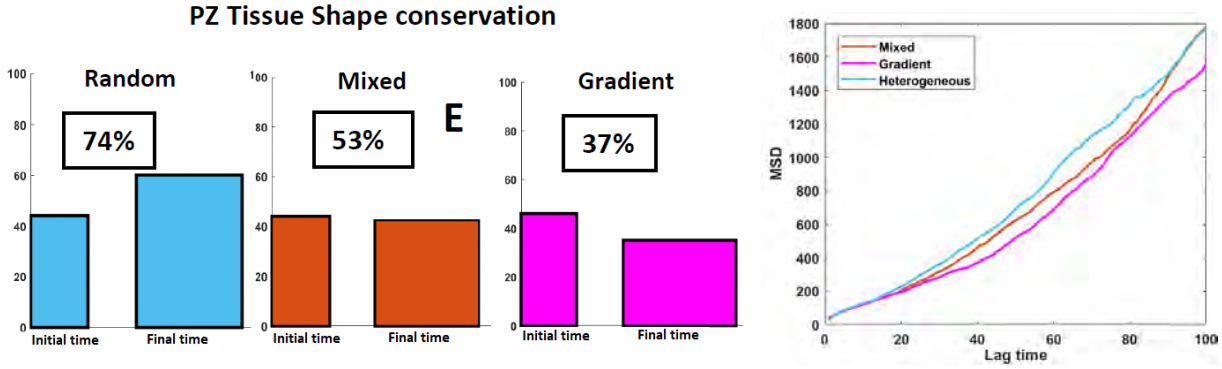

Figure 2.23 – Left: Comparison of PZ shape conservation between initial and final time in each model. Right: Mean square displacement (MSD) as a function of lag time in each model.

Remark 2.3.4. ***[On the adhesion and non-mixing rules].*** *The Sox2-dependent adhesion as well as the non-mixing rule were found to be essential for the model to reproduce axis elongation. Without them, cells mix extensively, and the PZ does not elongate as progenitors do not sense the pressure from NT cells anterior to them. These two model hypotheses need to be tested and validated in vivo. They can lead to interesting conclusions which can explain cell-cell cohesion in the NT and in the PZ, and explain cell-cell segregation.*

Remark 2.3.5. ***[Comparison of the mixed agent-based model and the ESVM: a micro-to-macro limit].*** *There are similarities between the mixed agent-based model and the ESVM presented in Section 2.1. They both consider cell proliferation and the natural cell diffusion (one on the microscopic scale as a Brownian motion and the other on the macroscopic scale with the Laplacian term). The non-mixing property included in the mixed model plays the same role as the repulsion pressure q_m in the ESVM: it prevents tissue mixing. The mixed model and the ESVM in fact model the same phenomena and incorporate the same processes but on different scales. This motivates the computation of the micro-to-macro limit of the mixed model. Our future work consists in computing the micro-to-macro limit and compare the resulting macroscopic description of the mixed model to the ESVM. It would then be interesting to see the form of the limiting macroscopic repulsion we obtain.*

Our short term perspective on the mixed model is to calibrate the noise more accurately by confronting quantitatively the *in silico* results and the biological data. This will help capture the precise temporal dynamics of the Sox2/Bra ratio in the PZ. More so, it allows us to determine the relationship between temporal fluctuations of the ratio and spatial heterogeneity. This goal will be further discussed in Chapter 7.

Chapter 3

Outline of the manuscript

This manuscript introduces two general modelling approaches to understand mechanisms behind axis elongation. The first modelling approach uses macroscopic models, and describes tissue kinetics during embryonic growth. The second approach relies on agent-based models to understand progenitor behavior and their contribution to tissue formation during elongation. The outline of this manuscript is as follows.

Chapter 4. This chapter is the result of a collaboration with Pierre Degond (CNRS, Institut de Mathématiques de Toulouse & Imperial College London), Sophie Hecht (CNRS, Laboratoire Jacques Louis Lions, Sorbonne Université) and Ariane Trescases (CNRS, Institut de Mathématiques de Toulouse). It is published in *Journal of Mathematical Biology* and is entitled *Multi-species viscous models for tissue growth: incompressible limit and qualitative behaviour.*
In this chapter we present macroscopic 2D viscous models which reproduce and explain tissue segregation and swirling motions with different types of segregations: an active and a passive one. We formally derive a free boundary formulation and show the well-posedness of the stationary systems. We exhibit regularity results on the velocity. Our analysis reveals a pressure jump on the tissues' boundaries and the appearance of a *ghost effect.*
My contribution: modeling, theoretical analysis of the models, numerical simulations, conception, writing.

Chapter 5. This chapter is a paper in preparation in collaboration with Bertrand Bénazéraf (CNRS, Centre de Biologie Intégrative, Toulouse), Pierre Degond and Ariane Trescases. It is entitled *A multi-tissue viscous model for long-term effects of mechanisms of axis elongation in the vertebrate embryos.*
In this chapter, we develop a 2D viscous model including cell proliferation and cell injection. After calibrating the model, we quantify the contribution, the role and the share of each mechanism on tissue formation, axis elongation and inter-tissue sliding by quantitatively comparing the model to biological data.
My contribution: modeling, numerical simulations, image analysis, statistics, conception, writing.

Chapter 6. This chapter is the result of a collaboration with the Bertrand Bénazéraf lab and Ariane Trescases. It was published in the journal *elife* and is entitled *Cell-to-cell heterogeneity in Sox2 and Bra expression guides progenitor motility and destiny.* In this publication I am co-first author alongside Guillaume Allio (Centre de Biologie Intégrative).
In this chapter we study the effect of the transcription factors Sox2 and Brachyury on progenitors and tissue formation during axis elongation. We show that Sox2 and Bra have antagonistic activities on cell velocity and cell fate: Bra promotes cell motility and mesodermal fate and Sox2 inhibits cell motility and promotes neural fate. Using an agent based approach, we reveal that cell-to-cell heterogeneity is responsible for tissue fluidity, tissue shape maintenance as well as elongation and cell diffusivity.
My contribution: modeling, numerical simulations, biological experiments, image analysis, statistics, conception, writing.

Chapter 7. We conclude with a discussion on the results in this manuscript, and present the short and long term perspectives of our work.

Chapter 4

Multi-species viscous models for tissue growth: incompressible limit and qualitative behavior

This chapter is taken from the paper [49] in collaboration with Pierre Degond, Sophie Hecht and Ariane Trescases.

Abstract

We introduce two 2D mechanical models reproducing the evolution of two viscous tissues in contact. Their main property is to model the swirling cell motions while keeping the tissues segregated, as observed during vertebrate embryo elongation. Segregation is encoded differently in the two models: by passive or active segregation (based on a mechanical repulsion pressure). We formally compute the incompressible limits of the two models, and obtain strictly segregated solutions. The two models thus obtained are compared. A striking feature in the active segregation model is the persistence of the repulsion pressure at the limit: a *ghost effect* is discussed and confronted to the biological data. Thanks to a transmission problem formulation at the incompressible limit, we show a pressure jump at the tissues' boundaries.

Contents

4.1 Introduction

During morphogenesis, shapes emerge as a result of cell and tissue dynamic interactions. For instance, during vertebrate morphogenesis the embryonic body shape is extending along the head-to-tail axis. Posterior tissues are organized in a very specific manner: the axially located neural tube (NT), which will form the future spinal cord, is surrounded by two stripes of presomitic mesoderm (PSM), which will give rise to muscle and vertebrae (Figure 4.1(a)). Thanks to live imaging and microscopy techniques, the cell and tissue dynamics of vertebrate development have been precisely described [24, 130]. Two striking phenomena are observed during embryo development.

The first one is the segregation of the NT and the PSM cells all along the axis, with the exception of a localized mixing area close to the progenitor zone (PZ). Cells from the PZ (depicted in yellow

in Figure 4.1(a)) migrate into the NT and the PSM, thus contributing to the tissues elongation. The segregation between the NT and the PSM is maintained throughout embryonic growth.

The second interesting observation is the appearance of swirling motions or vortices within the PSM, due to cell movements. Distinct medio-lateral cell movements are seen in the posterior zone of the embryo corresponding to the exit of progenitor cells into the PSM and the NT. Anteriorly, cell movements exhibit more complicated patterns. Globally we see latero-medial cell vortices forming, but a closer look at the anterior region reveals some ajacent areas displaying medio-lateral and latero-medial vortices [24]. The cell rotational movements are schematically represented in Figure 4.1(b).

Based on these observations, our aim is to build and study mathematical models that allow to recover and explain these two phenomena in growing tissues.

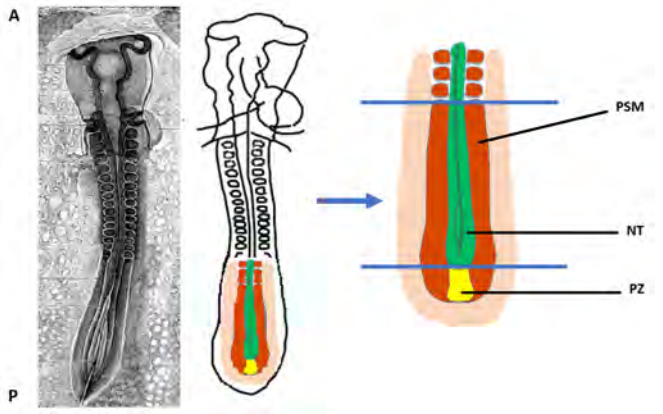

(a) Quail embryo, bright field image [59] (left) and sketches of the posterior embryo (right).

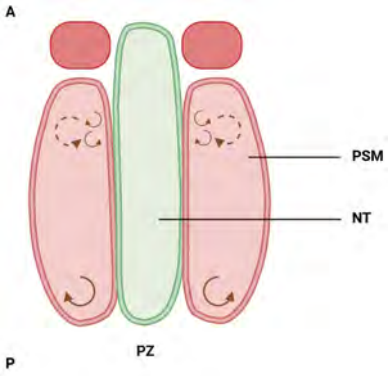

(b) Sketch of the cell rotations inside the PSM. As anterior cell movements are less obvious compared to the posterior ones, the arrows representing the global vortices are dashed. Small vortices of opposite directions are also observed in the anterior region.

Figure 4.1 – Schematics of the tissues (a) and the cell movements (b). The notations A and P respectively denote the anterior and the posterior parts of the embryo.

In mathematical modelling, when the scale of interest is of the same order as that of a cell (or an individual), which occurs when we are interested in cell trajectories and cell-cell interactions, we turn to microscopic or agent-based models. When the behavior of interest occurs on a tissue or collective scale, macroscopic models based on PDEs (partial differential equations) are used to describe the dynamics. They describe the evolution of some quantities related to the tissue such as density, velocity, pressure, etc. Macroscopic models are greatly useful in the context of tissue growth [65, 80, 101]. They provide a better understanding of biological phenomena such as cell

diffusion and proliferation [98], local and non-local cell interactions [69], chemotaxis [92], and tumor dynamics [6, 14, 36, 99, 124, 153]. In our framework, as we are interested in tissue interplay, we turn to macroscopic models to describe the embryonic growth.

To take into account the observations in the growing embryo, two modelling questions arise. Firstly, how can we model the swirling motions and their origin? And secondly, what kind of mathematical constraints should the tissues' densities obey to segregate and remain segregated? To answer the first question, we consider the tissues as viscous fluids where swirling motions originate from a nontrivial curl of the tissue velocity. Then, our approach consists of introducing tissue friction through viscosity by imposing the Brinkman law for the tissue's velocities. The Brinkman law can be derived from the Navier Stokes equations, which consists of a second order elliptic equation for the tissue velocity v. It takes the following form,

$$-\beta\Delta v + v = -\nabla p, \tag{4.1}$$

where p is the pressure inside the tissue and $\beta > 0$ is the viscosity coefficient of the tissue. When considered in a 2D (or 3D) bounded domain with Dirichlet boundary conditions, this equation produces a non-zero curl in general.

To tackle the segregation problem, it is first interesting to note that several models in literature exhibit a propagated or passive segregation [18, 34, 50, 105], that is, if initially the tissues are segregated, they remain segregated for all times. On the other hand, active segregation has also been considered, for example with a chemical interplay leading to tissular separation [89], or with a mechanical force promoting segregation [39]. To test the differences between a passive and an active form of segregation and their effects on tissue dynamics, we build two multi-species macroscopic PDE models describing the evolution of the tissue density, as well as its pressure and its velocity. The first model is endowed with passive segregation (VM) and the second with active segregation (ESVM) where we introduce a mechanical pressure denoted by q that will enforce tissue segregation. As we would like to see swirling motions emerge, we consider the Brinkman law for the velocity in the two models.

In literature from Biology and population dynamics, multi-species models were developed to account for interactions between different populations which affect the dynamics of the system. Early models such as the Lotka-Volterra system [104, 150] were studied and applied to competing/cooperating species. Other models were developed to account for attraction/repulsion between the species and volume-filling constraint, based on non-local [22, 23] or local effects [34, 51]. Emerging segregation has been studied for such models, see [18, 34, 50, 63, 105].

Segregation between tissues suggests the use of a geometric description of each tissue, where we no longer look at the evolution of the density but rather at that of the tissue shape. Based on the ESVM and the VM, can we derive such a geometric description ? Indeed, geometric models

are often obtained as the outcome of fluid-like evolution models by computing an asymptotic limit known as the incompressible limit.

In this paper, we formally compute the incompressible limit of the ESVM and of the VM and obtain two incompressible models, respectively L-ESVM and L-VM. The aim of this paper is to study these four models and investigate the links between them. Namely, we investigate the effects of segregation on tissue dynamics before the incompressible limit and at the incompressible limit. The two ESVM and VM models coincide when the densities are taken initially segregated (that is, active and passive segregations produce the same effect), under some additional but natural assumptions on the parameters. This equivalence between passive and active segregation for initially segregated densities holds at the incompressible limit. We also study comparatively the qualitative behavior of the two limit models. In fact, we show that the L-ESVM and the L-VM exhibit fully segregated solutions at the limit, and yet, in the L-ESVM the active segregation force still produces a finite effect on the tissue dynamics, which we call a *ghost effect*. These results are summarized in Figure 4.2.

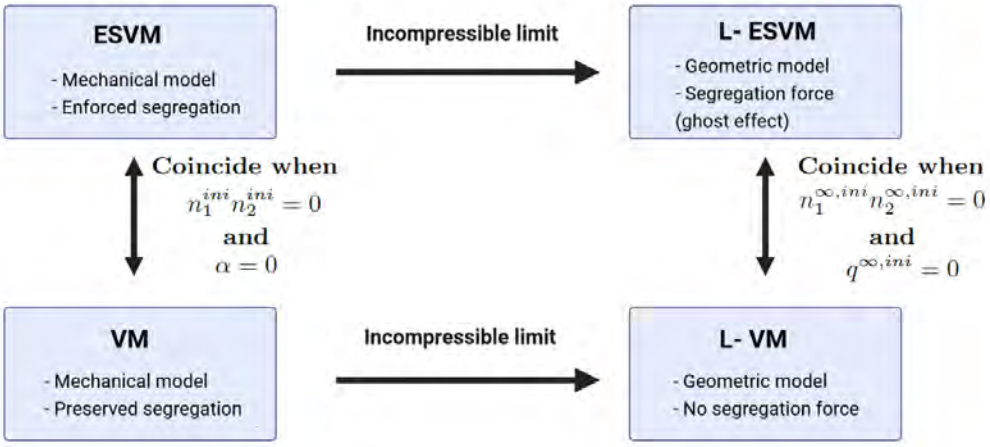

Figure 4.2 – Links between the models: ESVM, VM, L-ESVM, and L-VM.

More precisely, the incompressible limit consists of considering the evolution model in an asymptotic regime where the pressure becomes (asymptotically) stiff. In the limit, one obtains a moving domain, which corresponds to the domain occupied by the tissue. This description of the tissue amounts to a free boundary problem. It was previously used and proved very useful in the context of tumor growth [17, 96, 125]. A free boundary approach was also used to model the elongation of the PSM [11]. It was shown that free boundary problems can be derived from evolution problems via the incompressible limit in many instances such as the porous media equation in the presence of a reaction term [27, 28, 74, 94, 96, 125], with active motion, or nutrients in the case of tumor growth [45, 46, 96, 125, 126], and for the Navier-Stokes equations with growth terms [148].

On multi-species models, the incompressible limit was done in cases which included the Darcy

law for the velocity v, that is,

$$v = -\nabla p, \tag{4.2}$$

where p is the pressure of the tissue, and the Brinkman law with the assumption that the velocity is the gradient of some potential K, that is,

$$v = -\nabla K \quad \text{and} \quad -\beta\Delta K + K = p, \tag{4.3}$$

with β the viscosity of the tissue [39, 47, 48, 50, 95]. Note that when the viscosity β is null in (4.1), we recover Darcy's law (4.2). The novelty of our work is computing the incompressible limit with a velocity following the Brinkman law with Dirichlet boundary conditions, so that in general it is not a gradient unlike in (4.3). In fact, in the Darcy case (4.2) and in the Brinkman case with gradient assumption as in (4.3), since the velocity takes the form of a gradient, the curl is null, which is not consistent with our observations on the vertebrate embryo.

The modelling setting of the problem is presented in the next section, together with some numerical illustrations. Section 4.3 is dedicated to the presentation of our main results. In Section 4.4 we compute the incompressible limit of the ESVM and derive a free boundary problem for the two tissues. The computation of the limit is followed by a discussion on the persistence of the repulsion pressure at the limit (*ghost effect*). In Section 4.5 we formulate the stationary free boundary problem as a transmission problem and prove well-posedness and regularity results on the velocities. In Section 4.6 we exhibit a formal proof of the segregation property in the VM in the special case when the tissues' viscosities are equal. We then go back to the stationary L-VM and prove the existence of a pressure jump across the interfaces. Finally, the results are discussed in Section 4.7. Appendix 4.8.1 is devoted to the derivation of the transmission problem, Appendix 4.8.4 to complementary numerical simulations and Appendix 4.8.8 to details on the numerical scheme.

4.2 The setting of the problem

4.2.1 Biophysical properties of the tissues

The quantification of multi-tissue kinetics in [24] demonstrates clockwise and counter clockwise vortices within each tissue along the antero-posterior axis. In our model, both tissues (PSM and NT) are endowed with a proliferation rate which we model with a pressure-dependent growth function. This choice of growth function is common in literature, as cells tend to decrease their division rate whenever they are in a high pressured environment. Furthermore, we use a density-dependent pressure law which accounts for increased pressure in highly dense environments. We

use a singular pressure law,

$$p(n) = \epsilon \frac{n}{1-n}, \tag{4.4}$$

with n the total density for the cell populations, and ϵ a parameter. Commonly in literature, a power pressure law is used of the form: $p(n) = n^\gamma$. Here we choose the singular pressure law (4.4) which prevents cells from overlapping. A pressure law of the form (4.4) was already used in [85] in the case of a single species, then in [50, 39] for two species. The PSM cells are mesenchymal, whereas the NT is an epithelial-like tissue where cells are densely packed. These discrepancies in bio-physical properties induce a difference in the viscosity of these two tissues. The Brinkman law (4.1) allows to consider these biophysical differences (by considering two different viscosities inside each tissue), as well as to observe rotational movements within the tissues.

4.2.2 The mechanical macroscopic models

Enforced Segregation Viscous Model (ESVM). We consider two population densities denoted by n_1 and n_2 representing respectively the cell density of the NT and the PSM. We endow each tissue with a viscosity parameter, here denoted by $\beta_1 > 0$ and $\beta_2 > 0$, and use the Brinkman law to govern the velocities v_1 and v_2 of each tissue. This law takes into account the effect of the viscosity on the pressure within the tissue and the pressure between the tissues (repulsion), thus linking these variables with an elliptic equation. We introduce the following viscous two-species viscous model, for all $(t, x) \in [0; +\infty) \times \mathbb{R}^d$:

$$\partial_t n_1 + \nabla \cdot (n_1 v_1) + \alpha \nabla \cdot (n_1 \nabla(\Delta n_1)) = n_1 G_1(p_1), \tag{4.5}$$

$$\partial_t n_2 + \nabla \cdot (n_2 v_2) + \alpha \nabla \cdot (n_2 \nabla(\Delta n_2)) = n_2 G_2(p_2), \tag{4.6}$$

$$-\beta_1 \Delta v_1 + v_1 = -\nabla p_1, \tag{4.7}$$

$$-\beta_2 \Delta v_2 + v_2 = -\nabla p_2, \tag{4.8}$$

$$p_1 = p_\epsilon(n_1 + n_2) + n_2 q_m(n_1 n_2), \tag{4.9}$$

$$p_2 = p_\epsilon(n_1 + n_2) + n_1 q_m(n_1 n_2), \tag{4.10}$$

$$q_m(r) = \frac{m}{m-1}((1+r)^{m-1} - 1),\ r = n_1 n_2, \tag{4.11}$$

$$p_\epsilon(n) = \epsilon \frac{n}{1-n},\ n = n_1 + n_2, \tag{4.12}$$

with $\alpha > 0$ a diffusion parameter linked to the width of the interface between the tissues, $m > 0$ the parameter controlling the repulsion pressure q_m, and $\epsilon > 0$ a parameter controlling the congestion pressure p_ϵ. The total pressures p_1 and p_2 of each tissue (in (4.9), (4.10)) are the sum of the congestion pressure p_ϵ and the repulsion pressure q_m, where p_ϵ is a function of the total density $n = n_1 + n_2$, and q_m a function of the product $r = n_1 n_2$ which is null whenever n_1 and n_2 are not in

contact. The functions G_i are the growth functions of tissue i. They are typically taken decreasing with a zero-value in some pressure value p_i^* to take into account homeostasis.
We complement the system with initial data,

$$\forall x \in \mathbb{R}^d, \quad n_1(t=0,x) = n_1^{ini}(x), \quad n_2(t=0,x) = n_2^{ini}(x), \tag{4.13}$$

on which we assume the following conditions,

$$\forall x \in \mathbb{R}^d, \quad n_1^{ini}(x) \geq 0, \quad n_2^{ini}(x) \geq 0, \quad \text{and} \quad n^{ini}(x) := n_1^{ini}(x) + n_2^{ini}(x) < 1, \tag{4.14}$$

where 1 stands for the maximum total density allowed by our singular pressure law (4.12). Moreover, given initially positive densities, we can check with a standard Stampacchia method that the model preserves the positivity of the densities for all times.

The model (4.5)-(4.12) was first introduced in [39] in the case where $\beta_1 = \beta_2 = 0$, that is, with Darcy's law for the velocity instead of the Brinkman law. The choice of Brinkman law first introduces boundary conditions on the velocity when we consider the model on a bounded domain in $\mathbb{R}^d$, giving rise to non trivial curl as a result of the boundary conditions. Second, it introduces a new parameter β, the viscosity coefficient, which in the case of the NT and the PSM has not been measured yet in literature. The model equations are derived from a gradient flow structure associated to a mechanical energy according to the Wasserstein metric. This energy incorporates terms such as the congestion pressure p_ϵ, the repulsion pressure q_m, and a term penalizing high gradients of the densities with a coefficient α. The fourth order term compensates for the instabilities caused by the repulsion pressure.

Authors in [39] show that this model segregates initially mixed densities in finite time, except for a small interface where mixing is allowed. The width of the mixing region depends on the parameters α and m, the repulsion parameter. By introducing the viscosities through the Brinkman law as in the equations (4.7) and (4.8), we account for the swirling motions and non trivial curl within the tissues. Interestingly, it was shown in [127, 47, 48, 95] that introducing viscosity when the velocity is in a gradient form induces pressure discontinuities on the boundaries. We prove that this discontinuity happens also when taking the velocity law (4.7), (4.8) in a bounded domain with prescribed boundary conditions. One can also notice similarities between our model and the Cahn-Hilliard equation which is also of fourth order and which promotes the segregation of two phases. On the other hand, we use the singular pressure law (4.12) described to prevent cell overlap, which in the two-species case is a function of the total densities.

In Section 4.3.1 we will compute the incompressible limit of the ESVM and recover a free boundary problem describing the geometric evolution of the tissue domains. We will look at the quantitative behavior of the ESVM at the incompressible limit in Section 4.5. Furthermore, we will

compare the ESVM to a model where there is no pressure enforcing segregation (that is, $q_m = 0$, and accordingly we also take $\alpha = 0$ in the ESVM), and with initially segregated densities. This model, referred to as the VM model, is endowed with passive segregation. We describe now the VM model.

Viscous model (VM). We consider two population densities n_1 and n_2 with their respective velocities v_1 and v_2. We use again the Brinkman law for the velocities, with viscosity parameters $\beta_1 > 0$ and $\beta_2 > 0$. Here we consider only the congestion pressure p_ϵ (and no repulsion pressure). Then, the two-species viscous model (VM) is as follows, for all $(t, x) \in [0; +\infty) \times \mathbb{R}^d$,

$$\partial_t n_1 + \nabla \cdot (n_1 v_1) = n_1 G_1(p_\epsilon), \tag{4.15}$$

$$\partial_t n_2 + \nabla \cdot (n_2 v_2) = n_2 G_2(p_\epsilon), \tag{4.16}$$

$$-\beta_1 \Delta v_1 + v_1 = -\nabla p_\epsilon, \tag{4.17}$$

$$-\beta_2 \Delta v_2 + v_2 = -\nabla p_\epsilon, \tag{4.18}$$

$$p_\epsilon = \epsilon \frac{n}{1-n}, \qquad n = n_1 + n_2, \tag{4.19}$$

where the model parameters satisfy (2.24).

This model preserves the segregation property, i.e, initially segregated densities remain segregated at all times: see Proposition 4.3.9. For this model, we also compute the incompressible limit and show some quantitative features at the limit.

Boundary conditions. For the numerical simulations in the next section, we set our problem in the square $[-1, 1]^2$ with boundary conditions that best describe the biological setting. In the embryo, the PSM is surrounded by a solid-like structure or wall (called the lateral plate) which plays the role of the lateral boundaries of our bounded domain. The fluid-like PSM ends at its upper boundary with small solid structures called somites (future vertebrae, see the red rounded squares in Figure 4.1). The cells adhere at the lateral walls and at the somites. Then, homogeneous Dirichlet boundary conditions on the velocity are a natural choice. Note that they imply zero flux boundary conditions on the density.

For our theoretical analysis in Sections 4.5 and 4.6 we consider a more general 2D (smooth) domain with homogeneous Dirichlet boundary conditions.

Note that in Section 4.4, the computations of the incompressible limit of the ESVM are formal and hold in any dimension d. For simplicity, we consider the case of the whole space, that is $\mathbb{R}^d$, though the results could be adapted easily to the case of a bounded domain.

4.2.3 Numerical illustrations

In this section we illustrate and compare the models in 2D with numerical simulations in Matlab. The models are considered in a square with zero flux boundary conditions on the densities and homogeneous Dirichlet boundary conditions on the velocities. We use a finite volume semi-implicit scheme on a staggered grid and, for the ESVM, we apply a relaxation method adapted from [39] consisting of reducing the order of the equations on the densities from fourth order to second order.

Initially, we consider that part of the NT and of the PSM are already formed. We represent part of the NT (the middle tissue) surrounded by two stripes of PSM (tissues on the left and right of the NT). This initial data is fully segregated with a rather sharp interface between the tissues as it corresponds to the anterior part of the tissues where segregation is the most apparent. More precisely, we take as initial data, ${n_1}^{ini} = 0.9\chi_{[-1/3;1/3]\times[-1;0]}$ and ${n_2}^{ini} = 0.9\chi_{([-1;-1/3]\cup[[1/3;1])\times[-1;0]}$ with χ the indicator function (as illustrated in Figure 4.3 (a)).

The PSM being endowed with a higher proliferation rate than the NT [24] and with a smaller viscosity coefficient as explained in section 4.2.1, we choose,

$$G_1(s) = 5 - s, \quad G_2(s) = 10 - s, \quad \beta_1 = 0.5, \quad \beta_2 = 0.1. \tag{4.20}$$

Finally, we pick $\epsilon = 0.1$, $m = 30$ and $\alpha = 0.001$. We refer the reader to Appendix 4.8.4 where we exhibit the role of each of the parameters m, α and ϵ on the behavior of the solution of the ESVM.

We first present a numerical illustration of the ESVM in Figure 4.4 Panels (a)–(b). In Panel (a) of Figure 4.4, we represent the tissue densities in the ESVM at time $t = 0.1$. We see that the NT and the PSM are growing and elongating along the vertical axis which represents the head-to-tail axis of the vertebrate embryo. We clearly see that geometric dynamics emerge, in the sense that the densities remain segregated and each density is either close to zero or to its maximum value (taken equal to 1 as per our pressure law (4.4)). This advocates for an incompressible regime. As a consequence of its higher proliferation rate and smaller viscosity, the PSM elongates faster than the NT. The tissues co-evolve and remain overall segregated, sharing only a thin interface (where the densities overlay).

In Figure 4.4 Panel (b), we illustrate that the ESVM produces a non-zero curl of the PSM velocity. Using the solutions (v_1, v_2) of the equations (4.7)-(4.8) in the ESVM, we compute the curl inside each tissue, and show the result for the velocity v_2 (only in the PSM) in Panel (b) where the black arrows are the velocity vectors and the heatmap represents the value of the curl. High curls are observed close to the lateral boundaries, especially in the posterior zone. This corresponds to the migration of cells from the PZ into the posterior PSM as described in Section 4.1, with clockwise vortices (negative curl) on the left wall and symmetrically counter-clockwise vortices (positive curl) on the right wall. In the posterior part, close to these lateral walls the velocity vectors clearly display swirling fluid motion. These curls are propagated inside the PSM and along the antero-

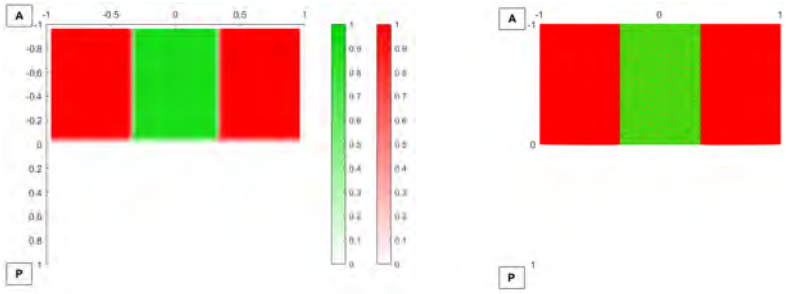

(a) Plot of the densities $n_1(t)$ of the NT (green color bar) and $n_2(t)$ of the PSM (red colorbar) at time $t = 0$ in the ESVM.

(b) Plot of the densities $n_1^\infty(t)$ of the NT in green and $n_2^\infty(t)$ of the PSM in red at time $t = 0$ in the L-ESVM. The density of each tissue is equal to 1.

Figure 4.3 – Initial conditions respectively for the ESVM and the VM (Panel (a)) and the L-ESVM (Panel (b)). The notations A and P respectively denote the anterior and the posterior parts of the embryo.

posterior axis. Anteriorly, we observe some adjacent regions of opposite curls on both sides of the interface. This is in accordance with the observations in the embryo, see Figure 4.1. Finally, in the anterior region the velocity vectors appear to cross directions, suggesting tissue contractions near the interface. Such contraction is due to the repulsion force q_m.

We now present in Figure 4.4 Panels (c)–(d) a numerical illustration of the ESVM in the case where the velocity is taken of gradient form in the Brinkman law as in (4.3). That is, we change the velocity laws used in the ESVM (4.7)-(4.8) (coupled with Dirichlet boundary conditions) and replace them with the following equations,

$$v_1 = -\nabla K_1, \quad \text{with } -\beta_1 \Delta K_1, + K_1 = p_1 \tag{4.21}$$

$$v_2 = -\nabla K_2, \quad \text{with } -\beta_2 \Delta K_2 + K_2 = p_2, \tag{4.22}$$

where K_1 and K_2 are potentials (coupled with homogeneous Neumann boundary conditions for the potentials K_i, $i = 1, 2$). All the other equations in the ESVM (equations on the densities and the expressions of the pressures) remain unchanged. Our choice of parameters also remains unchanged and is taken as in (4.20). We solve this new system and compute the curl of the velocities v_1 and v_2 using the equations (4.21)-(4.22). In Figure 4.4(d) we represent curl v_2 by the heatmap overlayed by the velocity vector v_2 (the arrows in black). In contrast with the ESVM, when the velocity is taken as a gradient, we observe an irrotational flow: the curl is null everywhere and the vector trajectories are rather straight and pointing towards the posterior. Figures 4.4(a)-(b) and (c)-(d) show two different dynamics emerging from the two laws considered for the velocity: one is irrotational (Figure 4.4(d)) and the other displays swirling motion (Figure 4.4(b)). Overall, the

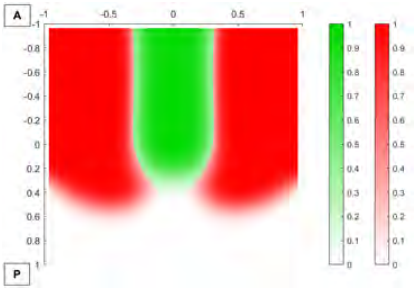

(a) PSM and NT densities in the ESVM.

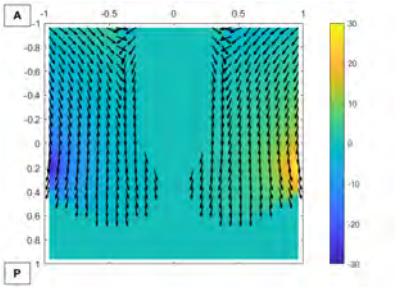

(b) PSM velocity and curl in the ESVM.

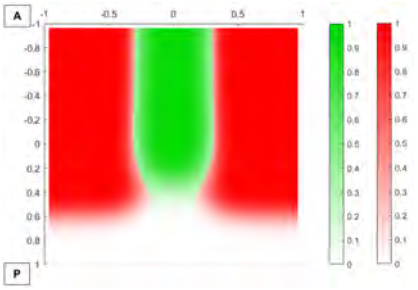

(c) PSM and NT densities in the ESVM using (4.21)-(4.22) for the velocities.

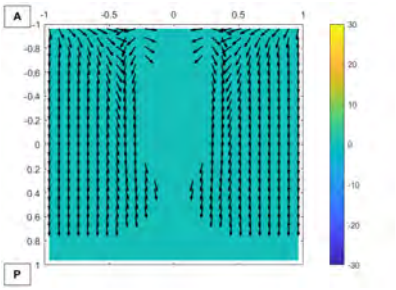

(d) PSM velocity and curl in the ESVM using (4.21)-(4.22) for the velocities.

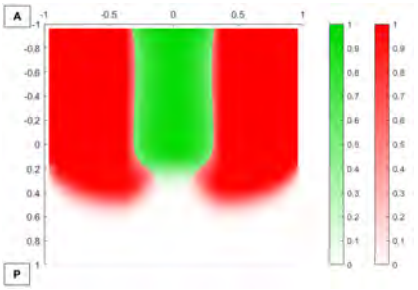

(e) PSM and NT densities in the VM.

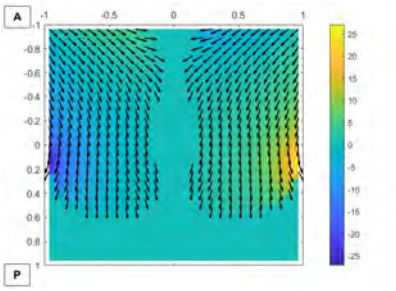

(f) PSM velocity and curl in the VM.

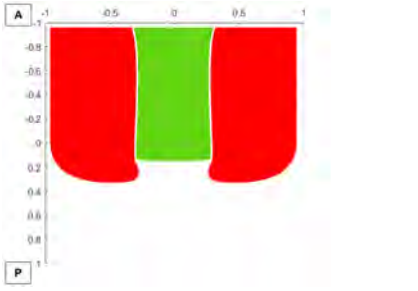

(g) PSM and NT densities in the L-ESVM in the case $q^\infty = 0$, equivalently in the L-VM.

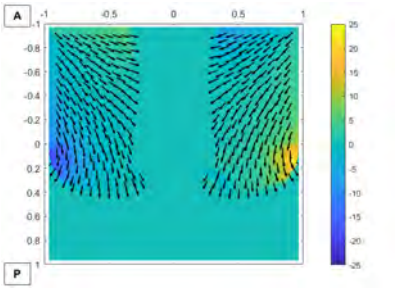

(h) PSM velocity and curl in the L-ESVM in the case $q^\infty = 0$, equivalently in the L-VM.

Figure 4.4 – Numerical simulations. The left panels illustrate the NT density n_1 (in green) and the PSM density n_2 (in red) and the right panels illustrate curl v_2 (heat map) overlayed by the vector $\frac{v_2}{\|v_2\|}$ (black arrows) at time $t = 0.1$ in respectively the ESVM (Panel (a)–(b)), the ESVM using (4.21)-(4.22) for the velocities (Panel (c)–(d)), the VM (Panel (e)–(f)) and the L-ESVM in the case $q^\infty = 0$, equivalently the L-VM (Panel (g)–(h)). The velocity vector $\frac{v_2}{\|v_2\|}$ is represented only in the regions where the density of the PSM is above a threshold equal to 0.1.

results of the ESVM describe more accurately the tissue evolution and cell movements observed in the vertebrate embryo, schematically represented in Figure 4.1(b).

We finally present a numerical illustration of the VM in Figure 4.4 Panels (e)–(f) and compare it with the ESVM. In the VM, as in the ESVM, we observe high curls in the posterior zone, especially close to the lateral boundaries. However, in contrast to the ESVM, we no longer see in the anterior region adjacent zones of opposite curls but instead we observe unidirectional latero-medial curls (counter clockwise on the left of the NT and clockwise on the right). Both models recover well the swirling motion in the posterior zone. Furthermore, each model, the ESVM and the VM, shows a specific feature observed in the anterior zone of the vertebrate embryo. The ESVM highlights the role of the repulsion pressure in creating alternating zones of opposite curls anteriorly, while the VM displays the global latero-medial curls reported in the anterior region of the PSM, as represented in Figure 4.1(b). A sensitivity analysis on the model parameters (especially those affecting the repulsion force) would allow to obtain a representation of the swirling motions as close as possible to the biological data. A future work will be dedicated to this sensitivity analysis.

The last set of simulations displayed in Figure 4.4 (Panels (g) and (h)) will be commented in Section 4.3.1 below.

4.3 Main results

4.3.1 Incompressible limit of the ESVM

Our first result is the formal incompressible limit of the two-species viscous model, where we take the parameters $\epsilon \to 0, \alpha \to 0$ and $m \to +\infty$. This allows us to derive a free boundary problem, as detailed in the following theorem.

Theorem 4.3.1. *(Formal)[Incompressible limit of the ESVM] Let n_1^{ini}, n_2^{ini} satisfy the conditions (4.14) and let n_1, n_2, v_1, v_2, p_1, p_2 solve the viscous two-species model (4.5)-(4.10) with (4.11)–(4.13). Assume that at the incompressible limit, that is, when ϵ and α go to zero and m goes to infinity, the quantities n_1, n_2, v_1, v_2, p_1, p_2, $q_m(n_1 n_2)$ converge (in a sufficiently strong sense) towards, respectively, n_1^∞, n_2^∞, v_1^∞, v_2^∞, p_1^∞, p_2^∞, q^∞. Then, these quantities satisfy the following*

system of equations for all $(t,x) \in [0;+\infty) \times \mathbb{R}^d$,

$$\partial_t n_1^\infty + \nabla \cdot (n_1^\infty v_1^\infty) = n_1^\infty G_1(p_1^\infty), \tag{4.23}$$
$$\partial_t n_2^\infty + \nabla \cdot (n_2^\infty v_2^\infty) = n_2^\infty G_2(p_2^\infty), \tag{4.24}$$
$$-\beta_1 \Delta v_1^\infty + v_1^\infty = -\nabla p_1^\infty, \tag{4.25}$$
$$-\beta_2 \Delta v_2^\infty + v_2^\infty = -\nabla p_2^\infty, \tag{4.26}$$
$$p_1^\infty = p^\infty + n_2^\infty q^\infty, \tag{4.27}$$
$$p_2^\infty = p^\infty + n_1^\infty q^\infty, \tag{4.28}$$

and the following relation holds,

$$p^\infty(1-n^\infty) = 0, \text{ where } n^\infty = n_1^\infty + n_2^\infty. \tag{4.29}$$

Moreover, we obtain full segregation of the two-species at the limit,

$$n_1^\infty n_2^\infty = 0. \tag{4.30}$$

The complementary relation prescribing the dynamics of the pressures inside the two tissues at the limit reads,

$$p^{\infty^2}\Big(\nabla \cdot (n_1^\infty v_1^\infty) + \nabla \cdot (n_2^\infty v_2^\infty)\Big) \;=\; p^{\infty^2}\Big(n_1^\infty G_1(p_1^\infty) + n_2^\infty G_2(p_2^\infty)\Big). \tag{4.31}$$

Finally, defining $K_1^\infty = n_1^\infty q^\infty$ *and* $K_2^\infty = n_2^\infty q^\infty$, *the equations prescribing the dynamics of the pressure due to repulsion at the limit read,*

$$\begin{aligned}
\partial_t K_1^\infty \;&+\; (q^\infty+1)\log(q^\infty+1)\nabla \cdot (n_1^\infty v_1^\infty) + (q^\infty+1)\log(q^\infty+1) n_1^\infty \nabla \cdot v_2^\infty \\
&+\; n_1^\infty v_2^\infty \cdot \nabla q^\infty - (q^\infty+1)\log(q^\infty+1)\nabla n_1^\infty \cdot v_2^\infty + q^\infty \nabla \cdot (n_1^\infty v_1^\infty) \\
&=\; (q^\infty+1)\log(q^\infty+1) n_1^\infty (G_1(p_1^\infty) + G_2(p_2^\infty)) + q^\infty n_1^\infty G_1(p_1^\infty),
\end{aligned} \tag{4.32}$$

$$\begin{aligned}
\partial_t K_2^\infty \;&+\; (q^\infty+1)\log(q^\infty+1)\nabla \cdot (n_2^\infty v_2^\infty) + (q^\infty+1)\log(q^\infty+1) n_2^\infty \nabla \cdot v_1^\infty \\
&+\; n_2^\infty v_1^\infty \cdot \nabla q^\infty - (q^\infty+1)\log(q^\infty+1)\nabla n_2^\infty \cdot v_1^\infty + q^\infty \nabla \cdot (n_2^\infty v_2^\infty) \\
&=\; (q^\infty+1)\log(q^\infty+1) n_2^\infty (G_1(p_1^\infty) + G_2(p_2^\infty)) + q^\infty n_2^\infty G_2(p_2^\infty).
\end{aligned} \tag{4.33}$$

We call L-ESVM the limiting system (4.23)–(4.33) *thus obtained.*

The proof of Theorem 4.3.1 is performed in Section 4.4.

This formal limit being established, we consider the situation where each tissue $i = 1, 2$ occupies exactly and fully a specific (moving) domain $\Omega_i(t)$, that is, the density $n_i^\infty(t, \cdot)$ is the indicator function of the domain $\Omega_i(t)$. Note that the congestion relation (4.29) imposes that the pressure p^∞ is null outside $\Omega_1 \cup \Omega_2$, and that the full segregation (4.30) imposes that Ω_1 and Ω_2 do not intersect.

From system (4.23)–(4.33), we can then deduce the evolution of the domains Ω_1 and Ω_2, thus giving rise to a geometrical description of the biological system. Indeed, the velocities of the exterior boundary of the first tissue's domain, the exterior boundary of the second tissue's domain and the interface of the two tissues' domains are given by $(v_1^\infty \cdot \vec{\nu})\vec{\nu}$, by $(v_2^\infty \cdot \vec{\mu})\vec{\mu}$, and by $(v_1^\infty \cdot \vec{\nu})\vec{\nu} = (v_2^\infty \cdot \vec{\mu})\vec{\mu}$, respectively, where $\vec{\nu}$ is the outward normal vector to Ω_1 and $\vec{\mu}$ is the outward normal vector to Ω_2 (on the interface between Ω_1 and Ω_2 we have $\vec{\nu} = -\vec{\mu}$). Such situation is represented in Figure 4.5.

We perform numerical simulations in Freefem++ (Figure 4.4(g)-(h)). Details on the numerical scheme can be found in Appendix 4.8.8. We illustrate the evolution of the free boundary problem in the case of the embryo, that is, a NT surrounded by two stripes of PSM. The initial conditions were taken as two indicator functions sharing a sharp interface, ${n_1}^{\infty,ini} = \chi_{[-1/3;1/3]\times[-1;0]}$ and ${n_2}^{\infty,ini} = \chi_{([-1;-1/3]\cup[[1/3;1])\times[-1;0]}$ with χ the indicator function, and we take $q^{\infty,ini} = 0$ (as illustrated in Figure 4.3(b)). Note that, as sketched in Figure 4.2, taking the initial densities segregated and the repulsion force $q^{\infty,ini} = 0$, the L-ESVM in fact coincides with the L-VM. Therefore, our numerical simulations illustrate both the L-ESVM and the L-VM. The parameters are taken as in the numerical illustrations of the ESVM, see (4.20). In Figure 4.4(g) we show the evolution of the free domains of the NT and of the PSM at $t = 0.1$. The tissues evolve while remaining completely segregated with a sharp interface throughout the simulation. The PSM, which has a higher proliferation rate and a smaller viscosity coefficient, tends to grow faster than the NT (central tissue) and occupies a wider space. Comparing Figure 4.4(g) with Figures 4.4(a) and 4.4(e) we see that the density profiles are qualitatively similar. This is in accordance with our choice of parameters α, m (in the ESVM) and ϵ (in the ESVM and VM) taken in their asymptotic ranges.

In Figure 4.4(h) we illustrate the curl of the PSM velocity computed with the L-ESVM. High curls are observed in the posterior zone close to the lateral walls, more precisely, negative curls on the left and positive curls on the right. Anteriorly, opposite curls are observed at the interface between the tissues. These profiles match very well those observed in the VM (Figure 4.4(f)) where the repulsion force q_m is absent. This is in accordance with our choice $q^\infty = 0$. Finally, we exhibit the velocity vector v_2^∞ in the L-ESVM. In the posterior zone, clear rotating vector trajectories are observed on the lateral walls where curls are high. Overall, our illustrations show that the three models VM, ESVM and L-ESVM reproduce the swirling motions observed in the embryo (Figure 4.1(b)). However, only the ESVM (in the asymptotic regime) was able to reproduce the adjacent

zones with opposite curls observed anteriorly in the embryo. This suggests that the repulsion pressure does not vanish at the incompressible limit and plays an important biophysical role at the limit as discussed in Section 4.4.4. It also suggests that some active segregation may be at play to maintain the tissues segregated. Finally our simulation of the L-ESVM displays similar dynamics as that of the ESVM (and the VM) in the asymptotic regime which demonstrates the relevance of the incompressible limit.

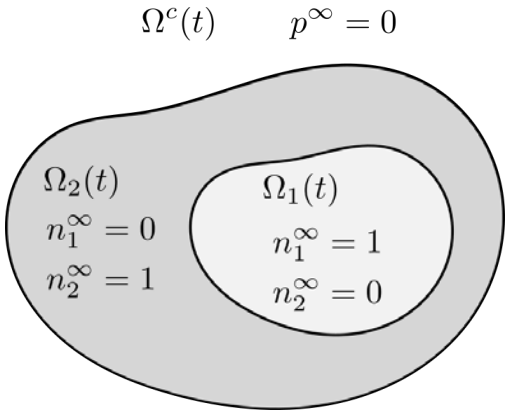

Figure 4.5 – Representation of the subdomains saturated with the two densities in the L-ESVM.

4.3.2 Study of the stationary L-ESVM (q given)

Still in the case when the densities are indicator functions (at the incompressible limit), we are now interested in the study of the stationary velocity-pressure system. For clarity we now remove the superscript "∞" from the variables n_i, v_i, q, p for $i = 1\,2$.

We work in a bounded domain $\Theta \subset \mathbb{R}^2$, and we consider two stationary subdomains Ω_1 and Ω_2. We suppose that Θ, Ω_1 and Ω_2 are as follows,

$$\Theta \text{ a smooth bounded domain in } \mathbb{R}^2, \Omega,\ \Omega_1,\ \Omega_2 \text{ subdomains of } \Theta \text{ such that} \tag{4.34}$$

$$\Omega_1 \cap \Omega_2 \text{ is empty, } \Gamma := \overline{\Omega_1} \cap \overline{\Omega_2} \text{ is non-empty,} \tag{4.35}$$

$$\Omega = \Omega_1 \cup \Omega_2 \text{ and } \overline{\Omega} \subset \Theta, \tag{4.36}$$

$$\text{and, defining } \Omega^c := \Theta \backslash \overline{\Omega},\ \text{the boundaries } \Gamma,\ \Gamma_1 := \overline{\Omega_1} \cap \overline{\Omega^c},\ \Gamma_2 = \overline{\Omega_2} \cap \overline{\Omega^c} \text{ are } \mathcal{C}^\infty. \tag{4.37}$$

Our analysis is conducted in a simplified framework, where we drop the equations (4.32) and (4.33) and consider instead that q is a given function on Ω. We assume,

$$q \in L^2(\Omega). \tag{4.38}$$

Finally, for simplicity, we suppose that the growth function is linear (and decreasing), that is,

$$G_1(s) = g_1(p_1^* - s), \quad G_2(s) = g_2(p_2^* - s), \tag{4.39}$$

for some g_1, g_2, p_1^*, $p_2^* > 0$.

In this framework, the system (4.23)–(4.31) at equilibrium and complemented with homogeneous Dirichlet boundary conditions becomes the following elliptic system on (v_1, v_2), for q given as in (4.38),

$$(S_2) \quad \begin{cases} -\beta_1 \Delta v_1 + v_1 = -\nabla[(p_1^* - \frac{1}{g_1}\nabla \cdot v_1)\chi_{\Omega_1} + (p_2^* - \frac{1}{g_2}\nabla \cdot v_2 + q)\chi_{\Omega_2}] & \text{on } \Theta, \\ -\beta_2 \Delta v_2 + v_2 = -\nabla[(p_2^* - \frac{1}{g_2}\nabla \cdot v_2)\chi_{\Omega_2} + (p_1^* - \frac{1}{g_1}\nabla \cdot v_1 + q)\chi_{\Omega_1}] & \text{on } \Theta, \\ v_1 = v_2 = 0 & \text{on } \partial\Theta, \end{cases}$$

For the existence theory and the elliptic regularity, we assume that the model parameters satisfy the following condition,

$$\beta_1 g_2 > \frac{1}{4}, \qquad \text{and} \qquad \beta_2 g_1 > \frac{1}{4}. \tag{4.40}$$

Notation 4.3.2. *Let $U \subset \mathbb{R}^2$ be a bounded domain. For $k \geq 0$, we use the notation $\mathcal{C}^k(\overline{U})$, or equivalently write " $\mathcal{C}^k$ up to the boundary of U ", in the classical sense, see [64]:*

$$\mathcal{C}^k(\overline{U}) = \{u \in \mathcal{C}^k(U) | D^\alpha u \text{ is uniformly continuous on } U \text{ for all } |\alpha| \leq k\}.$$

Thus if $u \in \mathcal{C}^k(\overline{U})$, then $D^\alpha u$ can be continuously extended to $\overline{U}$ for each multi-index α, with $|\alpha| \leq k$.

For $\mu \in (0,1)$, we use the notation $\mathcal{C}^{0,\mu}(\overline{U})$ for (uniformly) Hölder continuous functions on U with exponent μ. Thus, such functions can be extended into a (uniformly) Hölder continuous functions on $\overline{U}$ with the same exponent μ.

Finally, for $k \geq 0$ and $\mu \in (0,1)$, we write,

$$\mathcal{C}^{k,\mu}(\overline{U}) = \{u \in \mathcal{C}^k(U) | D^\alpha u \in \mathcal{C}^{0,\mu}(\overline{U}) \text{ for all } |\alpha| \leq k\}.$$

Theorem 4.3.3. *[Well-posedness and regularity, stationary L-ESVM] Let Θ, Ω_1 and Ω_2 be bounded domains as in (4.34)–(4.37), and let $\beta_1, \beta_2, g_1, g_2 > 0$ satisfy the condition (4.40). Let q as in (4.38). Then, there exists a unique solution $(v_1, v_2) \in H_0^1(\Theta)^2 \times H_0^1(\Theta)^2$ to system (S_2). Note in particular that (v_1, v_2) is continuous across the interfaces $\Gamma_1, \Gamma_2, \Gamma$.*

Furthermore, if $q \in \mathcal{C}^{0,\mu}(\overline{\Omega_1}) \cap \mathcal{C}^{0,\mu}(\overline{\Omega_2})$ for some $\mu \in (0,1)$, then the solution (v_1, v_2) to system (S_2) lies in $\mathcal{C}^{1,\alpha'}(\overline{\Omega_1}) \cap \mathcal{C}^{1,\alpha'}(\overline{\Omega_2}) \cap \mathcal{C}^{1,\alpha'}(\overline{\Omega^c})$, with $0 < \alpha' \leq \min(\mu, \frac{1}{4})$.

The proof of Theorem 4.3.3 is performed in Section 4.5.

Remark 4.3.4. *Note that q is defined only in Ω, so that we do not need any information on q in regions where both densities are simultaneously equal to zero.*

Remark 4.3.5. *The result can be extended to the case of (smooth) non-homogeneous Dirichlet boundary conditions.*

Remark 4.3.6. *Since $q = 0$ is always a particular solution of (the stationary versions of) Eq. (4.32) and (4.33) independently of (v_1, v_2), system (S_2) with $q = 0$ gives a solution to the original system L-ESVM taken at equilibrium. Note that the case where $q = 0$ on Ω is included in the well-posedness and regularity results.*

We can now rewrite system (S_2) as a transmission problem, giving rise to non-trivial transmission conditions at the interfaces Γ, Γ_1 and Γ_2. To this end we introduce the following notation: for D a domain of $\mathbb{R}^2$ and h a continuous function on D that can be continuously extended on $\overline{D}$, then, for $x \in \partial D$, we note

$$(h)_D(x) \coloneqq \lim_{\substack{y \in D, \\ y \to x}} h(y). \tag{4.41}$$

Proposition 4.3.7 (Transmission problem, stationary L-ESVM)**.** *Assume (4.34)-(4.37), (4.40), and $q \in \mathcal{C}^{0,\mu}(\overline{\Omega_1}) \cap \mathcal{C}^{0,\mu}(\overline{\Omega_2})$ for some $\mu \in (0,1)$. Then the solution of system (S_2) solves the following transmission problem (T_2) considered on Θ and coupled with homogeneous Dirichlet boundary conditions on $\partial\Theta$,*

$$(T_{2,\Omega_1}) \begin{cases} -\beta_1 \Delta v_1 + v_1 - \frac{1}{g_1} \nabla \nabla \cdot v_1 = 0 & \text{in } \Omega_1, \\ -\beta_2 \Delta v_2 + v_2 - \frac{1}{g_1} \nabla \nabla \cdot v_1 = -\nabla q & \text{in } \Omega_1. \end{cases}$$

$$(T_{2,\Omega_2}) \begin{cases} -\beta_1 \Delta v_1 + v_1 - \frac{1}{g_2} \nabla \nabla \cdot v_2 = -\nabla q & \text{in } \Omega_2, \\ -\beta_2 \Delta v_2 + v_2 - \frac{1}{g_2} \nabla \nabla \cdot v_2 = 0 & \text{in } \Omega_2. \end{cases}$$

$$(T_{2,\Omega^c}) \begin{cases} -\beta_1 \Delta v_1 + v_1 = 0 & \text{in } \Omega^c, \\ -\beta_2 \Delta v_2 + v_2 = 0 & \text{in } \Omega^c. \end{cases}$$

$$(T_{2,\Gamma_1}) \begin{cases} \beta_1 [(\nabla v_1)_{\Omega_1} - (\nabla v_1)_{\Omega^c}] \cdot \vec{\nu} = [p_1^* - \frac{1}{g_1} (\nabla \cdot v_1)_{\Omega_1}] \vec{\nu} & \text{on } \Gamma_1, \\ \beta_2 [(\nabla v_2)_{\Omega_1} - (\nabla v_2)_{\Omega^c}] \cdot \vec{\nu} = [p_1^* + (q)_{\Omega_1} - \frac{1}{g_1} (\nabla \cdot v_1)_{\Omega_1}] \vec{\nu} & \text{on } \Gamma_1, \\ (v_1)_{\Omega_1} = (v_1)_{\Omega^c}, \quad (v_2)_{\Omega_1} = (v_2)_{\Omega^c} & \text{on } \Gamma_1. \end{cases}$$

$$(T_{2,\Gamma_2}) \begin{cases} \beta_1 [(\nabla v_1)_{\Omega_2} - (\nabla v_1)_{\Omega^c}] \cdot \vec{\mu} = [p_2^* + (q)_{\Omega_2} - \frac{1}{g_2} (\nabla \cdot v_2)_{\Omega_2}] \vec{\mu} & \text{on } \Gamma_2, \\ \beta_2 [(\nabla v_2)_{\Omega_2} - (\nabla v_2)_{\Omega^c}] \cdot \vec{\mu} = [p_2^* - \frac{1}{g_2} (\nabla \cdot v_2)_{\Omega_2}] \vec{\mu} & \text{on } \Gamma_2, \\ (v_1)_{\Omega_2} = (v_1)_{\Omega^c}, \quad (v_2)_{\Omega_2} = (v_2)_{\Omega^c} & \text{on } \Gamma_2. \end{cases}$$

$$(T_{2,\Gamma})\begin{cases} \beta_1[(\nabla v_1)_{\Omega_1} - (\nabla v_1)_{\Omega_2}]\cdot\vec{\nu} = [(p_1^* - p_2^*) - (q)_{\Omega_2} + \frac{1}{g_2}(\nabla\cdot v_2)_{\Omega_2} - \frac{1}{g_1}(\nabla\cdot v_1)_{\Omega_1}]\vec{\nu} & \text{on } \Gamma, \\ \beta_2[(\nabla v_2)_{\Omega_1} - (\nabla v_2)_{\Omega_2}]\cdot\vec{\nu} = [(p_1^* - p_2^*) + (q)_{\Omega_1} + \frac{1}{g_2}(\nabla\cdot v_2)_{\Omega_2} - \frac{1}{g_1}(\nabla\cdot v_1)_{\Omega_1}]\vec{\nu} & \text{on } \Gamma, \\ (v_1)_{\Omega_1} = (v_1)_{\Omega_2}, \quad (v_2)_{\Omega_1} = (v_2)_{\Omega_2}, \quad v_1\cdot\vec{\nu} = v_2\cdot\vec{\nu} & \text{on } \Gamma. \end{cases}$$

The proof of Proposition 4.3.7 is performed in Section 4.5.2.

To obtain more regularity on the solution, we assume the following additional condition on the domains:

$$\partial\Omega \text{ is smooth } (\mathcal{C}^\infty). \tag{4.42}$$

A typical situation where the domains satisfy the assumption above is the situation where one tissue is encompassed within the other one, such as represented in Figure 4.5. We obtain the following result.

Theorem 4.3.8. *[Further regularity, two concentric species] Let Θ, Ω_1 and Ω_2 be bounded domains as in (4.34)–(4.37), which satisfy furthermore (4.42). Let $\beta_1, \beta_2, g_1, g_2 > 0$ satisfy the condition (4.40). Let $q \in \mathcal{C}^\infty(\overline{\Omega_1}) \cap \mathcal{C}^\infty(\overline{\Omega_2})$, then the solution (v_1, v_2) to system (S_2) lies in $\mathcal{C}^\infty(\overline{\Omega_1}) \cap \mathcal{C}^\infty(\overline{\Omega_2}) \cap \mathcal{C}^\infty(\overline{\Omega^c})$.*

The proof of Therorem 4.3.8 is performed in Section 4.5.3.

4.3.3 Segregation in the VM and its incompressible limit (the L-VM)

We recall that in the VM, defined in (4.15)–(4.19), there is no enforced segregation, contrarily to the ESVM. However, the VM seems to preserve segregation, that is, initially segregated densities remain segregated at all times. We prove it formally in the special case where $\beta_1 = \beta_2$ and exhibit arguments in favor of the segregation property for the case $\beta_1 \neq \beta_2$.

Proposition 4.3.9. *(Formal) [Segregation property, VM] Let n_1, n_2 solve (4.15)–(4.19). Suppose that $\beta_1 = \beta_2$, and that the growth functions G_1, G_2 are upper bounded such that,*

$$\exists G_m > 0, G_1 \leq G_m,\ G_2 \leq G_m. \tag{4.43}$$

If the initial densities are fully segregated, that is, $n_1^{ini} n_2^{ini} = 0$ on $\mathbb{R}^d$, then the densities remain segregated for all times:

$$n_1 n_2(t,x) = 0,\ \forall (t,x) \in [0;+\infty)\times\mathbb{R}^d. \tag{4.44}$$

The proof of Proposition 4.3.9 is performed in Section 4.6.1.

Remark 4.3.10. *In the case when $\beta_1 \neq \beta_2$, we conjecture that the same segregation property holds. Indeed, we observe it numerically as exhibited in the numerical simulations performed in dimension*

1 in Appendix 4.8.7. To prove it, the main argument would be to prove that the normal velocities $v_1 \cdot \vec{\nu}$ and $v_2 \cdot \vec{\nu}$ are equal on the interface. We note here that in [17], the case of two tissues obeying Darcy's law and responding differently to compression was studied (with different parameters for Darcy's law). It was shown, both numerically and theoretically, that the segregation property holds for such case. Interestingly, this segregation property is related to the pressure gradient jump. Going back to our case with Brinkman law and with different viscosity coefficients, our numerical illustrations also suggest, similarly to [17], that the gradient of the pressure has jumps at the interface, see Appendix 4.8.7.

The incompressible limit of the VM is formally obtained by taking $\epsilon \to 0$. Then we obtain the following system L-VM, for all $(t, x) \in [0; +\infty) \times \mathbb{R}^d$:

$$\partial_t n_1^\infty + \nabla \cdot (n_1^\infty v_1^\infty) = n_1^\infty G_1(p^\infty), \tag{4.45}$$

$$\partial_t n_2^\infty + \nabla \cdot (n_2^\infty v_2^\infty) = n_2^\infty G_2(p^\infty), \tag{4.46}$$

$$-\beta_1 \Delta v_1^\infty + v_1^\infty = -\nabla p^\infty, \tag{4.47}$$

$$-\beta_2 \Delta v_2^\infty + v_2^\infty = -\nabla p^\infty, \tag{4.48}$$

and the following relation holds,

$$p^\infty (1 - n^\infty) = 0, \text{ where } n^\infty = n_1^\infty + n_2^\infty. \tag{4.49}$$

The complementary relation prescribing the dynamics of the pressure due to congestion at the limit reads,

$$p^{\infty^2} \Big(\nabla \cdot (n_1^\infty v_1^\infty) + \nabla \cdot (n_2^\infty v_2^\infty) \Big) \quad = \quad p^{\infty^2} \Big(n_1^\infty G_1(p^\infty) + n_2^\infty G_2(p^\infty) \Big). \tag{4.50}$$

Remark 4.3.11. *Using the same method as for the VM, we can show the segregation property holds for the L-VM when $\beta_1 = \beta_2$. Following the same reasoning as in Remark 4.3.10, we have some evidence that the segregation property in the L-VM holds for all β_1, β_2, that is, when initially segregated, the tissues remain segregated for all times:*

$$n_1^\infty n_2^\infty = 0, \ \forall (t, x) \in [0; +\infty) \times \mathbb{R}^d. \tag{4.51}$$

The main difference between the ESVM and the VM lies in the dynamics of the segregation. In fact, even for initially mixed densities, the ESVM system will lead at the limit to the relation $n_1^\infty n_2^\infty = 0$. This is not the case for the VM, which does not enforce segregation at the limit. However, taking initially segregated densities for the ESVM and for the VM, we get that $q^m(n_1^{ini} n_2^{ini}) = 0$ for the ESVM, and taking also $\alpha = 0$ we find that both systems coincide. As a

consequence their limits will also coincide in this case. The equivalence of the systems L-ESVM and L-VM when the initial densities $n_1^{\infty,ini}, n_2^{\infty,ini}$ are segregated can be obtained directly, taking furthermore $q^{\infty,ini} = q^{\infty}(t=0,\cdot) = 0$ in the L-ESVM (Figure 4.2). The transmission problem for the stationary L-VM is obtained by taking $q = 0$ in (T_2). Well-posedness and regularity for the stationary L-VM are then straightforward from Theorems 4.3.3 and 4.3.8, when the assumptions (4.34)-(4.37), and (4.40)-(4.42) are still assumed.

4.3.4 On the pressure jump in the stationary L-VM

Finally, we show a striking feature: a pressure jump at the boundaries and interfaces in the stationary L-VM (or equivalently, the stationary L-ESVM when $q = 0$). In the following we consider linear growth functions as in (4.39) with $g_1, g_2, p_1^*, p_2^* > 0$. Then using (4.49) and (4.50) we can express the pressure on Ω_1, Ω_2 and Ω^c as a function of the velocities v_1 and v_2 as:

$$p = \begin{cases} p_1^* - \frac{1}{g_1}(\nabla \cdot v_1)_{\Omega_1} & \text{on } \Omega_1, \\ p_2^* - \frac{1}{g_2}(\nabla \cdot v_2)_{\Omega_2} & \text{on } \Omega_2, \\ 0 & \text{on } \Omega^c. \end{cases} \tag{4.52}$$

Proposition 4.3.12 (Pressure jump, stationary L-VM)**.** *Suppose (4.34)-(4.37), (4.40) and* (4.42)*. Let $q = 0$ and let $(v_1, v_2) \in H_0^1(\Theta)^2 \times H_0^1(\Theta)^2$ be the solution of (S_2) given by Theorem 4.3.3. Then, the pressure p of the L-VM given by* (4.52) *is discontinuous across the interfaces $\Gamma_1 \cup \Gamma_2 \cup \Gamma$.*

Proposition 4.3.12 is proven in Section 4.6.2.

Remark 4.3.13. *For the case of the L-ESVM, it is clear from (T_{2,Γ_1}), (T_{2,Γ_2}), and $(T_{2,\Gamma})$ that for the pressure to be continuous on the interfaces, it is required for q to be identically zero on all interfaces $\Gamma_1 \cup \Gamma_2 \cup \Gamma$. The pressure jump of the L-ESVM is then obvious for any non-vanishing q at any point of the interfaces Γ, Γ_1 and Γ_2. Further work is needed in the general case.*

4.4 Incompressible limit of the two species viscous model

4.4.1 Computation of the incompressible limit

In this section we perform the proof of the formal limit of the ESVM defined by the system (4.5)-(4.12).

Proof of Theorem 4.3.1. The incompressible limit of the system defined by the equations (4.5)-(4.12), is obtained by taking $\epsilon \to 0$, then $m \to \infty$ and $\alpha \to 0$.

First, the equation (4.12) can be written as, $(1-n)p_\epsilon = \epsilon n$. Taking the limit as $\epsilon \to 0$ we get,

$$p^\infty(1-n^\infty) = 0. \tag{4.53}$$

Then, straightforward computations show that the expression of q_m in Eq. (4.11) gives,

$$\left(\frac{m-1}{m}q_m + 1\right)^{\frac{m}{m-1}} = (1+r)^m = \left(\frac{m-1}{m}q_m + 1\right)(1+r).$$

Passing to the limit when $m \to +\infty$, and using that we assume $q_m \xrightarrow{m\to\infty} q^\infty$, we obtain full segregation of the species at the limit,

$$r^\infty = n_1^\infty n_2^\infty = 0. \tag{4.54}$$

Now, taking the limit in (4.5)–(4.10), when $\epsilon \to 0, m \to +\infty$ and $\alpha \to 0$, under the assumption that all quantities converge, we get the system (4.23)-(4.28) for all $(t,x) \in [0;+\infty) \times \mathbb{R}^d$.

It now remains to obtain an equation to characterize the evolution of p^∞ and q^∞.

Equation for the congestion pressure. We obtain the equation satisfied by the total density $n = n_1 + n_2$ by summing (4.5) and (4.6):

$$\partial_t n + \nabla\cdot(n_1 v_1 + n_2 v_2) + \alpha\nabla\cdot(n_1\nabla(\Delta n_1) + n_2\nabla(\Delta n_2)) = n_1 G_1(p_1) + n_2 G_2(p_2). \tag{4.55}$$

To recover the equation that controls the pressure inside the domain $\Omega(t)$, we multiply (4.55) by $p_\epsilon'(n) = \frac{1}{\epsilon}(p_\epsilon+\epsilon)^2$, and obtain the following equation satisfied by p_ϵ:

$$\begin{aligned}\epsilon\partial_t p_\epsilon + (p_\epsilon+\epsilon)^2\nabla\cdot(n_1v_1+n_2v_2) &= -(p_\epsilon+\epsilon)^2\alpha\nabla\cdot(n_1\nabla(\Delta n_1)+n_2\nabla(\Delta n_2)) \\ &\quad +(p_\epsilon+\epsilon)^2(n_1G_1(p_1)+n_2G_2(p_2)),\end{aligned}$$

We pass to the limit $\epsilon \to 0$ in the latter equation, then $m \to \infty$, and $\alpha \to 0$, we get at the limit Eq. (4.31).

Equation for the repulsion pressure. Let $K_1 = n_1 q_m$, then the equation on $n_1\partial_t q_m$ is as follows:

$$\begin{aligned}n_1\partial_t q_m &+ r(q_m)'\nabla\cdot(n_1v_1) + n_1^2(q_m)'\nabla\cdot(n_2v_2) \\ &= n_1 r(q_m)'(G_1(p_1)+G_2(p_2)) - \alpha r(q_m)'\nabla\cdot(n_1\nabla(\Delta n_1)) - \alpha n_1^2(q_m)'\nabla\cdot(n_2\nabla(\Delta n_2)).\end{aligned}$$

Recalling that $q_m(r) = \frac{m}{m-1}[(1+r)^{m-1} - 1]$, we compute $q'(r) = m(1+r)^{m-2}$, and we use the following expressions,

$$(1+r)^{m-1} = \frac{m-1}{m} q_m + 1 \quad \text{and} \quad \log(\frac{m-1}{m} q_m + 1) = (m-1)\log(1+r).$$

Then we can write ,

$$r(q_m)' = \frac{r}{\log(1+r)} \frac{m}{m-1} (\frac{m-1}{m} q_m + 1)^{\frac{m-2}{m-1}} \log(\frac{m-1}{m} q_m + 1).$$

Replacing the expression of $r(q_m)'$ in the above equation we obtain:

$$\begin{aligned}
n_1 \partial_t q_m &+ \frac{r}{\log(1+r)} \frac{m}{m-1} (\frac{m-1}{m} q_m + 1)^{\frac{m-2}{m-1}} \log(\frac{m-1}{m} q_m + 1) \nabla \cdot (n_1 v_1) \\
&+ \frac{r}{\log(1+r)} \frac{m}{m-1} (\frac{m-1}{m} q_m + 1)^{\frac{m-2}{m-1}} \log(\frac{m-1}{m} q_m + 1) n_1 \nabla \cdot v_2 \\
&+ n_1^2 v_2 \cdot \nabla n_2 (q_m)' \\
&= \frac{r}{\log(1+r)} \frac{m}{m-1} (\frac{m-1}{m} q_m + 1)^{\frac{m-2}{m-1}} \log(\frac{m-1}{m} q_m + 1) n_1 (G_1 + G_2) \\
&\quad - \alpha \frac{r}{\log(1+r)} \frac{m}{m-1} (\frac{m-1}{m} q_m + 1)^{\frac{m-2}{m-1}} \log(\frac{m-1}{m} q_m + 1) \nabla \cdot (n_1 \nabla (\Delta n_1)) \\
&\quad - \alpha n_1^2 (q_m)' \nabla \cdot (n_2 \nabla (\Delta n_2)).
\end{aligned}$$

The equation on K_1 becomes:

$$\begin{aligned}
\partial_t K_1 &+ \frac{r}{\log(1+r)} \frac{m}{m-1} (\frac{m-1}{m} q_m + 1)^{\frac{m-2}{m-1}} \log(\frac{m-1}{m} q_m + 1) \nabla \cdot (n_1 v_1) \\
&+ \frac{r}{\log(1+r)} \frac{m}{m-1} (\frac{m-1}{m} q_m + 1)^{\frac{m-2}{m-1}} \log(\frac{m-1}{m} q_m + 1) n_1 \nabla \cdot v_2 \\
&+ n_1^2 \nabla n_2 \cdot v_2 (q_m)' + q_m \nabla \cdot (n_1 v_1) + q_m \alpha \nabla \cdot (n_1 \nabla (\Delta n_1)) \\
&= \frac{r}{\log(1+r)} \frac{m}{m-1} (\frac{m-1}{m} q_m + 1)^{\frac{m-2}{m-1}} \log(\frac{m-1}{m} q_m + 1) n_1 (G_1 + G_2) \\
&\quad - \alpha \frac{r}{\log(1+r)} \frac{m}{m-1} (\frac{m-1}{m} q_m + 1)^{\frac{m-2}{m-1}} \log(\frac{m-1}{m} q_m + 1) \nabla \cdot (n_1 \nabla (\Delta n_1)) \\
&\quad - \alpha n_1^2 (q_m)' \nabla \cdot (n_2 \nabla (\Delta n_2)) + q_m n_1 G_1.
\end{aligned}$$

Moreover we have the following equalities,

$$\begin{aligned}
n_1^2 \nabla n_2 \cdot v_2 (q_m)' &= n_1 v_2 \cdot \nabla q_m - r(q_m)' \nabla n_1 \cdot v_2, \\
\alpha n_1^2 (q_m)' \nabla \cdot (n_2 \nabla (\Delta n_2)) &= \alpha [n_1 \nabla q_m - r(q_m)' \nabla n_1] \cdot \nabla \Delta n_2 + \alpha n_1 r(q_m)' \Delta^2 n_2.
\end{aligned}$$

Then the equation on K_1 becomes :

$$\begin{aligned}
\partial_t K_1 \quad + \quad & \frac{r}{\log(1+r)}\frac{m}{m-1}\left(\frac{m-1}{m}q_m+1\right)^{\frac{m-2}{m-1}}\log\left(\frac{m-1}{m}q_m+1\right)\nabla\cdot(n_1v_1)\\
+ \quad & \frac{r}{\log(1+r)}\frac{m}{m-1}\left(\frac{m-1}{m}q_m+1\right)^{\frac{m-2}{m-1}}\log\left(\frac{m-1}{m}q_m+1\right)n_1\nabla\cdot v_2\\
+ \quad & n_1v_2\cdot\nabla q_m-\frac{r}{\log(1+r)}\frac{m}{m-1}\left(\frac{m-1}{m}q_m+1\right)^{\frac{m-2}{m-1}}\log\left(\frac{m-1}{m}q_m+1\right)\nabla n_1\cdot v_2\\
& +q_m\nabla\cdot(n_1v_1)+q_m\alpha\nabla\cdot(n_1\nabla(\Delta n_1))\\
= \quad & \frac{r}{\log(1+r)}\frac{m}{m-1}\left(\frac{m-1}{m}q_m+1\right)^{\frac{m-2}{m-1}}\log\left(\frac{m-1}{m}q_m+1\right)n_1(G_1+G_2)\\
& -\alpha\frac{r}{\log(1+r)}\frac{m}{m-1}\left(\frac{m-1}{m}q_m+1\right)^{\frac{m-2}{m-1}}\log\left(\frac{m-1}{m}q_m+1\right)\nabla\cdot(n_1\nabla(\Delta n_1))\\
& -\alpha n_1\nabla q_m\cdot\nabla\Delta n_2+\alpha\frac{r}{\log(1+r)}\frac{m}{m-1}\left(\frac{m-1}{m}q_m+1\right)^{\frac{m-2}{m-1}}\log\left(\frac{m-1}{m}q_m+1\right)\nabla n_1\cdot\nabla\Delta n_2\\
& -\alpha n_1\frac{r}{\log(1+r)}\frac{m}{m-1}\left(\frac{m-1}{m}q_m+1\right)^{\frac{m-2}{m-1}}\log\left(\frac{m-1}{m}q_m+1\right)\Delta^2 n_2+q_mn_1G_1.
\end{aligned}$$

Finally, assuming that the limit to all the quantities exists, and remembering (4.54), we formally pass to the limit in the above equation when m goes to infinity and α,ϵ go to zero and obtain on Θ,

$$\begin{aligned}
\partial_t K_1^\infty \quad + \quad & (q^\infty+1)\log(q^\infty+1)\nabla\cdot(n_1^\infty v_1^\infty)+(q^\infty+1)\log(q^\infty+1)n_1^\infty\nabla\cdot v_2^\infty\\
+ \quad & n_1^\infty v_2^\infty\cdot\nabla q^\infty-(q^\infty+1)\log(q^\infty+1)\nabla n_1^\infty\cdot v_2^\infty+q^\infty\nabla\cdot(n_1^\infty v_1^\infty)\\
= \quad & (q^\infty+1)\log(q^\infty+1)n_1^\infty(G_1(p_1^\infty)+G_2(p_2^\infty))+q^\infty n_1^\infty G_1(p_1^\infty).
\end{aligned}$$

An analogous computation holds for K_2^∞ on Θ, leading to Eq. (4.33). This ends the proof of the theorem. ■

4.4.2 Free boundary problem

We now explain how this system generates a free boundary problem. Motivated by the relation (4.53), we define the domain,

$$\Omega(t) \coloneqq \{x|\ p^\infty(\cdot,t)>0\}, \tag{4.56}$$

and we note that,

$$\Omega(t)=\{x|\ p^\infty(\cdot,t)>0\}\subset\{x|\ n^\infty(\cdot,t)=1\},\ a.e. \tag{4.57}$$

Using Eq. (4.54) and the inclusion (4.57), we can decompose $\Omega(t)$ into two subdomains $\Omega_1(t)$ and $\Omega_2(t)$ such that,

$$\Omega_1(t) = \{x|\ n_1^\infty = 1\} \cap \Omega(t) \ \text{ and } \ \Omega_2(t) = \{x|\ n_2^\infty = 1\} \cap \Omega(t),$$

with,

$$\Omega_1(t) \cap \Omega_2(t) = \varnothing \text{ and } \Omega_1(t) \cup \Omega_2(t) = \Omega(t).$$

In fact, in (4.57), the two domains coincide almost everywhere, for almost all times. Indeed, let us assume that on some time-space domain $U \in \mathbb{R}^{d+1}$, we have simultaneously $p^\infty = 0$ and $n^\infty = 1$ (with for example $n_1^\infty = 1$ and $n_2^\infty = 0$). Then by equation (4.23) we have $0 = \partial_t n_1^\infty = n_1^\infty(G_1(0) - \nabla \cdot v_1^\infty)$ in U, so that $\nabla \cdot v_1^\infty = G_1(0) = g_1 p_1^* > 0$ in U. On the other hand, applying the divergence operator to (4.25), one gets $\nabla \cdot v_1^\infty = 0$, which is absurd. Therefore, U is of measure zero, and finally we have for a.e $t \geq 0$,

$$\Omega(t) = \{x|\ p^\infty(\cdot, t) > 0\} = \{x|\ n^\infty(\cdot, t) = 1\}, \text{ a.e.}$$

Furthermore, the complementary relations (4.31), (4.32) and (4.33) can be rewritten on each subdomain. First, Eq. (4.31) does not give additional information outside $\Omega(t)$, but on $\Omega(t)$ it can be rewritten as,

$$\nabla \cdot v_1^\infty = G_1(p_1^\infty) \quad \text{on } \Omega_1(t), \qquad \text{and} \qquad \nabla \cdot v_2^\infty = G_2(p_2^\infty) \quad \text{on } \Omega_2(t).$$

Then, from (4.32), the equation of q^∞ on $\Omega_1(t)$ becomes,

$$\partial_t q^\infty + (q^\infty + 1)\nabla \cdot (\log(q^\infty + 1) v_2^\infty) = (q^\infty + 1)\log(q^\infty + 1) G_2(p_2^\infty). \tag{4.58}$$

Similarly in $\Omega_2(t)$ we obtain from (4.33),

$$\partial_t q^\infty + (q^\infty + 1)\nabla \cdot (\log(q^\infty + 1) v_1^\infty) = (q^\infty + 1)\log(q^\infty + 1) G_1(p_1^\infty). \tag{4.59}$$

Finally, we compute K_1^∞ and K_2^∞ in $\Theta \backslash \Omega(t)$ where $0 \leq n_1^\infty < 1$ and $0 \leq n_2^\infty < 1$. Taking $p_1^\infty = 0$ in (4.32) in areas where $n_2^\infty = 0$ and $0 < n_1^\infty < 1$ we derive the following equation,

$$\begin{aligned} \partial_t K_1^\infty \ &+ \ (q^\infty + 1)\log(q^\infty + 1)\nabla \cdot (n_1^\infty v_1^\infty) + (q^\infty + 1)\log(q^\infty + 1) n_1^\infty \nabla \cdot v_2^\infty \\ &+ \ n_1^\infty v_2^\infty \cdot \nabla q^\infty - (q^\infty + 1)\log(q^\infty + 1)\nabla n_1^\infty \cdot v_2^\infty + q^\infty \nabla \cdot (n_1^\infty v_1^\infty) \\ &= \ (q^\infty + 1)\log(q^\infty + 1) n_1^\infty (G_1(0) + G_2(p_2^\infty)) + q^\infty n_1^\infty G_1(0), \end{aligned}$$

And to compute K_2^∞ in areas where $n_1^\infty = 0$ and $0 < n_2^\infty < 1$, we take $p_2^\infty = 0$ in (4.33) and derive

the following equation:

$$\begin{aligned}\partial_t K_2^\infty &+ (q^\infty+1)\log(q^\infty+1)\nabla\cdot(n_2^\infty v_2^\infty) + (q^\infty+1)\log(q^\infty+1)n_2^\infty\nabla\cdot v_1^\infty \\ &+ n_2^\infty v_1^\infty\cdot\nabla q^\infty - (q^\infty+1)\log(q^\infty+1)\nabla n_2^\infty\cdot v_1^\infty + q^\infty\nabla\cdot(n_2^\infty v_2^\infty) \\ &= (q^\infty+1)\log(q^\infty+1)n_2^\infty(G_1(p_1^\infty)+G_2(0)) + q^\infty n_2^\infty G_2(0).\end{aligned}$$

Finally, note that the equations (4.32) and (4.33) are very related to the choice of the repulsion pressure q_m. In particular, the presence of the terms $\log(q^\infty+1)$ comes from the power law in Eq. (4.11).

4.4.3 Velocities of the interfaces

Finally, we complete here the derivation of the free boundary problem entailed by the incompressible limit by computing the velocities of the interfaces. To this end, we consider the case where each tissue i occupies fully its domain Ω_i, that is, we assume that $n_1^\infty = \chi_{\Omega_1}(t)$ and $n_2^\infty = \chi_{\Omega_2}(t)$. One can verify that in this case (n_1^∞, n_2^∞) solve the equations (4.23) and (4.24) on each subdomain $\Omega_i(t)$, $i = 1$, 2 and $\Omega^c(t)$.

We then compute the velocity of $\partial\Omega(t) = (\partial\Omega_1(t)\cap\partial\Omega(t))\cup(\partial\Omega_2(t)\cap\partial\Omega(t))$ and of the interface between the two tissues $\Gamma(t) = \partial\Omega_1(t)\cap\partial\Omega_2(t)$.

We test (4.23) with some $\phi\in\mathcal{C}_c^\infty(\mathbb{R}^d)$,

$$\partial_t\int_{\mathbb{R}^d} n_1^\infty\phi\,dx = \int_{\mathbb{R}^d}\partial_t n_1^\infty\phi\,dx = \int_{\mathbb{R}^d} n_1^\infty v_1^\infty\cdot\nabla\phi\,dx + \int_{\mathbb{R}^d} n_1^\infty G_1(p_1^\infty)\phi\,dx.$$

Hence using Green's formula, and that $n_1^\infty = 0$ on $\Omega_1^c(t)$, we can write,

$$\partial_t\int_{\Omega_1(t)}\phi\,dx = -\int_{\Omega_1(t)}\nabla\cdot v_1^\infty\phi\,dx + \int_{\partial\Omega_1(t)} v_1^\infty\cdot\vec{\nu}\phi\,d\sigma(x) + \int_{\Omega_1(t)} G_1(p_1^\infty)\phi\,dx,$$

with $\vec{\nu}$ the outward normal vector to $\Omega_1(t)$ and $d\sigma$ the surface measure on the boundaries. Using the complementary relation (4.31) on the subdomain $\Omega_1(t)$ we obtain,

$$\partial_t\int_{\Omega_1(t)}\phi\,dx = \int_{\partial\Omega_1(t)\cap\partial\Omega(t)} v_1^\infty\cdot\vec{\nu}\phi\,d\sigma(x) + \int_{\Gamma(t)} v_1^\infty\cdot\vec{\nu}\phi\,d\sigma(x), \tag{4.60}$$

We recall that $\Gamma(t) = \partial\Omega_1(t)\cap\partial\Omega_2(t)$ is the interface between the two densities, and $\partial\Omega_1(t)\cap\partial\Omega(t)$ is the exterior boundary of $\Omega_1(t)$.

We now introduce $V_{\partial\Omega_1(t)\cap\partial\Omega(t)}$ the velocity of the exterior boundary of $\Omega_1(t)$ along the outward normal vector $\vec{\nu}$, and $V_{\Gamma(t)}$ the velocity of the interface $\Gamma(t)$ along the vector $\vec{\nu}$. Using Reynolds

transport theorem on moving domains, the LHS gives,

$$\begin{aligned}\partial_t \int_{\Omega_1(t)} \phi \, dx &= \int_{\partial\Omega_1(t)} V_{\partial\Omega_1(t)} \cdot \vec{\nu}\phi \, d\sigma(x) \\ &= \int_{\partial\Omega_1(t)\cap\partial\Omega(t)} V_{\partial\Omega_1(t)} \cdot \vec{\nu}\phi \, d\sigma(x) + \int_{\Gamma(t)} V_{\partial\Omega_1(t)} \cdot \vec{\nu}\phi \, d\sigma(x), \end{aligned} \tag{4.61}$$

Since (4.60) and (4.61) are satisfied for all $\phi \in \mathcal{C}_c^\infty(\mathbb{R}^d)$, particularly by extension of $\phi \in \mathcal{C}_c^\infty(\partial\Omega_1(t)\cap \partial\Omega(t))$ we deduce the following relation,

$$V_{\partial\Omega_1(t)\cap\partial\Omega(t)} = v_1^\infty \cdot \vec{\nu},$$

similarly by extension of $\phi \in \mathcal{C}_c^\infty(\Gamma(t))$ we deduce,

$$V_{\Gamma(t)} = v_1^\infty \cdot \vec{\nu}.$$

Finally, by a symmetric reasoning, defining $\vec{\mu}$ the outward normal vector to $\Omega_2(t)$, we obtain the velocity of the exterior boundary of $\Omega_2(t)$,

$$V_{\partial\Omega_2(t)\cap\partial\Omega(t)} = v_2^\infty \cdot \vec{\mu},$$

as well as the continuity of the velocity along the interface $\Gamma(t)$,

$$v_1^\infty \cdot \vec{\nu} = v_2^\infty \cdot \vec{\nu} \quad \text{on } \Gamma(t).$$

4.4.4 On the limit of the repulsion pressure

In this section we study the behavior of the repulsion pressure q_m in the mechanical model at the incompressible limit. We notice that $q^\infty = 0$ gives an admissible solution for the problem (4.23)–(4.33). Indeed, since the system at the incompressible limit is fully segregated (4.30), it might be relevant to consider that at the limit the repulsion pressure vanishes. The question we want to address is the following: is it relevant to consider cases where the repulsion pressure persists at the incompressible limit, that is, q^∞ is not identically null ? Our numerical simulations suggest that q^∞ does not vanish at the incompressible limit, and they highlight its role in creating adjacent zones of opposite curls in the anterior part of the PSM. To explore further the role of this repulsion force, we proceed with the following formal analysis.

Here we are interested in the case where densities at the incompressible limit are indicator functions (which is a case where the free boundary model is particularly relevant). We then suppose that n_1^m and n_2^m converge respectively towards χ_{Ω_1} and χ_{Ω_2} in a sufficiently strong sense, locally uniformly in time, and we write the Taylor expansion of n_1^m and n_2^m with respect to the parameter

m (assuming that such expansion exists),

$$n_1^m = \chi_{\Omega_1} + \frac{1}{m} h_1 + o(m^{-1}), \tag{4.62}$$

$$n_2^m = \chi_{\Omega_2} + \frac{1}{m} h_2 + o(m^{-1}). \tag{4.63}$$

We can then compute the product,

$$n_1^m n_2^m = \frac{1}{m} \left(h_2 \chi_{\Omega_1} + h_1 \chi_{\Omega_2} \right) + o(m^{-1}),$$

so that the repulsion pressure becomes at the limit,

$$\begin{aligned} q_m &= \frac{m}{m-1}[(1 + n_1^m n_2^m)^{m-1} - 1] \\ &= \frac{m}{m-1} \left(\exp \left\{ (m-1) \log \left(1 + \frac{1}{m} (h_2 \chi_{\Omega_1} + h_1 \chi_{\Omega_2}) + o(m^{-1}) \right) \right\} - 1 \right) \\ &\xrightarrow{m \to +\infty} \exp \left\{ h_2 \chi_{\Omega_1} + h_1 \chi_{\Omega_2} \right\} - 1. \end{aligned} \tag{4.64}$$

Finally, rewriting this last expression, we have shown that,

$$q^\infty = \chi_{\Omega_1} \left(\exp(h_2) - 1 \right) + \chi_{\Omega_2} \left(\exp(h_1) - 1 \right). \tag{4.65}$$

Interpretation. In the Taylor expansion (4.62) expressed in terms of small values of the parameter $1/m$, the term of order zero gives the asymptotic behavior of the density n_1^m. We see that the coefficient of first order in $1/m$ in (4.62) (i.e the quantity h_1) appears in the final expression of q^∞ at the incompressible limit under the form $h_1 \chi_{\Omega_2}$. It is remarkable that the repulsion force persists *a priori* everywhere on the domain, and not only at the interface. One could interpret this phenomenon as a repulsion force emerging from microscopic residuals of the tissue 1 inside tissue 2 (and *vice versa*). The situation where the repulsion force vanishes at the limit then corresponds to a modelling situation where such microscopic effects are neglected (fast segregation regime). Note that $q^\infty = 0$ gives a particular solution of (4.58)–(4.59) (see remark 4.3.6).

In fact, q^∞ cannot be neglected in general at the limit as it produces an effect on the dynamics. We note that in (4.65) the repulsion only persists in the domain $\Omega_1 \cup \Omega_2$ (see Remark 4.3.4), that is, the repulsion force produces a finite effect only in regions fully occupied by the densities.

Moreover, the persistence of the repulsion pressure q^∞ at the limit can be seen as a *ghost effect*. This terminology originates from the framework of rarefied gas dynamics. For instance, in rarefied gases, steady flows can be induced by temperature fields. When a continuum limit is performed on the Boltzmann equation on the basis of kinetic theory, in the sense that the Knudsen number of the system tends to zero, these flows vanish. This means that no condensation nor evaporation occurs,

and the components are at rest. However, it was shown that these vanishing flows produce a finite effect on the gas behavior at the limit. This is known as the *ghost effect*, originally discovered by Sone et al [137, 139, 138, 140, 145]. The *ghost effect* has been described in different physical settings ([7, 8, 9, 137]. These works show that the Navier-Stokes equation (or the heat-conduction equation) must be coupled with the *ghost effect* to fully describe the gas dynamics at the continuum limit [138]. This was shown by doing an asymptotic analysis on the Boltzmann equation, by expansion in the Knudsen number, which allowed the derivation of the fluid-dynamics equations at the limit and the *ghost effect*. In our case, if we assume that the Taylor expansion in $1/m$ holds, the *ghost effect* appears in terms of first order in $1/m$ similarly to [7, 138, 145].

4.5 Analysis of the stationary L-ESVM (q given)

In this section, we study the stationary L-ESVM in the framework described in section 4.3.2. We recall that the system is considered in a bounded domain $\Theta \subset \mathbb{R}^2$ ($d = 2$) with homogeneous Dirichlet boundary conditions on the velocity. We consider three subdomains Ω, Ω_1 and Ω_2 which satisfy the assumptions (4.34)–(4.37). In the simplified framework considered here, the equations (4.32) and (4.33) are removed and instead, q is given as in (4.38). We also choose the growth functions G_1 and G_2 to be linear as in (4.39). For clarity, we remove the superscripts "∞" from all the variables in this section.

The resulting problem is the following system on (v_1, v_2),

$$(S_2)\quad \begin{cases} -\beta_1\Delta v_1 + v_1 = -\nabla[(p_1^* - \frac{1}{g_1}\nabla\cdot v_1)\chi_{\Omega_1} + (p_2^* - \frac{1}{g_2}\nabla\cdot v_2 + q)\chi_{\Omega_2}] & \text{on } \Theta, \\ -\beta_2\Delta v_2 + v_2 = -\nabla[(p_2^* - \frac{1}{g_2}\nabla\cdot v_2)\chi_{\Omega_2} + (p_1^* - \frac{1}{g_1}\nabla\cdot v_1 + q)\chi_{\Omega_1}] & \text{on } \Theta, \\ v_1 = v_2 = 0 & \text{on } \partial\Theta, \end{cases}$$

with $\chi_{\Omega_1}, \chi_{\Omega_2}$ the indicator functions of the domains Ω_1, Ω_2 respectively, and where g_1, g_2, p_1^*, $p_2^* > 0$ and q is a given function on Ω.

4.5.1 Well-posedness and regularity of the stationary linear system.

We prove here Theorem 4.3.3. We first start with the well-posedness.

Proposition 4.5.1. *For $q \in L^2(\Omega)$, there exists a unique solution $(v_1, v_2) \in H_0^1(\Theta)^2 \times H_0^1(\Theta)^2$ to problem (S_2) under the condition (4.40) on the model parameters.*

Proof. The proof is done using the Lax-Milgram theorem. We can write the weak formulation of (S_2) as

$$(\tilde{V})\begin{cases} \text{Find } (v_1, v_2) \in H_0^1(\Theta)^2 \times H_0^1(\Theta)^2, \text{ such that} \\ B((v_1, v_2), (\phi_1, \phi_2)) = l((\phi_1, \phi_2)), \quad \forall (\phi_1, \phi_2) \in H_0^1(\Theta)^2 \times H_0^1(\Theta)^2, \end{cases}$$

where we define the bilinear map B as,

$$\begin{aligned} B((v_1,v_2),(\phi_1,\phi_2)) &= \beta_1\int_\Theta \nabla v_1 : \nabla\phi_1\,dx + \beta_2\int_\Theta \nabla v_2 : \nabla\phi_2\,dx \\ &+ \int_\Theta v_1\cdot\phi_1\,dx + \int_\Theta v_2\cdot\phi_2\,dx \\ &+ \frac{1}{g_1}\int_\Theta (\nabla\cdot v_1)(\nabla\cdot\phi_1)\chi_{\Omega_1}\,dx + \frac{1}{g_2}\int_\Theta (\nabla\cdot v_2)(\nabla\cdot\phi_2)\chi_{\Omega_2}\,dx \\ &+ \frac{1}{g_1}\int_\Theta (\nabla\cdot v_1)(\nabla\cdot\phi_2)\chi_{\Omega_1}\,dx + \frac{1}{g_2}\int_\Theta (\nabla\cdot v_2)(\nabla\cdot\phi_1)\chi_{\Omega_2}\,dx, \end{aligned}$$

and the linear application l as,

$$l((\phi_1,\phi_2)) = \int_{\Omega_1}(p_1^*+q)(\nabla\cdot\phi_1+\nabla\cdot\phi_2)\,dx + \int_{\Omega_2}(p_2^*+q)(\nabla\cdot\phi_2+\nabla\cdot\phi_1)\,dx.$$

To prove the continuity of the bilinear application we do the following:

$$\begin{aligned} |B((v_1,v_2),(\phi_1,\phi_2))| &\le \beta_1\|\nabla v_1\|_{L^2(\Theta)}\|\nabla\phi_1\|_{L^2(\Theta)} + \|v_1\|_{L^2(\Theta)}\|\phi_1\|_{L^2(\Theta)} \\ &+ \frac{1}{g_1}\|\nabla\cdot v_1\|_{L^2(\Theta)}\|\nabla\cdot\phi_1\|_{L^2(\Theta)} + \beta_2\|\nabla v_2\|_{L^2(\Theta)}\|\nabla\phi_2\|_{L^2(\Theta)} \\ &+ \|v_2\|_{L^2(\Theta)}\|\phi_2\|_{L^2(\Theta)} + \frac{1}{g_2}\|\nabla\cdot v_2\|_{L^2(\Theta)}\|\nabla\cdot\phi_2\|_{L^2(\Theta)} \\ &+ \frac{1}{g_1}\|\nabla\cdot v_1\|_{L^2(\Theta)}\|\nabla\cdot\phi_2\|_{L^2(\Theta)} + \frac{1}{g_2}\|\nabla\cdot v_2\|_{L^2(\Theta)}\|\nabla\cdot\phi_1\|_{L^2(\Theta)} \\ &\le \left(1+\min\left(\beta_1+\frac{2}{g_1},\beta_2+\frac{2}{g_2}\right)\right)\|(v_1,v_2)\|_{H_0^1(\Theta)^2\times H_0^1(\Theta)^2}\|(\phi_1,\phi_2)\|_{H_0^1(\Theta)^2\times H_0^1(\Theta)^2}, \end{aligned}$$

where we used Cauchy-Schwarz inequality and that,

$$\|\nabla\cdot v\|^2_{L^2(\Theta)} \le \|\nabla v\|^2_{L^2(\Theta)}. \tag{4.66}$$

For the coercivity of the bilinear application we use again Cauchy-Schwarz's inequality and the

inequality (4.66),

$$\begin{aligned} B((v_1,v_2),(v_1,v_2)) &= \beta_1\|\nabla v_1\|^2_{L^2(\Theta)} + \|v_1\|^2_{L^2(\Theta)} + \frac{1}{g_1}\|\nabla\cdot v_1\|^2_{L^2(\Omega_1)} \\ &\quad +\beta_2\|\nabla v_2\|^2_{L^2(\Theta)} + \|v_2\|^2_{L^2(\Theta)} + \frac{1}{g_2}\|\nabla\cdot v_2\|^2_{L^2(\Omega_2)} \\ &\quad +\frac{1}{g_1}\int_{\Omega_1}\nabla\cdot v_1\nabla\cdot v_2\,dx + \frac{1}{g_2}\int_{\Omega_2}\nabla\cdot v_2\nabla\cdot v_1\,dx \\ &\geq \beta_1\|\nabla v_1\|^2_{L^2(\Theta)} + \|v_1\|^2_{L^2(\Theta)} + \beta_2\|\nabla v_2\|^2_{L^2(\Theta)} + \|v_2\|^2_{L^2(\Theta)} \\ &\quad -\frac{1}{4g_1}\|\nabla\cdot v_2\|^2_{L^2(\Omega_1)} - \frac{1}{4g_2}\|\nabla\cdot v_1\|^2_{L^2(\Omega_2)} \\ &\geq \left(\beta_1 - \frac{1}{4g_2}\right)\|\nabla v_1\|^2_{L^2(\Theta)} + \left(\beta_2 - \frac{1}{4g_1}\right)\|\nabla v_2\|^2_{L^2(\Theta)} \\ &\quad +\|v_2\|^2_{L^2(\Theta)} + \|v_1\|^2_{L^2(\Theta)}, \end{aligned}$$

which gives the coercivity of B under the condition (4.40).

Finally we obtain the continuity of the linear application l by :

$$|l((\phi_1,\phi_2))| \leq C(p_1^* + p_2^* + \|q\|_{L^2(\Omega)})\|(\phi_1,\phi_2)\|_{H_0^1(\Theta)^2\times H_0^1(\Theta)^2}.$$

Then by the Lax-Milgram theorem there exists a unique solution $(v_1,v_2)\in H_0^1(\Theta)^2\times H_0^1(\Theta)^2$ to (S_2). ■

Whenever the repulsion pressure q is assumed to be smooth on each subdomain, we can obtain more regularity on the velocities by applying the results of elliptic regularity for transmission problems from [102]:

Proposition 4.5.2 (Elliptic regularity). *For a given $q\in\mathcal{C}^{0,\mu}(\overline{\Omega_1})\cap\mathcal{C}^{0,\mu}(\overline{\Omega_2})$ for some $0<\mu<1$, and if the domains satisfy the conditions (4.34)-(4.37) and the condition on the model parameters (4.40), then the solution (v_1,v_2) to the system (S_2) is $\mathcal{C}^{1,\alpha'}(\overline{\Omega_1})\cap\mathcal{C}^{1,\alpha'}(\overline{\Omega_2})\cap\mathcal{C}^{1,\alpha'}(\overline{\Omega^c})$, with $0<\alpha'\leq\min(\mu,\frac{1}{4})$.*

Proof. This is a direct application of Theorem 1.1 and Remark 1.2 in [102]. To apply this theorem, we first check that the domains satisfy the appropriate requirements. In fact, we assume (4.35) and (4.37). Then, it remains to check that the second order differential operator of (S_2) satisfies the weak ellipticity condition, that is

$$B((\phi^1,\phi^2),(\phi^1,\phi^2))\geq\lambda\|\nabla\phi\|^2_{L^2(\Theta)},\qquad\forall\phi=(\phi^1,\phi^2)\in H_0^1(\Theta)^4,$$

for some $\lambda>0$. This condition coincides with the coercivity condition of the bilinear application B. It is satisfied with $\lambda=\min\left(\beta_1-\frac{1}{4g_2},\beta_2-\frac{1}{4g_1}\right)$, which is positive thanks to (4.40).

Finally, note that Theorem 1.1 in [102] gives the regularity result away from $\partial\Omega$. Thanks to the assumption in (4.36), this already gives the regularity on $\overline{\Omega_i}$ for $i = 1, 2$. Thanks to the homogeneous Dirichlet boundary conditions, to obtain the regularity up to $\partial\Theta$, it suffices to slightly move away the boundary $\partial\Theta$, extending the velocities by zero on the new domain. ■

Proof of Theorem 4.3.3. Finally, Theorem 4.3.3 is a consequence of Propositions 4.5.1 and 4.5.2. ■

4.5.2 Transmission problem of the stationary linear system

We show here that system (S_2) can be rewritten as the transmission problem (T_2).

Proof of Proposition 4.3.7. Recall that the conditions (4.34)-(4.37) and (4.40) are still assumed and that $q \in \mathcal{C}^{0,\mu}(\overline{\Omega_1}) \cap \mathcal{C}^{0,\mu}(\overline{\Omega_2})$, for some $\mu \in (0,1)$.

First, by testing system (S_2) with a test function compactly supported in Ω_1, it is clear that the system (T_{2,Ω_1}) is satisfied in a distributional sense (actually, against test functions in $H_0^1(\Omega_1)$ thanks to the regularity obtained from Theorem 4.3.3, and even in a classical sense thanks to interior elliptic regularity). The same applies in the other subdomains, so that (T_{2,Ω_1}), (T_{2,Ω_2}) and (T_{2,Ω^c}) are satisfied on their respective domains.

To obtain the transmission conditions, we consider a test function $\phi \in \mathcal{C}_c^\infty(\Theta)^2$, and thanks to $\chi_{\Omega_1^n}$, $\chi_{\Omega_2^n}$, and $\chi_{\Omega_c^n}$ smooth approximations of respectively χ_{Ω_1}, χ_{Ω_2}, and χ_{Ω^c}, we construct a new test function $\tilde{\phi}_n \in \mathcal{C}_c^\infty(\Theta)^2$ as $\tilde{\phi}_n = \phi[1 - \chi_{\Omega_1^n} - \chi_{\Omega_2^n} - \chi_{\Omega_c^n}]$. Then we multiply (dot product) each one of the equations of (S_2) with the test function $\tilde{\phi}_n$ and integrate, and we pass to the limit when n tends to infinity. By identifying the quantities thus obtained on each section of the boundaries, one gets the transmission conditions (T_{2,Γ_1}), (T_{2,Γ_2}) and $(T_{2,\Gamma})$ (see Appendix 4.8.1 for details on the derivation of the transmission problem in the simple case of one species which can be similarly extended to the case of two species). ■

4.5.3 Further regularity for the stationary linear system

In this section we show the proof of Theorem 4.3.8. We recall that the conditions (4.34)-(4.37) and (4.40)-(4.42) are assumed and that $q \in \mathcal{C}^\infty(\overline{\Omega_1}) \cap \mathcal{C}^\infty(\overline{\Omega_2})$.

Proof of Theorem 4.3.8. The regularity result is a direct consequence of Proposition 1.4 in [102]. In fact, the well-posedness of the stationary L-ESVM for a given $q \in \mathcal{C}^\infty(\overline{\Omega_1}) \cap \mathcal{C}^\infty(\overline{\Omega_2})$ is ensured by Theorem 4.3.3. Moreover, under (4.42), we do not allow more than two subdomains to be in contact, thus all the boundary domains $\partial\Omega_1, \partial\Omega_2$, and $\partial\Omega$ are smooth, and we gain the desired regularity. ■

4.6 Analysis of the L-VM

In this section we first show a formal proof of the segregation property of the VM. We are then interested in the quantitative behavior of the stationary L-VM. We show the existence of a pressure jump using the formalism of a transmission problem.

4.6.1 Proof of the segregation property

This section is dedicated to the formal proof of Proposition 4.3.9.

Proof of Proposition 4.3.9. We present a formal proof of the segregation property in the case $\beta_1 = \beta_2$. We introduce the population fractions c_1 and c_2 on the set where $n > 0$,

$$c_1 \coloneqq \frac{n_1}{n}, \quad c_2 \coloneqq \frac{n_2}{n}.$$

We note that the full segregation (4.44) can be written as,

$$nc_1c_2 = 0.$$

Given $\beta_1 = \beta_2$, we obtain $v_1 = v_2$ in (4.17)-(4.18). We use equations (4.15) and (4.16) to derive an equation for the product nc_1c_2. It reads,

$$\partial_t(nc_1c_2) = -\nabla \cdot (nc_1c_2v_1) + nc_1c_2 \left(c_2G_1(p_\epsilon) + c_1G_2(p_\epsilon)\right).$$

Integrating on $\mathbb{R}^d$ we obtain,

$$\frac{d}{dt}\int_{\mathbb{R}^d}(nc_1c_2)\,dx = \int_{\mathbb{R}^d} nc_1c_2\left(c_2G_1(p_\epsilon) + c_1G_2(p_\epsilon)\right)\,dx. \tag{4.67}$$

Under the assumption on the growth functions (4.43), and assuming $n_1 \geq 0, n_2 \geq 0$, equation (4.67) yields,

$$\frac{d}{dt}\int_{\mathbb{R}^d}(nc_1c_2)\,dx \leq G_m \int_{\mathbb{R}^d} nc_1c_2\,dx.$$

We deduce by solving the differential inequality that if the densities are initially segregated, that is, $n^{ini}c_1^{ini}c_2^{ini} = 0$, then,

$$nc_1c_2 = 0, \quad \forall (t,x) \in [0;+\infty) \times \mathbb{R}^d.$$

■

4.6.2 Pressure jump of the stationary L-VM

The corresponding stationary transmission problem for the L-VM is a special case of the transmission problem for the L-ESVM in the case where $q = 0$. From proposition 4.3.7, we obtain the following transmission problem by taking $q = 0$ in (T_2),

$$(T_{VM})\begin{cases}
-\beta_1\Delta v_1 + v_1 = 0 & \text{in } \Omega^c,\\
-\beta_1\Delta v_1 + v_1 - \frac{1}{g_1}\nabla\nabla\cdot v_1 = 0 & \text{in } \Omega_1,\\
-\beta_1\Delta v_1 + v_1 - \frac{1}{g_2}\nabla\nabla\cdot v_2 = 0 & \text{in } \Omega_2,\\
-\beta_2\Delta v_2 + v_2 = 0 & \text{in } \Omega^c,\\
-\beta_2\Delta v_2 + v_2 - \frac{1}{g_2}\nabla\nabla\cdot v_2 = 0 & \text{in } \Omega_2,\\
-\beta_2\Delta v_2 + v_2 - \frac{1}{g_1}\nabla\nabla\cdot v_1 = 0 & \text{in } \Omega_1,\\
\beta_1[(\nabla v_1)_{\Omega_1} - (\nabla v_1)_{\Omega^c}]\cdot\vec{\nu} = [p_1^* - \frac{1}{g_1}(\nabla\cdot v_1)_{\Omega_1})]\vec{\nu} & \text{on } \Gamma_1,\\
\beta_2[(\nabla v_2)_{\Omega_1} - (\nabla v_2)_{\Omega^c}]\cdot\vec{\nu} = [p_1^* - \frac{1}{g_1}(\nabla\cdot v_1)_{\Omega_1})]\vec{\nu} & \text{on } \Gamma_1,\\
\beta_1[(\nabla v_1)_{\Omega_2} - (\nabla v_1)_{\Omega^c}]\cdot\vec{\mu} = [p_2^* - \frac{1}{g_2}(\nabla\cdot v_2)_{\Omega_2})]\vec{\mu} & \text{on } \Gamma_2,\\
\beta_2[(\nabla v_2)_{\Omega_2} - (\nabla v_2)_{\Omega^c}]\cdot\vec{\mu} = [p_2^* - \frac{1}{g_2}(\nabla\cdot v_2)_{\Omega_2})]\vec{\mu} & \text{on } \Gamma_2,\\
\beta_1[(\nabla v_1)_{\Omega_1} - (\nabla v_1)_{\Omega_2}]\cdot\vec{\nu} = [(p_1^* - p_2^*) + \frac{1}{g_2}(\nabla\cdot v_2)_{\Omega_2}) - \frac{1}{g_1}(\nabla\cdot v_1)_{\Omega_1}]\vec{\nu} & \text{on } \Gamma,\\
\beta_2[(\nabla v_2)_{\Omega_1} - (\nabla v_2)_{\Omega_2}]\cdot\vec{\nu} = [(p_1^* - p_2^*) + \frac{1}{g_2}(\nabla\cdot v_2)_{\Omega_2}) - \frac{1}{g_1}(\nabla\cdot v_1)_{\Omega_1}]\vec{\nu} & \text{on } \Gamma,\\
(v_1)_{\Omega_1} = (v_1)_{\Omega_2}, \quad (v_2)_{\Omega_1} = (v_2)_{\Omega_2}, \quad v_1\cdot\vec{\nu} = v_2\cdot\vec{\nu}, & \text{on } \Gamma,\\
(v_1)_{\Omega_1} = (v_1)_{\Omega^c}, \quad (v_2)_{\Omega_1} = (v_2)_{\Omega^c}, & \text{on } \Gamma_1,\\
(v_1)_{\Omega_2} = (v_1)_{\Omega^c}, \quad (v_2)_{\Omega_2} = (v_2)_{\Omega^c}, & \text{on } \Gamma_2,\\
v_1 = v_2 = 0 & \text{on } \partial\Theta.
\end{cases}$$

We recall that with our choice of linear growth functions $G_1(s) = g_1(p_1^* - s)$, and $G_2(s) = g_2(p_2^* - s)$ with $g_1, g_2, p_1^*, p_2^* > 0$, the expression of the pressure p on the interfaces Γ_1, Γ_2 and Γ reduces to (4.52), so that the transmission conditions on the interfaces become,

$$\begin{cases}
\beta_1[(\nabla v_1)_{\Omega_1} - (\nabla v_1)_{\Omega^c}]\cdot\vec{\nu} = \beta_2[(\nabla v_2)_{\Omega_1} - (\nabla v_2)_{\Omega^c}]\cdot\vec{\nu} = [(p)_{\Omega_1} - (p)_{\Omega^c}]\vec{\nu} & \text{on } \Gamma_1,\\
\beta_1[(\nabla v_1)_{\Omega_2} - (\nabla v_1)_{\Omega^c}]\cdot\vec{\mu} = \beta_2[(\nabla v_2)_{\Omega_2} - (\nabla v_2)_{\Omega^c}]\cdot\vec{\mu} = [(p)_{\Omega_2} - (p)_{\Omega^c}]\vec{\mu} & \text{on } \Gamma_2,\\
\beta_1[(\nabla v_1)_{\Omega_1} - (\nabla v_1)_{\Omega_2}]\cdot\vec{\nu} = \beta_2[(\nabla v_2)_{\Omega_1} - (\nabla v_2)_{\Omega_2}]\cdot\vec{\nu} = [(p)_{\Omega_1} - (p)_{\Omega_2}]\vec{\nu} & \text{on } \Gamma.
\end{cases} \tag{4.68}$$

In models incorporating surface tension, the pressure jump depends on the free boundary curvature (see [4] for example in the case of a Cahn-Hilliard equation). In our case, the presence of the viscosity parameters $\beta_i > 0$ is behind the discontinuity of the pressure as can be seen in (4.68). This is in accordance with previous results on Darcy's law [125]. In the case where the velocity follows the Brinkman law and taken of gradient form, which is the framework of [127], a pressure jump is also shown (see also [103] for explicit computations of the pressure jump in multi-dimensions).

Remark 4.6.1. *When $\beta_1 = \beta_2$ we have $v_1 = v_2$, which yields $\nabla\cdot v_1 = \nabla\cdot v_2$. Since on the interface*

we have $\nabla \cdot v_1 = G_1(p) = g_1(p_1^* - p)$ *and* $\nabla \cdot v_2 = G_2(p) = g_2(p_2^* - p)$*, the pressure jump vanishes at the interface and* p *is continuous on* Γ*.*

We now prove the existence of a pressure jump. Since, from (4.68), the jumps of the pressure and the jumps of the gradients of the velocities are very related, we first prove that the gradients of the velocities have jumps.

Proposition 4.6.2. *Under the assumptions (4.34)-(4.37) and (4.40), we have* $v_1, v_2 \notin H^2(\Theta)^2$*, with* (v_1, v_2) *the solution of the system* (T_{VM})*.*

Proof. Let (v_1, v_2) be the solution of the (T_{VM}). Then by Theorem 4.3.3 $(v_1, v_2) \in H_0^1(\Theta)^2 \times H_0^1(\Theta)^2$. Furthermore by Theorem 4.3.8, v_1, v_2 lie in $\mathcal{C}^\infty(\overline{\Omega_1}) \cap \mathcal{C}^\infty(\overline{\Omega_2}) \cap \mathcal{C}^\infty(\overline{\Omega^c})$. Then we have v_1, v_2 in $H^2(\Omega_1)^2 \cap H^2(\Omega_2)^2 \cap H^2(\Omega^c)^2$. We now proceed by contradiction: let us assume that $v_1, v_2 \in H^2(\Theta)^2$ and show that there is a contradiction. For each of the three first equations in (T_{VM}), we multiply (dot product) by $-\Delta v_1$ and integrate on their respective domains. By summing the result, we obtain thanks to an additional Green's identity,

$$\beta_1 \|\Delta v_1\|^2_{L^2(\Theta)} + \|\nabla v_1\|^2_{L^2(\Theta)} = -\frac{1}{g_1}\int_{\Omega_1} \nabla\nabla\cdot v_1 \cdot \Delta v_1 \, dx - \frac{1}{g_2}\int_{\Omega_2} \nabla\nabla\cdot v_2 \cdot \Delta v_1 \, dx. \tag{4.69}$$

Using twice Green's identity, we compute the last term as,

$$\begin{aligned}
& -\frac{1}{g_2}\int_{\Omega_2} \nabla\nabla\cdot v_2 \cdot \Delta v_1 \, dx \\
= \; & \frac{1}{g_2}\int_{\Omega_2} \nabla\cdot v_2 \, \Delta\nabla\cdot v_1 \, dx - \frac{1}{g_2}\int_{\partial\Omega_2} \nabla\cdot v_2 \, \Delta v_1 \cdot \vec{\mu} \, d\sigma(x) \\
= \; & -\frac{1}{g_2}\int_{\Omega_2} \nabla(\nabla\cdot v_2)\cdot\nabla(\nabla\cdot v_1) \, dx + \frac{1}{g_2}\int_{\partial\Omega_2} \nabla\cdot v_2 \, \nabla(\nabla\cdot v_1)\cdot\vec{\mu} \, d\sigma(x) \\
& -\frac{1}{g_2}\int_{\partial\Omega_2} \nabla\cdot v_2 \, \Delta v_1 \cdot \vec{\mu} \, d\sigma(x).
\end{aligned} \tag{4.70}$$

Reinserting in (4.69) and using the same computation for the first term of the right-hand-side, we obtain,

$$\begin{aligned}
\beta_1 \|\Delta v_1\|^2_{L^2(\Theta)} \; + \; & \|\nabla v_1\|^2_{L^2(\Theta)} \\
= \; & -\frac{1}{g_1}\int_{\Omega_1} \nabla(\nabla\cdot v_1)\cdot\nabla(\nabla\cdot v_1) \, dx + \frac{1}{g_1}\int_{\partial\Omega_1} \nabla\cdot v_1 \, [\nabla(\nabla\cdot v_1) - \Delta v_1]\cdot\vec{\nu} \, d\sigma(x) \\
& -\frac{1}{g_2}\int_{\Omega_2} \nabla(\nabla\cdot v_2)\cdot\nabla(\nabla\cdot v_1) \, dx \\
& +\frac{1}{g_2}\int_{\partial\Omega_2} \nabla\cdot v_2 \, [\nabla(\nabla\cdot v_1) - \Delta v_1]\cdot\vec{\mu} \, d\sigma(x).
\end{aligned} \tag{4.71}$$

Now, using the assumption $v_1, v_2 \in H^2(\Theta)^2$, we get that ∇v_1 and ∇v_2 are continuous across all

interfaces Γ_1, Γ_2, Γ. We therefore deduce from (T_{VM}) that,

$$0 = [p_1^* - \frac{1}{g_1}(\nabla \cdot v_1)_{\Omega_1})]\vec{\nu} \quad \text{on } \Gamma_1, \tag{4.72}$$

$$0 = [p_2^* - \frac{1}{g_2}(\nabla \cdot v_2)_{\Omega_2})]\vec{\mu} \quad \text{on } \Gamma_2, \tag{4.73}$$

$$0 = [(p_1^* - p_2^*) + \frac{1}{g_2}(\nabla \cdot v_2)_{\Omega_2}) - \frac{1}{g_1}(\nabla \cdot v_1)_{\Omega_1}]\vec{\nu} \quad \text{on } \Gamma\,. \tag{4.74}$$

Coming back to (4.71), we get,

$$\begin{aligned}
&\beta_1\|\Delta v_1\|^2_{L^2(\Theta)} + \|\nabla v_1\|^2_{L^2(\Theta)} + \frac{1}{g_1}\|\nabla(\nabla \cdot v_1)\|^2_{L^2(\Omega_1)} + \frac{1}{g_2}\int_{\Omega_2} \nabla(\nabla \cdot v_2) \cdot \nabla(\nabla \cdot v_1)\, dx \\
= \;& \frac{1}{g_1}\int_{\partial\Omega_1} \nabla \cdot v_1 \; [\nabla(\nabla \cdot v_1) - \Delta v_1] \cdot \vec{\nu}\, d\sigma(x) + \frac{1}{g_2}\int_{\partial\Omega_2} \nabla \cdot v_2 \; [\nabla(\nabla \cdot v_1) - \Delta v_1] \cdot \vec{\mu}\, d\sigma(x) \\
= \;& p_1^*\int_{\Gamma_1} [\nabla(\nabla \cdot v_1) - \Delta v_1] \cdot \vec{\nu}\, d\sigma(x) + p_2^*\int_{\Gamma_2} [\nabla(\nabla \cdot v_1) - \Delta v_1] \cdot \vec{\mu}\, d\sigma(x) \\
&+ \int_{\Gamma} \left(\frac{1}{g_1}\nabla \cdot v_1 - \frac{1}{g_2}\nabla \cdot v_2\right) [\nabla(\nabla \cdot v_1) - \Delta v_1] \cdot \vec{\nu}\, d\sigma(x) \\
= \;& p_1^*\int_{\Gamma_1} [\nabla(\nabla \cdot v_1) - \Delta v_1] \cdot \vec{\nu}\, d\sigma(x) + p_2^*\int_{\Gamma_2} [\nabla(\nabla \cdot v_1) - \Delta v_1] \cdot \vec{\mu}\, d\sigma(x) \\
&+ \int_{\Gamma} (p_1^* - p_2^*) \; [\nabla(\nabla \cdot v_1) - \Delta v_1] \cdot \vec{\nu}\, d\sigma(x) \\
= \;& p_1^*\int_{\partial\Omega_1} [\nabla(\nabla \cdot v_1) - \Delta v_1] \cdot \vec{\nu}\, d\sigma(x) + p_2^*\int_{\partial\Omega_2} [\nabla(\nabla \cdot v_1) - \Delta v_1] \cdot \vec{\mu}\, d\sigma(x).
\end{aligned} \tag{4.75}$$

Applying a final Green's identity gives, for $j = 1, 2$,

$$\int_{\partial\Omega_j} [\nabla(\nabla \cdot v_1) - \Delta v_1] \cdot \vec{\nu}\, d\sigma(x) = \int_{\Omega_j} \nabla \cdot [\nabla(\nabla \cdot v_1) - \Delta v_1]\; dx = 0,$$

so that,

$$\beta_1\|\Delta v_1\|^2_{L^2(\Theta)} + \|\nabla v_1\|^2_{L^2(\Theta)} + \frac{1}{g_1}\|\nabla(\nabla \cdot v_1)\|^2_{L^2(\Omega_1)} + \frac{1}{g_2}\int_{\Omega_2} \nabla(\nabla \cdot v_2) \cdot \nabla(\nabla \cdot v_1)\, dx = 0\,.$$

Following the same procedure for v_2, and summing the result, we finally get

$$\begin{aligned}
&\beta_1\|\Delta v_1\|^2_{L^2(\Theta)} + \beta_2\|\Delta v_2\|^2_{L^2(\Theta)} + \|\nabla v_1\|^2_{L^2(\Theta)} + \|\nabla v_2\|^2_{L^2(\Theta)} \\
&\qquad + \frac{1}{g_1}\|\nabla(\nabla \cdot v_1)\|^2_{L^2(\Omega_1)} + \frac{1}{g_2}\|\nabla(\nabla \cdot v_2)\|^2_{L^2(\Omega_2)} \\
&+ \frac{1}{g_1}\int_{\Omega_1} \nabla(\nabla \cdot v_2) \cdot \nabla(\nabla \cdot v_1)\, dx + \frac{1}{g_2}\int_{\Omega_2} \nabla(\nabla \cdot v_2) \cdot \nabla(\nabla \cdot v_1)\, dx \quad = 0\,.
\end{aligned}$$

Then using Young's inequality on the two last terms we get

$$\begin{aligned}
&\beta_1\|\Delta v_1\|_{L^2(\Theta)^2} + \|\nabla v_1\|_{L^2(\Theta)^2} + \beta_2\|\Delta v_2\|_{L^2(\Theta)^2} + \|\nabla v_2\|_{L^2(\Theta)^2} \\
&\qquad + \frac{1}{g_2}\|\nabla\nabla\cdot v_2\|^2_{L^2(\Omega_2)^2} + \frac{1}{g_1}\|\nabla\nabla\cdot v_1\|^2_{L^2(\Omega_1)^2} \\
\leq\ & \frac{1}{g_1}\|\nabla\nabla\cdot v_1\|^2_{L^2(\Omega_1)^2} + \frac{1}{4g_1}\|\nabla\nabla\cdot v_2\|^2_{L^2(\Omega_1)^2} + \frac{1}{g_2}\|\nabla\nabla\cdot v_2\|^2_{L^2(\Omega_2)^2} + \frac{1}{4g_2}\|\nabla\nabla\cdot v_1\|^2_{L^2(\Omega_2)^2}
\end{aligned}$$

We then can write

$$\left(\beta_1 - \frac{1}{4g_2}\right)\|D^2 v_1\|^2_{L^2(\Theta)^2} + \|\nabla v_1\|^2_{L^2(\Theta)^2} + \left(\beta_2 - \frac{1}{4g_1}\right)\|D^2 v_2\|^2_{L^2(\Theta)^2} + \|\nabla v_2\|^2_{L^2(\Theta)^2} \leq 0.$$

The ellipticity condition (4.40) gives positive coefficients in the above inequality. Then we can deduce that $\nabla v_1 \equiv 0$ on Θ. This is incompatible with (4.72), so that we have a contradiction, which proves the result.

■

As a corollary we obtain Proposition 4.3.12.

Proof of Proposition 4.3.12. Taking $\phi \in (\mathcal{C}^\infty_c(\Theta))^2$ we have, using the C^∞ regularity of v_1 on each subset $\overline{\Omega}_1$, $\overline{\Omega}_2$ and $\overline{\Omega^c}$,

$$\begin{aligned}
\langle \Delta v_1, \phi\rangle &= \int_\Theta v_1\cdot\Delta\phi\,dx \\
&= \int_{\Omega_1} v_1\cdot\Delta\phi\,dx + \int_{\Omega_2} v_1\cdot\Delta\phi\,dx + \int_{\Omega^c} v_1\cdot\Delta\phi\,dx \\
&= \int_{\Omega_1} \Delta v_1\cdot\phi\,dx + \int_{\Omega_2} \Delta v_1\cdot\phi\,dx + \int_{\Omega^c} \Delta v_1\cdot\phi\,dx \\
&\quad + \int_{\Gamma_1\cup\Gamma} \nabla\phi\, v_1\cdot\vec{\nu}\,d\sigma(x) + \int_{\Gamma_2\cup\Gamma} \nabla\phi\, v_1\cdot\vec{\mu}\,d\sigma(x) + \int_{\Gamma_1\cup\Gamma_2\cup\partial\Theta} \nabla\phi\, v_1\cdot\vec{\tau}\,d\sigma(x) \\
&\quad - \int_{\Gamma_1\cup\Gamma} (\nabla v_1)_{\Omega_1}\,\phi\cdot\vec{\nu}\,d\sigma(x) - \int_{\Gamma_2\cup\Gamma} (\nabla v_1)_{\Omega_2}\,\phi\cdot\vec{\mu}\,d\sigma(x) \\
&\quad - \int_{\Gamma_1\cup\Gamma_2\cup\partial\Theta} (\nabla v_1)_{\Omega^c}\,\phi\cdot\vec{\tau}\,d\sigma(x),
\end{aligned}$$

where $\vec{\tau}$ is the outward normal vector to Ω^c. In particular we have $\vec{\tau} = -\vec{\nu}$ on Γ_1 and $\vec{\tau} = -\vec{\mu}$ on Γ_2. Now, let us assume that p is continuous across $\Gamma_1\cup\Gamma_2\cup\Gamma$. Then by the transmission conditions in (4.68), we have that the jump of $\nabla v_1\cdot\vec{\nu}$ across $\Gamma_1\cup\Gamma_2\cup\Gamma$ is zero. Therefore, in the above computation, the integrals on all the interfaces vanish. Finally we can write,

$$|\langle\Delta v_1,\phi\rangle| \leq \|\phi\|_{L^2(\Theta)}\left(\|D^2 v_1\|_{L^2(\Omega_1)^2} + \|D^2 v_1\|_{L^2(\Omega_2)^2} + \|D^2 v_1\|_{L^2(\Omega^c)^2}\right),$$

then $\Delta v_1 \in L^2(\Theta)^2$ and we obtain $v_1 \in H^2(\Theta)^2$. Similarly we get $v_2 \in H^2(\Theta)^2$. This is impossible according to Proposition 4.6.2, and therefore, we have proved that p cannot be continuous across the interfaces. ■

4.7 Discussion

We presented an evolution model of two proliferating tissues in contact with each other and subject to an enforced segregation (ESVM). Apart from the enforced segregation, the novelty of this model lies in the law of the velocity: it is governed by the Brinkman law considered in a bounded domain, whose boundaries might affect the dynamics of the system. This setting allows to see swirling motions (non trivial curl) within the tissues, which corresponds to our biological motivation coming from the modelling of the embryo elongation.

We then established the formal incompressible limit for this model and obtained an incompressible system (L-ESVM) with a geometric description of the free boundaries. In this step we derived an evolution equation on the repulsion pressure, which, unintuitively, remains present at the limit, even though we attain full segregation. This repulsion pressure affects the dynamics of the shape of the tissues, specifically the velocities of the outer boundaries of the tissues and of their common interface. We called this a *ghost effect*. This effect is also supported by our numerical tests that show a finite effect of the repulsion pressure in the ESVM in its incompressible asymptotic regime.

One first question that arises is: what does this remaining repulsion pressure reveal about the embryo's tissues ? Having a closer look at our numerical simulations, we observed that the repulsion pressure affects the swirling motions in the PSM. More precisely, it allows adjacent zones of opposite curls to appear in the anterior part of the PSM, a pattern that is observed in the experiments on the bird embryo. Such pattern is not recovered when only passive segregation is assumed, that is, when the repulsion pressure is removed from the model. This suggests that an active segregation is at play to maintain tissue segregation in the vertebrate embryo. This question still requires to be fully explored numerically and compared to experimental data. This will be the subject of a future work.

A second striking feature arising from the model at the incompressible limit is the existence of a pressure jump across the interfaces. We showed this result in particular in situations where the repulsion pressure vanishes. This feature had already been observed in the specific case where the velocity obeys the Brinkman law and can be written as a gradient in [127]. This situation is for example met if the system is considered in the whole space. Here, we extend the result to situations in bounded domains with boundary conditions that may affect the dynamics. We mention that the pressure jump should also exist in the case where the repulsion pressure does not vanish, as the jump is viscosity-induced.

The derivation of the incompressible system that we presented here is formal. The case of a

velocity that is not in a gradient form, and in the case of a single species, has not been made rigorous yet. We pursue this aim in a future work.

4.8 Appendix

4.8.1 Derivation of the transmission problem

This section is devoted to the derivation of the transmission problems in $\mathbb{R}^2$. We first do the complete computations of the derivation of the transmission problem in the case of a single species for simplicity. Similar rigorous computations (though not shown in this paper) hold for the transmission problems (T_2) and (T_{VM}) respectively for the L-ESVM for a given q^∞ and for the L-VM. We then present a formal version of the transmission problem when q^∞ is a stationary solution of (4.32)-(4.33) (and not anymore a given L^2 function as in the simplified framework of section 4.3.2 and section 4.5).

4.8.2 Derivation of the transmission problem for the single species case

If we take either densities (n_1 or n_2) equal to zero in the VM, we obtain a single species model (SS) for the density and the velocity. The system (SS) is as follows: for all $(t,x) \in [0;+\infty) \times \mathbb{R}^d$,

$$\partial_t n + \nabla \cdot (nv) = nG(p_\epsilon), \tag{4.76}$$

$$-\beta \Delta v + v = -\nabla p_\epsilon, \tag{4.77}$$

$$p_\epsilon = \epsilon \frac{n}{1-n}. \tag{4.78}$$

Notice here that this system, with the general form of the velocity we consider, includes the system in [127] where the velocity is of gradient form. In this case, we can also obtain the incompressible limit by taking $\epsilon \to 0$, and the limiting system can be easily deduced from (4.23)-(4.29) by taking either n_1^∞ or n_2^∞ equal to zero, and $q^\infty = 0$.

A stationary transmission problem can also be formalized, and we obtain, as a straightforward consequence of the two-species case, the well-posedness and the elliptic regularity results (Theorem 4.3.8) as well as the expression of the pressure jump (Proposition 4.3.12). Note that the one-species system is elliptic for any $\beta > 0$ and $g > 0$, so that the results apply without any supplementary condition on these parameters.

The stationary system on the velocity in the single species case is posed in a bounded domain $\Theta \subset \mathbb{R}^2$. We assume $\Omega \subset \Theta$ to be a smooth bounded subdomain with $\overline{\Omega} \subset \Theta$.

The one-species problem coupled with homogeneous Dirichlet boundary conditions on v^∞ is as

follows,

$$(S_1)\quad \begin{cases} -\beta\Delta v^\infty + v^\infty = -\nabla[(p^* - \frac{1}{g}\nabla\cdot v^\infty)\chi_\Omega] & \text{on } \Theta, \\ v^\infty = 0 & \text{on } \partial\Theta, \end{cases}$$

with χ_Ω the indicator function of the domain Ω.

Proposition 4.8.1 (Transmission problem, one species)**.** *Let Ω be a smooth bounded domain with $\overline{\Omega} \subset \Theta$, and let $\Gamma := \partial\Omega$ and $\Omega^c := \Theta\backslash\overline{\Omega}$. Let $\beta > 0$, $g > 0$ and $p^* > 0$.*

Then the solution of system (S_1) solves the following transmission problem (T_1),

$$(T_1)\quad \begin{cases} -\beta\Delta v^\infty + v^\infty - \frac{1}{g}\nabla(\nabla\cdot v^\infty) = 0 & \text{in } \Omega, \\ -\beta\Delta v^\infty + v^\infty = 0 & \text{in } \Omega^c, \\ \beta[(\nabla v^\infty)_\Omega - (\nabla v^\infty)_{\Omega^c}]\vec{\nu} = [p^* - \frac{1}{g}(\nabla\cdot v^\infty)_\Omega]\vec{\nu} & \text{on } \Gamma, \\ (v^\infty)_\Omega = (v^\infty)_{\Omega^c} & \text{on } \Gamma, \\ v^\infty = 0 & \text{on } \partial\Theta, \end{cases}$$

with $\vec{\nu}$ the outward normal on Γ and with the notations $(\cdot)_\Omega$ and $(\cdot)_{\Omega^c}$ defined in (4.41).

Remark 4.8.2. *Note that in the following proof we only use the C^1 regularity of v^∞ in each subdomain (up to the boundary) $\overline{\Omega}$ and $\overline{\Omega^c}$. This ensures that the proof remains valid for the case of more than one species, thanks to Theorem 4.3.3.*

Proof. We consider the weak formulation of (S_1),

$$\beta\int_\Theta \nabla v^\infty : \nabla\phi\, dx + \int_\Theta v^\infty\cdot\phi\, dx + \int_\Theta \left(p^* - \frac{1}{g}\nabla\cdot v^\infty\right)\chi_\Omega\nabla\cdot\phi\, dx = 0, \text{ for all } \phi \in \mathcal{C}_c^\infty(\Theta)^2 \quad (4.79)$$

where the Frobenius inner product is used in the first integral. Then by extension of test functions $\phi \in \mathcal{C}_c^\infty(\Omega)^2$ (by 0 outside Ω) we obtain,

$$-\beta\Delta v^\infty - \frac{1}{g}\nabla(\nabla\cdot v^\infty) + v^\infty = 0 \quad \text{in } \mathcal{D}'(\Omega).$$

Similarly, by extension of test functions $\phi \in \mathcal{C}_c^\infty(\Omega^c)^2$ (by 0 outside Ω^c) we obtain,

$$-\beta\Delta v^\infty + v^\infty = 0 \quad \text{in } \mathcal{D}'(\Omega^c).$$

It remains to obtain the transmission conditions at the interface. For this, we use a sequence of smooth functions $(\chi_n)_n$ that are localized around the interface. More precisely these functions satisfy the following properties,

$$\chi_n \in C^\infty(\Theta), \qquad \text{for all } n \geq 0 \text{ large enough}, \quad (4.80)$$

as well as,

$$\chi_n \xrightarrow[n\to\infty]{L^p(\Theta)} 0, \quad \text{for all } p \in [1,\infty), \tag{4.81}$$

and finally, for any function $w \in C(\overline{\Omega}) \cap C(\overline{\Omega^c})$,

$$\lim_{n\to+\infty} \int_\Theta w \cdot \nabla \chi_n \, dx = \int_\Gamma (w)_{\Omega^c} \cdot \vec{\nu} \, d\sigma(x) - \int_\Gamma (w)_\Omega \cdot \vec{\nu} \, d\sigma(x), \tag{4.82}$$

with the notations of (4.41), with $\vec{\nu}$ the normal vector to Γ and $d\sigma(x)$ the surface measure along Γ. Such sequence can be constructed explicitly.

Now, we consider a test function $\phi \in \mathcal{C}_c^\infty(\Theta)^2$, which does not necessarily vanish close to Γ, and define $\tilde{\phi}_n \coloneqq \phi\chi_n$. We insert the test function $\tilde{\phi}_n$ in (4.79) and get,

$$\beta \int_\Theta \nabla v^\infty : \nabla \tilde{\phi}_n \, dx + \int_\Theta v^\infty \cdot \tilde{\phi}_n \, dx = \int_\Theta (p^* - \frac{1}{g} \nabla \cdot v^\infty) \chi_\Omega \nabla \cdot \tilde{\phi}_n \, dx, \tag{4.83}$$

which we rewrite,

$$\begin{aligned} \beta \int_\Theta \chi_n \nabla v^\infty : \nabla \phi \, dx \quad &+ \quad \beta \int_\Theta \nabla v^\infty : (\nabla \chi_n \otimes \phi) \, dx + \int_\Theta v^\infty \cdot \phi \chi_n \, dx \qquad (4.84) \\ &= \int_\Theta \chi_n (p^* - \frac{1}{g} \nabla \cdot v^\infty) \chi_\Omega \nabla \cdot \phi \, dx \\ &\quad + \int_\Theta (p^* - \frac{1}{g} \nabla \cdot v^\infty) \chi_\Omega (\nabla \chi_n) \cdot \phi \, dx. \qquad (4.85) \end{aligned}$$

Now using the convergences (4.81) and (4.82) together with the C^1 regularity of v^∞ on each subdomain $\overline{\Omega}$ and $\overline{\Omega^c}$ (up to the boundaries), we can pass to the limit $n \longrightarrow \infty$ and get,

$$\beta \int_\Gamma ((\nabla v^\infty)_{\Omega^c} - (\nabla v^\infty)_\Omega) : (\vec{\nu} \otimes \phi) \, d\sigma(x) = - \int_\Gamma (p^* - \frac{1}{g} (\nabla \cdot v^\infty)_\Omega) \phi \cdot \vec{\nu} \, d\sigma(x).$$

As this is verified for all $\phi \in \mathcal{C}_c^\infty(\Theta)^2$, particularly by extension of $\phi \in \mathcal{C}_c^\infty(\Gamma)^2$, we have the following condition on the interface,

$$\beta[(\nabla v^\infty)_\Omega - (\nabla v^\infty)_{\Omega^c}] \cdot \vec{\nu} = [p^* - \frac{1}{g} (\nabla \cdot v^\infty)_\Omega] \vec{\nu} \quad \text{on} \quad \Gamma. \tag{4.86}$$

Then we see that a solution to the variational problem (S_1), using the regularity result and the computations above, is a solution to (T_1), where the continuity condition comes from the fact that v^∞ is in $H^1(\Theta)^2$ and is then continuous across any hypersurface of Θ. ■

This section was dedicated to the rigorous derivation of the transmission problem in the single-species case. Similar computations can be made for the two-species case by adapting the choice of the test function $\tilde{\phi}_n$ to be localized on the interface between the two tissues and on their outer

boundaries.

4.8.3 A formal transmission problem for the general two species case

We now present the transmission problem one can obtain formally for the stationary L-ESVM, when Θ, Ω_1, Ω_2 are chosen as in (4.34)–(4.37). Contrarily to the simplified framework of section 4.3.2 and section 4.5, where q is considered given, q is here a stationary solution of (4.32)-(4.33). We can rewrite these equations as in (4.58) in Ω_1 and (4.59) in Ω_2. Then, supposing that q is smooth enough inside each subdomain Ω_1 and Ω_2, the limiting model defined by the equations (4.23)-(4.33) is equivalent at equilibrium to the following transmission problem (T_2^*) considered on Θ, and coupled with Dirichlet boundary conditions on $\partial\Theta$,

$$(T^*_{2,\Omega_1})\begin{cases} -\beta_1\Delta v_1 + v_1 - \frac{1}{g_1}\nabla\nabla\cdot v_1 = 0 & \text{in } \Omega_1,\\ -\beta_2\Delta v_2 + v_2 - \frac{1}{g_1}\nabla\nabla\cdot v_1 = -\nabla q & \text{in } \Omega_1,\\ \nabla\cdot(\log(q+1)v_2) = g_2\log(q+1)[p_2^* - (p_1^* - \frac{1}{g_1}\nabla\cdot v_1 + q)] & \text{in } \Omega_1. \end{cases}$$

$$(T^*_{2,\Omega_2})\begin{cases} -\beta_1\Delta v_1 + v_1 - \frac{1}{g_2}\nabla\nabla\cdot v_2 = -\nabla q & \text{in } \Omega_2,\\ -\beta_2\Delta v_2 + v_2 - \frac{1}{g_2}\nabla\nabla\cdot v_2 = 0 & \text{in } \Omega_2,\\ \nabla\cdot(\log(q+1)v_1) = g_1\log(q+1)[p_1^* - (p_2^* - \frac{1}{g_2}\nabla\cdot v_2 + q)] & \text{in } \Omega_2. \end{cases}$$

$$(T^*_{2,\Omega^c})\begin{cases} -\beta_1\Delta v_1 + v_1 = 0 \quad \text{in } \Omega^c,\\ -\beta_2\Delta v_2 + v_2 = 0 \quad \text{in } \Omega^c. \end{cases}$$

$$(T^*_{2,\Gamma_1})\begin{cases} \beta_1[(\nabla v_1)_{\Omega_1} - (\nabla v_1)_{\Omega^c}]\cdot\vec{\nu} = [p_1^* - \frac{1}{g_1}(\nabla\cdot v_1)_{\Omega_1}]\vec{\nu} & \text{on } \Gamma_1,\\ \beta_2[(\nabla v_2)_{\Omega_1} - (\nabla v_2)_{\Omega^c}]\cdot\vec{\nu} = [p_1^* + (q)_{\Omega_1} - \frac{1}{g_1}(\nabla\cdot v_1)_{\Omega_1}]\vec{\nu} & \text{on } \Gamma_1,\\ (v_1)_{\Omega_1} = (v_1)_{\Omega^c}, \quad (v_2)_{\Omega_1} = (v_2)_{\Omega^c}, \quad (v_2 q)_{\Omega_1}\cdot\vec{\nu} = 0 & \text{on } \Gamma_1. \end{cases}$$

$$(T^*_{2,\Gamma_2})\begin{cases} \beta_1[(\nabla v_1)_{\Omega_2} - (\nabla v_1)_{\Omega^c}]\cdot\vec{\nu} = [p_2^* + (q)_{\Omega_2} - \frac{1}{g_2}(\nabla\cdot v_2)_{\Omega_2}]\vec{\nu} & \text{on } \Gamma_2,\\ \beta_2[(\nabla v_2)_{\Omega_2} - (\nabla v_2)_{\Omega^c}]\cdot\vec{\nu} = [p_2^* - \frac{1}{g_2}(\nabla\cdot v_2)_{\Omega_2}]\vec{\nu} & \text{on } \Gamma_2,\\ (v_1)_{\Omega_2} = (v_1)_{\Omega^c}, \quad (v_2)_{\Omega_2} = (v_2)_{\Omega^c}, \quad (v_1 q)_{\Omega_2}\cdot\vec{\nu} = 0 & \text{on } \Gamma_2. \end{cases}$$

$$(T^*_{2,\Gamma})\begin{cases} \beta_1[(\nabla v_1)_{\Omega_1} - (\nabla v_1)_{\Omega_2}]\cdot\vec{\nu} = [(p_1^* - p_2^*) - (q)_{\Omega_2} + \frac{1}{g_2}(\nabla\cdot v_2)_{\Omega_2} - \frac{1}{g_1}(\nabla\cdot v_1)_{\Omega_1}]\vec{\nu} & \text{on } \Gamma,\\ \beta_2[(\nabla v_2)_{\Omega_1} - (\nabla v_2)_{\Omega_2}]\cdot\vec{\nu} = [(p_1^* - p_2^*) + (q)_{\Omega_1} + \frac{1}{g_2}(\nabla\cdot v_2)_{\Omega_2} - \frac{1}{g_1}(\nabla\cdot v_1)_{\Omega_1}]\vec{\nu} & \text{on } \Gamma,\\ (v_1)_{\Omega_1} = (v_1)_{\Omega_2}, \quad (v_2)_{\Omega_1} = (v_2)_{\Omega_2}, \quad v_1\cdot\vec{\nu} = v_2\cdot\vec{\nu}, \quad (q)_{\Omega_1} = (q)_{\Omega_2} & \text{on } \Gamma. \end{cases}$$

This transmission problem gives us some insight on the behaviour of the system. It shows on the one hand that q does not have a jump on $\Gamma_1, \Gamma_2, \Gamma$, unlike the pressure p. On the other hand we can observe that the jumps of the gradients of the velocities of the two species at the interface Γ are not equal in general.

4.8.4 Complementary numerical simulations

4.8.5 Segregation in the ESVM for initially mixed densities

In this section we exhibit the role of the repulsion pressure in the ESVM in segregating initially mixed densities. We consider initially two mixed densities n_1 and n_2 with $n_1^{ini}(x) = 0.7\chi_{\{X\in\mathbb{R}^2;\|X\|\leq 0.3\}}$, and $n_2^{ini}(x) = 0.2\chi_{\{X=(x,y)\in\mathbb{R}^2;(x-0.4)^2+y^2\leq 0.3\}}$, with χ the indicator function, see Figure 4.6a. We use the following parameters $m = 30, \alpha = 0.001, \epsilon = 0.1$, and choose the growth functions and viscosities as in (4.20). At initial time, the densities share a mixing region n_1n_2 represented in Figure 4.6c. At $t = 0.1$ we observe the segregation of the densities n_1 and n_2, see Figure 4.6b. In Figure 4.6d, we represent the mixing region between the densities at $t = 0.1$ and notice that the maximum of n_1n_2 is largely reduced compared to $n_1^{ini}n_2^{ini}$.

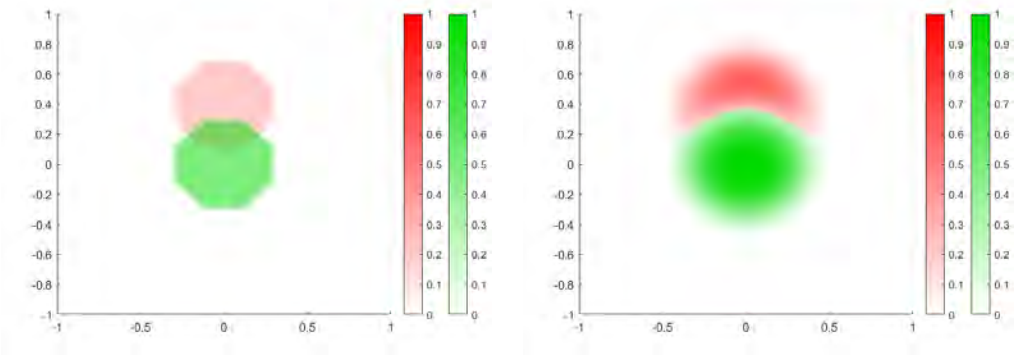

(a) Initial conditions of n_1 and n_2.

(b) The densities n_1 and n_2 at $t = 0.1$.

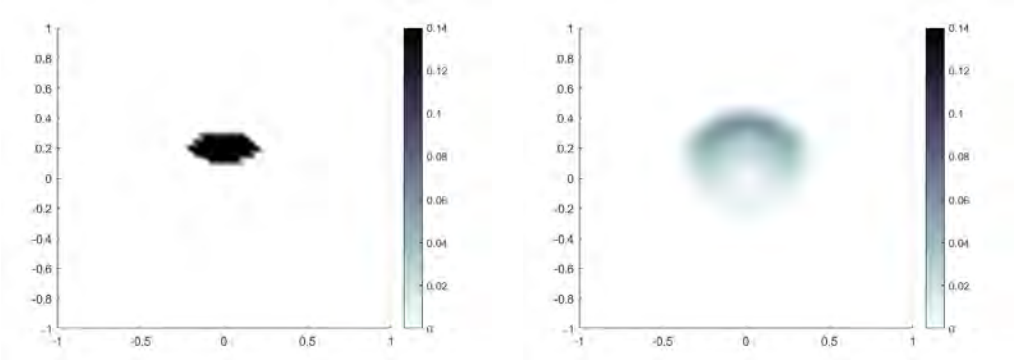

(c) The mixing region n_1n_2 between the densities at initial time.

(d) The mixing region n_1n_2 between the densities at $t = 0.1$.

Figure 4.6 – Segregation of two initially mixed population densities in the ESVM. The top panels represent the densities n_1 and n_2 respectively at time $t = 0$ in Panel (a) and $t = 0.1$ in Panel (b). The bottom panels represent the mixing region n_1n_2 respectively at $t = 0$ in Panel (c) and $t = 0.1$ in Panel (d).

These simulations highlight the role of the repulsion pressure in segregating the densities in

finite time. This segregation is not perfect as some mixing still appears at the interface between the densities. At the incompressible limit we recover full segregation as proven in Section 4.4.

4.8.6 Effects of ϵ, α, and m on the solution of the ESVM

In this section we investigate the role of each of the parameters ϵ, α, and m on the solution of the ESVM in the case of the vertebrate embryo. In Figure 4.7, we represent the densities n_1 and n_2 in the left panels and the mixing region (the product $n_1 n_2$) in the right panels for different sets of parameters (m, α, ϵ) in the ESVM, at final time $t = 0.1$.
In Figures 4.7a-4.7b the ESVM is simulated with the parameters $(m, \alpha, \epsilon) = (30, 0.001, 0.1)$, similar to those used in section 4.2.3. In Figure 4.7b, we notice the very thin region of mixing at the interface between the densities.
In Figures 4.7c-4.7d we change the value of the repulsion parameter to $m = 10$ (with α and ϵ unchanged). We notice that the densities' shapes are affected and the density overlap is more significant. Decreasing the parameter m then results in a concentrated mixing around the interface.
When changing the parameter α as in Figures 4.7e-4.7f where we set it to $\alpha = 0.01$, the width of the mixing region increases significantly compared to 4.7b. This shows that large values of α result in the mixing of the densities on a larger region. Changing α also appears to affect the shape of the densities, with the PSM (density in red) enveloping posteriorly the NT (green species) compared to Figure 4.7a. We note here that our choice of the parameter α is sufficient to maintain the stability of the system ESVM. We refer the reader to [39] where authors exhibit in dimension 1 (and with Darcy's law for the velocities) the role of small values of α in creating instabilities with the appearance of alternating population densities.
Finally, we change the parameter ϵ and set it to 1 in Figures 4.7g-4.7h. The mixing between the densities is qualitatively not affected. The densities n_1 and n_2 reach a maximum of around 0.87 (lighter colors on the colorbar) compared to the other simulations where $\epsilon = 0.1$ and the maximum is reached at around 0.98. A smaller ϵ increases the densities which become closer to the maximal density 1 as per our choice of pressure law (4.4). This observation exhibits the role of the parameter ϵ in controlling the congestion of the densities.
We note here that α and m cannot independently tend to their respective asymptotic limits as they are both involved in the segregation of the densities. In fact, α cannot be taken too small when m is large as it balances the instability of the system ESVM caused by the segregation pressure.
Overall, the observed effects of ϵ, α and m on the ESVM in this preliminary parameter study are aligned with those observed in [39].

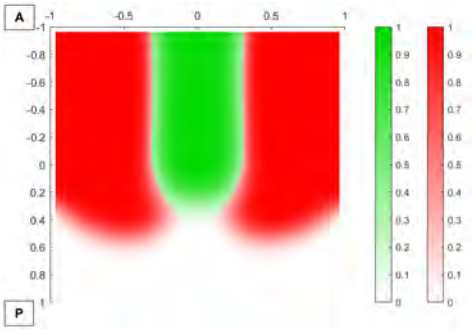

(a) The densities n_1, n_2 with $(m, \alpha, \epsilon) = (30, 0.001, 0.1)$ at $t = 0.1$.

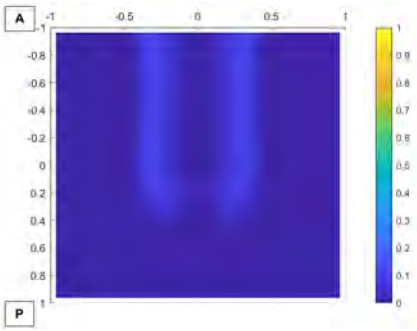

(b) The mixing region $n_1 n_2$ with $(m, \alpha, \epsilon) = (30, 0.001, 0.1)$ at $t = 0.1$.

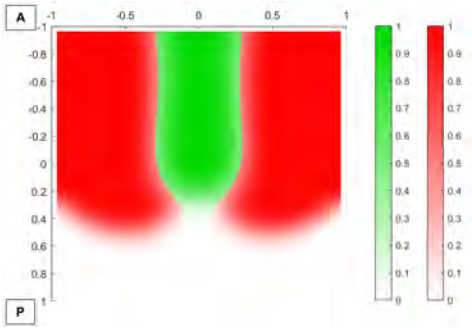

(c) Variation of m: the densities n_1, n_2 with $(m, \alpha, \epsilon) = (10, 0.001, 0.1)$ at $t = 0.1$.

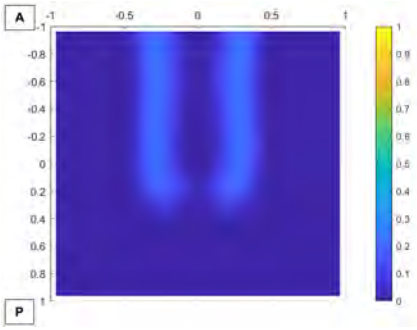

(d) Variation of m: the mixing region $n_1 n_2$ with $(m, \alpha, \epsilon) = (10, 0.001, 0.1)$ at $t = 0.1$.

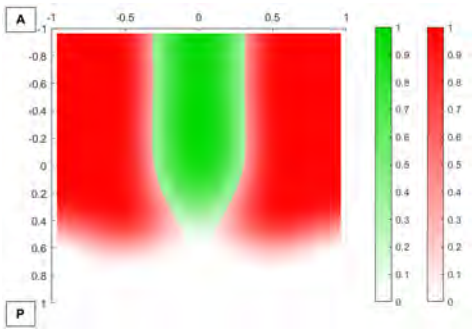

(e) Variation of α: the densities n_1, n_2 with $(m, \alpha, \epsilon) = (30, 0.01, 0.1)$ at final time $t = 0.1$.

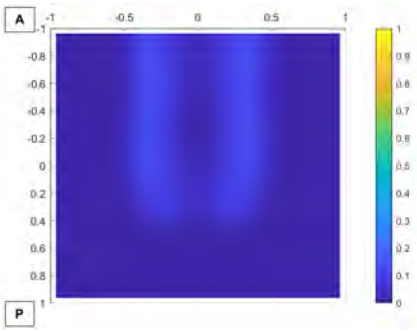

(f) Variation of α: the mixing region $n_1 n_2$ with $(m, \alpha, \epsilon) = (30, 0.01, 0.1)$ at $t = 0.1$.

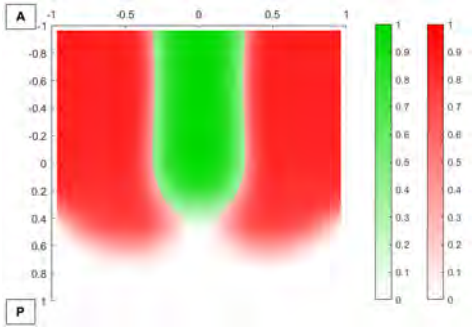

(g) Variation of ϵ: the densities n_1, n_2 with $(m, \alpha, \epsilon) = (30, 0.001, 1)$ at $t = 0.1$.

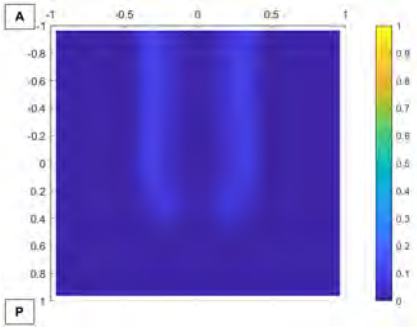

(h) Variation of ϵ: the mixing region $n_1 n_2$ with $(m, \alpha, \epsilon) = (30, 0.001, 1)$ at $t = 0.1$.

Figure 4.7 – The left panels illustrate the densities n_1 (in green) and n_2 (in red) and the right panels illustrate the mixing region $n_1 n_2$ at $t = 0.1$ in the ESVM with different sets of parameters (m, α, ϵ).

4.8.7 Segregation in the VM and in the L-VM

In this section we support our conjecture in Remark 4.3.10 by exhibiting numerical simulations of the VM with $\epsilon = 1$, and the VM in asymptotic regime with $\epsilon = 0.1$ in dimension 1 for clarity. The densities are initially segregated with ${n_1}^{ini}(x) = 0.8\chi_{[0.3;1]}(x)$ (in green) and ${n_2}^{ini}(x) = 0.8\chi_{[-1;-0.3]}(x)$ (in red) and the viscosities are taken as $(\beta_1, \beta_2) = (3, 1)$. In Figures 4.8a and 4.8c we show the initial data n_1, n_2, p_ϵ respectively in the VM with $\epsilon = 1$ and in the VM with $\epsilon = 0.1$. At $t = 10$, the green and red densities appear to maintain their segregation throughout their evolution in the case $\epsilon = 1$, see Figure 4.8b, and $\epsilon = 0.1$, see Figure 4.8d. The pressure p_ϵ in orange is continuous (Figures 4.8b-4.8d) as expected as it is a function of the total density $n = n_1 + n_2$, but its gradient exhibits sharp discontinuities at the interface.
To sum up, these simulations are strongly in favor of our conjecture (Remark 4.3.10) that the VM and the L-VM propagate segregation from initial data.

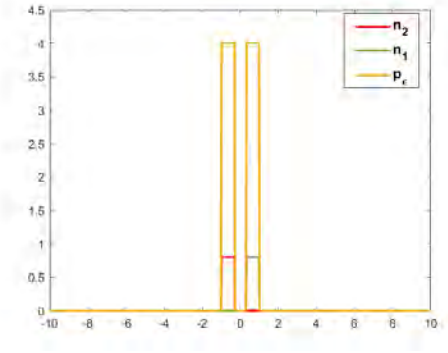

(a) Initial conditions of the densities n_1 and n_2 and the pressure p_ϵ in the VM with $\epsilon = 1$.

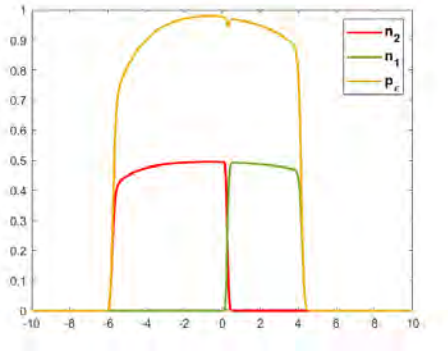

(b) The densities n_1 and n_2 and the pressure p_ϵ at $t = 10$, with $\epsilon = 1$.

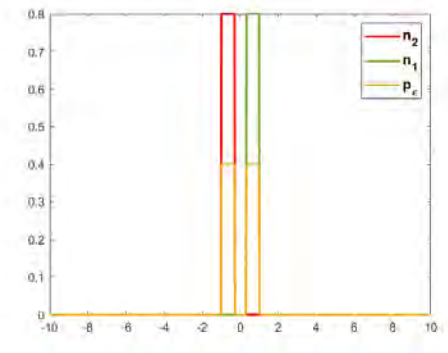

(c) Initial conditions of the densities n_1 and n_2 and the pressure p_ϵ in the VM with $\epsilon = 0.1$.

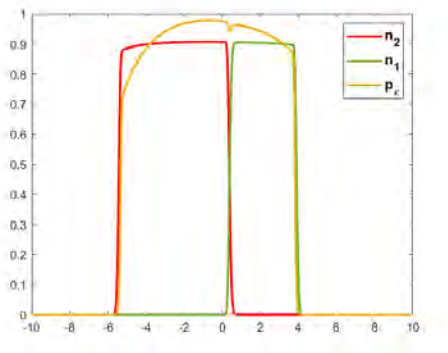

(d) The densities n_1 and n_2 and the pressure p_ϵ at $t = 10$, with $\epsilon = 0.1$.

Figure 4.8 – Left: initial conditions for the densities n_1, n_2 and the pressure p_ϵ in the VM for $\epsilon = 1$ (top) and $\epsilon = 0.1$ (bottom). Right: the densities and the pressure at $t = 10$ in the VM for $\epsilon = 1$ (top) and $\epsilon = 0.1$ (bottom).

4.8.8 Numerical scheme for the L-VM

The numerical simulations of the L-VM are performed in Freefem++ [84] using a finite element scheme. The densities are initialized as indicator functions,

$$n_1{}^{ini}(x) = \chi_{\Omega_1^{ini}}(x) \quad \text{and} \quad n_2{}^{ini}(x) = \chi_{\Omega_2^{ini}}(x),$$

with $\Omega_1^{ini} = [-1/3; 1/3] \times [-1; 0]$ and $\Omega_2^{ini} = ([-1; -1/3] \cup [1/3; 1]) \times [-1; 0]$. We consider solutions under the form of an indicator function and therefore:

$$n_1(x,t) = \chi_{\Omega_1(t)}(x) \quad \text{and} \quad n_2(x,t) = \chi_{\Omega_2(t)}(x).$$

The growth functions are considered linear as in (4.39). At the initialization a triangular mesh is generated by Freefem++. At each time step the velocity is computed according to the variational formulation of (4.47)-(4.48), combined with the complementary relation (4.50). Thus for all $(\phi_1, \phi_2) \in \mathcal{C}_c^\infty(\Theta)$ we have,

$$\beta_1 \int_\Theta \nabla v_1^\infty : \nabla \phi_1 + \int_\Theta v_1^\infty \cdot \phi_1 = \int_{\Omega_1(t)} (p_1^* - \frac{1}{g_1} \nabla \cdot v_1^\infty)\ \nabla \cdot \phi_1 + \int_{\Omega_2(t)} (p_2^* - \frac{1}{g_2} \nabla \cdot v_2^\infty)\ \nabla \cdot \phi_1,$$

$$\beta_2 \int_\Theta \nabla v_2^\infty : \nabla \phi_2 + \int_\Theta v_2^\infty \cdot \phi_2 = \int_{\Omega_1(t)} (p_1^* - \frac{1}{g_1} \nabla \cdot v_1^\infty)\ \nabla \cdot \phi_2 + \int_{\Omega_2(t)} (p_2^* - \frac{1}{g_2} \nabla \cdot v_2^\infty)\ \nabla \cdot \phi_2.$$

The solutions of this system with Dirichlet boundary conditions are easily computed in Freefem++ using piecewise constant discontinuous finite element ($P0$ element). We then compute the new domains Ω_1 and Ω_2 by moving the mesh with the new velocities. Note that the movement of the mesh needs to be carefully performed to ensure triangles are not flipping over.

4.8.9 Complementary notes on the derivation of the transmission problem for the single species case

We now make explicit the construction of the sequence $(\chi_n)_n$ satisfying (4.80)–(4.82).

Construction of χ_n. We construct a smooth sequence of functions $(\chi_n)_n$ around the interface. To do so we first introduce B_n defined as,

$$B_n := \left\{ Y \in \Theta \mid d(Y, \Gamma) \leq \frac{1}{n} \right\}. \tag{4.87}$$

Then we construct χ_n as a smooth approximation of χ_{B_n} where χ_{B_n} is the indicator function of B_n (defined on $\mathbb{R}^2$), as follows,

$$\chi_n = \chi_{B_n} * \Psi_n, \tag{4.88}$$

where $(\Psi_n)_{n\geq 1}$ a sequence of mollifiers on $\mathbb{R}^2$ defined as,

$$\Psi_n \coloneqq \frac{K_n}{\|K_n\|_1}, \text{ and } K_n(X) \coloneqq n^2 K(nX), \tag{4.89}$$

with

$$K(X) = \begin{cases} \exp\left(\frac{1}{\|X\|^2-1}\right) & \|X\| < 1,\ X \in \mathbb{R}^2, \\ \\ 0 & \text{otherwise.} \end{cases}$$

This mollifier is endowed with the following properties,

$$\Psi_n \in C_c^\infty\left(\mathbb{R}^2\right), \quad \text{supp}\Psi_n \subset \overline{\mathrm{B}\left(0, \frac{1}{n}\right)}, \quad \int \Psi_n = 1, \quad \Psi_n \geq 0 \text{ on } \mathbb{R}^2,$$

so that by convolution the fact that the support of χ_n is included in Θ for n large enough ($n \geq 2d(\Gamma, \partial\Theta)^{-1}$), and the regularity in (4.80) are easily verified.

Proof of property (4.81). To prove (4.81) we first see that,

$$\|\chi_{B_n}\|_p^p = meas\left(B_n\right). \tag{4.90}$$

Moreover, using the compactness of Γ, we can construct a finite number N of points such that $N \leq \ell(\Gamma)n + 1$, with $\ell(\Gamma)$ the length of the unidimensional curve Γ, and such that two successive points X_i and X_{i+1} ($i \in \{1, \ldots, N-1\}$) are spaced across Γ by a curve length of at most $\frac{1}{n}$. Then the following holds,

$$B_n = \bigcup_{X\in\Gamma} \overline{B\left(X, \frac{1}{n}\right)} \cap \Theta \subset \bigcup_{i=1}^{i=N} B\left(X_i, \frac{2}{n}\right) \cap \Theta.$$

Then for $p \in [1, \infty)$ we can compute,

$$\begin{aligned} \|\chi_n\|_p^p &\leq \|\chi_{B_n}\|_p^p \|\Psi_n\|_1^p \\ &\leq meas\left(\bigcup_{i=1}^{i=N} B(X_i, \frac{2}{n}) \cap \Theta\right) \\ &\leq \sum_{i=1}^{i=N} meas\left(B(X_i, \frac{2}{n}) \cap \Theta\right) \\ &\leq N 4\pi \frac{1}{n^2} \\ &\leq 4\pi(n+1)\frac{\ell(\Gamma)}{n^2} \xrightarrow[n\to+\infty]{} 0, \end{aligned}$$

and this concludes the proof of (4.81).

Proof of property (4.82). We first define $\Gamma_n^c \coloneqq \partial B_n \cap \Omega^c$ and $\Gamma_n \coloneqq \partial B_n \cap \Omega$, we can write,

$$\Gamma_n^c = \{x \in \Omega^c \,|\, d(x,\Gamma) = \frac{1}{n}\} \quad \text{and} \quad \Gamma_n = \{x \in \Omega \,|\, d(x,\Gamma) = \frac{1}{n}\}. \tag{4.91}$$

Now using the C^2 regularity of the boundary, and taking n large enough, we can describe those two boundaries as,

$$\Gamma_n^c = \{x + \frac{1}{n}\vec{\nu}(x)\,;\, x \in \Gamma\} \text{ and } \Gamma_n = \{x - \frac{1}{n}\vec{\nu}(x)\,;\, x \in \Gamma\}, \text{ with } x \in \Gamma \mapsto x - \frac{1}{n}\vec{\nu}(x) \in \Gamma_n \text{ injective,} \tag{4.92}$$

and $\vec{\nu}$ is the normal vector to the interface Γ pointing from Ω to Ω^c. The relations in (4.92) are proved at the end of this section.

To show the equality in (4.82) we use the fact that χ_n is a convolution. Then we have for all $x \in \Theta$,

$$\begin{aligned}
\nabla\chi_n(x) &= \int_{\mathbb{R}^2} \nabla\psi_n(x-y)\chi_{B_n}(y)dy \\
&= \int_{B_n} \nabla\psi_n(x-y)dy \\
&= -\int_{\Gamma_n} \psi_n(x-s)\vec{\nu_n}(s)d\sigma_n(s) + \int_{\Gamma_n^c} \psi_n(x-s)\vec{\nu_n}(s)d\sigma_n(s),
\end{aligned}$$

where we call $\sigma_n(s)$ the Lebesgue measure on Γ_n, and $\vec{\nu_n}$ the normal vector to Γ_n.

Then we can write for all $x \in \Theta$,

$$\begin{aligned}
\int_\Theta w\cdot\nabla\chi_n(x)dx &= -\int_\Theta w(x)\cdot\int_{\Gamma_n}\psi_n(x-s)\vec{\nu_n}(s)d\sigma_n(s)dx \\
&\quad + \int_\Theta w(x)\cdot\int_{\Gamma_n^c}\psi_n(x-s)\vec{\nu_n}(s)d\sigma_n(s)dx \\
&= -\int_{\Gamma_n}\int_\Theta w(x)\cdot\frac{n^2}{\|K\|_{L^1}}K(n(x-s))\vec{\nu_n}(s)dxd\sigma_n(s) \\
&\quad + \int_{\Gamma_n^c}\int_\Theta w(x)\cdot\frac{n^2}{\|K\|_{L^1}}K(n(x-s))\vec{\nu_n}(s)dxd\sigma_n(s) \\
&\overset{z:=n(x-s)}{=} -\int_{\Gamma_n}\int_\Theta w\left(\frac{z}{n}+s\right)\cdot\frac{K(z)}{\|K\|_{L^1}}\vec{\nu_n}(s)dzd\sigma_n(s) \\
&\quad + \int_{\Gamma_n^c}\int_\Theta w\left(\frac{z}{n}+s\right)\cdot\frac{K(z)}{\|K\|_{L^1}}\vec{\nu_n}(s)dzd\sigma_n(s) \\
&= -\int_\Theta\left(\int_{\Gamma_n} w\left(\frac{z}{n}+s\right)\cdot\vec{\nu_n}(s)d\sigma_n(s)\right)\frac{K(z)}{\|K\|_{L^1}}dz \\
&\quad + \int_\Theta\left(\int_{\Gamma_n^c} w\left(\frac{z}{n}+s\right)\cdot\vec{\nu_n}(s)d\sigma_n(s)\right)\frac{K(z)}{\|K\|_{L^1}}dz.
\end{aligned} \tag{4.93}$$

Using (4.92) we can consider the following change of variables,

$$s' \in \Gamma \mapsto s' - \frac{1}{n}\vec{\nu}(s') \in \Gamma_n.$$

with $\vec{\nu}$ the normal vector to Γ. As $\Gamma \in C^2$, it is locally the graph of a C^2 function $U : [s_1 - R, s_1 + R] \to \mathbb{R}$, $R > 0$. Then for $s' \in \Gamma$ we can write,

$$s' = (s_1, U(s_1)), \quad \vec{\nu}(s') = \frac{(U'(s_1), -1)}{\sqrt{1 + U'^2}}.$$

We call γ the application,

$$\gamma : [s_1 - R, s_1 + R] \longrightarrow \Gamma, \quad k \mapsto \gamma(k) = (k, U(k)). \tag{4.94}$$

Thus we can define the application γ_n as,

$$\gamma_n : [s_1 - R, s_1 + R] \longrightarrow \Gamma_n, \quad k \mapsto \gamma(k) - \frac{1}{n}\vec{\nu}(\gamma(k)) = \left(k - \frac{1}{n}\vec{\nu}_1(\gamma(k)), U(k) - \frac{1}{n}\vec{\nu}_2(\gamma(k))\right) \tag{4.95}$$

Then for any function f that is continuous on Γ_n we have,

$$\begin{aligned}
\int_{\Gamma_n} f(s)ds &= \int_{s_1-R}^{s_1+R} f(\gamma_n(k))|\gamma_n'(k)|dk \\
&= \int_{s_1-R}^{s_1+R} f\left(\gamma(k) - \frac{1}{n}\vec{\nu}(\gamma(k))\right)|\gamma'(k) - \frac{1}{n}\vec{\nu}'(k)|dk \\
&= \int_{\Gamma} f\left(s' - \frac{1}{n}\vec{\nu}(s')\right)\frac{|\gamma'\circ\gamma^{-1}(s') - \frac{1}{n}\vec{\nu}'\left(\gamma'\circ\gamma^{-1}(s')\right)|}{|\gamma'\circ\gamma^{-1}(s')|}ds'.
\end{aligned} \tag{4.96}$$

Having the following,

$$\vec{\nu}' = \left(U''\left(1+U'^2\right)^{-1/2}\left(1 - U'\left(1+U'^2\right)^{-1}\right), U'U''\left(1+U'^2\right)^{-3/2}\right), \quad \gamma' = \left(1, U'\right),$$

we can compute the Jacobian appearing in (4.96) in terms of the function U which yields,

$$\begin{aligned}
J(s') &:= \frac{|\gamma'\circ\gamma^{-1}(s')\left(Id - \frac{1}{n}\vec{\nu}'\right)|}{|\gamma'\circ\gamma^{-1}(s')|} \\
&= \frac{1}{(1+U'^2)^{1/2}}\left[\left(1 - \frac{1}{n}\left(U''\left(1+U'^2\right)^{-1/2}\left(1 - U'\left(1+U'^2\right)^{-1}\right)\right)\right)^2\right. \\
&\quad \left. + \left(U' - \frac{1}{n}\left(U'U''\left(1+U'^2\right)^{-3/2}\right)\right)^2\right]^{1/2}.
\end{aligned} \tag{4.97}$$

Going back to (4.93) and doing the change of variables described in (4.96) we obtain,

$$\int_{\Gamma_n} w\left(\frac{z}{n}+s\right)\cdot\vec{\nu_n}(s)d\sigma_n(s)=\int_{\Gamma} w\left(\frac{z}{n}+s'-\frac{1}{n}\vec{\nu}(s')\right)\cdot\vec{\nu_n}\left(s'-\frac{1}{n}\vec{\nu}(s')\right)\,J(s')\,d\sigma(s'), \quad (4.98)$$

where $d\sigma(s')$ is the Lebesgue measure on Γ. From the expression of the Jacobian (4.97) we see that,

$$J(s') \xrightarrow[n\to+\infty]{} \frac{\sqrt{1+U'^2}}{\sqrt{1+U'^2}}=1. \quad (4.99)$$

And we have the following bound for (4.98),

$$\left|w\left(\frac{z}{n}+s'-\frac{1}{n}\vec{\nu}(s')\right)\cdot\vec{\nu_n}\left(s'-\frac{1}{n}\vec{\nu}(s')\right)\,J(s')\right|\leq\|wJ\|_\infty\in L^1(\Omega),$$

with $\|J\|_\infty<+\infty$ as $U\in C^2$.
Furthermore, we have the pointwise convergence of the normal vectors, i.e,

$$\vec{\nu_n}\left(s'-\frac{1}{n}\vec{\nu}(s')\right)\xrightarrow[n\to+\infty]{}\vec{\nu}(s'),\ \forall s'\in\Gamma. \quad (4.100)$$

Indeed, let γ and γ_n be respectively as (4.94) and (4.95). Then we can write the unitary normal vector on Γ as,

$$\vec{\nu}(\gamma(k))=\mathcal{R}_{\frac{\pi}{2}}\frac{\gamma'(k)}{\|\gamma'(k)\|}=\frac{(U'(k),-1)}{\|\gamma'(k)\|}, \quad (4.101)$$

and the unitary normal vector on Γ_n as,

$$\vec{\nu}(\gamma_n(k))=\mathcal{R}_{\frac{\pi}{2}}\frac{\gamma_n'(k)}{\|\gamma_n'(k)\|}=\frac{\left(U'(k)-\frac{1}{n}\vec{\nu}_1'(\gamma(k)),-1+\frac{1}{n}\vec{\nu}_2'(\gamma(k))\right)}{\|\gamma_n'(k)\|}. \quad (4.102)$$

Then it suffices to prove that $\gamma_n'(k)\xrightarrow[n\to+\infty]{}\gamma'(k)$, for every k, and as the application $x\mapsto\frac{x}{\|x\|}$ is continuous, we obtain the desired convergence of the normal vectors.
Then we compute for every k,

$$\begin{aligned}\gamma_n'(k)-\gamma'(k) &= -\frac{1}{n}\partial_k\left(\vec{\nu}\left(\gamma\left(k\right)\right)\right)\\ &\overset{\text{From (4.101)}}{=} -\frac{1}{n}\mathcal{R}_{\frac{\pi}{2}}\partial_k\left(\frac{\gamma'(k)}{\|\gamma'(k)\|}\right)\\ &= -\frac{1}{n}\mathcal{R}_{\frac{\pi}{2}}\frac{\gamma''(k)\|\gamma'(k)\|^2-\gamma''(k)\cdot\gamma'(k)\gamma'(k)}{\|\gamma'(k)\|^3}, \quad (4.103)\end{aligned}$$

Finally, as $\gamma \in C^2$, all the quantities in (4.103) are bounded, it follows that,

$$\begin{aligned} \|\gamma_n'(k) - \gamma'(k)\| \quad &\leq \quad \frac{1}{n}K \\ &\xrightarrow[n\to+\infty]{} \quad 0 \end{aligned} \tag{4.104}$$

with $K > 0$ constant. And this concludes the proof of the convergence of the normal vectors.

Then by the dominated convergence theorem the first integral in (4.93) gives,

$$\begin{aligned} -\int_\Theta \left(\int_\Gamma w(\frac{z}{n} + s' - \frac{1}{n}\vec{\nu}(s')) \cdot \vec{\nu_n}(s' - \frac{1}{n}\vec{\nu}(s'))\, J(s')\, d\sigma(s') \right) \frac{K(z)}{\|K\|_{L^1}} dz \\ \xrightarrow[n\to+\infty]{} -\int_\Gamma \big(w(s')\big)_\Omega \cdot \vec{\nu}(s') ds'. \end{aligned} \tag{4.105}$$

Doing the same computations for the second integral in (4.93), we obtain the desired result in (4.82).

We end this section with the proof of (4.92).

Proof of property (4.92). We prove the second equality in (4.92), the first one follows from the same computations.

We start by defining a constant $r^* > 0$ which will be useful in the computations that follow.

We have $\Gamma \in C^2$ then for each point $Y^* \in \Gamma$, it is locally the graph of a C^2 function $U : (y^* - R, y^* + R) \to \mathbb{R}$, with $R > 0$ such that,

$$Y^* = (y^*, U(y^*)), \quad \vec{\nu}(Y^*) = \frac{(U'(y^*), -1)}{\sqrt{1 + U'(y^*)^2}}, \tag{4.106}$$

with $\vec{\nu}(Y^*)$ the normal vector to Γ at the point Y^*. Then the curvature C of Γ at the point $Y^* \in \Gamma$ can be expressed as $C(Y^*) = \dfrac{U''(y^*)}{(1 + U'(y^*)^2)^{3/2}}$. We define r^* as,

$$r^* := \min\left(\frac{1}{2\gamma}, \frac{1}{2\|\nabla\vec{\nu}\|_\infty} \right), \tag{4.107}$$

with $\gamma = \max_h C$ the maximal curvature of Γ, and h is any C^2 parametrization of Γ.

Let,

$$n > \frac{1}{r^*}. \tag{4.108}$$

Let $X^* \in \Gamma_n$, then from (4.91), and using the compactness of Γ, there exists $Y^* \in \Gamma$ such that,

$$d(X^*, \Gamma) = \|X^* - Y^*\| = \frac{1}{n}. \tag{4.109}$$

We recall that as $\Gamma \in C^2$, (4.106) holds for $Y^* \in \Gamma$. We introduce the C^1 function,

$$F : (y^* - R, y^* + R) \to \mathbb{R}, \quad y \mapsto F(y) \coloneqq \|X^* - (y, U(y))\|^2.$$

By (4.109), we see that F reaches a local minimum in y^*, so that,

$$F'(y^*) = 2(Y^* - X^*) \cdot (1, U'(y^*)) = 0. \tag{4.110}$$

Using the expression of $\vec{\nu}$ in (4.106), we therefore have,

$$X^* - Y^* = \lambda \vec{\nu}(Y^*), \tag{4.111}$$

with $\lambda = -\sqrt{1 + U'(y^*)^2}\,(\tilde{x} - U(y^*))$, where $X^* = (x^*, \tilde{x})$.
We then compute,

$$\begin{aligned} \frac{1}{n^2} &= \|X^* - Y^*\|^2 \\ &= (x^* - y^*)^2 + (\tilde{x} - U(y^*))^2 \\ &\overset{\text{From (4.110)}}{=} U'(y^*)^2\,(\tilde{x} - U(y^*))^2 + (\tilde{x} - U(y^*))^2 \\ &= (U(y^*) - \tilde{x})^2\left(1 + U'(y^*)^2\right) \\ &= \lambda^2. \end{aligned} \tag{4.112}$$

Since $X^* \in \Gamma_n \subset \Omega$, we have that $\lambda < 0$, and finally,

$$\lambda = -\frac{1}{n}. \tag{4.113}$$

We now prove that, for n verifying (4.108), Y^* is unique. Assume there exists $Z^* \in \Gamma$ verifying,

$$X^* = Z^* - \frac{1}{n}\vec{\nu}(Z^*),$$

then we have under (4.108),

$$\|Y^* - Z^*\| = \frac{1}{n}\|\vec{\nu}(Y^*) - \vec{\nu}(Z^*)\| \leq \frac{1}{n}\|\nabla \nu\|_\infty \|Y^* - Z^*\| \leq \frac{1}{2}\|Y^* - Z^*\|. \tag{4.114}$$

This gives $Y^* = Z^*$, and with (4.111) it concludes the proof which yields the first inclusion,

$$\Gamma_n \subset \{x - \frac{1}{n}\vec{\nu}(x)\,;\, x \in \Gamma\}. \tag{4.115}$$

Conversely, consider $Y^* \in \Gamma$ such that,

$$Y^* - \frac{1}{n}\vec{\nu}(Y^*) = X^*.$$

We show that $X^* \in \Gamma_n$. As $\Gamma \in C^2$, the domain Ω satisfies the uniform two-sided ball condition, that is, it satisfies the uniform interior and exterior ball condition. The uniform interior ball condition states that there exists $r > 0$ such that for all $Y^* \in \Gamma$, there exists $Y \in \Omega$ such that,

$$B(Y, r) \cap \Omega = \emptyset, \quad \Gamma \cap \partial B(Y, r) = Y^* \in \Gamma. \tag{4.116}$$

Then $B(Y, r)$ is tangent to the tangent plane of Γ in Y^*, thus, $Y \in \{Y^* + t\nu;\, t \in \mathbb{R}\}$.
Note that Ω satisfies a uniform exterior ball condition if $\Theta \backslash \Omega$ satisfies the uniform interior ball condition.
In our case, as $Y^* \in \Gamma$, we denote by $B^+_{Y^*}(Y, r^*)$ the interior ball at Y^* with radius r^* as in (4.107) and center Y as in (4.116). Then we have $\Gamma \cap \partial B^+_{Y^*}(Y, r^*) = Y^* \in \Gamma$, and $Y \in \{Y^* + t\nu;\, t \in \mathbb{R}\}$. Thus, having assumed (4.108), and as $Y^* - \frac{1}{n}\vec{\nu}(Y^*) \in \{Y^* + t\nu;\, t \in \mathbb{R}\}$, it follows that,

$$B\left(Y^* - \frac{1}{n}\vec{\nu}(Y^*), \frac{1}{n}\right) \subset B^+_{Y^*}(Y, r^*).$$

Note that the same reasoning applies if the ball is exterior to Ω.
We finally obtain,

$$d(X^*, \Gamma) = d(Y^* - \frac{1}{n}\vec{\nu}(Y^*), \Gamma) = \|Y^* - \frac{1}{n}\vec{\nu}(Y^*) - Y^*\| = \frac{1}{n}, \tag{4.117}$$

and $X^* \in \Gamma_n$. This yields,

$$\{x - \frac{1}{n}\vec{\nu}(x)\,;\, x \in \Gamma\} \subset \Gamma_n. \tag{4.118}$$

The previous inclusion (4.118) together with (4.115) yield,

$$\Gamma_n = \{x - \frac{1}{n}\vec{\nu}(x)\,;\, x \in \Gamma\}. \tag{4.119}$$

Similar computations hold to prove,

$$\Gamma_n^c = \{x + \frac{1}{n}\vec{\nu}(x)\,;\, x \in \Gamma\},$$

and this concludes the proof of (4.92).

This section was dedicated to the rigorous derivation of the transmission problem in the single-species case. Similar computations can be made for the two-species case by adapting the choice of the test function $\tilde{\phi_n}$ to be localized on the interface between the two tissues and on their outer

boundaries.

Chapter 5

A multi-tissue viscous model for long-term effects of mechanisms of axis elongation in the vertebrate embryo

Abstract

This chapter is a paper in preparation in collaboration with Bertrand Bénazéraf, Pierre Degond and Ariane Trescases. In this chapter, we introduce a new mathematical macroscopic model for axis elongation. We calibrate it using biological data to bring the model closer to the vertebrate embryo. We validate the model by comparing it to existing biological results in literature. We then conduct *in silico* experiments to test different biological hypotheses.

Contents

We recall that in Objective 2, we aim to determine the role, the contribution and the share of each of cell proliferation in the PSM and in the NT and injection of new cells from the PZ into the PSM and the NT. In Chapter 4, we introduced four mechanical PDE models and studied them theoretically. In this chapter, we construct a variant of these models that is closer to the biological model that is the vertebrate embryo. We calibrate the new model and validate it by comparing it

to the biological data at hand. We then conduct *in silico* experiments to test different biological hypotheses and meet Objective 2.

Biological experiments are particularly challenging when one wants to evaluate the contribution of a single phenomenon on an entire process governed by multiple phenomena. This is due to the fact that, when experimenting on live embryos, properties are intertwined. This means that inhibiting proliferation, can affect cell motility, and vice versa. This makes the quantification of the relative contribution of each mechanism difficult and even impossible. For that reason we turn to mathematical modelling.

To attain Objective 2, we need a model that allows us to do the quantification we want. As explained in Chapter 1, macroscopic models for axis elongation often do not take into account cell division in the tissues, and explain axis elongation with only cell injection, which is not in line with our modelling approach. On the other hand, the models we presented to answer Objective 1, that is the VM, the ESVM, the L-VM and the L-ESVM reproduce well tissue elongation and the swirling motions observed in the embryo. However, they do not allow, in their present forms, to quantify the effect of cell injection from the PZ as it is not an element of the models. For that reason, inspired by the VM, we construct in this chapter a model that takes into account both cell injection and cell proliferation as drivers of growth. This new model inherits the properties of the VM, meaning that it maintains tissue segregation and allows the appearance of swirling motions in the PSM and is also complex enough to serve our Objective 2.
The reason why we do not use the ESVM is that it encompasses more parameters than the VM and which cannot be determined in the vertebrate embryo such as the repulsion parameter m. It also entails fourth order PDEs which are less practical to simulate numerically. Furthermore, we do not use the incompressible version of the VM nor of the ESVM, that is the L-VM and the L-ESVM, as we need the congestion parameter ϵ in the expression of the pressure to be big, or at least not in its asymptotic range. This is due to the fact that the PSM and the NT display density antero-posterior gradients during their elongation and we need to account for these density profiles in our model. We recall that this is not possible when ϵ is very small as this implies a regime where the densities are constant (either equal to their maximal density or equal to zero, see Chapter 4).

Building this new model as a version of the VM closer to the vertebrate embryo, permits a quantitative comparison with the biological data. In order to do so, a crucial step is to calibrate the model. Some parameters in our model can be found in literature. However, other parameters were not measured in vertebrate embryos. For that reason, we do our own quantification using image analysis and inject the parameters in the model. We note that these measured parameters can be used as future references in literature on vertebrate embryos. We explore this new model

numerically, by testing different sets of parameters *in silico*. With the biological data at hand, we compare the simulations of the mathematical model with the deviated sets of parameters with the treated embryos *in vivo*. Our method highlights the governing combination of mechanisms driving elongation.

First, we recall the VM.

The Viscous Model (VM). We consider two cell population densities $n_1(t,x)$ (representing the NT) and $n_2(t,x)$ (representing the PSM) evolving in space and time. We consider both tissues as viscous ones, and confer them with viscosity parameters, respectively β_1 and β_2, and use the Brinkman law to govern the velocities v_1 and v_2 of each tissue. The model equations are as follows. For all $(t,x) \in [0;+\infty) \times \mathbb{R}^d$,

$$\partial_t n_1 + \nabla \cdot (n_1 v_1) = n_1 G_1(p_\epsilon), \tag{5.1}$$

$$\partial_t n_2 + \nabla \cdot (n_2 v_2) = n_2 G_2(p_\epsilon), \tag{5.2}$$

$$-\beta_1 \Delta v_1 + v_1 = -\nabla p_\epsilon, \tag{5.3}$$

$$-\beta_2 \Delta v_2 + v_2 = -\nabla p_\epsilon, \tag{5.4}$$

$$p_\epsilon = \epsilon \frac{n}{1-n}, \qquad n = n_1 + n_2. \tag{5.5}$$

Strategy: additional ingredients to the VM. Our aim in Objective 2 is to test not only the differential proliferation within the tissues, but also to test the contribution of the incoming cells from the PZ into the PSM and the NT. For that reason, we introduce a variant of the VM which we call the VMI (the Viscous Model with Injection). Its novelty is mainly in its source term which will be added in the right hand side of the equations (5.1)-(5.2) which accounts for the appearance of new cells from the PZ at the posterior tip of the embryo. Although it is feasible to consider the PZ as a third tissue and construct a model with three population densities, it introduces more modelling hypotheses and more complexity to our study. Our strategy allows us not to consider the PZ as a third tissue, but to consider its contribution to tissue formation. Finally, in our theoretical study of the VM some constants were taken equal to 1 for simplicity, such as the tissue friction and the maximal density. In this chapter, we calibrate the model and use specific values measured in the vertebrate embryo. For simplicity, the growth functions G_i, and as they are close to being constant, are taken as constants determined in [24]. We then calibrate the model and conduct *in silico* experiments and compare them with the biological data.

5.1 The Viscous Model with Injection (VMI)

The new model: the VM with cell Injection (VMI). With these added ingredients to the VM, and using the same notations as for the VM, the new model which we call the VMI reads, for all $(t,x) \in [0;+\infty) \times \mathbb{R}^2$,

$$\partial_t n_1 + \nabla \cdot (n_1 v_1) = n_1 g_1 + \frac{\kappa_{NT}}{\delta} \chi_{PZ^\delta \cap PSM}, \tag{5.6}$$

$$\partial_t n_2 + \nabla \cdot (n_2 v_2) = n_2 g_2 + \frac{\kappa_{PSM}}{\delta} \chi_{PZ^\delta \cap PSM} \tag{5.7}$$

$$-\beta_1 \Delta v_1 + \mu v_1 = -\nabla p_\epsilon, \tag{5.8}$$

$$-\beta_2 \Delta v_2 + \mu v_2 = -\nabla p_\epsilon, \tag{5.9}$$

$$p_\epsilon = \epsilon \frac{n}{n_{max} - n}, \qquad n = n_1 + n_2. \tag{5.10}$$

The evolution equations on the densities (5.6)-(5.7) differ from those of the VM (5.1)-(5.2) in the reaction terms. In these terms, the growth functions are taken as constants equal to g_i (but not equal) in (5.6)-(5.7). Also in the source term, an additional term accounts for the entry of new cells with flux κ_{NT} and κ_{PSM} in respectively the NT in (5.6) and the PSM in (5.7). These new cells coming from the PZ and into the respective tissues are added only at the elongating tip of each tissue in a region denoted $PZ^\delta \cap NT$ for the region of entry of new cells in the NT and $PZ^\delta \cap PSM$ for that of the PSM. The width of the entry zone is denoted δ. In the Brinkman law for the velocities (5.8)-(5.9) the parameter μ represents the friction between the tissue and its surroundings. Finally, the pressure law (5.10) is taken the same as in the VM, with the maximal density 1 replaced by the value n_{max} which represents the maximal density inside the tissues measured *in vivo*. Adding these parameters enriches the model and allows us to capture more phenomena affecting axis elongation.

5.2 Model assumptions and calibration

In what follows we list a few model assumptions.

Model assumptions. To complete our description of the VMI, we made three assumptions:

1. We represent a projection of the 3D embryo onto a 2D plane. The average depth of the tissues (NT and PSM) being $h = 50\,\mu m$. This is due to the fact that most of our biological data at hand are in 2D and that the depth of the tissues is very small which advocates for a 2D description.

0. In equations (5.6)-(5.7) χ is the indicator function.

2. The friction coefficient for the PSM and the NT are both taken equal to μ. We made this assumption as, to our knowledge, the friction of the NT with its surrounding tissues is not a known parameter in literature.

3. As n_1 is the density of the NT and the PZ is attached to the NT at its posterior tip, we determine the posterior tip y_0 as the following,

$$y_0 = \inf_{y\in\mathbb{R}} \left\{ n_1(t,y) > \frac{1000\, cells}{100\, \mu m^2} \right\}.$$

Then we determine the evolution of the set PZ^δ in the densities' equations using the following characterization:

$$PZ^\delta(t) \cap NT = [a_1; b_1] \times [y_0 - \frac{\delta}{2}; y_0 + \frac{\delta}{2}],$$

with $[a_1; b_1]$ the width of the NT which will be defined in the numerical setting. Similarly we can define,

$$PZ^\delta(t) \cap PSM = [a_2; b_2] \cup [a_3; b_3] \times [y_0 - \frac{\delta}{2}; y_0 + \frac{\delta}{2}],$$

with $[a_2; b_2]$ and $[a_3; b_3]$ the width of respectively the left and the right PSM which will be defined in the numerical setting.

Remark 5.2.1. *We choose the posterior tip (the PZ) at the same line for the PSM and the NT. The results obtained in the simulations are coherent with the biological data, and we see that this choice does not introduce any bias to the system, see Figures 5.12a-5.12b.*

In what follows we list the parameters in this model and their value with their respective units, their source (reference in literature) and the method used to measure them.

Model Calibration. The parameters in the VMI are listed in what follows:

- $g_1 \approx \frac{1}{10.83}$ $[hour^{-1}]$. The cell proliferation rate in the NT was measured in [24] using EdU and found to be constant across stages of development.

- $\kappa_{NT} \approx 3.4$ $[cells \cdot hour^{-1} \cdot \mu m^{-1}]$. Using image analysis on transgenic quail embryos, we measured on the Imaris software the entry of new cells from the PZ into the NT observed in 3D. The method will be detailed in the next paragraph.

- $g_2 \approx \frac{1}{8.75}$ $[hour^{-1}]$. The cell proliferation rate in the PSM was measured in [24] using EdU and was found to be constant across stages of development.

- $\kappa_{PSM} \approx 5$ $[cells \cdot hour^{-1} \cdot \mu m^{-1}]$. Using image analysis on transgenic quail embryos, we measured on the Imaris software the entry of new cells from the PZ into the PSM observed in 3D. The method will be detailed in the next paragraph.

- We choose the width of the entry zone δ to be equal to one mesh size.

- $\beta_1 \approx 10^4 - 10^5\ [Pa \cdot s]$. The viscosity of the NT was measured in [108] using pipette aspiration technique. We note here that $\beta_1 > \beta_2$ according to [108], meaning that the NT is more viscous than the PSM. We set $\beta_1 = 3 \times 10^4$.

- $\mu \approx 10^{12} - 10^{13}\ [Pa \cdot s/m^2]$. The friction between the PSM and its surrounding tissues -NT, lateral plate, ectoderm, endoderm- was estimated in a recent paper [129]. We set $\mu = 10^{12}$.

- $\beta_2 \approx 10^4 - 10^5\ [Pa \cdot s]$. The viscosity of the PSM was measured in [108] and in [129] using pipette aspiration technique. We set $\beta_2 = 2 \times 10^4$.

- $n_{max} \approx 2800\ [cells/100\mu m^3]$. The maximal density in the tissues can be deduced from [24] where an averaged density map was represented along the antero-posterior axis of the vertebrate embryo, see Figure 1.16 (A-C).

- $\epsilon = 10$. This free parameter controls the congestion pressure p_ϵ. It was fixed such that we obtain the right elongation speed of the tissues.

Protocol to measure cell injection. We use the Imaris software on live movies of transgenic quails taken from [24]. We first construct a reference frame following the elongation of the PZ. We look at a Z-stack located ventrally to capture cell exit from the PZ and into the PSM. We construct a zone of size $[l \times L \times h] = [100\mu m \times 200\mu m \times 10\mu m]$ at the interface between the PSM and the PZ, see Figure 5.1. We count the cells inside this zone at initial time. At final time we obtain a file with all the cells captured throughout the movie with their velocities and positions. We filter these cells by removing the ones with small or no outward velocity (pointing towards the PSM which corresponds to cell exit) and denote the remaining cell number N. Finally, we compute the average velocity $\overline{V}$ in the direction of cell exit of the remaining N cells. It then suffices to compute,

$$\text{Number of cells exiting the PSM per hour} = \frac{N\overline{V}}{l}.$$

To obtain the parameter κ_{PSM} we divide the obtained number of cells exiting the PSM per hour by the width of the PSM (approximately $100\mu m$). We multiply this number by the remaining Z-stacks in the 3D tissues which add up to the depth of the considered tissues of $50\mu m$, as the considered zone of entry is taken as deep as a few cell diameters to capture the cells. We follow the same protocol for the NT by looking at Z-stacks located dorsally to capture cell entry into the NT.

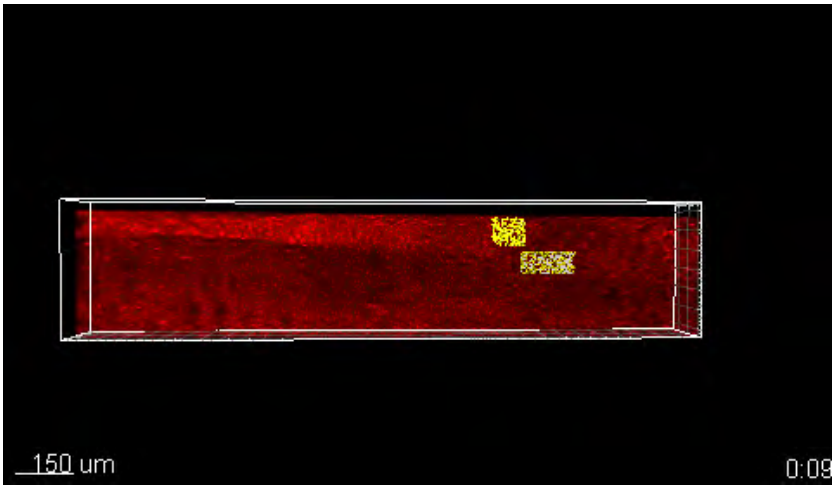

Figure 5.1 – The constructed zone (yellow square) on the interface between the PSM and the PZ and on the interface between the NT and the PZ and the cells counted inside (dots and trajectories).

5.3 Numerical setting

Numerical setting and initial condition. The numerical domain is the rectangle $[l \times L] = [300\mu m \times 4500\mu m]$. We consider the embryo at stage 11HH with a portion of the NT already formed, corresponding to $L/3 = 1500\mu m$ in length and $71\mu m$ in width that is $[114\mu m; 185\mu m]$. The NT is flanked with two PSM on the right and on the left, with length $L/3 = 1500\mu m$ and width of $100\mu m$ from either side of the NT, that is $[0\mu m; 100\mu m] \cup [200\mu m; 300\mu m]$, see Figure 5.2a. The density in the NT is approximately constant and very high [24]. Then we take the initial NT density as follows,

$$n_1^{ini}(x) = \frac{950\, cells}{\mu m^2} \chi_{y \leq L/3},$$

which corresponds to $\frac{19\, cells}{\mu m^3}$ as in [24] projected on the depth of the tissues. As for the PSM, and as the embryo shows a clear antero posterior density gradient [24], we impose this gradient on the initial condition, that is,

$$n_2^{ini}(x) = \frac{850\, cells}{\mu m^2} \chi_{y \leq L/8} + \left(\alpha_1 (y - L/8)^2 + \alpha_2\right) \chi_{L/8 \leq y \leq L/3},$$

with χ the indicator function and $\alpha_1 < 0, \alpha_2 > 0$ computed such that the PSM density antero-posterior gradient ranges from $\frac{850\, cells}{\mu m^2}$, to $\frac{600\, cells}{\mu m^2}$, which respectively correspond to $\frac{17\, cells}{\mu m^3}$ and $\frac{12\, cells}{\mu m^3}$ as in [24] projected on the depth of the tissues.

The lateral numerical walls correspond to the lateral plate which is a dense structure. The upper wall (which corresponds to the anterior of the vertebrate body) models the presence of

somites which are also dense structures. For these reasons, we set no flux boundary conditions as well as homogeneous Dirichlet for the velocities. These conditions state that no density can flow out of the walls, and that when cells come in contact with these walls they adhere to them and stop moving.

5.4 Numerical simulations of the VMI: the wild-type embryo *in silico*

The wild-type embryo *in silico*. Using the list of parameters above, we simulated the equivalent of a wild-type embryo *in silico* for 12 hours of biological time, see Figures 5.2a-5.2b.

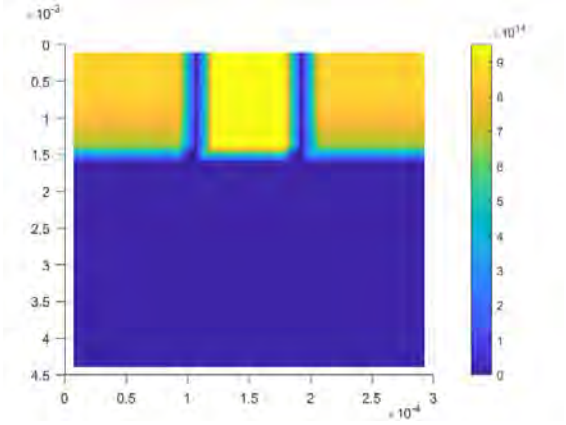

(a) Initial condition. The NT is the middle tissue and the PSM on its right and left.

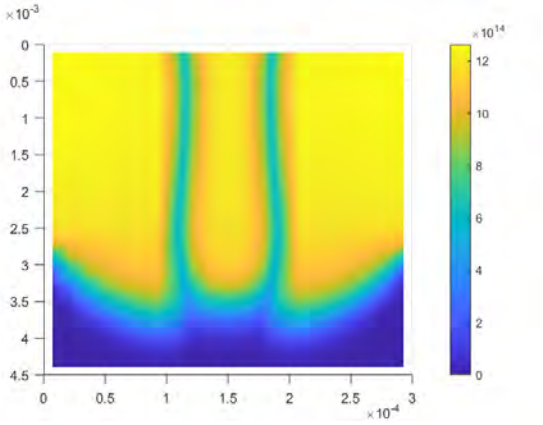

(b) The tissues (PSM and NT) at $t = 12$ hours.

Figure 5.2 – Numerical simulations of the VMI in the case of the wild-type embryo. The left panel (a) is the initial condition of the densities. The right panel (b) is the density profiles at the final time $t = 12$ hours. The axes are in meters.

We first observe that the tissues have elongated towards the posterior and that the densities have increased along the antero-posterior axis. We see that the density gradient in the PSM is preserved with a lower density in the posterior compared to the anterior. We also see that the NT exhibits an antero-posterior gradient. The NT appears thin at the end of the simulation. This suggests that throughout the growth, the PSM exerts lateral forces on the NT, while maintaining tissue segregation. We measured the elongation rate and found it equal to $V \approx 4 \times 10^{-2}\,\mu m/s$, which is in the range described in [25, 129]. We plotted the total pressure in the tissues at $t = 12$ hours in Figure 5.3f and found it in the range $20 - 90\,Pa$. The pressure matches quantitatively the measured stress in the posterior tissues [108, 109].

Taking a closer look at the velocities in each tissue, we see in Figure 5.3a that the PSM velocity vector exhibits several interesting behaviors which differ along the antero-posterior axis. Anteriorly,

the vectors point towards the NT, which supports our previous statement that the PSM pushes the NT laterally. Along the antero-posterior axis, the vectors exhibit a clear rotation towards the numerical walls, which supports the appearance of swirling motions in the PSM. Posteriorly, the vectors point towards the posterior but also laterally, which suggests an expansion of the PSM and its elongation. In Figure 5.3b, the vectors in the NT exhibit a different behavior than those of the PSM. Centrally, the vectors point towards the posterior. Anteriorly on the interface between the PSM and the NT, the vectors point inwards in response to the PSM compression. Posteriorly on the interface, the vectors display an outwards direction which suggests expansion. These movements are further supported by the plot of streamlines in Figure 5.3c which show a clear swirling movement in the PSM, compression of the NT and expansion posteriorly in the PSM and in the NT in Figure 5.3d. In Figure 5.3e, we represent the velocity vector v_1 (green, NT) and v_2 (red, PSM) along a strip of the axis at final time. We see the clear antero-posterior velocity gradient in both tissues, with small velocities anteriorly and high velocities posteriorly. This velocity profile is in accordance with [25] where authors prove the existence of an antero-posterior gradient in the PSM. Our results show that this motility gradient is also present in the NT.

We then investigated the possible sliding between the tissues by computing the central velocities in each tissue. To compute the central velocities, we take two mesh cells inside the PSM (and three mesh cells inside the NT) and compute the average velocity over these two cells on each point of the antero-posterior axis, see Figure 5.4.

Remark 5.4.1 (Central velocities.)**.** *For the central velocities, we use the central mesh cells as this method is very close to the analysis done in [24]. This renders the comparison of our numerical results with the biological data more accurate. For the PSM velocities, we take two central meshes i_0 and i_0+1 inside the PSM and we compute for every mesh cell j on the antero-posterior axis,*

$$\overline{V^{\alpha}_{y_j}} = \frac{v^{\alpha}_{i_0\, y_j} n^{\alpha}_{i_0\, j} + v^{\alpha}_{i_0+1\, y_j} n^{\alpha}_{i_0+1\, j}}{n^{\alpha}_{i_0\, j} + n^{\alpha}_{i_0+1\, j}}, \text{ with } \alpha = 1, 2.$$

We can do the same computations for the NT velocities by considering three mesh cells inside the NT as per Figure 5.4.

Remark 5.4.2. *In Figures 5.5a we represent the velocities only up to the PZ (the posterior tip of the tissues). We also note that the velocities exhibit a decrease posteriorly due to our choice of boundary conditions (homogeneous Dirichlet for the velocity), which prescribes zero velocity on the lower numerical wall.*

The results are plotted in Figure 5.5a at final time in the international unit system m/s. We discuss our results in other units to facilitate the comparison with results in literature. The PSM velocity (in red) increases along the antero-posterior axis ranging from $1.2 \mu m/min$ to $3.6\ \mu m/min$,

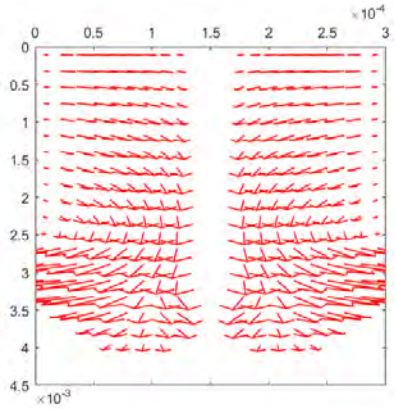

(a) The PSM velocity vector v_2 at $t =$ 12 hours.

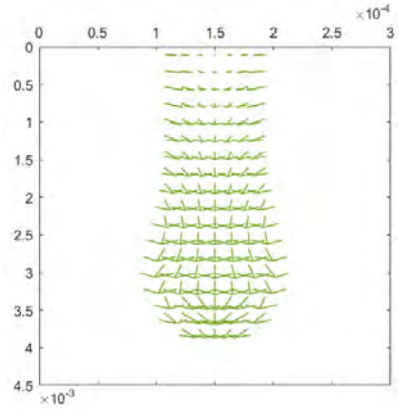

(b) The NT velocity vector v_1 at $t =$ 12 hours.

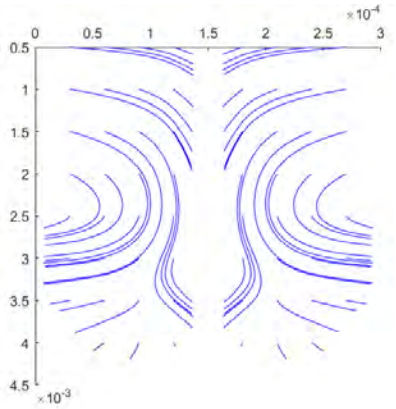

(c) The streamlines of v_2 at $t = 12$ hours.

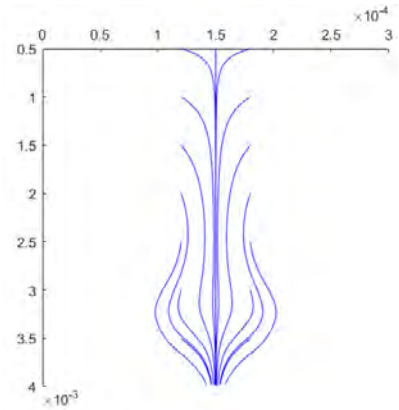

(d) The streamlines of v_1 at $t = 12$ hours.

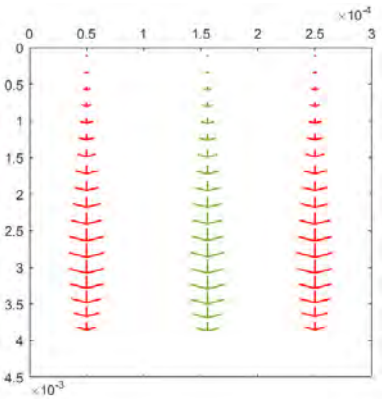

(e) The velocity vectors v_1 (green) and v_2 (red) at $t = 12$ hours, along a section of the antero-posterior axis in each tissue.

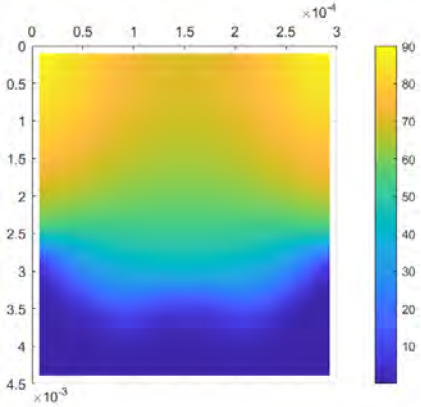

(f) The pressure profile in the tissues at $t = 12$ hours. Colorbar is in Pascal unit.

Figure 5.3 – Numerical simulations of the VMI in the case of the wild-type embryo. In the top panels (a)– (b) we represent the velocities of respectively the PSM and the NT. They are drawn only where the respective densities are above a certain threshold which we defined at $\frac{2\,cells}{\mu m^2}$. The middle panels (c)–(d) are the streamlines of respectively v_2 and v_1 $t = 12$ hours. The left bottom panel (e) is the velocity vectors v_2 (red) and v_1 (green) along a section of respectively the PSM and the NT at $t = 12$ hours. The axes are in meters. The right bottom panel (f) is the total pressure in the tissues. The colorbar is in Pascal.

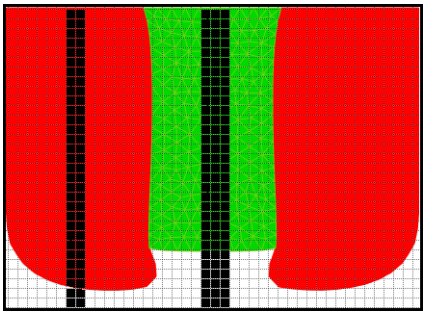

Figure 5.4 – Schema of the tissues with the mesh (background). We compute the average velocities in the PSM and the in the NT on the mesh sizes colored in black respectively in mid PSM and mid NT and along the antero-posterior axis.

which matches the values measured in [25]. The NT velocity (in green) reaches 4.2 $\mu m/min$ in the most posterior region. Interestingly, we see that the NT velocity is higher than that of the PSM. This suggests that the NT slides along the PSM towards the posterior. The plot in Figure 5.5a matches the profile of the measured velocities in [24]. To further test this sliding, we took two reference points or "bulks of cells" in Figure 5.5b at $t = 0$, one in the PSM at $(35\mu m, 964\mu m)$ and one in the NT at $(135\mu m, 964\mu m)$. We plotted the trajectories of these points along 6 hours (from mid simulation (6 hours) till the end of the simulation (12 hours)) using the central velocities computed in Figure 5.5a. The resulting trajectories emphasize on the inter-tissue sliding, as the point in the NT reaches more posterior locations than the point in the PSM. This is most probably due to the fact that the PSM point undergoes many deviations as a result of swirling motions.

In Figure 5.5d (left) we represent the difference between the last posterior location of the NT reference and that of the PSM. We see that for these two sets of points which can be considered as mid-anterior points, the sliding is of about $47\mu m$. We wanted to test whether this sliding is also present in the mid-posterior part of the tissues. We took two different reference points in the NT $(135\mu m, 1392\mu m)$ and in the PSM $(35\mu m, 1392\mu m)$ and computed their trajectories in the y-component, see Figure 5.5c. We see that the trajectory of the point in the PSM is slightly more posterior-driven than that of the NT point. The sliding between these two points is almost zero as seen in Figure 5.5d (right) where the difference in the final posterior position of the two points is almost the same.

Our results clearly show an inter-tissue sliding in the vertebrate embryo throughout its elongation. They also suggest that the NT slides past the PSM mainly in the mid-anterior part of the tissues. These results confirm the hypothesized inter-tissue sliding in [24]. This validates our model.

We now want to investigate the contribution of differential proliferation as well as differential cell injection from the PZ and into the PSM and NT on axis elongation and inter-tissue sliding.

Mainly we want to answer two questions: **What is the effect of differential proliferation and of differential injection on axis elongation ?** and **is differential proliferation and/or differential injection behind the inter-tissue sliding ?**

5.5 Effect of differential proliferation and differential injection on axis elongation and inter-tissue sliding

We want to test the effect and contribution of differential proliferation and differential injection on axis elongation, tissue growth, and sliding between the tissues. For that reason, we run four numerical simulations with the following different sets of parameters:

1. Simulation 1: we set both numerical proliferation rates equal to that of the PSM, that is, $g_1 = g_2 = 1/8.75$ hours.
2. Simulation 2: we set both numerical proliferation rates equal to that of the NT, that is, $g_1 = g_2 = 1/10.83$ hours.
3. Simulation 3: we set both numerical injections of new cells from the PZ equal to that of the NT, that is, $\kappa_{PSM} = \kappa_{NT} = 3\ cells \cdot hours^{-1} \cdot \mu m^{-1}$.
4. Simulation 4: we set both numerical injections of new cells from the PZ equal to that of the PSM, that is, $\kappa_{PSM} = \kappa_{NT} = 5\ cells \cdot hours^{-1} \cdot \mu m^{-1}$.

We run these simulations and compare the results on four grounds :

- Density profiles
- Velocities of the NT and PSM
- Elongation rate
- Sliding between the tissues

Comparison of density profiles. We look at the density profiles at final time ($t = 12$ hours of biological time) in all four simulations and compare them to the WT case. In Figure 5.6b we represent the NT and PSM densities in the case where the injection rates of the tissues are equal to that of the PSM. We notice that the densities are almost identical to the wild-type case in Figure 5.6a. We also noted no difference in the maximal densities nor in tissue shape. Similarly, although not shown here, when the injection rate was taken equal to that of the NT, we noted no difference with the WT case. When comparing the WT case to the case where the proliferation rates are taken equal to that of the PSM (Figure 5.6c), we observed a significantly wider NT especially in the posterior region, and more elongated tissues. Interestingly, when the proliferation rates were taken equal to that of the NT, the NT was also very wide anteriorly and posteriorly. We also noted

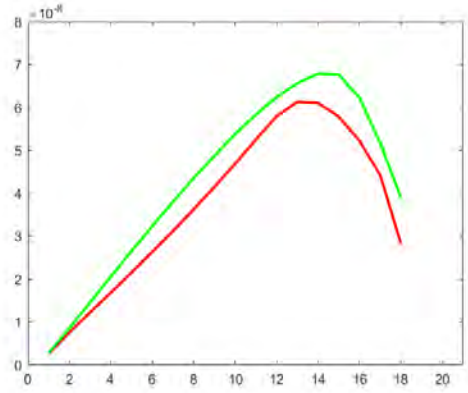

(a) Central velocities in the PSM (red) and in the NT (green) along the antero-posterior axis at $t = 12$ hours. The y-axis is in m/s (value of the velocity) and the x-axis represents the mesh cells along the antero-posterior axis.

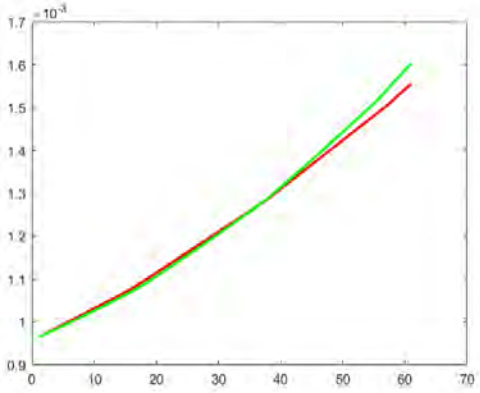

(b) Trajectories in the y-component of two reference points taken initially in the PSM (in red) at $(35\mu m, 964\mu m)$ and in the NT (in green) at $(135\mu m, 964\mu m)$ with respect to time. The y-axis is in meters (position along the antero-posterior axis), the x-axis represents time.

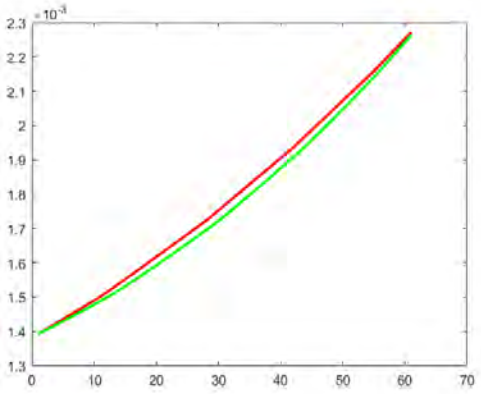

(c) Trajectories in the y-component of two reference points taken initially in the PSM (in red) at $(35\mu m, 1392\mu m)$ and in the NT (in green) at $(135\mu m, 1392\mu m)$ with respect to time. The y-axis is in meters (position along the antero-posterior axis), the x-axis represents time.

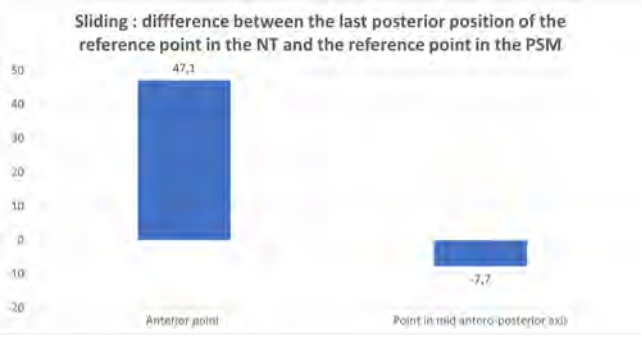

(d) Difference between the last posterior location of the reference point in the NT and the reference point in the PSM when the points are at $y = 964\mu m$ (left) and $y = 1392\mu m$ (right).

Figure 5.5 – Upper left panel (a): plot of the central velocity of the PSM (red) and of the NT (green), along the antero posterior axis. Upper right panel (b): trajectories of two reference points taken initially in the PSM at $(35\mu m, 964\mu m)$ and in the NT at $(135\mu m, 964\mu m)$ with respect to time. Lower left panel 5.5c trajectories of two reference points taken initially in the PSM at $(35\mu m, 1392\mu m)$ and in the NT at $(135\mu m, 1392\mu m)$ with respect to time. Lower right panel: Sliding between the two reference points considered in the NT and in the PSM (left histogram for $y = 964\mu m$, right histogram for $y = 1392\mu m$).

that the maximal density in both tissues was reduced (colorbar in Figure 5.6d). The elongation of the tissues was also affected as tissues were significantly shorter at $t = 12$ hours. **These results suggest a direct influence of cell proliferation on tissue elongation and tissue shape. Our results show that cell injection has little effect on the density profiles, tissue shape and elongation compared to cell proliferation.**

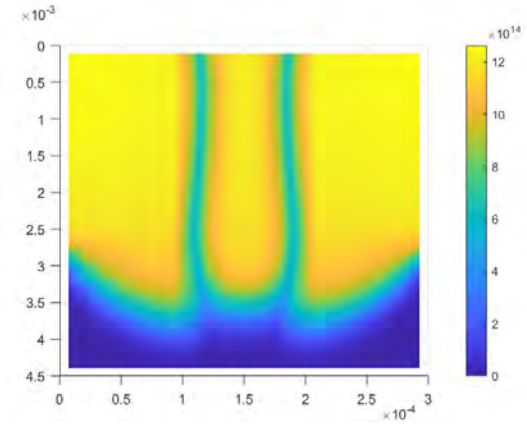

(a) Final time: wild-type.

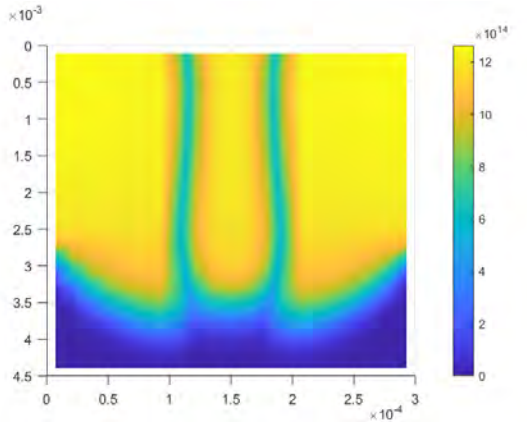

(b) Final time: injection rates equal to that of the PSM.

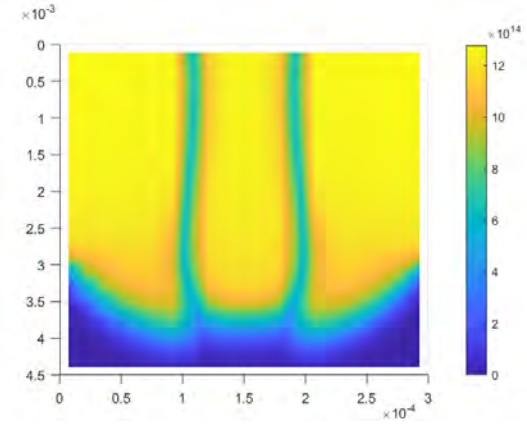

(c) Final time: proliferation rates equal to that of the PSM.

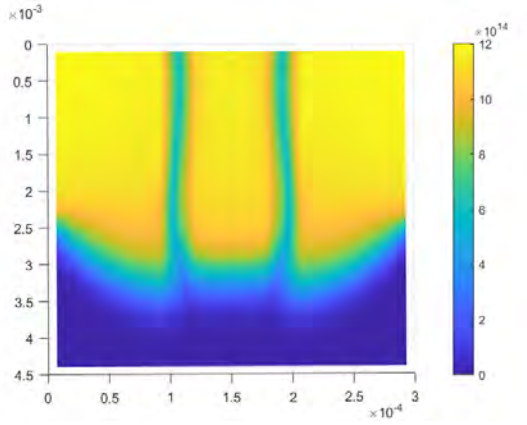

(d) Final time: proliferation rates equal to that of the NT.

Figure 5.6 – Density profiles in the wild-type case (Panel (a)), when injection rates are equal to that of the PSM (Panel (b)), when proliferation rates are equal to that of the PSM (Panel (c)) and when proliferation rates are equal to that of the NT (Panel (d)).

Comparison of tissue velocity. For the same sets of simulations described above, we took a closer look at the central velocities of the NT and PSM. The central velocities of the NT and of the PSM seemed to be identical to the WT case (Figure 5.7a) when the injection rates were equal to that of the PSM in Figure 5.7b. Similarly, although not shown here, when the injection rate

was taken equal to that of the NT, we noted no differences with the WT case. In Figure 5.7c, we represent the velocities when the proliferation rates are taken equal to that of the PSM. We notice the NT velocity increases and reaches a higher maximum value. In Figure 5.8 we represent the NT velocity v_1 at final time in the case the proliferation rates are equal to that of the PSM. The velocity vectors show a clear expansion of the NT posteriorly which supports the profiles in Figure 5.7c. Strikingly, when the proliferation rates were equal to that of the NT, in Figure 5.7d, both the NT and the PSM velocities exhibit a significant decrease compared to the WT case and reach a lower maximum. **Altogether, these results show that a higher proliferation in the NT leads to tissue expansion posteriorly. A lower proliferation in the PSM leads to a significant reduction in the PSM velocity and in the NT velocity. Finally, injection of new cells from the PZ into the PSM and the NT seems to have little effect on the velocity profiles compared to cell proliferation.**

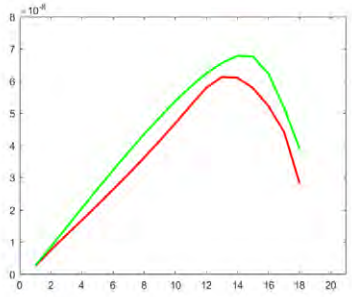

(a) Central velocities (NT in green, PSM in red): wild-type at $t = 12$ hours.

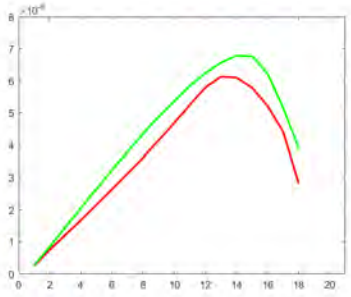

(b) Central velocities (NT in green, PSM in red): injection rates equal to that of the PSM.

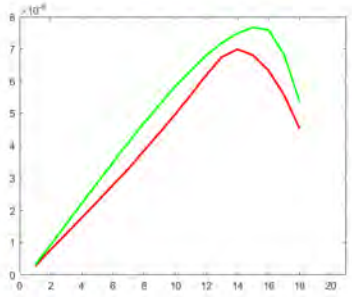

(c) Central velocities (NT in green, PSM in red): proliferation rates equal to that of the PSM at $t = 12$ hours.

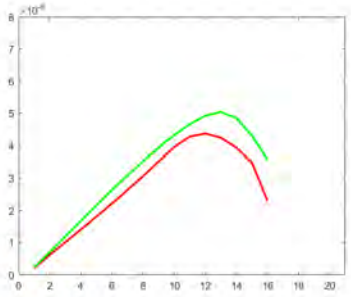

(d) Central velocities (NT in green, PSM in red): proliferation rates equal to that of the NT at $t = 12$ hours.

Figure 5.7 – Central velocities of the NT in green and the PSM in red at $t = 12$ hours in the wild-type case (Panel (a)), when injection rates are equal to that of the PSM (Panel (b)), when proliferation rates are equal to that of the PSM (Panel (c)) and when proliferation rates are equal to that of the NT (Panel (d)). The y-axis is in units m/s (value of the velocity), the x-axis represents the mesh cells along the antero-posterior axis.

Remark 5.5.1. *The density and velocity profiles in the WT case (Figures 5.6a-5.7a) and in the case the injection rates are equal (Figures 5.6b-5.7b) are extremely similar but the values are nevertheless slightly different.*

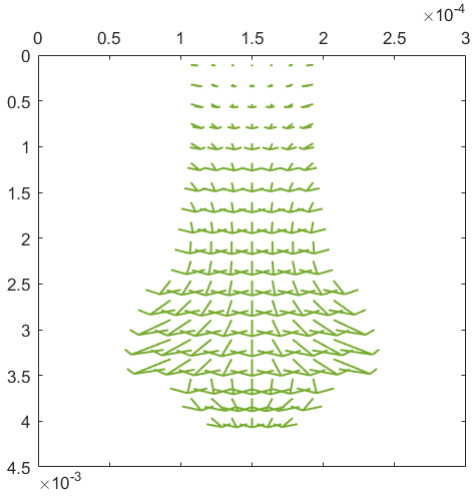

Figure 5.8 – NT velocity v_1 at final time: proliferation rates equal to that of the PSM.

Comparison of elongation rates. We then compared the elongation rates for all four sets of simulations. The first striking observation is the significant decrease, compared to the WT case, in the elongation rate in the case when the proliferation rates in the PSM and in the NT are equal to that of the NT, see Figure 5.9. This observation was supported by the density profile in Figure 5.6d and in the average velocities in Figure 5.7d. We also noted a higher elongation rate in the case when proliferation rates were equal to that of the PSM compared to the WT embryo. **These two observations suggest that proliferation promotes elongation.** We did not observe any difference in the elongation rate in the case the injection rates were equal to that of the PSM or that of the NT.

Comparison of inter-tissue sliding. Finally, we compared the sliding between the NT and the PSM. We took two reference points, one in the PSM at $(35\mu m, 964\mu m)$ and one in the NT at $(135\mu m, 964\mu m)$ at initial time. We computed their trajectories using the central velocities in Figure 5.7 and represented them starting 6 hours of biological time until 12 hours. In Figure 5.10, we represent the final posterior location (y-component) of these two points in each simulation to compare the sliding. We observe that when the proliferation rates are equal to that of the NT, two phenomena occur: 1) both reference points traveled less towards the posterior 2) the sliding between these two points was significantly reduced compared the WT case. This observation is congruent with the reduction of the velocities in both tissues in Figure 5.7d. We also deduce that

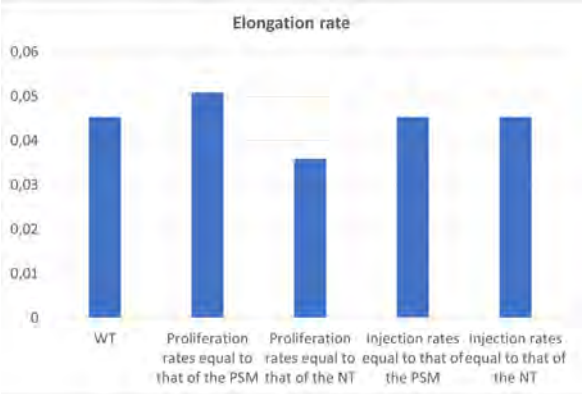

Figure 5.9 – Comparison of elongation rates (from left to right): in the wild type case, when proliferation rates are equal to that of the PSM, when proliferation rates are equal to that of the NT, when injection rates are equal to that of the PSM, when injection rates are equal to that of the NT. The y-axis is in unit $\mu m/s$.

when proliferation rates were equal to that of the PSM, the reference points travel more to the posterior. Differential injection seemed to have no effect on the sliding.

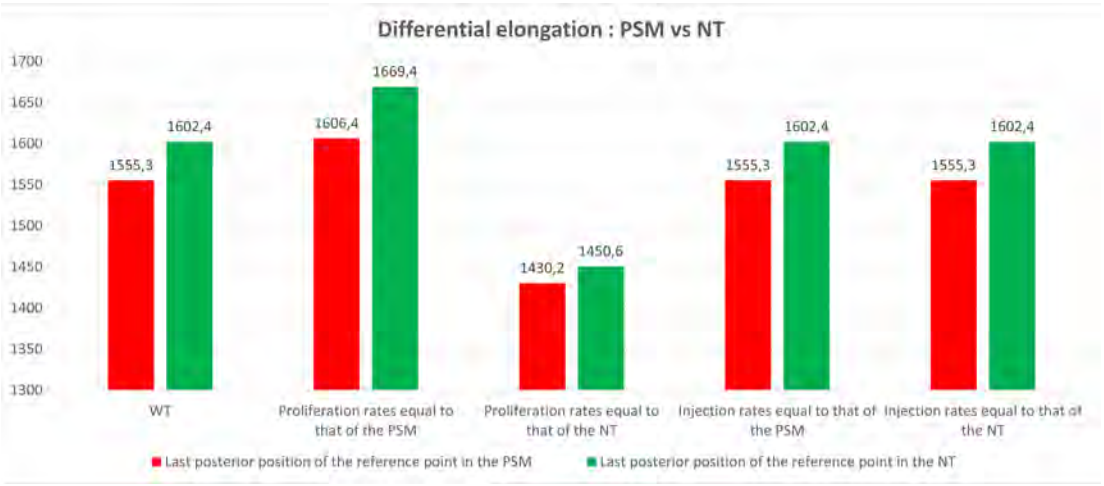

Figure 5.10 – Comparison of differential elongation. From left to right: in the wild type case, when proliferation rates are equal to that of the PSM, when proliferation rates are equal to that of the NT, when injection rates are equal to that of the PSM, when injection rates are equal to that of the NT. The y-axis unit in microns.

For more clarity, we plotted in Figure 5.11 the difference in final posterior locations between the two reference points. We observe that, compared to the WT case, an increase in the proliferation of the NT increases the sliding up to $63\mu m$ (by 50%). On the contrary, a decrease in the PSM proliferation rate drastically reduced the inter-tissue sliding to $20\mu m$ (by 50%). This result shows that interfering with the proliferation rate of the PSM not only affects the PSM but also the

dynamics of the NT, and vice versa.

These results suggest that a reduction in the proliferation rate in the PSM reduces the sliding between the tissues. Interestingly, an increase in the proliferation of the NT yields a more important sliding. In both cases we notice that interfering with the proliferation rate of one of the tissues affects the dynamics of both tissues. Finally, our results also suggest that injection of new cells from the PZ into the NT and the PSM does not affect inter-tissue sliding.

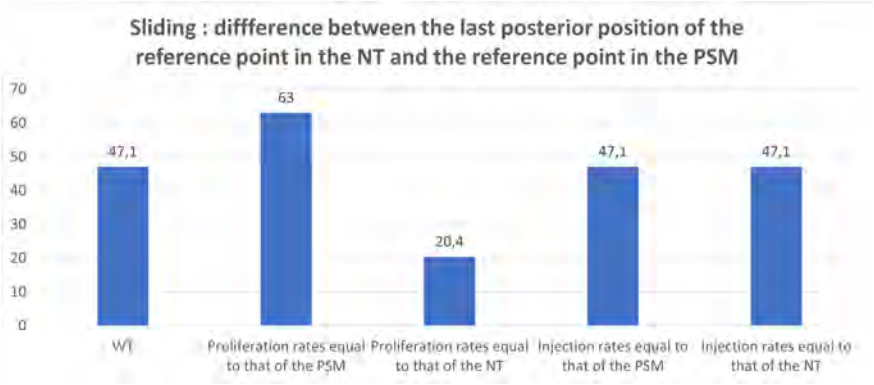

Figure 5.11 – Comparison of the inter-tissue sliding: difference of posterior travel distance between the NT and the PSM reference points from Figure 5.10. From left to right: in the wild type case, when proliferation rates are equal to that of the PSM, when proliferation rates are equal to that of the NT, when injection rates are equal to that of the PSM, when injection rates are equal to that of the NT. The y-axis unit in microns.

5.6 Extreme cases

In this section we want to investigate the contribution of each mechanism (proliferation and injection) on axis elongation. In what follows we exhibit *in silico* experiments of extreme cases where we completely inhibit each of these mechanisms to quantify its role on axis elongation. Namely, we do the following three sets of simulations:

1. Simulation 1: we completely inhibit the proliferation in the NT: $g_1 = 0$.
2. Simulation 2: we completely inhibit the proliferation in the PSM: $g_2 = 0$.
3. Simulation 3: we completely inhibit the injection of new cells in both tissues $\kappa_{NT} = \kappa_{PSM} = 0$.

With these simulations we conduct a similar study as before by looking at the density and velocity profiles, tissue shape, elongation rates and inter-tissue sliding.

Comparison of density profiles. Our first observation is that when the injection rates are both taken equal to zero, the density profiles appear identical to those in the WT case, see Figures 5.12a-5.12b. When the proliferation rate of the PSM is taken equal to zero as in Figure 5.12c, the NT grows laterally and becomes abnormally large and pushes the PSM towards the lateral walls. The PSM reduces in size and in its density. Lateral compression from the PSM on the axial tissues is absent due to the lack of a dense PSM. This severely affects tissue elongation as the growth becomes lateral rather than vertical towards the posterior. When the proliferation rate of the NT is null as in Figure 5.12d, the NT becomes extremely thin and the PSM invades its space. The NT is being compressed laterally by the growing PSM. Interestingly, this compression allows for some (significant) elongation to happen, similar to a displacement due to the convergence-extension phenomenon, and this elongation is more significant than the case when the NT's proliferation rate is normal. **These results strongly suggest that cell proliferation has a crucial contribution to axis elongation unlike the injection of new cells from the PZ. They also suggest that inhibiting proliferation in one of the tissues interferes with the multi-tissue dynamics. It maintains lateral compression of the NT by the PSM, which promotes the elongation of the posterior tissues. The model proposes that the active growth of both posterior tissues is necessary for normal tissue formation and axis elongation.**

Comparison of tissue velocity. In Figure 5.13, we compute the central velocities in each tissue at final time and along the antero-posterior axis. Compared to the wild-type case in Figure 5.13a, when both injection rates are taken equal to zero in Figure 5.13b, the central velocities displayed no notable change in their profiles. When the proliferation of the PSM is null (Figure 5.13c), we observe the decrease of the velocities in both tissues all along the antero-posterior axis. This is congruent with the fact that very little elongation occurs in this case. As the NT is growing and elongating, its velocity is higher than that of the PSM posteriorly. Finally, when the proliferation rate of the NT is null as in Figure 5.13d, the NT velocity is reduced but remains significant. This is the result of the lateral compression from the PSM which drives the NT towards the posterior, similar to a convergence-extension effect. The PSM velocity is also reduced in this case. **These results highlight the role of cell proliferation in both long-term tissue formation and posterior growth.**

Comparison of elongation rates. We compared the elongation rates in the three simulations and compared them to the WT case in Figure 5.14. The elongation rates in the cases where the proliferation rates were taken equal to zero in either tissue were severally diminished compared to the WT. We noted no difference in the elongation rate when the injection rates were both equal to zero. **These results exhibit the importance of cell proliferation in posterior tissues to sustain tissue elongation.**

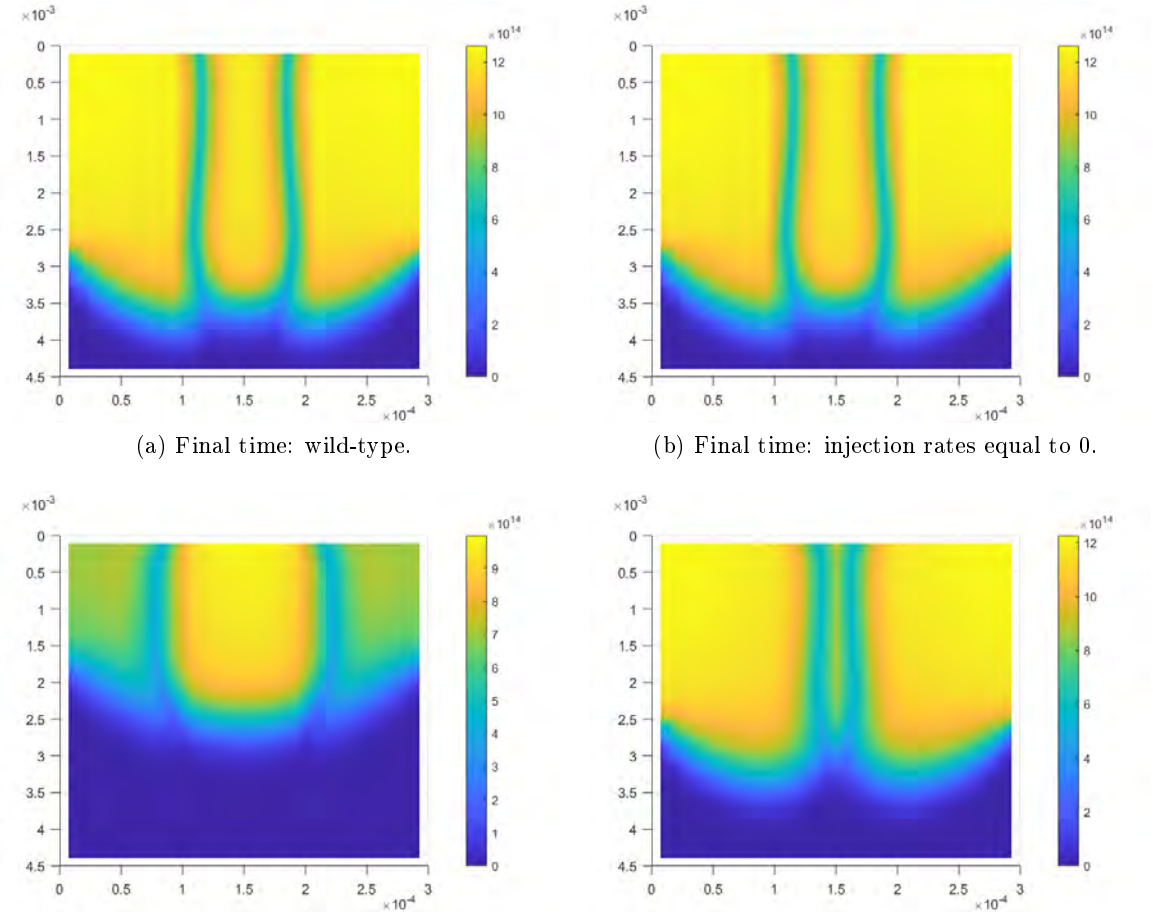

(a) Final time: wild-type.

(b) Final time: injection rates equal to 0.

(c) Final time: PSM proliferation rate equal to 0.

(d) Final time: NT proliferation rate equal to 0.

Figure 5.12 – Density profiles in the wild-type case (Panel (a)), when injection rates are equal to 0 in the PSM and NT (Panel (b)), when PSM proliferation rate is equal to 0 (Panel (c)) and when NT proliferation rate is equal to 0 (Panel (d)).

Comparison of inter-tissue sliding. In Figure 5.15, we study the inter-tissue sliding in each simulation case. We took two reference points, one in the PSM at $(35\mu m, 964\mu m)$ and one in the NT at $(135\mu m, 964\mu m)$ at initial time. We computed their trajectories using the central velocities in Figure 5.13. We represent in Figure 5.15 the posterior end of the trajectories of each reference point at final time for each simulation. For clarity, we also represented the difference (in y-distance) between these two points in Figure 5.16. We observe when the NT proliferation rate is taken equal to zero that the points in both tissues travel less towards the posterior compared to the WT case. The sliding is significantly increased in this case (up to $110\mu m$) mainly because the point in the PSM travels much less to the posterior. This is in accordance with the velocity profiles and the density profiles where we observe that the PSM compresses the NT, allowing for the NT's elongation. Thus the PSM movement is more lateral than towards the posterior. In the case the PSM proliferation

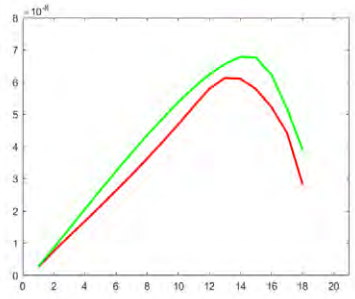

(a) Central velocities (NT in green, PSM in red): wild-type at $t = 12$ hours.

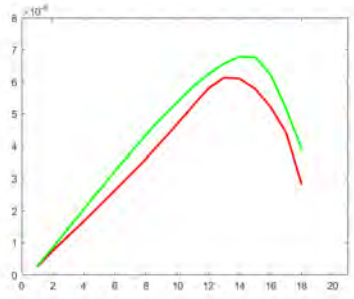

(b) Central velocities (NT in green, PSM in red): Injection rates in the PSM and NT are equal to 0 at $t = 12$ hours.

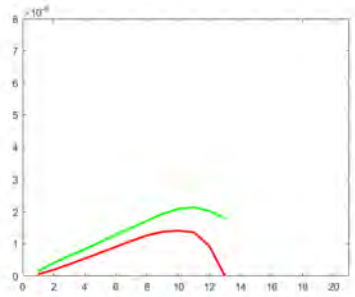

(c) Central velocities (NT in green, PSM in red): PSM proliferation rate equal to 0 at $t = 12$ hours.

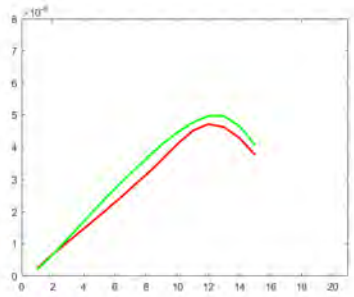

(d) Central velocities (NT in green, PSM in red): NT proliferation rate equal to 0 at $t = 12$ hours.

Figure 5.13 – Central velocities of the NT in green and the PSM in red in the wild-type case (Panel (a)), when injection rates are equal to 0 in the PSM and in the NT (Panel (b)), when PSM proliferation rate is equal to 0 (Panel (c)) and when NT proliferation rate is equal to 0 (Panel (d)). The y-axis is in units m/s (value of the velocity), the x-axis represents the mesh cells along the antero-posterior axis.

rate is zero, the points travels much less to the posterior compared to the WT case. The sliding is also significant compared to the WT and reaches $68\mu m$. When both injection rates are taken equal to zero, sliding still occurs, but it is identical to that of the WT case. **Our results are clearly indicative of the role of cell proliferation on inter-tissue sliding: inhibiting cell proliferation in either tissue has a positive effect on sliding. Proliferation also affects the posterior movement of cells.**

Finally, we exhibit a last extreme case where we set the numerical cell proliferation in the PSM and in the NT to zero, and keep cell injection. The question we want to answer is: **is cell injection from the PZ enough to sustain axis elongation ?** We present the results in the following.

In Figure 5.17a, we see that in the absence of cell proliferation, the tissues are short and little

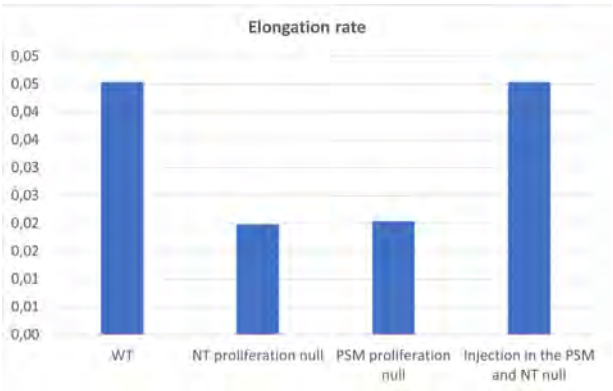

Figure 5.14 – Comparison of elongation rates (from left to right): in the wild type case, when NT proliferation rate is equal to 0, when PSM proliferation rate is equal to 0, when injection rates in the PSM and in the NT are equal to 0. The y-axis is in unit $\mu m/s$.

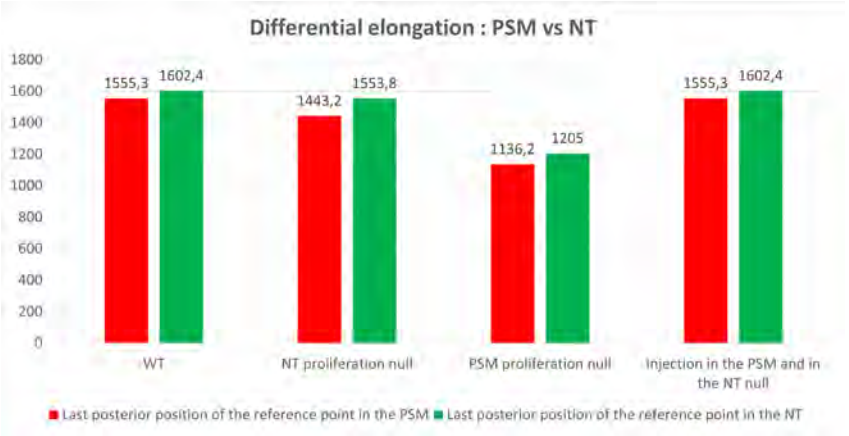

Figure 5.15 – Comparison of differential elongation (from left to right): in the WT case, when NT proliferation rate is equal to 0, when PSM proliferation rate is equal to 0, when injection rates in the PSM and in the NT are equal to 0. The y-axis is in microns.

elongation occurred. The tissues are not very dense as shown on the colorbar. The velocities in Figure 5.17b are very low which is congruent with the fact that little elongation happens in this case. **These results seem to suggest that cell injection alone is not sufficient to sustain the elongation process, and that proliferation is necessary for long-term tissue formation.**

5.7 Comparison with the biological data

Our numerical simulations mainly highlight the crucial role of cell proliferation, especially in the PSM, on long-term axis elongation, tissue formation and inter-tissue sliding, unlike cell injection from the PZ which seems to have little effect compared to cell proliferation.

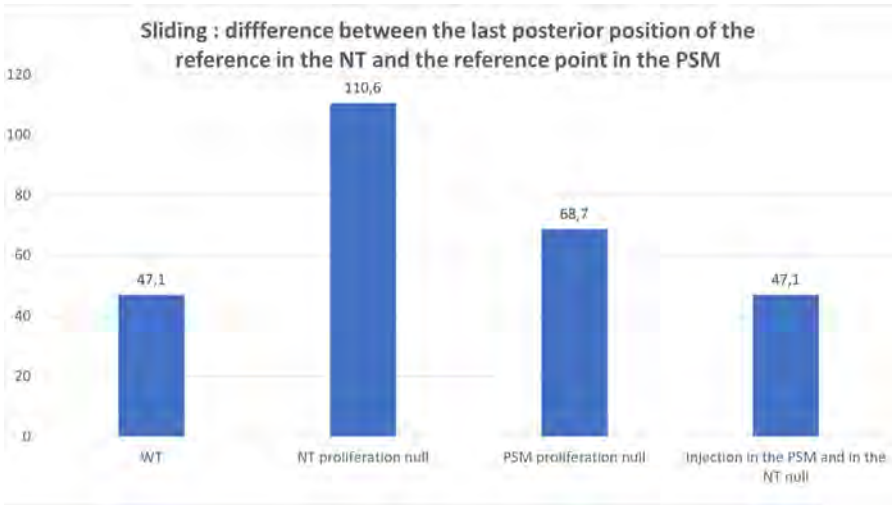

Figure 5.16 – Comparison of the inter-tissue sliding: difference of posterior travel distance between the NT and the PSM reference points from Figure 5.15. From left to right: in the wild type case, when NT proliferation rate is equal to 0, when PSM proliferation rate is equal to 0, when injection rates in the PSM and in the NT are equal to 0. The y-axis is in microns.

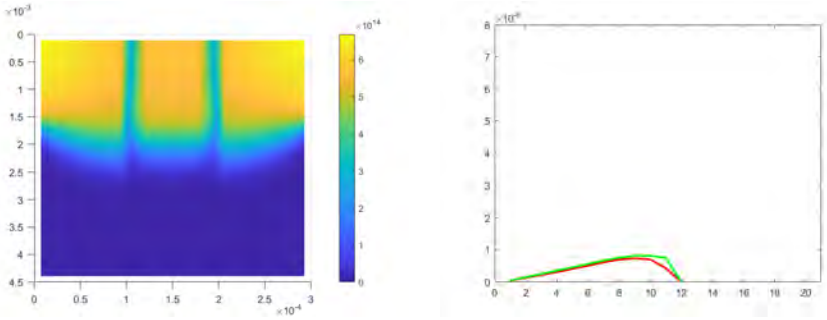

(a) Final time: no proliferation in the PSM and in the NT, only injection.

(b) Central velocities (NT in green, PSM in red): no proliferation in the PSM and in the NT, only injection.

Figure 5.17 – Densities at final time ($t = 12$ hours) in the case the proliferation rates in the PSM and in the NT are equal to zero and only injection is considered (Panel (a)). The y-axis is in meters. Central velocities of the NT in green and the PSM in red (Panel (b)) in the same case. The y-axis is in unit m/s (value of the velocity), the x-axis represents the mesh cells along the antero-posterior axis .

First and foremost, the results of the numerical simulations of the WT case match excellently the results *in vivo* found in [24]. Indeed, the density profiles reproduce well tissue formation, axis elongation and tissue densification along the antero-posterior axis. This is in accordance with the measured densities and tissue lengths in [24]. Our simulated WT case exhibits gradient profiles in the velocities in the PSM, which aligns with the measured velocities in [25]. Our model exhibits a gradient profile in the NT's velocity which matches the velocity measurements in [24]. Furthermore,

in the WT case, we show that tissues do not elongate towards the posterior at the same velocity which induces a sliding which we quantified. This sliding was first hypothesized and proposed in [24]. Our model confirms this hypothesis.

In addition, in [25] the authors compare the elongation rate of the WT chicken embryo with that of embryos with ablated tissues. Authors show that ablating the PZ has very little effect on axis elongation. Ablating the entire PZ tissue leads to the total inhibition of cell injection from the PZ into the PSM and NT. This is equivalent in our mathematical model, to the extreme case where we set the numerical cell injection rates κ_{PSM} and κ_{NT} to zero. Our numerical simulations showed that in this case, the elongation is not affected, nor is tissue formation. This is in accordance with the results in [25] on PZ ablations. Our model further proposes that inhibiting cell injection yields the same inter-tissue sliding as in the WT case. This means that cell injection has no effect on the sliding. On the other hand, our numerical simulations also confirm that the PSM growth is paramount during axis elongation. This is in accordance with [25] where authors show that ablating the posterior PSM severely impacts the elongation rate of the chicken embryo. This is equivalent in our numerical simulations to the extreme case where we set the numerical PSM cell proliferation rate g_2 to zero, see Figure 5.12c. Our numerical experiments showed that the elongation rate in this case, for long times (12 hours) was very small compared to the WT case, due to the lack of compression. This result is in accordance with the ablated posterior PSM case in [25]. Our model further suggests that both posterior tissues, the PSM and the NT, do not form properly in this case and elongate very little and have very low velocities. We also propose that in this case, cells travels much less to the posterior, and that inter-tissue sliding increases.

The numerical simulations which test the effect of differential proliferation on axis elongation and tissue formation predicted that, when the proliferation rate of the PSM is taken equal to that of the NT (which quantitatively implies a reduction of the proliferation rate in the PSM), the NT is significantly wider along the antero- posterior axis. To test this hypothesis, we acquired the live images of the transgenic quail embryos in [24]. The first set of live movies was of WT quail embryos. The second set was of quail embryos with electroporated P27 protein (cell cycle inhibitor) in the PSM which considerably down-regulates cell proliferation in the PSM. We compared the NT width in both sets at three locations along the antero-posterior axis: at the last formed somite, then $250\mu m$ lower to the last formed somite, then $500\mu m$ lower. The results are presented in Figure 5.18. We see that the NT width in the P27 treated embryos is wider than the NT in the WT case all along the antero-posterior axis. We performed a t-test on the collected data and found that the difference in NT width is significant. These measurements validate the mathematical model's predictions.

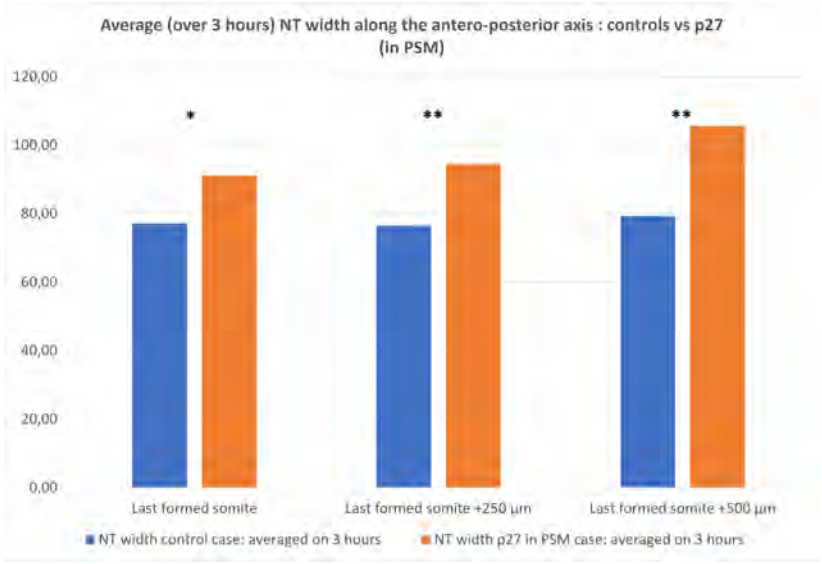

Figure 5.18 – Averaged NT width over three antero-posterior locations: at the last formed somite, $250\mu m$ lower, and $500\mu m$ lower, in the wild-type embryo (blue) and in the P27 in the PSM treated embryos (in orange). Stars indicate the significance of the t-test (p-value<0.05, $N = 7$ embryos).

5.8 Sensitivity analysis

The VMI is endowed with multiple parameters carefully calibrated to fit the biological data and to make the model as close as possible to the vertebrate embryo. In this section, we conduct a sensitivity analysis on the VMI through parameter variation. The objective is twofold. First, we want to test different scenarios in the VMI to understand which parameters affect the most the outputs of the model. This entails changing the parameters of growth, cell injection, viscosity, friction and congestion sensing and to analyze the consequent embryo behavior. Second, this sensitivity analysis allows to investigate scenarios where embryos have not taken the "normal" route of development and yet are able to form properly. This sensitivity analysis can therefore bring insight onto the heterogeneities found throughout the developmental stages of the vertebrate embryo.
In what follows, we vary each parameter at a time and run the simulation for 12 hours of biological time and look at the density profiles at final time and compare them to those of the WT simulation.

In Figure 5.19, the first phenomena we observe and which we emphasized on in Section 5.6 is the absence of tissue formation in the absence of cell proliferation, see Figure 5.19a, 5.19e. Interestingly, a reduction of cell proliferation by 60% yields some tissue formation, however, as we see in Figures 5.19b, 5.19f the pressure forces are insufficient to sustain normal formation and elongation. For example we see in Figure 5.19f that the NT is extremely slim as it does not have the appropriate density to resist the lateral pressure induced by the PSM, which becomes very wide. When we

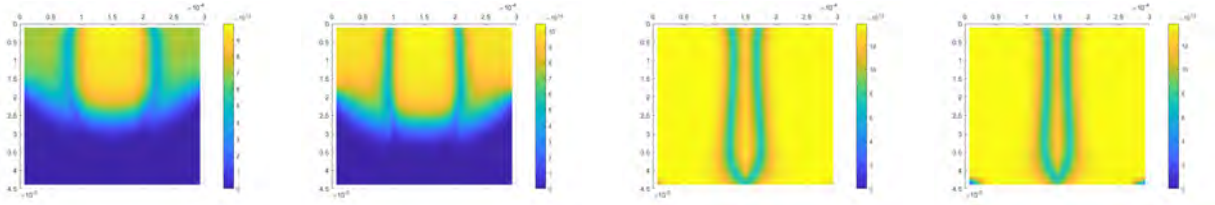

(a) PSM growth rate reduced by 100%.

(b) PSM growth rate reduced by 60%.

(c) PSM growth rate increased by 60%.

(d) PSM growth rate increased by 100%.

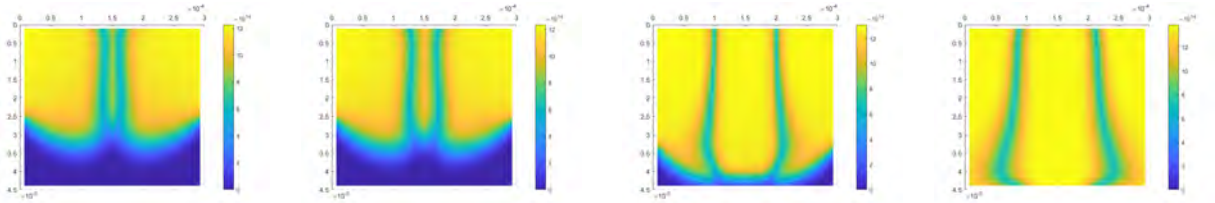

(e) NT growth rate reduced by 100%.

(f) NT growth rate reduced by 60%.

(g) NT growth rate increased by 60%.

(h) NT growth rate increased by 100%.

Figure 5.19 – Upper panel: densities at final time with the PSM growth rate reduced by 100% and 60% in respectively Panel (a) and Panel (b), and increased by 60% and 100% in respectively Panel (c) and Panel (d). Bottom panel: densities at final time with the NT growth rate reduced by 100% and 60% in respectively Panel (e) and Panel (f), and increased by 60% and 100% in respectively Panel (g) and Panel (h).

increase the growth rate of the PSM, and as it already proliferates faster than the NT, we first observe a substantial increase in tissue density (in the PSM). The PSM invades the NT making it slimmer (Figures 5.19c, 5.19d). The opposite phenomena occurs when the NT's proliferation rate is increased, as it becomes wider along the antero posterior axis, see Figures 5.19g, 5.19h. In both cases of growth increase (in the NT and in the PSM), we notice a significant increase in tissue elongation. Overall, we observe a clear sensitivity of the VMI to the growth parameters which affect tissue formation and dimensions, as well as elongation.

We next vary the injection parameters in each tissue, see Figure 5.20. We first note, as mentioned in Section 5.6, that inhibiting the injection in either of the two tissues does not affect the density shape nor elongation, see Figures 5.20a, 5.20d. We then increased the injection rate in the PSM (Figure 5.20b) and in the NT (Figure 5.20e) by 1200%, which corresponds respectively to an injection of $0.03614\,cells/second$ in the PSM and $0.1807\,cells/second$ in the NT. For comparison, we recall that the measured injection rate in the PSM is of $0.0278\,cells/second$ and in the NT of $0.0139\,cells/second$. We notice that this injection rate is still insufficient to affect the densities at final time. Finally, we increased the injection rate in the PSM (Figure 5.20c) and in the NT (Figure 5.20f) to $20\,cells/second$. The same conclusion holds. We note here that the injection rate

of $20\,cells/second$ is not biological and the simulation only depicts an extreme case. The densities in the VMI are therefore not greatly affected by the injection rate in the tissues.

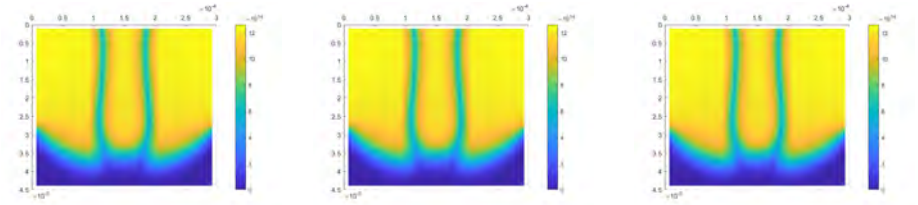

(a) PSM injection rate : $0\,cells/s$.

(b) PSM injection rate : $0.3614\,cells/s$.

(c) PSM injection rate : $20\,cells/s$.

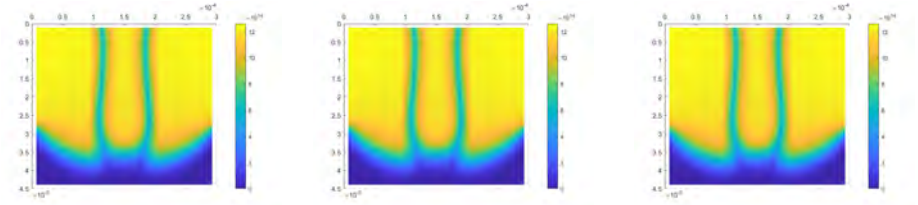

(d) NT injection rate : $0\,cells/s$.

(e) NT injection rate : $0.1807\,cells/s$.

(f) NT injection rate : $20\,cells/s$.

Figure 5.20 – Upper panel: densities at final time with the PSM injection rate equal to $0\,cells/s$, $0.3614\,cells/s$, and $20\,cells/s$ in respectively Panel (a), Panel (b), and Panel (c). Bottom panel: densities at final time with the NT injection rate equal to $0\,cells/s$, $0.1807\,cells/s$, and $20\,cells/s$ in respectively Panel (d), Panel (e), and Panel (f).

We now look at the sensitivity of the VMI with respect to the viscosity coefficients. In Figure 5.21, we observe very interesting and different phenomena than those observed in the Figure 5.19.

Looking at the upper panels, we see in Figure 5.21a that the PSM is much more fluid and surrounds the more viscous tissue (the NT), which cannot elongate any further. The NT is much wider than that of the WT case, and the PSM is slim anteriorly and expands posteriorly and invades the posterior space. As we consider the elongating tip to be the tip of the NT, we deduce that elongation is severely damaged in this case. When looking at the case of a 90% reduction of the NT's viscosity in Figure 5.21e, we observe a completely different phenomena. The NT is fluidified and undergoes lateral pressures from the PSM. This induces a tooth-paste-like effect where the PSM squeezes the NT out from the central axis of elongation and out of the posterior tip. A similar behavior, yet not to the same extent, is observed in Figure 5.21f with a 50% reduction of the viscosity of the NT. In Figures 5.21b, 5.21c, 5.21g we observe density profiles closer to the WT case, where elongation and tissue formation occur. We then simulated the case where the PSM's viscosity coefficient is increased by 150%, see Figure 5.21d. Interestingly, we observe the same phenomenon as the one in Figure 5.21f, that is, the PSM plays the role of two lateral rigid growing walls which squeeze the NT out of the posterior tip. When the NT's viscosity is increased

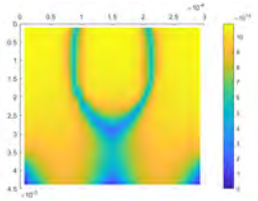

(a) PSM viscosity coefficient reduced by 90%.

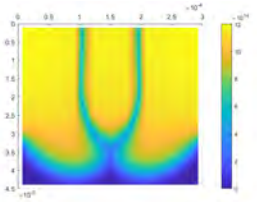

(b) PSM viscosity coefficient reduced by 50%.

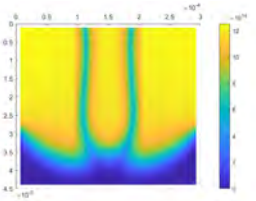

(c) PSM viscosity coefficient reduced by 10%.

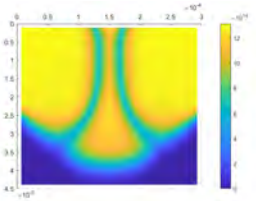

(d) PSM viscosity coefficient increased by 150%.

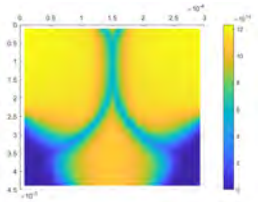

(e) NT viscosity coefficient reduced by 90%.

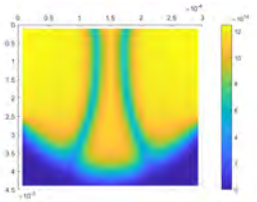

(f) NT viscosity coefficient reduced by 50%.

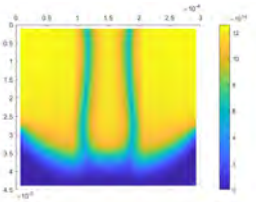

(g) NT viscosity coefficient reduced by 10%.

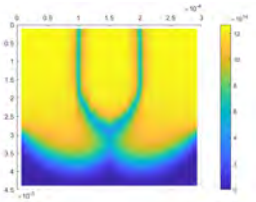

(h) NT viscosity coefficient increased by 150%.

Figure 5.21 – Upper panel: densities at final time with the PSM viscosity coefficient reduced by 90%, 50% and 10% in respectively Panel (a), Panel (b), and (c) and increased by 150% in Panel (d). Bottom panel: densities at final time with the PSM viscosity coefficient reduced by 90%, 50% and 10% in respectively Panel (e), Panel (f), and (g) and increased by 150% in Panel (h).

by 150%, the NT plays the role of a firm obstacle to the now fluid PSM (compared to the NT) which surrounds it. Similar behavior is observed in the Figure 5.21a. In conclusion, we observe a significant sensitivity of the VMI to the viscosity parameters. The visco-elastic properties of each of the NT and of the PSM and the balance between them seems to play a key role in the final density profiles.

In Figure 5.22, we vary the friction parameter while keeping it equal for both tissues.

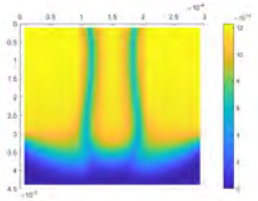

(a) Friction coefficient reduced by 90%.

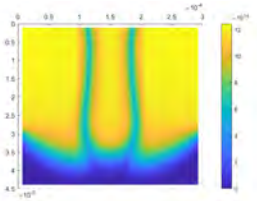

(b) Friction coefficient reduced by 50%.

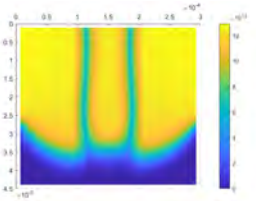

(c) Friction coefficient increased by 150%.

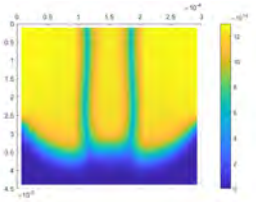

(d) Friction coefficient increased by 190%.

Figure 5.22 – Densities at final time with the friction coefficient reduced by 90% and 50% in respectively Panel (a), Panel (b), and increased by 150% and 190% in Panel (c) and Panel (d).

Generally, we observe that friction does not have a great effect on tissue density. However, we notice for example in Figure 5.22a that due to the friction reduction, the PSM's shape posteriorly

differs from the WT as friction with the lateral plate is less significant. Overall, we see that friction acts as a drag force on the tissues since we observe slightly less elongation in Figures 5.22c, 5.22d where friction is increased compared to the WT case and to Figures 5.22a, 5.22b.
We now turn our attention to the congestion pressure parameter ϵ, which controls the congestion sensing of the cells in the tissues.

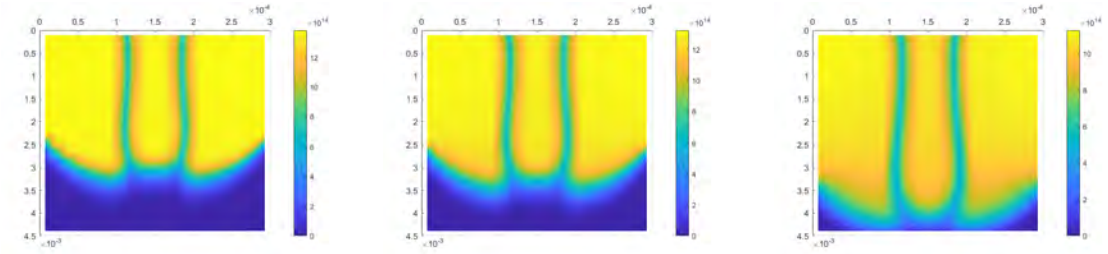

(a) Congestion-sensing coefficient (ϵ) reduced by 90%.

(b) Congestion-sensing coefficient (ϵ) reduced by 50%.

(c) Congestion-sensing coefficient (ϵ) increased by 150%.

Figure 5.23 – Densities at final time with the congestion-sensing coefficient (ϵ) reduced by 90% and 50% in respectively Panel (a), Panel (b), and increased by 150% in Panel (c).

In Figure 5.23, we see that the parameter ϵ affects the maximal densities reached by the tissues as well as the elongation rate, which motivated us to leave it as a free parameter to fit the appropriate elongation rate observed in the vertebrate embryo. In Figure 5.23a we observe that the tissues are extremely congested and dense and are not driven towards the posterior as much as in the WT case. In Figure 5.23c, the tissues are less dense compared to the WT, and elongation is more significant.

Overall, our sensitivity analysis reveals a clear effect of growth, viscosity, and congestion sensing on tissue density, formation, shape and elongation and overrules the role of cell injection.

5.9 The VMI for the PSM and the notochord

In this section, we explore the VMI with different embryonic tissues. We replace the NT in the VMI with the notochord and simulate the dynamics of the PSM and the notochord for 12 hours of biological time. The notochord is also an axial tissue (located ventrally to the NT) and is endowed with different properties than the NT. First, it proliferates much less, the cell cycle of notochord cells is of 28.06 hours, as measured in [24]. We use this parameter in our simulations. Second, it is less dense than the NT. In [24] authors measure the notochord density and find around $16 cells/\mu m^3$. We use this density in our simulations and project it in the 2D plane using the depth of the tissues $h = 50\mu m$. The notochord is not injected with new cells from the PZ, we set this

parameter to zero in our simulations. Finally, we set the viscosity of the notochord equal to that of the PSM. With these parameters, we run the simulation of the VMI and present the results in Figures 5.24-5.25.

In Figure 5.24a we immediately see that we recover the notochord's shape observed *in vivo*. Furthermore, due to its lower proliferation rate, the notochord is compressed laterally by the PSM. In Figure 5.24b we see that the notochord also exhibits a velocity gradient along the antero-posterior axis (in blue). Looking at the average velocities in Figure 5.24c, the notochord has a much higher velocity than that of the PSM, which is in line with the measurements in [24]. We took two reference points one in the PSM at $(35\mu m, 964\mu m)$ and one in the notochord at $(135\mu m, 964\mu m)$ and computed their posterior trajectories with respect to time (during 6 hours) using the central velocities shown in Figure 5.24c. The notochord's reference point (Figure 5.24d) travels much more towards the posterior than the reference point in the PSM. This is congruent with the fact that the central notochord velocity is much higher than that of the PSM. We noted the last posterior position of the two reference points in Figure 5.25a, and their difference in Figure 5.25b (right), compared to the PSM and NT in the WT simulation (left). We effectively see that the notochord reference point reaches $1854\mu m$ posteriorly compared to the PSM reference point which reaches around $1448\mu m$. The sliding between these two points attains $405\mu m$ which is 10 times bigger than the sliding we obtained when we ran the simulation with the PSM and the NT.

Our results match the velocity profile of the notochord in [24]. They also exhibit the very high sliding between the notochord and the PSM which was observed in [24], and which we quantify in our simulations. Finally, we see that the VMI is a model which can test the dynamics of many embryonic tissues and reproduce accurately their kinematics and can predict and quantify the possible inter-tissue sliding and velocity profiles.

5.10 Conclusion

In this chapter, we constructed a new model -the VMI- which we calibrated and compared to the biological data. The VMI in the WT case matches excellently the biological data measured in the vertebrate embryo. The model confirms the hypothesis that inter-tissue sliding occurs in the WT embryo. We ran multiple *in silico* experiments with different sets of parameters to test the effect of differential proliferation and of differential cell injection from the PZ on axis elongation and inter-tissue sliding. Our model suggests that differential injection does not affect the inter-tissue sliding nor axis elongation, which strongly favors the hypothesis that inter-tissue sliding is induced by differential proliferation in the WT embryo. The model shows that sliding increases when the NT proliferates more than its normal rate, and that sliding decreases when the PSM

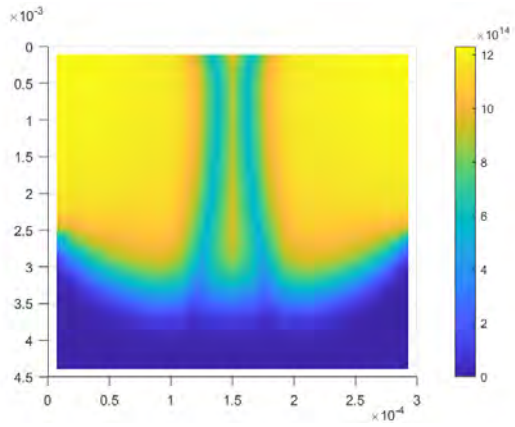

(a) Final time: the PSM (left and right tissue) and the notochord (middle tissue).

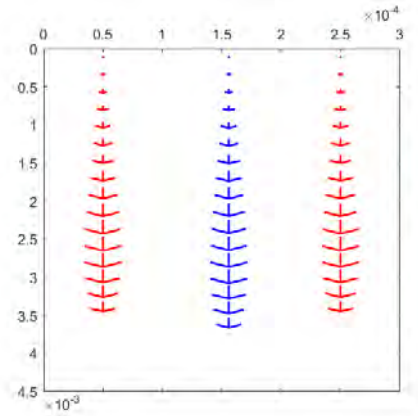

(b) The velocity vectors of the PSM (red) and of the notochord (blue) at $t = 12$ hours, along a section of the antero-posterior axis in each tissue.

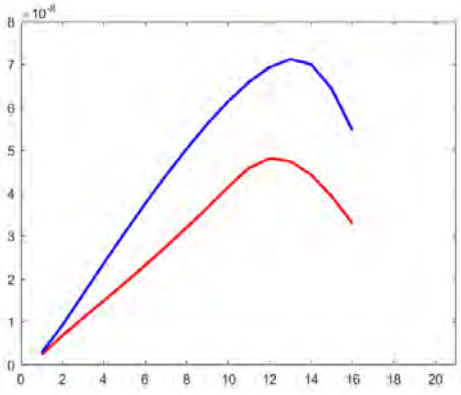

(c) Central velocities (notochord in blue and PSM in red) along the antero-posterior axis. The y-axis is in m/s (value of the velocity) and the x-axis represents the mesh cells along the antero-posterior axis.

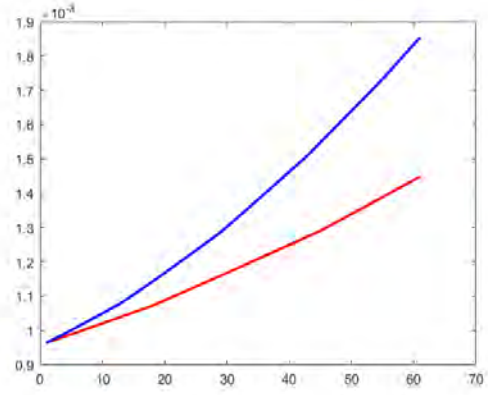

(d) Trajectories (y-component) with respect to time of two reference points one in the PSM (red) at $(35\mu m, 964\mu m)$ and one in the notochord (blue) at $(135\mu m, 964\mu m)$. The y-axis is in meters (representing the position along the antero-posterior axis) and the x-axis represents time.

Figure 5.24 – Panel (a): densities at final time ($t = 12$ hours) of the PSM (lateral tissue) and the notochord (axial tissue). Panel (b): velocities -y-component- of the notochord in blue and of the PSM in red at $t = 12$ hours along a section of the antero-posterior axis in each tissue. Panel (c): central velocities of the notochord (blue) and of the PSM (red) along the antero-posterior axis. The y-axis is in units m/s (value of the velocity) and the x-axis represents the mesh cells along the antero-posterior axis. Panel (d): trajectories (y-component) with respect to time of two reference points one in the PSM (red) at $(35\mu m, 964\mu m)$ and one in the notochord (blue) at $(135\mu m, 964\mu m)$. The y-axis is in meters, the x-axis represents time.

proliferates less than its normal rate. This result suggests that sliding is also directly related to the proliferation of each tissue independently. Our simulations further highlight the crucial role of

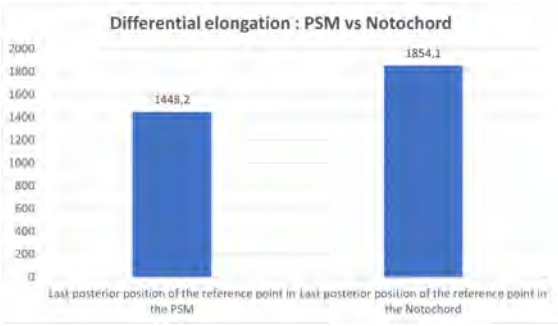

(a) Comparison of the differential elongation (final posterior position) of the trajectories of the reference point in the PSM (left) taken initially at $(35\mu m, 964\mu m)$ and the reference point in the notochord (right) taken initially at $(135\mu m, 964\mu m)$.

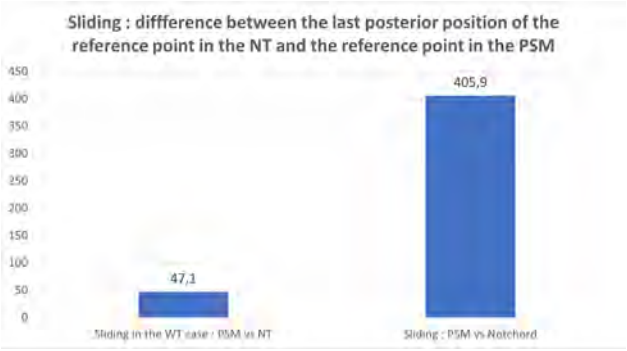

(b) Difference between the last posterior position of the reference point in the PSM and the reference point in the notochord (right), compared to the difference between the last posterior position of the reference point in the PSM and the reference point in the NT simulated in the wild-type case.

Figure 5.25 – Panel (a): last posterior position of the reference point in the PSM (left) and of the reference point in the notochord (right) at $t = 12$ hours. The y-axis is in microns. Panel (b): difference between the last posterior position of the reference point in the PSM and the reference point the notochord (right) compared to the difference between the last posterior position of the reference point in the PSM and the reference point in the NT simulated in the wild-type case. The y-axis is in microns.

cell proliferation on axis elongation and tissue formation and show that it is the main mechanism driving elongation on the long-term. We compared some of our model hypotheses, such as NT width, to the biological data and confirmed these hypotheses. We conducted a sensitivity analysis on the VMI and established the main parameters affecting the model outputs. We also used our model to simulate a different set of tissues, that is the PSM and the notochord, and showed that the model can also reproduce the dynamics observed *in vivo* and can predict interesting tissue behavior. The VMI proves to be polyvalent and multi-functional. Altogether, our results in this chapter give us a better understanding of the dynamics in the vertebrate embryo.

Chapter 6

Cell-to-cell heterogeneity in Sox2 and Bra expression guides progenitor motility and destiny

---

This chapter is taken from the paper [130] in collaboration with the Bénazéraf lab and Ariane Trescases.

Abstract

Although cell-to-cell heterogeneity in gene and protein expression within cell populations has been widely documented, we know little about its biological functions. By studying progenitors of the posterior region of bird embryos, we found that expression levels of transcription factors Sox2 and Bra, respectively involved in neural tube (NT) and mesoderm specification, display a high degree of cell-to-cell heterogeneity. By combining forced expression and down-regulation approaches with time-lapse imaging, we demonstrate that Sox2-to-Bra ratio guides progenitors' motility and their ability to stay in or exit the progenitor zone to integrate neural or mesodermal tissues. Indeed, high Bra levels confer high motility that pushes cells to join the paraxial mesoderm, while high levels of Sox2 tend to inhibit cell movement forcing cells to integrate the NT. Mathematical modelling captures the importance of cell motility regulation in this process and further suggests that randomness in Sox2/Bra cell-to-cell distribution favors cell rearrangements and tissue shape conservation.

RESEARCH ARTICLE

Cell-to-cell heterogeneity in Sox2 and Bra expression guides progenitor motility and destiny

Michèle Romanos[1,2†], Guillaume Allio[1†], Myriam Roussigné[1], Léa Combres[1], Nathalie Escalas[1], Cathy Soula[1], François Médevielle[1], Benjamin Steventon[3], Ariane Trescases[2], Bertrand Bénazéraf[1]*

[1]Molecular, Cellular and Developmenrtal biology department (MCD), Centre de Biologie Intégrative (CBI), Université de Toulouse, CNRS, UPS, Toulouse, France; [2]Institut de Mathématiques de Toulouse UMR 5219, Université de Toulouse, Toulouse, France; [3]Department of Genetics, University of Cambridge, Cambridge, United Kingdom

Abstract Although cell-to-cell heterogeneity in gene and protein expression within cell populations has been widely documented, we know little about its biological functions. By studying progenitors of the posterior region of bird embryos, we found that expression levels of transcription factors Sox2 and Bra, respectively involved in neural tube (NT) and mesoderm specification, display a high degree of cell-to-cell heterogeneity. By combining forced expression and downregulation approaches with time-lapse imaging, we demonstrate that Sox2-to-Bra ratio guides progenitor's motility and their ability to stay in or exit the progenitor zone to integrate neural or mesodermal tissues. Indeed, high Bra levels confer high motility that pushes cells to join the paraxial mesoderm, while high levels of Sox2 tend to inhibit cell movement forcing cells to integrate the NT. Mathematical modeling captures the importance of cell motility regulation in this process and further suggests that randomness in Sox2/Bra cell-to-cell distribution favors cell rearrangements and tissue shape conservation.

***For correspondence:** bertrand.benazeraf@univ-tlse3.fr

[†]These authors contributed equally to this work

Competing interests: The authors declare that no competing interests exist.

Funding: See page 18

Preprinted: 18 November 2020
Received: 15 January 2021
Accepted: 13 September 2021
Published: 05 October 2021

Reviewing editor: Marianne E Bronner, California Institute of Technology, United States

Introduction

Cells are the functional units of living organisms. During embryogenesis, they divide and specify in multiple cell types that organize spatially into tissues and organs. Specification events take place under the influences of the cell's own history and of environmental clues. Over the last years, access to new technologies has revealed that embryonic cells often display an unappreciated level of heterogeneity. For instance, gene expression analyses suggest that, within the same embryonic tissue, cells that were thought to be either equivalent or different are actually organized into a continuum of various specification states (***Farrell et al., 2018***; ***Wagner et al., 2018***). The impact of this new level of complexity on morphogenesis has not been extensively explored due to the difficulty of experimentally manipulating expression levels within targeted populations of cells in vivo. Progenitor cells located at the posterior tip of the vertebrate embryo, in an area known as the progenitor zone (PZ), constitute a great model to study how a population of stem-like cells develops into different cell types. The use of fluorescent tracers in bird and mouse embryos has revealed that cells of the PZ, called here posterior progenitors, contribute to formation of the presomitic mesoderm (PSM), the mesodermal tissue that generates muscle and vertebrae but also of the neural tube (NT), the neuro-ectodermal tissue that gives rise to the central nervous system (***Selleck and Stern, 1991***; ***Iimura et al., 2007***; ***Wilson and Beddington, 1996***; ***Psychoyos and Stern, 1996***). These studies also evidenced different cell behaviors with some cells exiting the PZ and others remaining resident

in this area. Grafting experiments next showed that resident posterior progenitors have the capacity to self-renew while providing new neural and mesodermal progenies (**Cambray and Wilson, 2002**; **McGrew et al., 2008**), thus indicating that the PZ contains progenitors of different tissues. Heterogeneity in the progeny of PZ cells was further confirmed by retrospective clonal analysis studies performed in the mouse embryo which revealed the existence of single progenitors, giving rise either to neural or mesodermal cells, but also of bi-potent progenitors, named neuro-mesodermal progenitors (NMPs), that generate both neural and mesodermal cells (**Tzouanacou et al., 2009**). The existence of bi-potent progenitors has since been shown at earlier stages of zebrafish development (**Attardi et al., 2018**) and in bird embryos (**Solovieva et al., 2020**; **Wood et al., 2019**; **Guillot et al., 2021**) (for reviews **Wymeersch et al., 2021**; **Sambasivan and Steventon, 2020**). Thus, to sustain the formation of tissues that compose the vertebrate body axis, the heterogeneous population of posterior progenitors must maintain an appropriate balance between the two choices of staying in place and self-renew or exit the progenitor region to contribute to the formation of the NT and the PSM. How this balance is established and controlled over time remains an open question.

Two transcription factors, Sox2 (SRY sex-determining region Y-box 2) and Bra (Brachyury), have been described for their respective roles in neural and mesodermal specification during embryonic development (**Herrmann et al., 1990**; **Bergsland et al., 2011**). Sox2 is known to be expressed in the neural progenitors that form the NT where it contributes to maintain their undifferentiated state. Its involvement in the neural specification has also been revealed by a study showing that ectopic expression of Sox2 in cells of the PSM is sufficient to reprogram these cells, which then adopt a neural identity (**Takemoto et al., 2011**). Bra protein was initially identified for its essential function in the formation of the paraxial mesoderm during the posterior extension phase (**Herrmann et al., 1990**; **Wilson et al., 1995**). Its crucial role in mesodermal specification has been demonstrated, in particular, by phenotypic study of chimeric mouse embryos composed of both Bra mutant and wild-type cells, and in which only wild-type cells are capable of generating posterior mesoderm (**Wilson and Beddington, 1997**). More recent studies have shown that Sox2 and Bra are expressed in posterior progenitors of developing embryos, indicating that activation of their expression takes place in progenitor cells before these cells colonize the NT or the PSM (**Olivera-Martinez et al., 2012**; **Wymeersch et al., 2016**; **Martin and Kimelman, 2012**). In addition, these studies have shown that both proteins are co-expressed in progenitor cells, an observation consistent with the presence of bi-potent progenitors in this tissue. Importantly, it has been found that mouse progenitors display regional differences in Sox2 and Bra expression levels with regions of higher Sox2 in the PZ being neural-fated, and those with higher Bra being mesoderm-fated (**Wymeersch et al., 2016**). Works done in mouse embryos and in in vitro systems derived from embryonic stem cells indicate that Bra and Sox2 influence the choice between neural and mesodermal lineages by their antagonistic activities on the regulation of neural and mesodermal gene expression (**Koch et al., 2017**; **Veenvliet et al., 2020**).

In this study, we aimed at understanding further the relationships between the processes of cell specification and tissue morphogenesis within the PZ, with a particular attention to cellular mechanisms underlying the tightly regulated balance between maintenance of residing posterior progenitors and production of exiting cells that contribute to the formation of mesodermal and neural tissues. By analyzing Sox2 and Bra expression in the PZ of the quail embryo, we show that these proteins are expressed with various levels from one cell to another, thus highlighting an important degree of cell-to-cell heterogeneity in this area. Using overexpression and downregulation approaches, we provide evidence that the relative levels of Sox2 and Bra proteins are a key determinant for posterior progenitor choice to stay in place or exit the PZ to join their destination tissues (neural and mesodermal). Time-lapse experiments further revealed that most posterior progenitors are highly migratory without strong directionality. Functional experiments then revealed that heterogeneous levels of Sox2 and Bra control cell motility: Bra promotes cell motility whereas Sox2 inhibits it indicating a crucial role of motility in guiding progenitors segregation. Mathematical modeling of this process suggests that the spatial distribution of Sox2/Bra heterogeneity is an important factor regulating morphogenesis. Indeed, while graded expression of Sox2/Bra confers a higher short-term stability in PZ shape, random distribution provides a higher rate of elongation, tissue fluidity, and long-term conservation of tissue shape.

Results

Levels of Sox2 and Bra proteins display high spatial cell-to-cell variability in the PZ

The transcription factors Sox2 and Bra are known to be co-expressed in progenitors of the PZ (***Olivera-Martinez et al., 2012***; ***Wymeersch et al., 2016***). As they differentiate from posterior progenitors, neural cells maintain Sox2 expression and downregulate Bra while mesodermal cells downregulate Sox2 and maintain Bra expression. Although Sox2 and Bra are recognized to be key players in driving neural and mesodermal cell fates, the spatial and temporal dynamics of these events remain to be elucidated. As a first step to address this question, we carefully examined the expression levels of the two proteins in the PZ of the quail embryo at stages HH10–11. As expected, analyses of immunodetection experiments revealed co-expression of Sox2 and Bra in nuclei of all PZ cells (***Figure 1A–C***) (n=8 embryos). Noticeably, we observed a high heterogeneity in the relative levels of Sox2 and Bra proteins between neighboring PZ cells. We indeed found intermingled cells displaying high Sox2 ($Sox2^{high}$) and low Bra (Bra^{low}) levels and, conversely, Bra^{high} and $Sox2^{low}$ levels as well as cells in which both proteins appear to be at equivalent levels. This cellular heterogeneity was very apparent when compared to the adjacent nascent tissues, that is, the NT and the PSM, where Sox2 and Bra protein levels were found to be very homogenous between neighboring cells (***Figure 1D–F***). Cell-to-cell heterogeneity in posterior progenitor was detected as early as stages HH5–6, a stage corresponding to initial activation of Sox2 and Bra co-expression in the quail embryo (***Figure 1—figure supplement 1***). We also observed heterogeneous levels of Sox2 and Bra proteins in PZ cells of chicken embryo, indicating that it is not a specific feature of quail (***Figure 1—figure supplement 2***). To infer how Sox2 and Bra protein levels go from being co-expressed in a heterogeneous manner in the PZ to being expressed homogeneously in the nascent tissues, we analyzed variations of their respective levels in a series of seven volumes (containing around 100 cells in each volume) located in a posterior to anterior path (from the PZ to the maturating tissues), corresponding to putative trajectories of PSM or NT cells (***Figure 1G–G'***). Data showed that the average expression level of Sox2 increases (+2.22 folds, n=7 embryos) while that of Bra decreases (−3.81 folds) following the neural path (***Figure 1G***). On the contrary, along the paraxial mesoderm path, the average expression level of Sox2 decreases (−2.12 folds, n=7 embryos) while Bra level first increases in the posterior PSM (1.14 folds, positions 1–2) and decreases anteriorly (−5.06 folds, positions 2–7) (***Figure 1G'***). Next, to define whether the cellular heterogeneity found in the PZ depends more on variability of one of the two transcription factors, we quantified protein levels per nuclei of cells populating the PZ. By plotting Sox2 and Bra levels in individual cells, we noticed a broader distribution for Sox2 levels (coefficient of variation of 41.8%) compared to Bra levels (coefficient of variation of 30.75%) (***Figure 1H***), indicating that the cell-to-cell heterogeneity in the PZ is preferentially driven by differences in Sox2 levels. To quantify Sox2 and Bra heterogeneity, we calculated the Sox2-to-Bra ratio (Sox2/Bra) for each cell of the PZ as well as for cells of the NT and PSM, and compared these values. Our data showed high divergences between the three tissues and confirmed the high heterogeneity previously observed in PZ cells (***Figure 1I***). It must however be noticed that these quantitative data revealed a broad range of cell distribution, highlighting, in particular, the presence of cells in the PZ displaying similar Sox2/Bra values as mesodermal or neural cells. We next asked whether the cellular heterogeneity caused by differences in Sox2 and Bra levels is present in the whole volume of the PZ or displays regionalization in this tissue. To address this issue, we analyzed spatial distribution of the Sox2/Bra values on optical transverse sections performed at anterior, mid, and posterior positions of the PZ (***Figure 1J–J'''***). This analysis confirmed the heterogeneity of Sox2/Bra values which are equally represented in the mid area of the PZ (***Figure 1J''***). Cells with a high ratio level ($Sox2^{High}$ Bra^{Low}) were found to be more represented in the most dorso-anterior part of the PZ (***Figure 1J'***) and cells with a low ratio level (Bra^{High} $Sox2^{Low}$) were found to be more represented in the most posterior part of the PZ (***Figure 1J'''***). This particular antero-posterior distribution was further confirmed by tissue expression analysis (***Figure 1—figure supplement 3***). However, it should be noted that variations of Sox2/Bra values were noticed in all these areas, indicating that the Sox2/Bra-related cell-to-cell heterogeneity is present in the whole PZ.

Altogether, our data, highlighting significant variability in Sox2 and Bra protein levels within neighboring progenitors of the PZ, evidence an extensive cell-to-cell heterogeneity of this cell population. Noticeably, despite an overall enrichment of $Sox2^{high}$ cells in the dorsal-anterior part of the

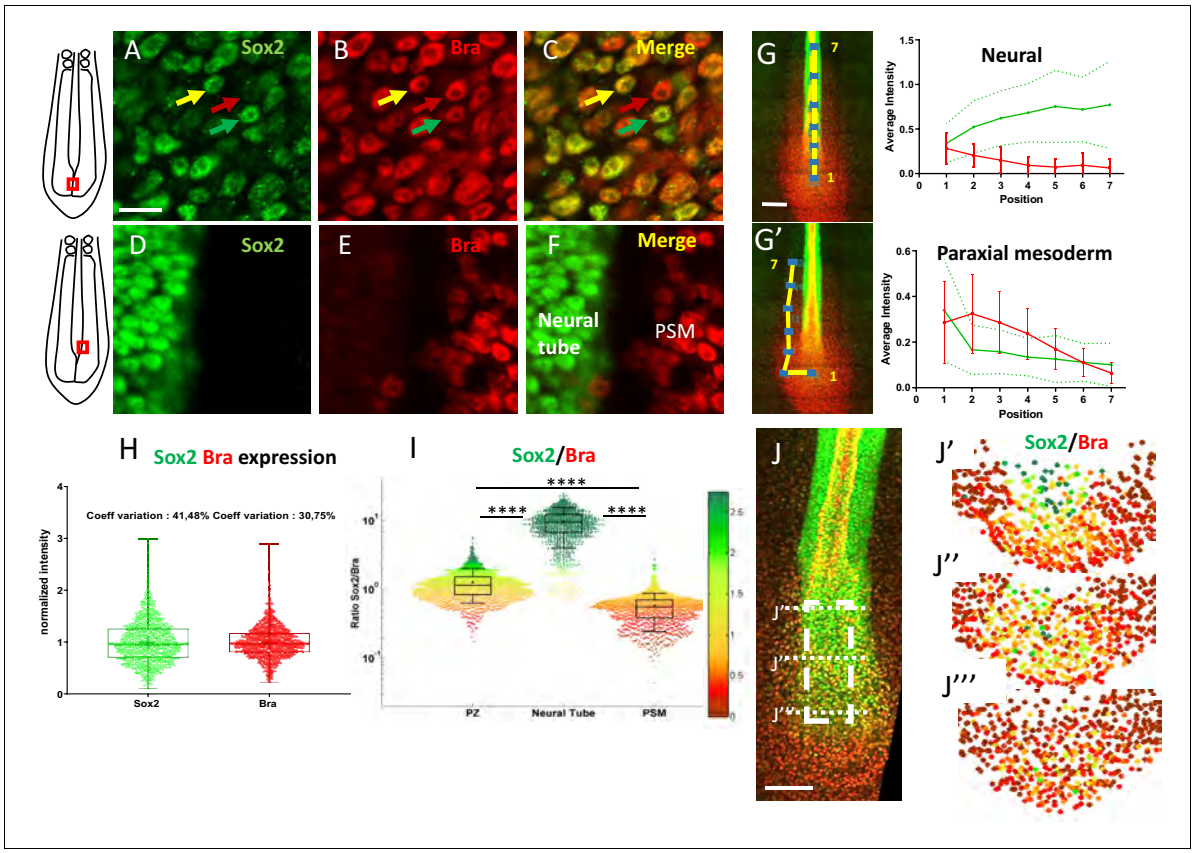

Figure 1. Posterior progenitors co-express Sox2 and Bra with a high degree of cell-to-cell heterogeneity. (**A–F**) Immunodetection of Sox2 (green) and Bra (red) analyzed at the cellular scale in the caudal part of stage HH11 quail embryo, either in the PZ (**A–C**) or in the nascent NT and the PSM (**D–F**). Overlay images are presented in (**C**) and (**F**). Note cell-to-cell heterogeneity in Sox2 and Bra levels in the PZ, with neighboring cells expressing higher level of Bra (red arrow), higher level of Sox2 (green arrow), or comparable levels of both proteins (yellow arrow), a feature not apparent in the nascent NT and PSM tissues. (**G, G'**) Measurements of Sox2 and Bra levels along putative trajectories (yellow lines) of NT (**G**) and PSM (**G'**) cells. Fluorescence measurements (blue squares, left images), numbered from 1 to 7, red bars and green dashed lines are errors bars (variability between embryos). (**H**) Distribution of normalized cell-to-cell expression of Sox2 and Bra in the PZ (n=8 embryos). (**I**) Cell distribution of Sox2/Bra levels in the PZ (n=9 embryos), the NT (n=7 embryos), and the PSM (n=8 embryos); ratios have been color-coded according to a red (higher Bra) to green (higher Sox2) scale shown on the right side. (**J–J'''**) Representation of the Sox2-to-Bra ratio (green to red same as (**I**)) in digital transversal sections (40 µm) made in the PZ (dashed lines in the double immunodetection image in (**J**)). Scale bars=10 µm in (**A–F**), 100 µm in (**G**) and (**J**). NT, neural tube; PSM, presomitic mesoderm; PZ, progenitor zone.

The online version of this article includes the following figure supplement(s) for figure 1:

Figure supplement 1. Sox2 and Bra protein co-expression and cell-to-cell heterogeneity start around stage HH5 in quail embryos.

Figure supplement 2. Chicken PZ cells co-express Sox2 and Bra proteins with a high degree of cell-to-cell heterogeneity.

Figure supplement 3. Sox2 and Bra expression patterns in PZ cells follow opposite gradients at the tissue level.

PZ and Bra^{high} cells in the most posterior part, no clear spatial regionalization of these cells was detected, indicating that the PZ is composed of a complex mixture of cells displaying variable Sox2/Bra levels. This variability is further lost as cells enter the NT or the PSM.

Relative levels of Sox2 and Bra in PZ cells influence their future tissue distribution

The fact that cell-to-cell heterogeneity caused by differences in the Sox2 and Bra levels is observed in PZ cells but not in the PSM and the NT cells was suggestive of a role of these relative protein levels in the decision to leave or not the PZ and to locate in a specific tissue. To test this possibility, we developed functional experiments aimed at increasing or decreasing Sox2 and Bra levels in PZ cells. In the early bird embryo (stages HH4–7), the future posterior progenitors are initially located in anterior epithelial structures: the epiblast and the primitive streak. We thus performed targeted electroporation of progenitors in the anterior primitive streak/epiblast of stage HH5 embryos to transfect expression vectors or morpholinos and further analyzed the subsequent distribution of targeted

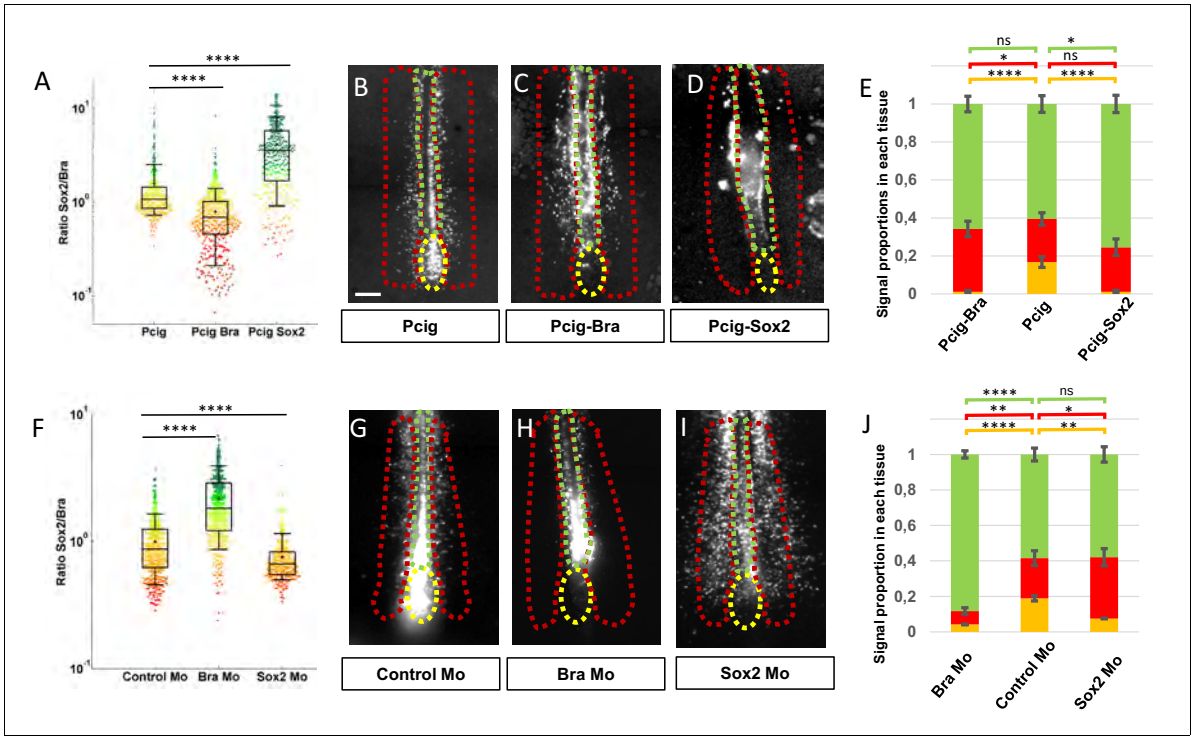

Figure 2. Sox2 and Bra levels are critical for progenitor maintenance and tissue distribution. (**A, F**) Sox2-to-Bra ratios calculated following Bra and Sox2 double immunodetection in the PZ performed 7 hr after electroporation. Values were normalized to the average ratio of non-transfected cells of the same region. (**A**) Sox2/Bra values in cells transfected with Bra (Pcig-Bra) and Sox2 (Pcig-Sox2) expression vectors compared to cells transfected with the empty vector (Pcig). (**F**) Sox2/Bra values in cells transfected with morpholinos directed against Bra (Bra-Mo) or Sox2 (Sox2- Mo) compared to cells transfected with a Control-Mo. Ratios were calculated on the basis of 286–590 cells and 3–5 embryos per condition. (**B–D**), (**G–I**) Ventral views of embryos collected 20 hr after electroporation showing the GFP signals (white). The PZ, the PSM, and the NT are delineated by yellow, red, and green dash lines, respectively. Expression vectors or morpholinos used are indicated below each picture. Scale bar=100 µm. (**E, J**) Staked histograms displaying the proportion of cells in the PZ (yellow), the PSM (red), and the NT (green). For each experimental condition, proportion of cells in a given tissue was compared to the same tissue of control embryos by unpaired Student's test (n=27 embryos for Pcig-Bra, n=21 embryos control for Pcig, and n=23 embryos for Pcig-Sox2; n=28 embryos for Bra-Mo, n=27 embryos for Control-Mo, and n=28 embryos for Sox2-Mo). Error bars represent the SEM. NT, neural tube; PSM, presomitic mesoderm; PZ, progenitor zone.

The online version of this article includes the following figure supplement(s) for figure 2:

Figure supplement 1. Efficient deregulation of Sox2 and Bra following electroporation of expression vectors and morpholinos.

Figure supplement 2. Quantification of Sox2 and Bra protein levels following electroporation of expression vectors and morpholinos.

Figure supplement 3. Effect of Sox2 and Bra overexpression on apoptosis and proliferation.

Figure supplement 4. Tissue localization of transfected cells after Sox2 and Bra overexpression and downregulation.

cells, focusing on the PZ, the PSM, and the NT (***Figure 2***). As early as 7 hr after electroporation, we could detect the expected modifications of Sox2 or Bra expression in PZ cells for both overexpression and downregulation experiments (***Figure 2—figure supplements 1*** and ***2***). We observed a significant decrease in the Sox2/Bra levels by either overexpressing Bra or downregulating Sox2 and a significant increase of this ratio when Sox2 was overexpressed or when Bra was downregulated (***Figure 2A,F***). After transfection of expression vectors or morpholinos, we next let the embryos develop until stages HH10–11 and examined fluorescent cell distribution in the different tissues. For this, we measured the fluorescence intensity of the reporter protein (GFP) in the PZ, the PSM, and the NT and calculated the percentage of fluorescence in each tissue. We obtained reproducible data using control expression vector with less than 20% of the fluorescent signal found in the PZ (16.78±2.83%), a little more than 20% in the PSM (22.64±3.30%), and about 60% in the NT (60.57±4.39%) (***Figure 2B,E***). We next found that overexpression of Bra leads to a marked reduction of the fluorescent signal in the PZ (1.17±0.57%) and to an increased signal in the PSM (33.04±4.06%) but has no effect on the NT signal (***Figure 2B,C,E***). Elevating Bra levels is thus sufficient to trigger cell exit from the PZ and to favor integration in the PSM. However, this is not sufficient to impede PZ cell contribution to form the NT. Similarly, we found that overexpression of Sox2 drives exit of the cells from the PZ (1.16±0.67%) favoring their localization in the NT (75.40±4.57%) without significantly affecting proportions of cells in the PSM (***Figure 2B,D,E***). To verify that the differences in fluorescence distributions we observed did not result from distinct apoptotic or proliferation rates, we quantified these parameters 7 hr after electroporation. Our data showed no major changes between the different experimental conditions, validating that protein misregulations indeed act by influencing the distribution of cells in the different tissues (***Figure 2—figure supplement 3***). Spatial distribution of the fluorescent signals obtained using control morpholinos appeared very similar to thoseobserved using the control expression vector (18.93±3.06%, 22.68±4.09%, and 58.38±3.63% for the PZ, the PSM, and the NT, respectively) (***Figure 2G,J***). We found that downregulation of Bra leads to exit of cells from the PZ (4.16±1.57%) and favors cell localization in the NT (88.23±2.04%) at the expense of the PSM (7.59±1.81%) (***Figure 2G,H,J***). Similarly, Sox2 downregulation triggers cell exit from the PZ (7.50±2.35%) and, as expected, leads to higher contribution of cells to the PSM (34.59±4.79%) but this does not occur at the expense of cell contribution to the NT (***Figure 2G,I,J***). These data have been validated by observation of cell distribution on transverse sections (***Figure 2—figure supplement 4***). It must be noticed that, transverse sections showed the presence of a large proportion of Bra-overexpressing cells located in the medial part of the paraxial mesoderm, very close to the NT, while only a few Bra-overexpressing cells were indeed located in the NT. We thus cannot exclude the possibility that, due to this particular cell distribution, the NT signal quantified on whole-mount embryos might have been slightly overestimated (***Figure 2E***). Even if it were the case, it does not question our main conclusions that Bra overexpression, in comparison to control conditions, favors the exit of progenitors from PZ and their subsequent localization into the paraxial mesoderm.

These data, showing that changing the Sox2-to-Bra ratio, tending either toward higher or lower values, is sufficient to trigger cell exit from the PZ, evidence that the relative levels of Sox2 and Bra proteins are the key determinant of PZ cell choice to stay in the PZ or exit this area to enter more mature tissues. Our data also point to the critical influence of the relative levels of Sox2 and Bra in controlling the final destination of cells exiting the PZ, with $Sox2^{high}$ (Bra^{low}) cells and Bra^{high} ($Sox2^{low}$) cells preferentially integrating the NT and the PSM, respectively.

PZ cells are highly motile without strong directionality

To better characterize the movements of posterior progenitors, either staying resident to the PZ or exiting this area, we examined their behaviors using live-cell imaging. We electroporated quail embryos at stage HH5 with a vector encoding for nuclear GFP and performed time-lapse imaging experiments from stage HH8 to stage HH12. At these stages (from stage HH8 onward), posterior progenitors are no longer located in the dorsal epithelium but rather within a dense and internal mesenchymal structure that prefigures the embryonic tailbud (***Schoenwolf and Delongo, 1980*** ; ***Guillot et al., 2021***). In order to compare migration properties between tissues, we focused on the PZ , the PSM and on the posterior NT (***Figure 3A***, ***Figure 3—video 1***). Because the three tissues have a global movement directed posteriorly due to the embryonic elongation, we generated two types of cellular tracking: the raw movement, in which the last-formed somite is set as a reference

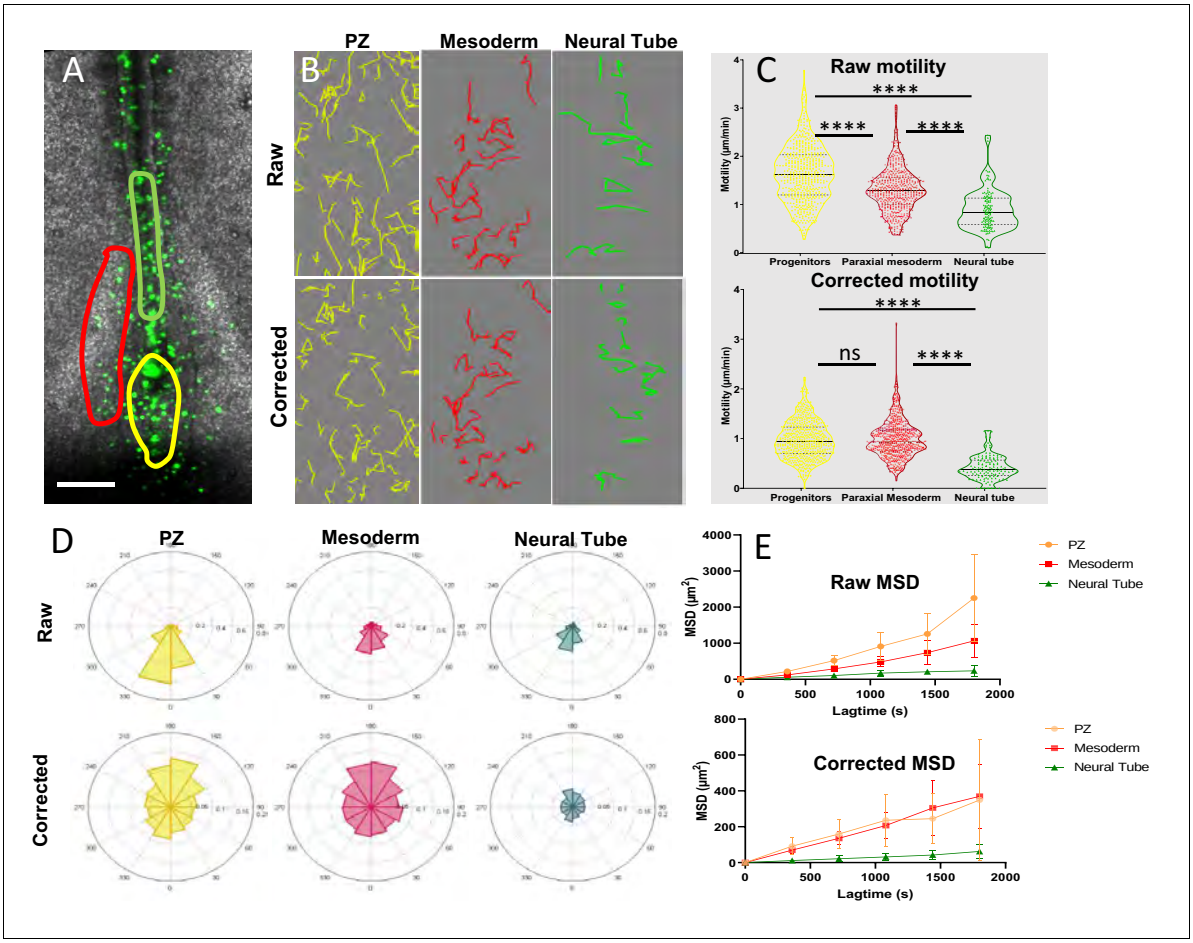

Figure 3. Progenitors display high motility without strong directionality. (**A**) Representative image of an H2B-GFP electroporated quail embryo (ventral view) analyzed by live imaging . Transfected cells are detected by the GFP signal (green) . The PZ, the nascent PSM, and the NT are delineated by yellow, red, and green lines respectively. (**B**) Examples of cell trajectories before (raw) and after tissue motion subtraction (corrected). (**C**) Distribution of the raw (top) and corrected (bottom) cell motilities computed in the different regions. (**D**) Directionality of motion assessed by the distribution of angles weighed by the velocity for the different regions, before and after tissue subtraction. (**E**) Assessment of diffusion by analysis of the mean squared displacement in function of time for the different regions (n=7 embryos, 538 cell trajectories analyzed in the PZ, 496 in the PSM, and 128 in the NT). Scale bar=100 µm. NT, neural tube; PSM, presomitic mesoderm; PZ, progenitor zone.

The online version of this article includes the following video and figure supplement(s) for figure 3:

Figure supplement 1. Distribution of motility frequencies.

Figure 3—video 1. Cellular migration in PZ, NT and PSM (corresponding to ***Figure 3***).

https://elifesciences.org/articles/66588#fig3video1

Figure 3—video 2. Progenitor migration expressing NLS-Scarlet and Sox2 reporter (N1N2-eGfp-Dest) (corresponding to ***Figure 3—figure supplement 1B***).

https://elifesciences.org/articles/66588#fig3video2

Figure 3—video 3. Posterior progenitor migration (corresponding to ***Figure 3***).

https://elifesciences.org/articles/66588#fig3video3

point, and the 'corrected' movement, in which the cellular movements are analyzed in reference to the ROI (***Figure 3B***). Tracking cell movements allowed for quantification of motility distribution, directionality of migration, and time-averaged mean squared displacement (MSD) (n=7 embryos) (***Figure 3C–E***) . First, we noticed that the average raw motility of PZ cells is higher than that of PSM or NT cells (***Figure 3C***, top panel). Raw directionality was also found more pronounced for PZ cells in the posterior direction compared to PSM or NT cells (***Figure 3D***, upper panel). These results thus confirm that the PZ is moving faster in a posterior direction than surrounding tissues, as previously measured using transgenic quail embryos (***Bénazéraf et al., 2017***). Analysis of local (corrected) motility revealed that PZ cells move in average as fast as PSM cells and significantly faster than NT cells (***Figure 3C***, bottom panel). The distribution of individually corrected PZ cell motilities is however different from the ones of PSM cells as analysis in the PZ showed slower moving cells (PZ corrected motility violin plot in ***Figure 3C*** is larger for slow values than the PSM counterpart and ***Figure 3—figure supplement 1A***), indicating that the motile behavior of PZ cells is more heterogeneous than that of PSM cells. To further characterize the heterogeneity of PZ cell motile behaviors, we co-electroporated a vector coding for a nuclear marker (NLS-Scarlet) with a Sox2 reporter that drives the expression of a destabilized form of eGFP (N1N2-eGFP-Pest). The fluorescence threshold was then adjusted so that only cells emitting high eGFP signal, that is, $Sox2^{high}$ cells, were detected. We then compared motilities of progenitors emitting or not the eGFP fluorescent signal and found that negative cells are more motile than positive cells (***Figure 3—figure supplement 1B***, ***Figure 3—video 2***), thus confirming diversity in cell motile behaviors within the PZ and pointing to cells expressing Sox2 as the least motile cells. As previously reported (***Bénazéraf et al., 2010***), we found that, after tissue correction, the motion of PSM cells was mostly non-directional with, however, a slight tendency toward anterior direction which is expected due to the posterior elongation movements of the reference tissue (***Figure 3D***, red plot in the lower panel). The distribution of corrected angles of PZ cell motilities was also found globally non-directed, with however a slight tendency toward anterior direction, to some extent more pronounced than for PSM cells, suggesting that our method is able to detect trajectories of cells exiting the PZ to integrate the NT or the PSM (***Figure 3D***, yellow plot lower panel). Examination of individual cell tracks further confirmed extensive non-directional local migration and neighbor exchanges within the PZ (***Figure 3—video 3***). As PZ cell movement was found being mostly non-directional, we next looked at their diffusive motion by plotting their MSDs, measured in each tissue over time, as it has been previously done for PSM cells (***Bénazéraf et al., 2010***). This analysis showed that the MSD of posterior progenitors is linear after tissue subtraction, as intense as the MSD of PSM cells and significantly higher than that of NT cells, thus demonstrating the diffusive nature of PZ cell movements (***Figure 3E***).

Taken together, these data evidenced that, in the referential of the progenitor region, PZ cell migration is diffusive/without displaying strong directionality (except a slight anterior tendency), with an average motility that is comparable to that of PSM cells and that is significantly higher than that of NT cells. The motility of individual PZ cells is however heterogeneous with some cells exhibiting high motile behavior, as do PSM cells, and others, characterized by higher levels of Sox2 expression, displaying low motility comparable to that of NT cells.

The Sox2-to-Bra ratio controls motility of PZ cells

To test if Sox2 and Bra could influence progenitor choice of staying in or exiting the PZ and contribute to NT or PSM by controlling cellular motility, we designed experiments combining functional assay and time-lapse imaging in vivo. Sox2 and Bra were either overexpressed or downregulated in PZ cells and the behaviors of posterior progenitors were followed by time-lapse imaging (***Figure 4A–F***). We first monitored raw cell motilities (***Figure 4—figure supplement 1***) and conducted subtraction of the tissue motion to gain insight into local motility and directionality (***Figure 4***). We found that Bra-overexpressing PZ cells display higher motility without significant differences in directionality when compared to control cells. By contrast, when PZ cells overexpress Sox2, we detected a significant reduction of their motility accompanied by an anterior bias in angle distribution compared to control cells (***Figure 4B,C,D***, and ***Figure 4—video 1***). We found that Bra downregulation leads to similar significant reduction of cell motility, as well as a change in directionality toward the anterior direction (***Figure 4B,E,F***). Conversely, Sox2 downregulation did not result in significant effect on average cell motility or directionality, even though a tendency toward a slight increase in motility was noticed (***Figure 4B,E,F*** and ***Figure 4—video 2***). To test if Sox2 and Bra act

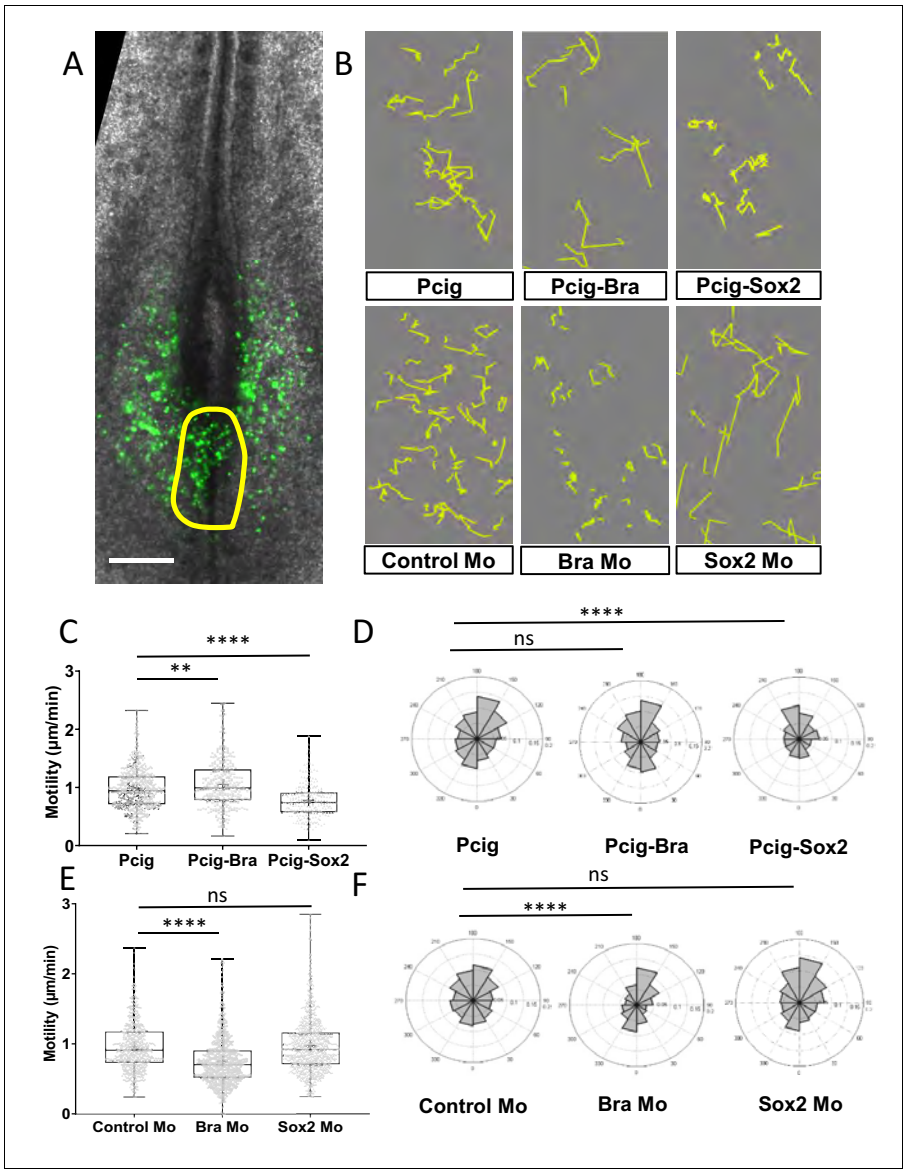

Figure 4. Sox2 and Bra deregulations affect progenitor motility. (**A**) Representative image of a Pcig electroporated quail embryo (ventral view) used to perform progenitor tracking and motility analysis. Transfected cells are detected by the GFP-signal (green) and the PZ is delineated by the yellow line. (**B**) Examples of cell tracks after correction in embryos electroporated with expression vectors or morpholinos indicated on each panel. (**C**, **E**) Distribution of PZ cell motilities after tissue motion subtraction in gain of function (**C**) and in downregulation (**E**) experiments. (**D**, **F**) Directionality of cell motion after tissue motion subtraction assessed by the distribution of angles in gain of function (**D**) and in downregulation (**F**) experiments (n=7 embryos and 541 trajectories for Pcig, n=5 embryos and 307 trajectories for Pcig-Bra, and n=5 embryos and 234 trajectories for Pcig-Sox2; n=5 embryos and 590 trajectories for Control-Mo, n=7 embryos and 753 trajectories for Bra-Mo, and n=5 Embryos and 874 trajectories for Sox2-Mo). Scale bar=100 µm. PZ, progenitor zone.

The online version of this article includes the following video and figure supplement(s) for figure 4:

Figure supplement 1. Effects of Sox2 and Bra on raw cell and tissue movements.

Figure supplement 2. Cell differentiation in response to Sox2 and Bra overexpression.

Figure 4 continued on next page

Figure 4 continued

Figure 4—video 1. Progenitor migration in Sox2 and Bra overexpression experiments (Corresponding to ***Figure 4***).
https://elifesciences.org/articles/66588#fig4video1

Figure 4—video 2. Progenitor migration in Sox2 and Bra Mo experiments (Corresponding to ***Figure 4***).
https://elifesciences.org/articles/66588#fig4video2

on motility downstream of neural and mesodermal differentiation processes, we checked the differentiation status of progenitors 7 hr after transfection, at a time when progenitors overexpressing Sox2 or Bra have not yet exited the PZ but when effects of Sox2 or Bra misregulation on cell motility can already be measured (data not shown). We found that neither the neural marker Pax6 nor the mesodermal marker Msgn1 was induced in PZ cells overexpressing Sox2 and Bra, respectively (***Figure 4—figure supplement 2***). These data thus strongly support the view that the effects of Sox2 and Bra on PZ cell motility is not a consequence of a drastic change in the differentiation process of progenitor cells.

These data, showing that changing the respective levels of Sox2 and Bra is sufficient to modulate PZ cell motility/migration properties, highlight a key role for these transcription factors in controlling PZ cell movements with Sox2 and Bra inhibiting and promoting cell motility, respectively. When cells have high Sox2/Bra levels, they migrate less and are left behind the PZ to be integrated into the NT. When cells have a low Sox2/Bra ratio, they tend to migrate more, mostly in a diffusive manner, explaining how they leave the PZ to be integrated into the surrounding PSM tissues.

Modeling spatial cellular heterogeneity and tissue morphogenesis

Our data showed that different levels of Sox2 and Bra affect progenitor motility and regulate their contribution to neural and mesodermal tissues. Cells displaying various levels of these proteins were found intermingled in all regions of the PZ, raising the question of the importance of apparent randomness in their spatial distribution on morphogenesis. Because this question is extremely difficult to tackle experimentally, we turned to agent-based mathematical modeling (***Figure 5***). We set up a model representing developmental times ranging from stage HH8 to stage HH12, a period when the NT, the PSM, and the PZ have already been formed. As there are few dorso-ventral tissue deformations during the selected time window (***Bénazéraf et al., 2017***), we designed a 2D model (X, Y). In this model, PZ cells express dynamic Sox2/Bra levels with a defined probability to switch into a Bra^{high} ($Sox2^{low}$) state (PSM state) or into a $Sox2^{high}$ (Bra^{low}) state (NT state). The motility is directly controlled by the Sox2-to-Bra ratio: Bra^{high} ($Sox2^{low}$) cells display high motility, $Sox2^{high}$ (Bra^{low}) cells display low motility, and undetermined progenitors, meaning cells in which the Sox2-to-Bra ratio is still fluctuating, display intermediate motility (***Figure 5A***). Based on the known cell-cell adhesion properties of NT ($Sox2^{high}$) and PSM (Bra^{high}) cells, we also considered the Sox2-to-Bra ratio as controlling cellular adhesion so that $Sox2^{high}$ (Bra^{low}) cells adhere more to each other than Bra^{high} ($Sox2^{low}$) cells. We as well integrated a non-mixing property between cell types in a way that physical boundaries are maintained between tissues (Appendix 1). Finally, we implemented cell proliferation rates and tissue shape to be as close as possible to biological measurements (***Bénazéraf et al., 2017*** Appendix 1). This framework allowed us to model different types of Sox2/Bra spatial distributions within the PZ. We first simulated a distribution that recapitulates the biological data, combining random cell distribution and gradient patterning, that is,. cell-to-cell variations combined with an enrichment in $Sox2^{high}$ cells anteriorly and in Bra^{high} cells posteriorly, as seen in ***Figure 1J*** (***Figure 5B***). We then verified that this model recapitulates the basic properties of the biological system. Simulations showed that the relative cell numbers (taking into account proliferation) evolve as expected with a stable number of PZ cells and an increased number of NT and PSM cells (***Figure 5C***). We also found that this model reproduces general trends with regard to cell motilities and non-directionality of cell movements (***Figure 5D,E***). We next explored the ability of the model to reproduce maintenance of residing posterior progenitors while the NT and PSM extend toward the posterior pole. Looking at different time points of the simulation process, we indeed observed that the PZ is maintained posteriorly during the elongation process (***Figure 5—video 1***). Our biological results pointed out a critical role of the motility control, however, in our model, Sox2 and Bra control cell motility, adhesion, and non-mixing properties. Thus, we wanted to know if motility is

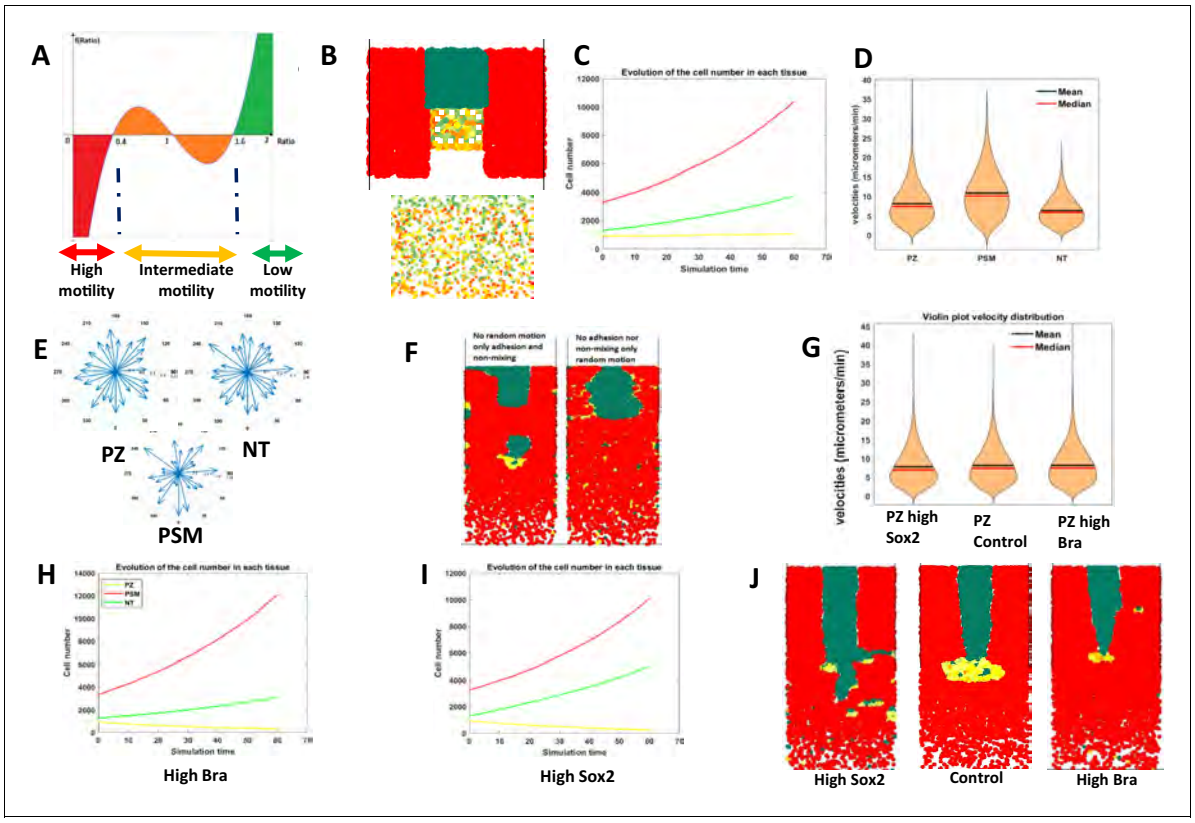

Figure 5. Mathematical modeling of progenitor behaviors downstream of Sox2 and Bra heterogeneous expression. (**A**) Graphical representation of the mathematical function defining the Sox2-to-Bra ratio dynamics. The Sox2/Bra value oscillates randomly from 0.4 to 1.6 and noise in the system ensures that some cells pass below 0.4 to be specified into PSM cells (red) while some cells pass above 1.6 to become NT cells (green). Low ratios (below 0.4) confer high motility , high ratios (above 1.6) inhibit motility and ratios between 0.4 and 1.6 confer intermediate levels of motility. (**B**) Posterior region showing the spatial heterogeneity of Sox2/Bra levels with a close-up on the PZ on the bottom panel. (**C**) Evolution of the number of each cell type over time. (**D**) Distribution of cell motilities. (**E**) Directionality of migration in the three tissues. (**F**) Simulation without random motility (left) or without non-mixing and adhesion (right) for progenitors. (**G**) Effects of deregulations of the Sox2/Bra values on cell motility (**G**), cell numbers (**H, I**), and on tissue evolution at 10 hr (**J**). NT, neural tube; PSM, presomitic mesoderm; PZ, progenitor zone.

The online version of this article includes the following video(s) for figure 5:

Figure 5—video 1. Mathematical simulations: combined random and graded expression of Sox2 and Bra (mixed).
https://elifesciences.org/articles/66588#fig5video1

Figure 5—video 2. Mathematical simulation of Sox2 and Bra overexpression on the mixed model.
https://elifesciences.org/articles/66588#fig5video2

indeed an important parameter in comparison to adhesion and non-mixing properties of progenitors in our model. It turns out that without either random motion or adhesion/non-mixing properties, integrity of the tissues is severely affected (***Figure 5F***), revealing the importance of these parameters in progenitors' behavior in controlling posterior tissue morphogenesis. To challenge further this model, we next tested its ability to recapitulate the experimental results we obtained by overexpressing or downregulating Sox2 and Bra. For this purpose, we explored the consequences on tissues and cell behaviors of numerically deregulating the Sox2/Bra values. As a result, Bra^{High} values increase PZ cell motility (***Figure 5G***), lead to generation of a higher number of PSM cells (***Figure 5H***), to a depletion of cells in the PZ, and to a shorter NT (***Figure 5J***; ***Figure 5—video 2***). On the opposite, $Sox2^{High}$ values lead to reduced PZ cell motility (***Figure 5G***), to a depletion of PZ

cells, to an increased number of NT cells, and to an enlarged NT (***Figure 5I,J***; ***Figure 5—video 2***). This model thus recapitulates with success the main biological effects of Sox2 and Bra on progenitor behaviors. To define which particular properties the distribution of heterogeneity, either random or gradient can confer, we created two extreme versions of this model: a first one in which the distribution of Sox2/Bra values in the PZ are fully random (random model) and a second one in which these values are strictly distributed along opposite gradients, that is, a decreasing gradient of Sox2 and an increasing gradient of Bra along the antero-posterior axis (gradient model). We next compared these two models with the initial mixed model (***Figure 6A***). We found that these two extreme cases (random and gradient models) exhibit the main properties regarding PZ maintenance and progenitor distribution than that observed in the mixed model (***Figure 6—video 1***, ***Figure 6—figure supplement 1***), suggesting that randomness and gradient features might both be at work in this system. We then analyzed in detail a set of additional parameters and compared these parameters for the different models. We first measured the distance traveled by the PZ over time to define the

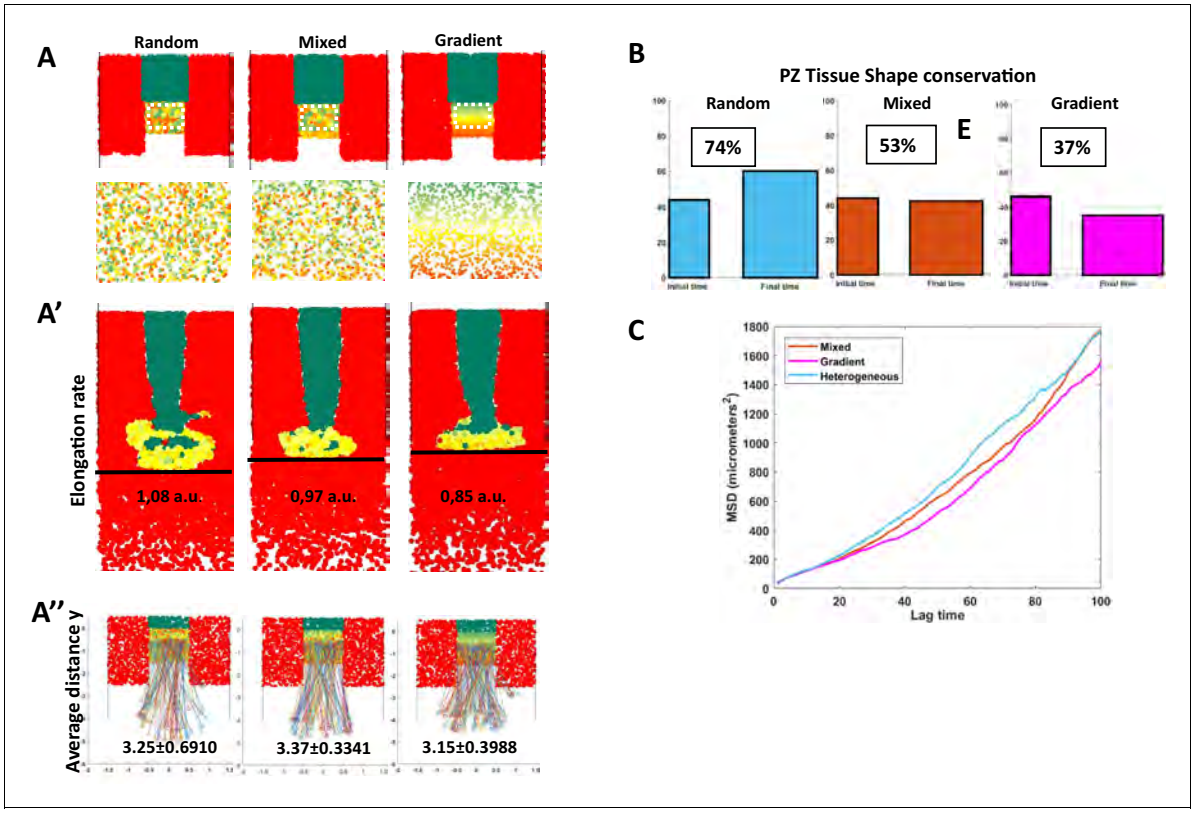

Figure 6. Comparison of spatial organizations by modeling. (**A**) Random model (left), mixed (defined in ***Figure 5***), and the graded model following opposite gradients (right). (**A**) Initial conditions and close-up of the PZ showing the spatial organization of Sox2/Bra levels (bottom panels). (**A'**) Elongation rates measured with the distance traveled by the posterior part of the PZ (black line) in 10 hr. (**A''**) Y displacement of resident progenitors located at the center (along the anteroposterior axis) of the PZ for each model. (**B**) Initial (left) and final (right) shapes of the PZ in the different models. Conservation of proportions (length/width) is noted in percentage (100% would correspond to an unchanged shape). (**C**) MSD calculated for progenitors in the three models. MSD, mean squared displacement; PZ, progenitor zone.

The online version of this article includes the following video and figure supplement(s) for figure 6:

Figure supplement 1. Directionality of migration, evolution of cell number, and velocity distribution in the random and gradient models.

Figure 6—video 1. Mathematical simulations of random, graded and mixed models.
https://elifesciences.org/articles/66588#fig6video1

elongation speed according to each model. We found differences between the three models, simulation of the random model showed faster elongation than simulation of the gradient model, while simulation of the mixed model resulted in an intermediate speed (***Figure 6A'***). To test if posterior movements of resident progenitors also differ between the three models, we tracked cells that remain in the PZ throughout the simulation and calculated the distances they traveled in the Y direction. This analysis showed that resident progenitors have traveled in a more posterior position in the random and the mixed models than in the gradient model, indicating that random distribution of Sox2/Bra values is more efficient in imposing a posterior movement to these cells than graded distribution (***Figure 6A''***). From the simulation movies, it was obvious that the shape of the PZ was different throughout the three types of simulations (***Figure 6—video 1***). By analyzing the PZ shape at the beginning and at the end of the simulation, we found that proportions (length/width) of the PZ were much more conserved over the elongation process in the random model compared to the gradient model where it became larger (medio-lateral) and shorter (antero-posterior) (***Figure 6B***). Once again, the mixed model gives results that are in between the two extreme models. Finally, to test if the changes we observed at the tissue scale could be due to changes in the diffusivity of cellular migration, we plotted the MSD through time for both the random and the gradient models. We found that the MSD of the random model is higher than that of the mixed model, which itself is higher than the MSD of the gradient model (***Figure 6C***), suggesting that the spatial heterogeneity in the expression of Sox2 and Bra is enhancing the diffusive behavior of PZ cells. This higher diffusivity can therefore bring more tissue fluidity to deform and remodel the PZ and maintain its global shape over long time scales. Indeed, we observed that the PZ, although progressively losing its initial shape in the gradient model, shows fewer transient deformations than in the random model, this stability being inherited in the mixed model (***Figure 6—video 1***).

Taken together, by exploring and comparing Sox2/Bra spatial distributions, our modeling data indicate that while the gradient pattern provides stability by limiting local and transient deformations, random distribution of cell-to-cell heterogeneity could promote cell rearrangements, tissue fluidity, and long-term conservation of tissue shape.

Discussion

In the present work, we bring evidence that variations of the Sox2-to-Bra ratio in progenitors of the PZ are critical to regulate progenitor motility and tissue destination. Our data support a model in which high levels of Sox2 give cells low motile properties and make them integrate the NT while high levels of Bra rather give them high motile and diffusive properties that push them to exit the PZ and integrate the PSM. Located in-between these low and high motile/diffusive cells are progenitors co-expressing Sox2 and Bra at comparable levels, that are moving with an intermediate speed and remain resident of the PZ as this tissue is moving posteriorly. We propose mathematical models to estimate the importance of spatial cell-to-cell heterogeneity created by variations of the Sox2-to-Bra ratio in the elongation process. As a whole, this study unravels how cellular motility is coupled to progenitors' segregation into different tissues and sheds a new light on how cell-to-cell heterogeneity might ensure robustness in morphogenesis.

In this work, we show that Sox2 and Bra proteins are co-expressed in PZ cells of quail embryos. This co-expression is a conserved property of vertebrate embryos since it has been previously reported in chick, zebrafish, mouse, and human embryos (***Olivera-Martinez et al., 2012***; ***Wymeersch et al., 2016***; ***Martin and Kimelman, 2012***). Interestingly, it has also been noticed that Sox2 and Bra are expressed at different levels and are therefore heterogeneously expressed in the PZ. In particular, it has been shown that cells from the anterior part of the PZ express high level of Sox2 and are fated toward the NT whereas cells from the posterior part of the PZ are expressing high levels of Bra and are fated toward mesodermal destiny (***Wymeersch et al., 2016***; ***Kawachi et al., 2020***). Even though our data showed that such a pattern is apparent in the quail PZ, an important finding of our work is that neighboring cells with variable levels of Sox2 and Bra are found in all areas of the PZ. How the distribution of this particular cell-to-cell heterogeneity is established and further maintained over the elongation process remains an open question. Graded activity of signaling pathways such as Wnt, FGF, and RA, all known to regulate Bra and Sox2 expression (***Ciruna and Rossant, 2001***; ***Yamaguchi et al., 1999***; ***Gouti et al., 2017***; ***Cunningham et al., 2016***;

Goto et al., 2017), together with dynamic cross-regulatory activities of Sox2 and Bra (*Koch et al., 2017*) and cell mixing are likely to contribute to create and maintain such a heterogeneity.

The antagonistic interaction between Sox2 and Bra has been proposed to determine fate decision of posterior progenitors (*Koch et al., 2017*). However, this has recently been questioned based on data obtained in mouse showing that Bra does not directly repress Sox2 (*Guibentif et al., 2021*). Interestingly, we also found that Bra-Mo does not lead to an upregulation of Sox2 (*Figure 2—figure supplement 2*). Due to the inhibitory relationships between Sox2 and Bra, it is therefore difficult to know if the ratio between them or the absolute levels are most important to drive their effects. Independently of their regulative interactions, the different levels of Sox2 and Bra expression we observed between posterior progenitors seem indicative of the presence of mixed cell populations in the PZ harboring different specification states: Bra^{High} progenitors being engaged toward the mesodermal fate, $Sox2^{High}$ toward the neural fate while progenitors with comparable levels of the two proteins being situated in between these two states. In agreement, we found that forced expression of Sox2 and downregulation of Bra favor the integration of posterior progenitors into the NT while forced expression of Bra and downregulation of Sox2 favor their distribution to the PSM. Downregulation or loss of Bra expression has been associated with retention of cells in the progenitor regions in mouse embryo studies, particularly in the tail bud at the level of the CNH (Chordo-Neural Hinge) (*Wilson et al., 1995*; *Wilson and Beddington, 1997*). Although we observed a clear decrease in the number of PZ cells in Bra-Mo compared to control conditions, it is possible that some of the Bra-Mo cells that are remaining in the PZ indeed reside in a region that will contribute to the CNH. Despite clear effects of our experimental approaches on cell localization in the different tissues, results could not explain why, in gain and loss-of-function experiments, preferential distribution of electroporated cells into the NT is not always paralleled by a decrease in their participation to PSM formation (or conversely) (*Figure 2E,J*). A possible explanation is that a progenitor which is already engaged toward a given fate is no longer competent to switch its fate and, thereby, to change its tissue destination. As mentioned above, we found the different types of progenitors intermingled in all areas of the PZ. Single-cell sequencing studies have revealed the molecular signatures of the different progenitor states; however, due to technical limitations, these studies could not reveal their exact locations within the posterior region. Fate maps studies around stages HH4–5 have shown that the distribution of progenitors along the antero-posterior axis of the epiblast/streak is translated in the distribution of their descendants along the medio-lateral axis in formed tissues of older embryos (NT, PSM, and lateral plate) (*Iimura et al., 2007*; *Psychoyos and Stern, 1996*). In this perspective, anterior cells which are expressing high levels of Sox2, give rise to neural cells and more posterior cells, expressing high levels of Bra, give rise to PSM (and eventually to lateral mesoderm for cells located even more caudally). The fact that we found Sox2 and Bra heterogeneously expressed within the PZ is rather suggestive of a more complex picture where position in the progenitor region does not systematically prefigure final tissue destination. Following this scenario, neighboring progenitors could give rise to progeny in different tissues, an observation that is consistent with prospective maps of the PZ in which a small number of labeled cells participate in different tissues (*Selleck and Stern, 1991*; *Iimura et al., 2007*; *Wilson and Beddington, 1996*; *Psychoyos and Stern, 1996*).

Analysis of our time-lapse experiments shows that most PZ cells are highly mobile and that this motility is mainly non-directional. Overexpression of Sox2 or downregulation of Bra strongly inhibits cell motility in the PZ leading to an anterior bias in the direction of progenitor movements. At the opposite, overexpression of Bra and, to some extends, downregulation of Sox2, favor a slight increase in PZ cell motility. Similarly, cells located axially in the zebrafish tailbud have been shown to display highly disordered motility, suggesting conservation of the role of high and non-directional progenitor's motility between vertebrate species (*Lawton et al., 2013*; *Das et al., 2017*). The fact that posterior progenitors often exchange neighbors offers an explanation on how the spatial heterogeneity of posterior progenitors is sorted out to form PSM and NT. Indeed, thanks to their highly migratory properties, Bra^{High} cells could make their way to the surrounding PSM by moving in between other cells including $Sox2^{High}$ cells that are less motile. It has been shown that Brachyury plays a role in cell migration (*Wilson et al., 1995*; *Wilson and Beddington, 1997*; *Turner et al., 2014*; *Wilson et al., 1993*). In particular, mouse cells that have a mutation in the Brachyury gene have lower migration speed than wild-type cells when isolated and cultured, explaining part of the mouse embryonic axis truncation phenotype (*Hashimoto et al., 1987*). Although a role for Sox2 in

the control of progenitor cell migration has, to our knowledge, not previously been reported, recent works have demonstrated that a rise of Sox2 expression promotes the transition of posterior progenitors to NT during chick embryo secondary neurulation (**Kawachi et al., 2020**) and that turning off Sox2 is necessary for NMP to enter the mesoderm in zebrafish embryo (**Kinney et al., 2020**). In addition, it has also been observed by time-lapse analysis that the dorsal zone between the PZ and the NT does not display excessive cell migration but rather local cell intercalations (**Roszko et al., 2007**; **Gonzalez-Gobartt et al., 2021a**). Taken together, these data confirm the hypothesis that $Sox2^{High}$ cells could be laid down as the PZ moves posteriorly. In our experiments, while a clear inhibition of cell motility can be obtained by Bra downregulation and Sox2 overexpression, only a subtle enhancement of cell motility was obtained by downregulating Sox2 and overexpressing Bra. These differences can be explained by the fact that posterior progenitor's Sox2/Bra ratios and motilities are much more similar to ratios and motilities of PSM cells than NT cells (**Figures 1** and **3**). Biasing progenitors with mesenchymal properties toward a neural state is therefore much more likely to give a difference in motility than a change toward another mesodermal state. In line with this explanation is the fact that during the course of axis elongation posterior progenitors undergo an epithelial-mesenchymal transition before reaching their full potential to give rise to progeny in the NT and the PSM (**Guillot et al., 2021**; **Goto et al., 2017**; **Dias et al., 2020**). Therefore, it is likely that even though Sox2/Bra heterogeneity is present since stage HH5, regulation of progenitor destiny by cellular motility is mostly active after stage HH8 when the progenitors have become mesenchymal with cellular properties that are closer to PSM cells. Indeed, we observed that PZ cell motilities were higher if analyzed between stages HH8 and HH12 compared to the earlier stages HH5 and HH8 (data not shown). Interestingly, the posterior global movement of the PZ region seems constant all along those different stages. Several works, performed in bird embryo, have indicated that physical constraints exerted by neighboring tissues, in particular the PSM, promote the posterior movement of the PZ (**Bénazéraf et al., 2017**; **Bénazéraf et al., 2010**; **Xiong et al., 2020**; **Regev et al., 2017**). It is therefore likely that the posterior movement of PZ cells is the result of both local re-arrangements and external forces acting on the whole region. How Sox2 and Bra are regulating local motility is still an open question. One interesting possibility that is taken into account in our mathematical models is that, as it has been demonstrated during NT dorso-ventral patterning (**Tsai et al., 2020**), differential adhesion between progenitors could regulate their segregation.

Based on our simulations, we propose that both a mix between spatially random and graded patterns heterogeneity in Sox2 and Bra expression are able to maintain progenitors caudally and to guide their progeny in the NT and the PSM. However, little is known about the role of spatial cell-to-cell heterogeneity during morphogenesis. Here, we propose that the spatially random pattern allows more posterior movements, cell rearrangements, and tissue fluidity in the PZ. Interestingly, this fluid-like state as well as disordered cellular movements have been described in PSM tissue to be key for zebrafish embryo axis elongation and morphogenesis (**Lawton et al., 2013**; **Das et al., 2017**; **Mongera et al., 2018**). In addition, the more efficient self-correction observed in the random model is also supportive of spatial cell-to-cell heterogeneity in the PZ providing plasticity to the system. Several studies have shown that this particular region of the embryo is able to regenerate after partial ablation (**Joubin and Stern, 1999**; **Yuan and Schoenwolf, 1999**). Spatial cell-to-cell heterogeneity, which allows easier re-organization of remaining cells than graded cell pattern, thus appears to be an enabling factor for self-correction. Moreover, if gradients of Sox2 and Bra are controlled by secreted signals, tissue ablation could be more detrimental to the diffusion of these signals (and re-patterning) than auto-organization of cell-to-cell heterogeneity. Spatial heterogeneity in gene and protein expression is a common trait of living systems and has been observed in many contexts including, early mouse embryos or cancer cells (**Prasetyanti and Medema, 2017**; **Fiorentino et al., 2020**). The link between cellular spatial heterogeneity and the robustness of morphogenetic processes that we describe here can therefore be relevant beyond the scope of developmental biology.

Materials and methods

Quail embryos and cultures

Fertilized eggs of quail (*Coturnix japonica*), obtained from commercial sources, were incubated at 38˚C at constant humidity and embryos were harvested at the desired stage of development. The

early development of quail being comparable to chicken, embryonic stages were defined using quail (**Ainsworth et al., 2010**) or chicken embryo development tables **Hamburger and Hamilton, 1951**. Embryos were grown ex ovo using the EC (early chick) technique (**Chapman et al., 2001**) for 6–20 hr at 39˚C in a humid atmosphere.

Expression vectors and morpholinos

cBra full-length cDNA was cloned by PCR using the following primers (5′-ACCATGGGC TCCCCGGAG-3′; 5′-CTACGCAAAGCAGTGCAGGTGC-3′) into Pcig (**Megason and McMahon, 2002**). cSox2 was cloned from Pccags-cSox2 (**Roellig et al., 2017**) using EcoRV/XbaI into Pcig to obtain Pcig-cSox2. N1N2-eGFP-Pest Sox2 gene reporter gene was obtained from Daniela Roellig (**Roellig et al., 2017**; **Uchikawa et al., 2003**). 3xnls-mScarlet was obtained from Addgene (**Chertkova et al., 2017**). Fluorescein-coupled morpholinos (Mo) were synthesized by Gene Tools. The nucleotide sequences of the morpholinos were designed to target the translation initiation site of quail Bra (5′-AAATCCCCCCCCCCTTCCCCGAG-3′) and Sox2 (5′-GTACATTCAAACTACTTTTGCC TGG-3′) mRNAs. The Mo (5′-CCTCTTACCTCAGTTACAATTTATA-3′) directed against the transcript of β-human globin was used as control.

Electroporation

We collected stages HH4–6 quail embryos. The solution containing the morpholinos (1 mM) and pCIG empty (1–2 µg/µl) as a carrier or the DNA solution containing expression vectors Pcig, pCIG-Bra, or pCIG-Sox2 (2–5 µg/µl) were microinjected between the vitelline membrane and the epiblast at the anterior region of the primitive streak (**Iimura and Pourquié, 2008**). The electrodes were positioned on either side of the embryo and five pulses of 5.2 V, with a duration of 50 ms, were carried out at a time interval of 200 ms. The embryos were screened for fluorescence and morphology and kept in culture for up to 24 hr. To observe the distribution of fluorescence in electroporated tissues, embryos were cultured overnight and fixed before being mounted, ventral side up. Transversal sections have been made with a cryostat on embryos embedded in gelatine (**Andrieu et al., 2020**).

Immunodetection, in situ hybridization and proliferation essay

For immunodetection, embryos of stages HH9–11 were fixed for 2 hr at room temperature in formaldehyde 4% in phosphate-buffered saline (PBS). Blocking and permeabilization were achieved by incubating the embryos in a solution containing Triton X-100 (0.5%) and donkey serum (1%) diluted in PBS for 2 hr. The embryos were then incubated with primary antibodies to Sox2 (1/5000, EMD Millipore, ab5603), Bra (1/500, R and D Systems, AF2085), cleaved Caspase3 (D175, 1/100, CST #9661S), or Pax6 (1/200, MBL, # JM-3636R-100) overnight at 4˚C under agitation. After washes, the embryos were incubated with secondary antibodies coupled with Alexa Fluor 555, Alexa Fluor 488 (1/1000, Thermo Fisher Scientific), and with DAPI (4′,6-diamidino-2-phenylindole, 1/1000, Thermo Fisher Scientific D1306) overnight at 4˚C under agitation. For in situ hybridization, probes for quail Mesogenin were amplified with the following primers 5′-CGGAGCACTCTGTCTGCTTA-3′ and 5′- TCCCTCATGTTCCTCTGTCA-3′. In situ protocol was adapted from **Denkers et al., 2004**. Proliferation rates were assessed by Edu staining (Click-iT EdU Alexa Fluor 647 Imaging Kit, Thermo Fisher Scientific, C10340) with a pulse of 1 hr duration, for details see **Bénazéraf et al., 2017**.

Image acquisition, processing, and quantification

Image acquisition for immunodetection and in situ hybridization was performed using Zeiss 710 laser and Leica SP8 confocal microscopes (20×, 40×, 63× objectives). Quantification of Sox2 and Bra levels in 3D was made with Fiji or with the spot function (DAPI staining) of Imaris. Immunodetection signals were normalized to DAPI signal to consider loss in intensity due to depth of the tissue. Immunodetection signals and ratios were calculated and plotted using Matlab. Quantification of protein levels in gain and loss of function experiments was performed 7 hr after electroporation by analyzing immunodetection signal levels within GFP positive progenitors and by normalizing to endogenous expressions measured in non-electroporated cells. Fluorescence distribution in tissues was acquired on a wide-field microscope Axio-imager type 2 (Colibri eight multi-diode light source, 10× objective). Images of electroporated embryos were processed with the Zen software that allows

the assembly of the different parts of the mosaic ('Stitch' function) and were then processed with the 'Stack focuser' plugin of the ImageJ software. The different tissues were delineated on ImageJ with the hands-free selection tool and the images were then binarized using the threshold tool. The total fluorescence intensity emitted by cells transfected with the different constructs was measured and the sum of the positive pixels for the different tissues was calculated. The percentage of fluorescence distribution in the different tissues was then calculated. Immunodetection/proliferation data were quantified using Imaris (Bitplane) and ImageJ/Fiji (***Schindelin et al., 2012***) sofwares.

Live imaging and cell tracking

Live Imaging was done using Zeiss Axio-imager type 2 (10× objective), as previously described (***Gonzalez-Gobartt et al., 2021b***; ***Bénazéraf et al., 2010***). Briefly, stages 7–8 electroporated embryos were cultured under the microscope at 38˚ in humid atmosphere. Two channels (GFP and brightfield), three fields of views, 10 Z levels were imaged every 6 min for each embryo (six embryos per experiment). Images were stitched and pixels in focus were selected using Stack Focuser (ImageJ). X, Y drift was corrected using MultiStackReg adapted from TurboReg (ImageJ) (***Thévenaz et al., 1998***). Image segmentation was done after background correction using Background Subtractor plugin (from the MOSAIC suite in ImageJ) and cell tracking was done using Particle Tracker 2D/3D plugin (ImageJ) (***Sbalzarini and Koumoutsakos, 2005***). A reference point was defined for each frame at the last formed somite using manual tracking. Regions of interest (ROIs) were defined manually and their posterior movement was defined by manual tracking of the tailbud movement. Subtraction of the tissue movement was done by defining the average motions of cells in the region. Violin plots were generated on Prism 8 (Graphpad). MSD and distribution of angles were calculated and plotted with a Matlab routine. Angle distribution was calculated from trajectories weighted with velocities, and plotted as rosewind plot using Matlab.

Data representation and statistical testing

Data were plotted using Excel (Microsoft), Prism (Graphpad), Matlab (Mathworks), and PlotsOfData (***Postma and Goedhart, 2019***). Kolmorogov-Sminorv test was used to test for differences in angle distributions in ***Figure 4D***,F. For all the other comparisons, unpaired Student's test was used, p<0.05*, p<0.001**, p<0.0001***, p<0.00001****, p>0.05 non-significant (ns).

Mathematical modeling

A cell population of 1100 progenitor cells, 1200 neural cells and 3200 PSM cells was initially distributed in their respective areas. Each cell type was endowed with its proliferation rate, that is, 11.49 hrs for progenitor cells, 10.83 hrs for neural cells, and 8.75 hrs for PSM cells. Each cell I was characterized by a given ratio of Sox2/Bra, named R_I(t), with an assigned value from 0 to 2 (depicted as 0–2 in ***Figure 5A*** to match with biological ratios), and by a 2D position (x_I(t),y_I(t)), each of these variables being time-dependent. In the random model an initial Sox2/Bra ratio value from 0.15 to 0.85 was randomly attributed to progenitor cells. At each time step, each cell updates its Sox2/Bra value through a stochastic differential equation, using the function represented in ***Figure 5A*** (+noise) and then updates its position (x,y), depending on the value of the ratio, by a biased/adapted random motion. Interaction properties between cells such as adhesion, maximum density, and packing were implemented in the bias of the random motion as detailed in Appendix 1. Simulations focused on the posterior body (1 unit=150 µm). Cells movements in the most anterior region were blocked, considering this region, composed of somites and neuroepithelial cells, as a very dense area, and, similarly, cell passage to either side of the PSM was blocked, considering the lateral plate to be a solid structure.

Acknowledgements

The authors thank Karine Guevorkian and Eric Théveneau for their critical reading of the manuscript. The authors thank rotation students Nils Vigier, Clément Peux and Khady Moussounda Niang as well as Brice Ronsin and Stephanie Bosch and the CBI imaging facility and Marion Aguirrebengoa for help with statistics. The authors thank Fabienne Pituello for hosting them and for her support. The authors also thank Pierre Degond and members of the Pituello, Soula, Theveneau, and Davy

teams for suggestions and stimulating discussions during the project. This work has been funded by ANR (JC) and the ARC foundation grants.

Additional information

Funding

Funder	Grant reference number	Author
Agence Nationale de la Recherche	MULTIEL ANRJC	Bertrand Benazeraf
Fondation ARC pour la Recherche sur le Cancer	PJA 20191209486	Bertrand Benazeraf

The funders had no role in study design, data collection and interpretation, or the decision to submit the work for publication.

Author contributions

Michèle Romanos, Conceptualization, Formal analysis, Validation, Investigation, Visualization, Methodology, Writing - original draft, Writing - review and editing; Guillaume Allio, Data curation, Formal analysis, Investigation, Methodology, Writing - original draft, Writing - review and editing; Myriam Roussigné, Formal analysis, Investigation, Visualization, Methodology; Léa Combres, Data curation, Formal analysis, Investigation; Nathalie Escalas, François Médevielle, Investigation, Methodology; Cathy Soula, Resources, Investigation, Writing - review and editing; Benjamin Steventon, Conceptualization, Investigation, Writing - review and editing; Ariane Trescases, Resources, Formal analysis, Supervision, Investigation, Methodology, Writing - review and editing; Bertrand Bénazéraf, Conceptualization, Resources, Data curation, Formal analysis, Supervision, Funding acquisition, Validation, Investigation, Visualization, Methodology, Writing - original draft, Project administration, Writing - review and editing

Author ORCIDs

Myriam Roussigné http://orcid.org/0000-0002-4240-4105
Benjamin Steventon https://orcid.org/0000-0001-7838-839X
Bertrand Bénazéraf https://orcid.org/0000-0002-1937-637X

Decision letter and Author response

Decision letter https://doi.org/10.7554/eLife.66588.sa1
Author response https://doi.org/10.7554/eLife.66588.sa2

Additional files

Supplementary files

- Transparent reporting form

Data availability

Source data files for Figures 1 and 3 (heterogeneity and motility) are provided on OSF.

The following datasets were generated:

Author(s)	Year	Dataset title	Dataset URL	Database and Identifier
Bénazéraf B, Allio G	2021	Movies H2B gfp electroporation quail	https://osf.io/up657/	Open Science Framework, up657
Bénazéraf B, Allio G	2021	Sox2 Bra immunostaining quail embryos stage 10 11HH	https://osf.io/mb5vh/	Open Science Framework, mb5vh

References

Ainsworth SJ, Stanley RL, Evans DJ. 2010. Developmental stages of the japanese quail. *Journal of Anatomy* **216**: 3–15. DOI: https://doi.org/10.1111/j.1469-7580.2009.01173.x, PMID: 19929907

Andrieu C, Montigny A, Bibonne A, Despin-Guitard E, Alfandari D, Théveneau E. 2020. MMP14 is required for delamination of chick neural crest cells independently of its catalytic activity. *Development* **147**:183954. DOI: https://doi.org/10.1242/dev.183954

Attardi A, Fulton T, Florescu M, Shah G, Muresan L, Lenz MO, Lancaster C, Huisken J, van Oudenaarden A, Steventon B. 2018. Neuromesodermal progenitors are a conserved source of spinal cord with divergent growth dynamics. *Development* **29**:166728. DOI: https://doi.org/10.1242/dev.166728

Bénazéraf B, Francois P, Baker RE, Denans N, Little CD, Pourquié O. 2010. A random cell motility gradient downstream of FGF controls elongation of an amniote embryo. *Nature* **466**:248–252. DOI: https://doi.org/10.1038/nature09151, PMID: 20613841

Bénazéraf B, Beaupeux M, Tchernookov M, Wallingford A, Salisbury T, Shirtz A, Shirtz A, Huss D, Pourquié O, François P, Lansford R. 2017. Multi-scale quantification of tissue behavior during amniote embryo Axis elongation. *Development* **144**:4462–4472. DOI: https://doi.org/10.1242/dev.150557, PMID: 28835474

Bergsland M, Ramsköld D, Zaouter C, Klum S, Sandberg R, Muhr J. 2011. Sequentially acting sox transcription factors in neural lineage development. *Genes & Development* **25**:2453–2464. DOI: https://doi.org/10.1101/gad.176008.111, PMID: 22085726

Cambray N, Wilson V. 2002. Axial progenitors with extensive potency are localised to the mouse chordoneural hinge. *Development* **129**:4855–4866. DOI: https://doi.org/10.1242/dev.129.20.4855, PMID: 12361976

Chapman SC, Collignon J, Schoenwolf GC, Lumsden A. 2001. Improved method for chick whole-embryo culture using a filter paper carrier. *Developmental Dynamics : An Official Publication of the American Association of Anatomists* **220**:284–289. DOI: https://doi.org/10.1002/1097-0177(20010301)220:3<284::AID-DVDY1102>3.0.CO;2-5, PMID: 11241836

Chertkova AO, Mastop M, Postma M, van Bommel N, van der Niet S, Batenburg KL. 2017. Robust and bright genetically encoded fluorescent markers for highlighting structures and compartments in mammalian cells. *bioRxiv*. DOI: https://doi.org/10.1101/160374

Ciruna B, Rossant J. 2001. FGF signaling regulates mesoderm cell fate specification and morphogenetic movement at the primitive streak. *Developmental Cell* **1**:37–49. DOI: https://doi.org/10.1016/S1534-5807(01)00017-X, PMID: 11703922

Cunningham TJ, Colas A, Duester G. 2016. Early molecular events during retinoic acid induced differentiation of neuromesodermal progenitors. *Biology Open* **5**:1821–1833. DOI: https://doi.org/10.1242/bio.020891, PMID: 27793834

Das D, Chatti V, Emonet T, Holley SA. 2017. Patterned disordered cell motion ensures vertebral column symmetry. *Developmental Cell* **42**:170–180. DOI: https://doi.org/10.1016/j.devcel.2017.06.020, PMID: 28743003

Denkers N, García-Villalba P, Rodesch CK, Nielson KR, Mauch TJ. 2004. FISHing for chick genes: triple-label whole-mount fluorescence in situ hybridization detects simultaneous and overlapping gene expression in avian embryos. *Developmental Dynamics : An Official Publication of the American Association of Anatomists* **229**: 651–657. DOI: https://doi.org/10.1002/dvdy.20005, PMID: 14991720

Dias A, Lozovska A, Wymeersch FJ, Nóvoa A, Binagui-Casas A, Sobral D, Martins GG, Wilson V, Mallo M. 2020. A Tgfbr1/Snai1-dependent developmental module at the core of vertebrate axial elongation. *eLife* **9**:e56615. DOI: https://doi.org/10.7554/eLife.56615, PMID: 32597756

Farrell JA, Wang Y, Riesenfeld SJ, Shekhar K, Regev A, Schier AF. 2018. Single-cell reconstruction of developmental trajectories during zebrafish embryogenesis. *Science* **360**:eaar3131. DOI: https://doi.org/10.1126/science.aar3131, PMID: 29700225

Fiorentino J, Torres-Padilla ME, Scialdone A. 2020. Measuring and modeling Single-Cell heterogeneity and fate decision in mouse embryos. *Annual Review of Genetics* **54**:167–187. DOI: https://doi.org/10.1146/annurev-genet-021920-110200, PMID: 32867543

Gonzalez-Gobartt E, Blanco-Ameijeiras J, Usieto S, Allio G, Benazeraf B, Martí E. 2021a. Cell intercalation driven by SMAD3 underlies secondary neural tube formation. *Developmental Cell* **56**:1147–1163. DOI: https://doi.org/10.1016/j.devcel.2021.03.023, PMID: 33878300

Gonzalez-Gobartt E, Allio G, Bénazéraf B, Martí E. 2021b. In vivo analysis of the Mesenchymal-to-Epithelial transition during chick secondary neurulation. *Methods in Molecular Biology* **2179**:183–197. DOI: https://doi.org/10.1007/978-1-0716-0779-4_16, PMID: 32939722

Goto H, Kimmey SC, Row RH, Matus DQ, Martin BL. 2017. FGF and canonical wnt signaling cooperate to induce paraxial mesoderm from tailbud neuromesodermal progenitors through regulation of a two-step epithelial to mesenchymal transition. *Development* **144**:1412–1424. DOI: https://doi.org/10.1242/dev.143578, PMID: 28242612

Gouti M, Delile J, Stamataki D, Wymeersch FJ, Huang Y, Kleinjung J, Wilson V, Briscoe J. 2017. A gene regulatory network balances neural and mesoderm specification during vertebrate trunk development. *Developmental Cell* **41**:243–261. DOI: https://doi.org/10.1016/j.devcel.2017.04.002, PMID: 28457792

Guibentif C, Griffiths JA, Imaz-Rosshandler I, Ghazanfar S, Nichols J, Wilson V, Göttgens B, Marioni JC. 2021. Diverse routes toward early somites in the mouse embryo. *Developmental Cell* **56**:141–153. DOI: https://doi.org/10.1016/j.devcel.2020.11.013, PMID: 33308481

Guillot C, Djeffal Y, Michaut A, Rabe B, Pourquié O. 2021. Dynamics of primitive streak regression controls the fate of neuromesodermal progenitors in the chicken embryo. *eLife* **10**:e64819. DOI: https://doi.org/10.7554/eLife.64819, PMID: 34227938

Hamburger V, Hamilton HL. 1951. A series of normal stages in the development of the chick embryo. *Journal of Morphology* **88**:49–92. DOI: https://doi.org/10.1002/jmor.1050880104, PMID: 24539719

Hashimoto K, Fujimoto H, Nakatsuji N. 1987. An ECM substratum allows mouse mesodermal cells isolated from the primitive streak to exhibit motility similar to that inside the embryo and reveals a deficiency in the T/T mutant cells. *Development* **100**:587–598. DOI: https://doi.org/10.1242/dev.100.4.587, PMID: 3327671

Herrmann BG, Labeit S, Poustka A, King TR, Lehrach H. 1990. Cloning of the T gene required in mesoderm formation in the mouse. *Nature* **343**:617–622. DOI: https://doi.org/10.1038/343617a0, PMID: 2154694

Iimura T, Yang X, Weijer CJ, Pourquié O. 2007. Dual mode of paraxial mesoderm formation during chick gastrulation. *PNAS* **104**:2744–2749. DOI: https://doi.org/10.1073/pnas.0610997104, PMID: 17299044

Iimura T, Pourquié O. 2008. Manipulation and electroporation of the avian segmental plate and somites in vitro. *Methods in Cell Biology* **87**:257–270. DOI: https://doi.org/10.1016/S0091-679X(08)00213-6, PMID: 18485301

Joubin K, Stern CD. 1999. Molecular interactions continuously define the organizer during the cell movements of gastrulation. *Cell* **98**:559–571. DOI: https://doi.org/10.1016/s0092-8674(00)80044-6, PMID: 10490096

Kawachi T, Shimokita E, Kudo R, Tadokoro R, Takahashi Y. 2020. Neural-fated self-renewing cells regulated by Sox2 during secondary neurulation in chicken tail bud. *Developmental Biology* **461**:160–171. DOI: https://doi.org/10.1016/j.ydbio.2020.02.007, PMID: 32059837

Kinney BA, Al Anber A, Row RH, Tseng YJ, Weidmann MD, Knaut H, Martin BL. 2020. Sox2 and canonical wnt signaling interact to activate a developmental checkpoint coordinating morphogenesis with mesoderm fate acquisition. *Cell Reports* **33**:108311. DOI: https://doi.org/10.1016/j.celrep.2020.108311, PMID: 33113369

Koch F, Scholze M, Wittler L, Schifferl D, Sudheer S, Grote P, Timmermann B, Macura K, Herrmann BG. 2017. Antagonistic activities of Sox2 and brachyury control the fate choice of Neuro-Mesodermal progenitors. *Developmental Cell* **42**:514–526. DOI: https://doi.org/10.1016/j.devcel.2017.07.021, PMID: 28826820

Lansey JC. 2020. Box and whiskers plot (without statistics toolbox). *MATLAB Central File Exchange*. https://www.mathworks.com/matlabcentral/fileexchange/42470-box-and-whiskers-plot-without-statistics-toolbox

Lawton AK, Nandi A, Stulberg MJ, Dray N, Sneddon MW, Pontius W, Emonet T, Holley SA. 2013. Regulated tissue fluidity steers zebrafish body elongation. *Development* **140**:573–582. DOI: https://doi.org/10.1242/dev.090381, PMID: 23293289

Martin BL, Kimelman D. 2012. Canonical wnt signaling dynamically controls multiple stem cell fate decisions during vertebrate body formation. *Developmental Cell* **22**:223–232. DOI: https://doi.org/10.1016/j.devcel.2011.11.001, PMID: 22264734

McGrew MJ, Sherman A, Lillico SG, Ellard FM, Radcliffe PA, Gilhooley HJ, Mitrophanous KA, Cambray N, Wilson V, Sang H. 2008. Localised axial progenitor cell populations in the avian tail bud are not committed to a posterior hox identity. *Development* **135**:2289–2299. DOI: https://doi.org/10.1242/dev.022020, PMID: 18508860

Megason SG, McMahon AP. 2002. A mitogen gradient of dorsal midline wnts organizes growth in the CNS. *Development* **129**:2087–2098. DOI: https://doi.org/10.1242/dev.129.9.2087, PMID: 11959819

Mongera A, Rowghanian P, Gustafson HJ, Shelton E, Kealhofer DA, Carn EK, Serwane F, Lucio AA, Giammona J, Campàs O. 2018. A fluid-to-solid jamming transition underlies vertebrate body Axis elongation. *Nature* **561**:401–405. DOI: https://doi.org/10.1038/s41586-018-0479-2, PMID: 30185907

Olivera-Martinez I, Harada H, Halley PA, Storey KG. 2012. Loss of FGF-dependent mesoderm identity and rise of endogenous retinoid signalling determine cessation of body Axis elongation. *PLOS Biology* **10**:e1001415. DOI: https://doi.org/10.1371/journal.pbio.1001415, PMID: 23118616

Postma M, Goedhart J. 2019. PlotsOfData-A web app for visualizing data together with their summaries. *PLOS Biology* **17**:e3000202. DOI: https://doi.org/10.1371/journal.pbio.3000202, PMID: 30917112

Prasetyanti PR, Medema JP. 2017. Intra-tumor heterogeneity from a Cancer stem cell perspective. *Molecular Cancer* **16**:41. DOI: https://doi.org/10.1186/s12943-017-0600-4, PMID: 28209166

Psychoyos D, Stern CD. 1996. Fates and migratory routes of primitive streak cells in the chick embryo. *Development* **122**:1523–1534. DOI: https://doi.org/10.1242/dev.122.5.1523, PMID: 8625839

Regev I, Guevorkian K, Pourquie O, Mahadevan L. 2017. Motility-gradient induced elongation of the vertebrate embryo. *bioRxiv*. DOI: https://doi.org/10.1101/187443

Roellig D, Tan-Cabugao J, Esaian S, Bronner ME. 2017. Dynamic transcriptional signature and cell fate analysis reveals plasticity of individual neural plate border cells. *eLife* **6**:e21620. DOI: https://doi.org/10.7554/eLife.21620, PMID: 28355135

Roszko I, Faure P, Mathis L. 2007. Stem cell growth becomes predominant while neural plate progenitor pool decreases during spinal cord elongation. *Developmental Biology* **304**:232–245. DOI: https://doi.org/10.1016/j.ydbio.2006.12.050, PMID: 17258701

Sambasivan R, Steventon B. 2020. Neuromesodermal progenitors: a basis for robust axial patterning in development and evolution. *Frontiers in Cell and Developmental Biology* **8**:607516. DOI: https://doi.org/10.3389/fcell.2020.607516, PMID: 33520989

Sbalzarini IF, Koumoutsakos P. 2005. Feature point tracking and trajectory analysis for video imaging in cell biology. *Journal of Structural Biology* **151**:182–195. DOI: https://doi.org/10.1016/j.jsb.2005.06.002, PMID: 16043363

Schindelin J, Arganda-Carreras I, Frise E, Kaynig V, Longair M, Pietzsch T, Preibisch S, Rueden C, Saalfeld S, Schmid B, Tinevez JY, White DJ, Hartenstein V, Eliceiri K, Tomancak P, Cardona A. 2012. Fiji: an open-source

platform for biological-image analysis. *Nature Methods* **9**:676–682. DOI: https://doi.org/10.1038/nmeth.2019, PMID: 22743772

Schoenwolf GC, Delongo J. 1980. Ultrastructure of secondary neurulation in the chick embryo. *The American Journal of Anatomy* **158**:43–63. DOI: https://doi.org/10.1002/aja.1001580106, PMID: 7416046

Selleck MA, Stern CD. 1991. Fate mapping and cell lineage analysis of Hensen's node in the chick embryo. *Development* **112**:615–626. DOI: https://doi.org/10.1242/dev.112.2.615, PMID: 1794328

Solovieva T, H-c L, Moverley A, Plachta N, Stern CD. 2020. The embryonic node functions as an instructive stem cell niche. *bioRxiv*. DOI: https://doi.org/10.1101/2020.11.10.376913

Stevenson I. 2020. *GitHub*. Beeswarm0.2.0. http://www.cbs.dtu.dk/~eklund/beeswarm/

Takemoto T, Uchikawa M, Yoshida M, Bell DM, Lovell-Badge R, Papaioannou VE, Kondoh H. 2011. Tbx6-dependent Sox2 regulation determines neural or mesodermal fate in axial stem cells. *Nature* **470**:394–398. DOI: https://doi.org/10.1038/nature09729, PMID: 21331042

Thévenaz P, Ruttimann UE, Unser M. 1998. A pyramid approach to subpixel registration based on intensity. *IEEE Transactions on Image Processing : A Publication of the IEEE Signal Processing Society* **7**:27–41. DOI: https://doi.org/10.1109/83.650848, PMID: 18267377

Tsai TY, Sikora M, Xia P, Colak-Champollion T, Knaut H, Heisenberg CP, Megason SG. 2020. An adhesion code ensures robust pattern formation during tissue morphogenesis. *Science* **370**:113–116. DOI: https://doi.org/10.1126/science.aba6637, PMID: 33004519

Turner DA, Hayward PC, Baillie-Johnson P, Rué P, Broome R, Faunes F, Martinez Arias A. 2014. Wnt/β-catenin and FGF signalling direct the specification and maintenance of a neuromesodermal axial progenitor in ensembles of mouse embryonic stem cells. *Development* **141**:4243–4253. DOI: https://doi.org/10.1242/dev.112979, PMID: 25371361

Tzouanacou E, Wegener A, Wymeersch FJ, Wilson V, Nicolas JF. 2009. Redefining the progression of lineage segregations during mammalian embryogenesis by clonal analysis. *Developmental Cell* **17**:365–376. DOI: https://doi.org/10.1016/j.devcel.2009.08.002, PMID: 19758561

Uchikawa M, Ishida Y, Takemoto T, Kamachi Y, Kondoh H. 2003. Functional analysis of chicken Sox2 enhancers highlights an array of diverse regulatory elements that are conserved in mammals. *Developmental Cell* **4**:509–519. DOI: https://doi.org/10.1016/s1534-5807(03)00088-1, PMID: 12689590

Veenvliet JV, Bolondi A, Kretzmer H, Haut L, Scholze-Wittler M, Schifferl D, Koch F, Guignard L, Kumar AS, Pustet M, Heimann S, Buschow R, Wittler L, Timmermann B, Meissner A, Herrmann BG. 2020. Mouse embryonic stem cells self-organize into trunk-like structures with neural tube and somites. *Science* **370**:aba4937. DOI: https://doi.org/10.1126/science.aba4937

Wagner DE, Weinreb C, Collins ZM, Briggs JA, Megason SG, Klein AM. 2018. Single-cell mapping of gene expression landscapes and lineage in the zebrafish embryo. *Science* **360**:981–987. DOI: https://doi.org/10.1126/science.aar4362, PMID: 29700229

Wilson V, Rashbass P, Beddington RS. 1993. Chimeric analysis of T (Brachyury) gene function. *Development* **117**:1321–1331. DOI: https://doi.org/10.1242/dev.117.4.1321, PMID: 8404534

Wilson V, Manson L, Skarnes WC, Beddington RS. 1995. The T gene is necessary for normal mesodermal morphogenetic cell movements during gastrulation. *Development* **121**:877–886. DOI: https://doi.org/10.1242/dev.121.3.877, PMID: 7720590

Wilson V, Beddington RS. 1996. Cell fate and morphogenetic movement in the late mouse primitive streak. *Mechanisms of Development* **55**:79–89. DOI: https://doi.org/10.1016/0925-4773(95)00493-9, PMID: 8734501

Wilson V, Beddington R. 1997. Expression of T protein in the primitive streak is necessary and sufficient for posterior mesoderm movement and somite differentiation. *Developmental Biology* **192**:45–58. DOI: https://doi.org/10.1006/dbio.1997.8701, PMID: 9405096

Wood TR, Kyrsting A, Stegmaier J, Kucinski I, Kaminski CF, Mikut R. 2019. Tissue mechanics determines cell fate in the axial stem zones. *bioRxiv*. DOI: https://doi.org/10.1101/622571

Wymeersch FJ, Huang Y, Blin G, Cambray N, Wilkie R, Wong FC, Wilson V. 2016. Position-dependent plasticity of distinct progenitor types in the primitive streak. *eLife* **5**:e10042. DOI: https://doi.org/10.7554/eLife.10042, PMID: 26780186

Wymeersch FJ, Wilson V, Tsakiridis A. 2021. Understanding axial progenitor biology *in vivo* and *in vitro*. *Development* **148**:dev180612. DOI: https://doi.org/10.1242/dev.180612, PMID: 33593754

Xiong F, Ma W, Bénazéraf B, Mahadevan L, Pourquié O. 2020. Mechanical coupling coordinates the Co-elongation of axial and paraxial tissues in avian embryos. *Developmental Cell* **55**:354–366. DOI: https://doi.org/10.1016/j.devcel.2020.08.007, PMID: 32918876

Yamaguchi TP, Takada S, Yoshikawa Y, Wu N, McMahon AP. 1999. T (Brachyury) is a direct target of Wnt3a during paraxial mesoderm specification. *Genes & Development* **13**:3185–3190. DOI: https://doi.org/10.1101/gad.13.24.3185, PMID: 10617567

Yuan S, Schoenwolf GC. 1999. Reconstitution of the organizer is both sufficient and required to re-establish a fully patterned body plan in avian embryos. *Development* **126**:2461–2473. DOI: https://doi.org/10.1242/dev.126.11.2461, PMID: 10226005

Appendix 1

Part 1: image analysis

Fixed tissue imaging

Sox2 and Bra intensity profile from PZ to NT or PSM (***Figure 1G,G'***)

Cubes containing approximately 100 nuclei are defined with Imaris along a path going from the PZ to the NT in one case, and from the PZ to the PSM in the other case. The cubes are separated by 70 µm distance approximately. The nuclei detection and data collection are done using the same methods as described previously for the immunodetection analysis. For each cube, the average of the nuclei normalized intensities is calculated and then reported to Graphpad to plot the intensity profile along the PZ-NT path or the PZ-PSM path.

Immunodetection analysis and calculation of SOX2/Bra level of expression (***Figure 1H–J***)

After the confocal acquisition, the volume acquired is analyzed with Imaris. The acquisition is done with three color channels: green channel is associated with the level of expression of Sox2, red channel is associated with Bra, and blue channel represents the DAPI staining. The ROIs are drawn with the pointer directly on the confocal imaged volume represented on the Imaris viewer. The dimensions of the ROI can be refined by entering the desired value in the dimension value fields. The 'Spot Detection' function of Imaris is used on the blue channel (DAPI staining) to automatically detect fluorescent nuclei with a user-defined radius equal to the actual radius of a nucleus into the ROI. The data of interest corresponding to the spot detected such as their identities, their position in the three dimensions of the space (X, Y, and Z) , the level of intensity in the three channels (green, red, and blue) are given by the 'statistics' tab. The data are collected on a csv table, opened in an Excel results table where the data is organized by spot identity and their dimensions. The Excel table is read with a homemade Matlab routine where the intensities of the Bra (red channel) and Sox2 (green channel) are normalized with the intensity of DAPI (blue channel) to consider the loss of fluorescent signal due to the depth. This operation is done for each spot. Then, the routine calculates the ratio of the intensity of Sox2 on the intensity of Bra for each spot. The data are plotted with the 'scatter' function of Matlab, in a 2D space representing the projection of the spots along one dimension depending on the orientation of the section used for the analysis. The spots are color-coded with their associated ratio value with a color bar going from red (low ratio, i.e., high Bra intensity, low Sox2 intensity) to green (high ratio, i.e., high Sox2 intensity, low Bra intensity). The scatter plots representing the Sox2/Bra ratio distribution are done with a Matlab code using the 'scatter' function and an adapted version of functions 'beeswarm' (***Stevenson, 2020***) for the distribution plot and 'bplot' (Matlab, ***Lansey, 2020***) for the whisker plot (10–90% interval). The Sox2 and Bra expression distribution plots and the calculation of the coefficient of variation are done with Graphpad.

Immunodetection analysis for Sox2 and Bra 3D intensity profiles ***Figure 1—figure supplement 3***

Raw confocal data are exported to ImageJ and automatically processed with a homemade ImageJ macro. First, a Gaussian filter is applied to the stack before using the binning tool giving a pixel with a value calculated from the average of 4 pixels (approximately 6 µm) in the x and y dimensions of the confocal stack. The macro process an average z-projection every four slices (approximately 8 µm) along the confocal stack with the plugin 'Grouped Z Projector.' Then, a ROI is drawn along the antero-posterior axis with a 40–50 µm width. For each pixel row of the ROI (x dimension), the average of pixels value constituting the row is calculated, giving an intensity profile along the length (y dimension) of the ROI. The operation is done for each average-projected slice. Then, an intensity profile is picked up every four average projected slices (approximately 32 µm), recorded in a CSV results table, and read in Matlab to build a 3D plot of the intensity profiles with the plot3 function.

Live imaging (*Figures 3* and *4*)

Movie reconstruction

The movie reconstruction has been done with an ImageJ/FIJI macro that automatizes several steps previously described (***Gonzalez-Gobartt et al., 2021b***). The movie reconstructed and processed is fully on-focus, aligned, and ready for the tracking phase.

Tracking analysis

The principle of the cell tracking method has been described (***Sbalzarini and Koumoutsakos, 2005***). The cells are tracked with Particle 2D/3D plugin in FIJI using this principle, allowing the reconstruction of trajectories with spots detected frame by frame. The interesting data (trajectory identity, coordinates of trajectory spots along the time-lapse movie (X, Y, Z)) are collected in a csv table results which are then read with a Matlab routine. Manual tracking of the last formed somite and the node are performed respectively to set the reference point and to get the displacement of the posterior area. The first steps of the automatized Matlab routine are to open the csv results table, to draw a reference line along the AP axis on the last frame of the movie using the 'imline' function and to draw the ROIs on the first frame of the movie with 'impoly' function. The ROIs will move along the movie accordingly to the manual tracking of the posterior area. Then, the trajectory spots contained in the ROIs are selected for analysis and their coordinates are corrected accordingly to the reference point (last formed somite). Spots are grouped by trajectory identity and calculations and plots are then performed.

In order to track the Sox2 reporters, the general method is the same as previously described. Once the spot detection is done frame by frame for each channel (Sox2 fluorescence channel, Bra fluorescence channel), the mean intensities are measured for each spot detected in both channels within a radius equal to the cell radius. The spots intensities are then classified depending on a user-defined threshold based on the general background value of the Sox2 fluorescence channel. This classification gives two classes: the Sox2+ class, that is, cells with high expression of Sox2, and Sox2− class, that is, cells with lower expression of Sox2. Then, the calculations and the plots are performed for Sox2+ and Sox2− classes.

Motility and directionality calculation

A displacement vector is computed for each cell, corresponding to the movement of a cell between two frames. A displacement vector forms a segment of a trajectory, and its norm defines the distance traveled by a cell between these two frames (***Appendix 1—figure 1***). This vector is created using the spot's coordinates of a trajectory in the table results, for every time interval along the trajectory. From this vector, motility and directionality are calculated. The motility corresponds to the norm of the displacement vector $\Delta\vec{r}$ of a cell between two frames divided by the time interval between two frames Δt.

$$\Delta r(t+\Delta t) = \left|\left|\Delta\vec{r}(t+dt)\right|\right| = \sqrt{(x(t+\Delta t)-x(t))^2+(y(t+\Delta t)-y(t))^2}$$

where x and y are the coordinates of the displacement vector.

$$motility(t+\Delta t) = \frac{\Delta r(t+\Delta t)}{\Delta t}$$

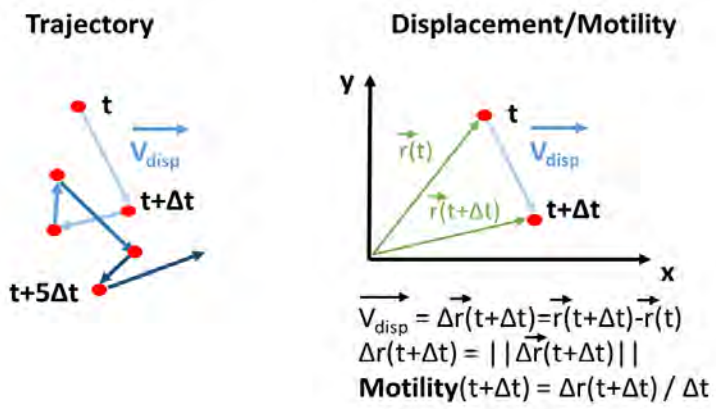

Appendix 1—figure 1. Trajectory and displacement/motility definition and calculation for tracking analysis.

The directionality is the property of being directional or maintaining a direction. In physics, this term is used to describe the preferential sensibility of a sensor or a broadcast system to a direction rather than others. Here, this term is used to describe the directional amplitude of a cell movement, taking into account its motility.

The displacement vector $\left(\vec{v}\right)$ between two frames is first compared to the reference line drawn previously $\left(\underset{v_{ref}}{\rightarrow}\right)$ as shown in ***Appendix 1—figure 2***. The angle between the displacement vector and the reference line is calculated for each time interval along the trajectory with the following formula using the cross product and the dot product between the two vectors:

$$\mathrm{Angle(t)} = \tan^{-1}\frac{\left|\left|\vec{\mathrm{v}}(\mathrm{t}) \wedge \underset{v_{ref}}{\rightarrow}\right|\right|}{\vec{\mathrm{v}}(\mathrm{t}) \cdot \underset{v_{ref}}{\rightarrow}}$$

The angle calculation is done for all the trajectories inside an ROI, and the displacement vectors are then allocated in 12 intervals (int_Θ) from 0° to 360° (30° intervals) depending on their angle values. The number of vectors allocated to an interval $\left(n\left(v_{disp}(int_\Theta)\right)\right)$ is divided by the total number of displacement vectors inside the ROI $\left(n_{total}\left(v_{disp}\right)\right)$ to get the direction proportion of the displacement vectors $\tau(int_\Theta)$ in the interval.

$$\tau(int_\Theta) = \frac{n\left(v_{disp}(int_\Theta)\right)}{n_{total}\left(v_{disp}\right)}$$

This proportion is weighted by the average motility $<mot\left(v_{disp}(int_\Theta)\right)>>$ calculated from displacement vectors whose angle is contained in this angle interval, giving the directional amplitude $A(int_\Theta)$ of the cell movement in this direction. The calculation is done for every angle interval.

$$A(int_\Theta) = \tau(int_\Theta) \cdot <mot\left(v_{disp}(int_\Theta)\right)>$$

MSD calculation

The mean square displacement (MSD) measures the deviation of the position of a particle with respect to a reference position over time. The MSD is used to analyze the mode of displacement of a particle and is commonly applied in biophysics for studying cells movements in vivo. Here, the

MSD is calculated for each cell trajectory using the spots coordinates from the table results within a defined time interval τ.

$$MSD(\tau) = <\Delta r^2(\tau) \geq <[r(t+\tau) - r(t)]^2>$$

where $r(t)$ is the position of the particle at time t, and τ is the lag time between the two positions taken by the particle used to calculate the displacement $\Delta r(\tau) = r(t+\tau) - r(t)$. The MSD is then averaged for all the particles contained in an ROI.

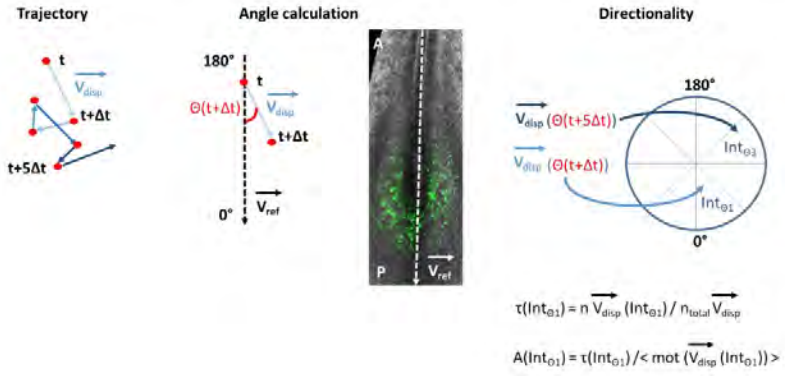

Appendix 1—figure 2. Angle and directionality calculation.

Average vector subtraction

According to ***Bénazéraf et al., 2010***, the average movement of electroporated cells in the ROIs corresponds to the extracellular matrix movements. For each ROI, the average velocity vector is defined for each frame by calculating the average velocity and the average direction (i.e., the average angle of the displacement vectors with the reference line) with the coordinates of all the trajectories spots inside the ROI between this frame and the previous one. The average velocity vector is subtracted frame by frame to give the corrected coordinates of all the trajectories inside the ROI, and the corrected motility, MSD and directionality are calculated from these corrected data using the same formulas as previously.

Save data

The data are collected and are saved in tables in the '.mat' format in a specific folder corresponding to each embryo.

Plots

The '.mat' files containing the data for plots are read with a Matlab routine which collects the data per variables (motility, MSD, and directionality), conditions, and ROIs for all the embryos. The MSD is averaged for all embryos per lag time and the directionalities are averaged for all embryos per angle intervals determined previously. For the MSD and the motility distributions, table results are opened with Matlab and then transferred to Graphpad. The rose wind plots are made in Matlab according to the number of angle intervals and using the 'rose and polar' functions from Matlab, showing the distribution of cells directionality in angle bins (here, 12 angle bins).

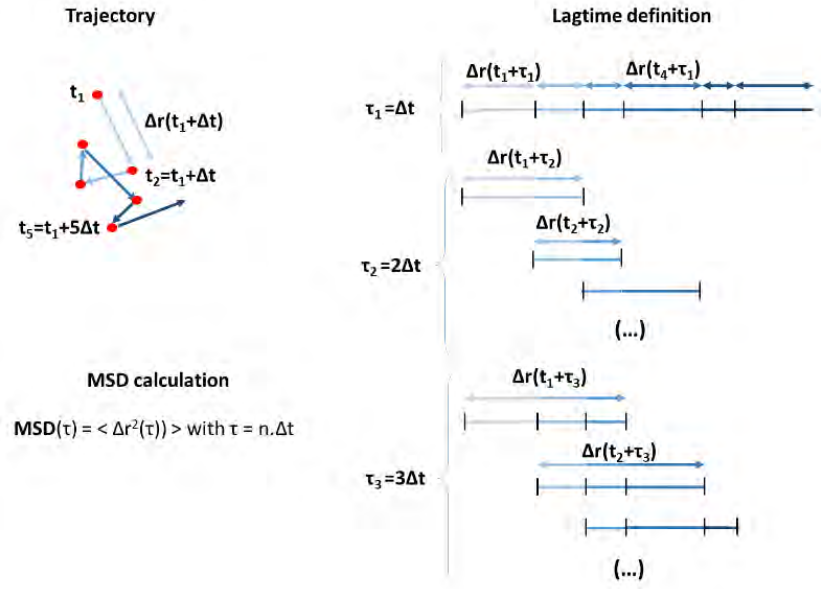

Appendix 1—figure 3. Lagtime definition and MSD calculation.

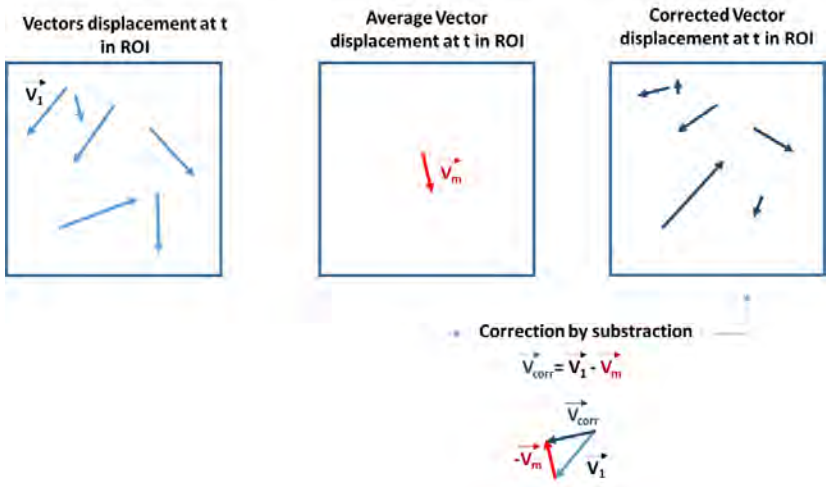

Appendix 1—figure 4. Average vector subtraction for vector correction.

Part 2: mathematical modeling

In this section, we will exhibit the details of the modeling choices. We develop three 2D agent-based models to better understand how the regulation of cell motility by specification factors Sox2 and Bra can influence progenitor behaviors during axis elongation, and to characterize the role of spatial heterogeneity and of a gradient organization of the PZ. We call the three models: (1) the random model

(Sox2/Bra levels are randomly distributed among progenitors), (2) the gradient model (Sox2/Bra levels are patterned in gradient pattern among progenitors), and (3) the mixed model.

The random model

Main variables of the model

In this model, we consider a cell population of N cells (with N=5500 at initial condition) the main variables are the cell type (defined by its Sox2/Bra level, details below), which defines its color in the simulation, and the cell position (random motion). Each of these variables is time-dependent.

Differentiation and evolution of Sox2/Bra levels

Each cell i is characterized by its type, represented here by the ratio $R_i(t) = \frac{Sox2}{Bra+Sox2}$ (see Remark 3): A ratio $R_i(t) = 0$ corresponds to a PSM cell (a red cell in the simulation), and a cell of ratio $R_i(t) = 1$ corresponds to a neural cell (a green cell in the simulation). Finally, a cell with a ratio $0<R_i(t)<1$ is a progenitor cell (different shades of yellow in the simulation), that has not yet differentiated.

To model heterogeneity and oscillations of transcription factors $R_i(t)$ of a cell i we use the following stochastic differential equation:

$$dR_i(t) = \big(100(R_i(t)-0.2)(R_i(t)-0.5)(R_i(t)-0.8)dt + k_r dB_i^R(t)\big)1_{R_i\in(0,1)}$$

with $dB_i^R(t)$ the increment of the Brownian motion associated to the ratio, it represents the various signals a cell receives, and affecting the expression levels of Sox2 and Bra, thus leading it to either cell fate: NT or PSM, corresponding to a ratio of 1 or 0, respectively. Moreover, k_r is a constant representing the intensity of the signal, it is related to the specification rate of the cells. Its value is such that the number of progenitors remains constant throughout the phases of development we are modeling, then in a way to keep the balance between the specification of the cells into either fate and their proliferation (see below for details on the proliferation). Finally, a cell with a ratio $0<R_i(t)<0.2$ is called a pre-mesodermal cell, whereas a cell with a ratio $0.8<R_i(t)<1$ is called a pre-neural cell.

Remark 1: In practice for the numerical simulations, we work discretely in time thus we replace the Brownian motion with a uniform variable $U_i^R(t) \in [-1;1]$ at each time step.

Remark 2: Ignoring the noise, the deterministic function governing the evolution of the ratio has five equilibriums at 0, 0.2, 0.5, 0.8, and 1 with 0, 0.5, and 1 stable equilibriums and 0.2 and 0.8 unstable equilibriums.

Remark 3: The quantity we chose to describe the cell type is the ratio $Sox2/(Bra+Sox2)$. In fact one can have in mind a more general quantity in $[0;1]$ such that 0 and 1 correspond respectively to the PSM and the NT cells, and such that this quantity obeys to the equation of the ratio.

Diffusion process

From literature (***Bénazéraf et al., 2010***) and the present analysis (***Figure 3***), we know that cells in the PZ, in the PSM, and in the NT have a non-directional motility. Thus, one way to model cell motility is using a random unbiased walk (diffusion process) whose intensity depends on the cell's ratio R_i. The stochastic differential equations read:

$$dx_i(t) = k_x dB_i^x(t) \times \mathfrak{B}(R_i(t)),$$

$$dy_i(t) = k_y dB_i^y(t) \times \mathfrak{B}(R_i(t)),$$

with dB_i^x, dB_i^y the increment of the Brownian motion associated to the position (in x and in y) of the cell. They represent the noise of the random walk affecting the cell's movements.

Remark: In practice, for the numerical simulations we work in a discrete environment in time, thus we replace the Brownian motions with uniform variables $v_i^x(t), v_i^y(t) \in [-1;1]$.

Furthermore, the variables $k_x and k_y$ represent the intensity of the diffusion, in accordance with our scale (here we took 1u =150 μm). Furthermore, the velocity function $\mathfrak{B}(R_i(t))$ has the following form:

$$V(R_i(t)) = \begin{cases} 1+\beta(\bar{R}-R_i(t))^2 & \text{if } 0 \le R_i(t) \le \bar{R} \\ 1 & \text{if } \bar{R} \le R_i(t) \le R^* \\ 1+\alpha(R^*-R_i(t))^2 & \text{if } R^* \le R_i(t) \le 1 \end{cases}$$

with α and β two positive constants: $\alpha = \frac{1-0.65}{(R^*-1)^2}, \beta = \frac{1-0.8}{\bar{R}^2}$, and $R^* = 0.8$, and $\bar{R} = 0.2$, are the thresholds that indicte the change of dynamics between progenitors and pre-neural, and progenitors and pre-mesodermal.

Proliferation

Each cell type is endowed with its average proliferation rate: 11.49 hr for the progenitor cells, 10.83 hr for the neural cells, and 8.75 hr for the PSM cells (***Bénazéraf et al., 2017***).

Then each cell, depending on its type, has a probability to proliferate given by b_{PSM} for PSM cells, b_{NT} for NT cells, and b_{PZ} for progenitors:

$$b_{PSM} = \frac{1}{8.75}, b_{NT} = \frac{1}{10.83}, b_{PZ} = \frac{1}{11.49}.$$

When a mother cell proliferates, it gives rise to one daughter cell, which inherits instantly its position and its ratio. The daughter cell is then integrated in the model and obeys to the equations. Depending on its type (PSM, NT, and PZ), it is added to the total cell number of its corresponding population.

Biophysical properties and cell-cell interactions

The system is confined between two horizontal lines, at x=1.5 and x=−1.5, representing the lateral plate which, based on its higher cellular density (***Bénazéraf et al., 2017***; ***Bénazéraf et al., 2010***) can be assumed to act as a physical barrier on either side of the PSM. The system is also limited from the most anterior part, at y=2, as we consider everything above that line to be of high density/epithelial (somites and anterior NT). Recall the scale we chose: $1u = 150\mu m$ (u=graph unit), and here we represent a portion of the posterior body (the most posterior), considering that a portion of the PSM and the NT has already been formed (further details in the section Initial condition).

Cells are endowed with properties that take into account possible interactions between cells. Indeed, cells with high Sox2 adhere, more or less depending on their level of Sox2. The adhesion dynamic is to search inside a neighborhood ϵ (a ball of radius ϵ representing $15\mu m$) for a pack of cells of the same type (a progenitor). The number of cells in this pack depends on the cell's level of Sox2. Therefore, cells of the NT adhere the most. This is a natural assumption as we know that the NT is an epithelium where cells are closely packed.

Moreover, to guarantee non-mixing, cells tend to move away from foreign high densities within a certain neighborhood (a ball of radius 2ε representing $30\mu m$). In particular, cells with various levels of Bra flee densities of all foreign cells. Furthermore, to keep well-defined physical boundaries between the tissues, and to avoid packing, we also ask neural cells to move away from high densities of PSM cells. Using these interaction rules, we created a model that presents self-organizing phenomena, with physical boundaries between the tissues.

Initial condition

We consider the embryo to be at a stage where a portion of the NT and the PSM has already been formed (anteriorly), for example at stage HH8. We distribute 1200 neural cells inside the square $[-0.05; 0.5] \times [0; 2]$, with an initial ratio of 1. As these cells are already differentiated into their neural fate, their ratio is not updated at each time step. We distribute 3200 PSM cells, which corresponds to 1600 from either side of the already formed NT, inside $[-1.5; -0.5] \cup [0.5; 1.5] \times [-2.5; 2]$, with an initial ratio of 0. These cells also do not update their ratio as they have already engaged in their mesodermal fate. Finally, we distribute 1100 progenitor cells inside the square $[-0.5; 0.5] \times [-1.5; 0]$.

Each progenitor cell i is attributed a random initial ratio in [0.15; 0.85]

Remark: By definition of the ratio and by its equation , we can see that progenitor cells with a ratio less than 0.2 are predestined to a mesodermal fate, and cells with a ratio higher than 0.8 are predestined to a neural fate. These pre-destined cells account for 14% of the total number of progenitor cells initially. The presence of these specified cells in our model is justified by the fact that we have noticed the presence of progenitors having Sox/Bra levels as high or as low as NT or PSM cells in the biological system (***Figure 1I***)

List of variables and their values:

K_r=0.27,

ε=0.1,

maxTN=5, representing the maximal density (number of cells in a neighborhood of size 2ε) a neural cell can withhold before fleeing the density,

maxPSM=4, representing the maximal density (number of cells in a neighborhood of size 2ε) a PSM cell can withhold before fleeing the density,

maxPZ=4, representing the maximal density (number of cells in a neighborhood of size 2ε) a progenitor cell can withhold before fleeing the density,

$\Delta t = 0.01$, the time step of the scheme, representing 6 s of real biological development,

Tmax=60, representing 10 hr of real biological development,

K_x=0.43,

K_y=0.43,

$R^\star = 0.8$,

$\tilde{R} = 0.2$.

Remark: One should note that the frame rate of the live imaging is 1 frame per 6 min. Thus, in our simulations, we save one frame each 6 min (corresponding to $60\Delta t$).

The gradient model

The purpose of this model is to impose a gradient-like structure to the PZ. More specifically, our aim is to have cells expressing high Sox2 in the most anterior PZ, and cells expressing high Bra in the most posterior PZ, while keeping the pool of progenitors. To do so, we divide the PZ into eight subdivisions in the direction of the y-axis, such that each subdivision contains the same number of cells. Cells in subdivisions 1–3 will be subjected to a signal coding for an overexpression of Sox2, and cells in subdivisions 6–8 will be subjected to a signal coding for an overexpression of Bra, while cells in subdivisions 4 and 5 will be subjected to a weak signal to keep the ratio of these cells near the equilibrium state 0.5, which will allow them to proliferate and keep the progenitor pool. Then, calling $f(R_i(t))100(R_i(t)-0.2)(R_i(t)-0.5)(R_i(t)-0.8)$, the equation for the ratio reads:

$$dR_i(t) = \begin{cases} f(R_i(t))dt + k_r dB_i^{R_a}(t) & \text{if} subdiv(1) \le y_i(t) \le subdiv(3) \\ f(R_i(t))dt + k_r dB_i^{R_b}(t) & \text{if} subdiv(4) \le y_i(t) \le subdiv(5) \\ f(R_i(t))dt + k_r dB_i^{R_c}(t) & \text{if} subdiv(6) \le y_i(t) \le subdiv(8) \end{cases}$$

with $dB_i^{R_a}(t), dB_i^{R_b}(t), dB_i^{R_c}(t)$ the increments of the Brownian motion of the cell in each subdivision, respectively replaced by $U_i^{R_a}(t), U_i^{R_b}(t), U_i^{R_c}(t)$ in the numerical simulations, with $U_i^{R_a}(t)$ a uniform random variable in $[-0.9; 1.1]$ corresponding to a high Sox2 signal in this region, $U_i^{R_c}(t)$ a uniform random variable in $[-1.1; 0.9]$ corresponding to a high Bra signal in this region, and $U_i^{R_b}(t)$ a uniform random variable in $[-0.1; 0.1]$ corresponding to a weak signal in this region where ratios will vary slightly, thus inhibiting specification and favoring the maintenance of the progenitor pool.

Thus, at each time step, cells evaluate their position, and update their ratio accordingly.

Remark: We do not change the velocity function $\Re(R_i)$, nor the interaction between cells nor the biophysical properties of the model. However, the initial distribution of the progenitor cells is changed to be gradient patterned (details in the paragraph Initial condition). The gradient structure is enforced into the new (updated) PZ at each time step.

Initial condition

The disposition of the tissues PSM, TN, and PZ remains the same as in the random model. The initial distribution of the PSM and NT cells is also unchanged. However, we change the initial distribution

of the PZ cells from a random one, to a gradient distribution as the following: we distribute 1100 progenitor cells inside the square $[-0.5; 0.5] \times [-1.5; 0]$. Each progenitor cell i is attributed an initial ratio in [0.15; 0.85] depending on its position in the PZ: cells with the highest ratio (closer to 1) will be placed anteriorly, whereas cells with the lowest ratio (closer to 0) will be placed posteriorly. Using a linear function in y, the ratios are initially distributed as the following:

$$R_i(t=0) = -\frac{0.15-0.85}{1.5} y_i(t=0) + 0.85$$

Remark: By definition of the ratio, its equation, and what we just described, we can see that progenitor cells with a ratio less than 0.2, predestined to a mesodermal fate, are now in the most posterior region of the PZ, and cells with a ratio higher than 0.8, predestined to a neural fate, are now placed in the most anterior part of the PZ.

List of variables and their values:

We kept most variables equal to the ones in the random model, however, some of them are not comparable then we had to change their values to meet the model hypotheses.

k_r=0.23

$\epsilon = 0.1$,

maxTN=5, representing the maximal density (number of cells in a neighborhood of size 2ϵ) a neural cell can withhold before fleeing the density,

maxPSM=4, representing the maximal density (number of cells in a neighborhood of size 2ε) a PSM cell can withhold before fleeing the density,

maxPZ=4, representing the maximal density (number of cells in a neighborhood of size 2ε) a progenitor cell can withhold before fleeing the density,

Δt = 0.01, the time step of the scheme, representing 6 s of real biological development,

Tmax=60, representing 10 hr of real biological development,

K_x=0.43,

K_y=0.43,

$R^\star = 0.8$,

$\bar{R} = 0.2$.

The mixed model

After studying the role of spatial heterogeneity and of a gradient structure of the PZ, we now want to have a model that is close to the biological reality. More specifically, our aim is to have cells expressing high Sox2 in the most anterior PZ, and cells expressing high Bra in the most posterior PZ, while keeping the pool of progenitors in the middle area expressing heterogeneous levels of Sox2 and Bra in a spatially heterogeneous pattern. To do so, we divide the PZ into eight subdivisions in the direction of the y-axis, such that each subdivision contains the same number of cells. Cells in subdivision 1 will be subjected to a signal coding for an overexpression of Sox2 (biased noise), and cells in subdivision 8 will be subjected to a signal coding for an overexpression of Bra (biased noise), while cells in subdivisions 2–7 will be subjected to an unbiased noise, thus creating spatial heterogeneity. Then, calling $f(R_i(t))100(R_i(t)-0.2)(R_i(t)-0.5)(R_i(t)-0.8)$, the equation for the ratio reads:

$$dR_i(t) = \begin{cases} f(R_i(t))dt + k_r dB_i^{R_a}(t) & \text{if } y_i(t) = subdiv(1) \\ f(R_i(t))dt + k_r dB_i^{R_b}(t) & \text{if } subdiv(2) \le y_i(t) \le subdiv(7) \\ f(R_i(t))dt + k_r dB_i^{R_c}(t) & \text{if } y_i(t) = subdiv(8) \end{cases}$$

with $dB_i^{R_a}(t), dB_i^{R_b}(t), dB_i^{R_c}(t)$ the increments of the Brownian motion of the cell in each subdivision, respectively replaced by $U_i^{R_a}(t), U_i^{R_b}(t), U_i^{R_c}(t)$ in the numerical simulations, with $U_i^{R_a}(t)$ a uniform random variable in $[-0.9; 1.1]$ corresponding to a high Sox2 signal in this region, $U_i^{R_c}(t)$ a uniform random variable in $[-1.1; 0.9]$ corresponding to a high Bra signal in this region, and $U_i^{R_b}(t)$ a uniform random variable in $[-1; 1]$ corresponding to the unbiased noise creating spatial heterogeneity. Thus, at each time step, cells evaluate their position, and update their ratio accordingly.

Remark: We do not change the velocity function $\mathfrak{B}(R_i)$, nor the interaction between cells nor the biophysical properties of the model. However, the initial distribution of the progenitor cells is changed to be a mixed pattern between the random pattern and the gradient pattern (details in the

paragraph Initial condition). The mixed structure is enforced into the new (updated) PZ at each time step.

Initial condition

The disposition of the tissues PSM, TN, and PZ remains the same as in the random and in the gradient model. The initial distribution of the PSM and NT cells is also unchanged. However, we change the initial distribution of the PZ cells to a mixed distribution as the following: we distribute 1100 progenitor cells inside the square $[-0.5; 0.5] \times [-1.5; 0]$. Each progenitor cell i is attributed an initial ratio in [0.15; 0.85], depending on its position in the PZ: cells in subdivision 1 (high in Sox2) are attributed a random ratio between 0.5 and 0.85, and cells in subdivision 8 are attributed a random ratio between 0.15 and 0.5. Finally, cells in the remaining subdivisions acquire a random ratio between 0.15 and 0.85.

List of variables and their values:

We kept most variables equal to the ones in the random and gradient models, however, some of them are not comparable then we had to change their values to meet the model hypotheses.

k_r=0.24,

ε=0.1,

maxTN=5, representing the maximal density (number of cells in a neighborhood of size 2ε) a neural cell can withhold before fleeing the density,

maxPSM=4, representing the maximal density (number of cells in a neighborhood of size 2ε) a PSM cell can withhold before fleeing the density,

maxPZ=4, representing the maximal density (number of cells in a neighborhood of size 2ε) a progenitor cell can withhold before fleeing the density,

Δt=0.01, the time step of the scheme, representing 6 s of real biological development,

Tmax=60, representing 10 hr of real biological development,

K_x=0.43,

K_y=0.43,

$R^\star = 0.8$,

$\bar{R} = 0.2$.

Case 1: high Sox2

To simulate the high Sox2 case in the mixed model, the only parameter we change is the noise in the equation of the ratio $R_i(t)$. In fact, instead of having a uniform variable in $[-1; 1]$, allowing cells to have an equal probability of differentiating to either PSM or neural cells, we shift the noise and insert a uniform variable in $[-0.92; 1.08]$. By doing so, cells have a higher probability to differentiate toward a neural ratio ($R_i(t)$=1).

Case 2: high Bra

To simulate the high Bra case in the mixed model, the only parameter we change is the noise in the equation of the ratio $R_i(t)$. In fact, instead of having a uniform variable in $[-1; 1]$, allowing cells to have an equal probability of differentiating to either PSM or neural cells, we shift the noise and insert a uniform variable in $[-1.08; 0.92]$. By doing so, cells have a higher probability to differentiate toward a PSM ratio ($R_i(t) = 0$).

Figures

In the following paragraph, we present the details of the computations of the violin plots and the angle plots. We used this approach to validate the model and compare its results to those of the live imaging analysis.

We do the same computations for all three models.

Cell tracking

To generate the violin plots, we save the cells' positions every 6 min (in real biological time, to correspond to the time points of the live imaging), this corresponds to 60 Δt in simulation time with our choice of Δt. To compute the cell velocity in each tissue, we consider a region of size $1u \times 1.5u$ in the PZ and the NT, and $0.8u \times 2u$ in the PSM. At each time step, these regions are translated posteriorly, following the displacement of the most anterior point of the PZ.

Then, for each tissue, we compute the velocity of each trajectory for the cells in the considered regions, between the time point t and t+6 min, starting from t=0 to t=10 hr. We only consider the cells initially present in the regions and up to the time when they exit the regions.

To plot the distribution of the angles in each tissue for every cell type we consider each cell (in the regions previously drawn in each tissue) and compute the angle between the trajectory and the reference vector pointing downwards (in the direction of the elongation) of each trajectory, between the time point t and t+6 min. This angle will fall into one of 24 bins (dividing the 360˚ disk into 24 subdivisions). Finally, we compute the mean velocity in every bin. We then multiply each mean velocity, in each bin, by the proportion of trajectories in that bin, this gives the length of the arrow plotted in each bin.

Tracking the shape of the progenitor zone

We upload the simulation generated by Matlab to the software ImageJ and manually track the most anterior and most posterior point of the PZ (per frame). This gives a track of the length of the PZ through time. For the width, as the PZ is moving and changing shapes, we choose to track the width of the mid-PZ throughout the simulation (tracking the mid-left and mid-right points). We then plot the rectangles hereby generated ($length \times width$) for initial time and final time.

We use the manual tracking of the most posterior point of the PZ to compute the elongation rate.

Mean square displacement

To compute the MSD of progenitor cells we use the following formula:

$$MSD(t) = \frac{1}{N}\sum_{i=1}^{N}\left((x_i(t) - x_i(0))^2 + (y_i(t) - y_i(0))^2\right)$$

with N the number of cells considered. Here, we consider all the progenitor cells up to the time when they differentiate.

Numerical scheme

We use the forward Euler method. The code was done using Matlab R2020a. The file contains three simulations:

- Simulation 1: Wild-type embryo (mixed model)
- Simulation 2: Case of high Sox2 and case of high Bra
- Simulation 3: Three models (random, mixed, and gradient)

Chapter 7

Discussion

In this Ph.D thesis we had three goals. The first one was to develop macroscopic PDE models which solutions are segregated and exhibit swirling motions, in an effort to apply them to the morphogenesis of the vertebrate embryo (Objective 1). Based on these models, we wanted to determine the contribution and the share of each morphogenetic mechanism on tissue formation and on the elongation of the vertebrate embryo (Objective 2). Lastly, we wanted to focus on the cellular behavior during tissue formation by investigating the role of two proteins (Sox2 and Bra) on a population of progenitors in the vertebrate embryo (Objective 3). In what follows, we present and discuss the main results of each chapter in this manuscript, and explain our future works and perspectives.

7.1 Objective 1. Develop macroscopic PDE models exhibiting segregated solutions and swirling motions

7.1.1 Our strategy

Our modelling approach in [49] relied on the basis that tissues can be considered as viscous fluids. Inspired by equations of fluid mechanics, we developed two 2D mechanical multi-tissue models where the description of the tissue is made through the mathematical description of its density and velocity. The velocity follows the Brinkman law which accounts for the tissue's viscosity. This law allowed us to obtain the swirling motions. We tested two types of segregations in the models. The first model (we called the VM) is endowed with passive segregation, that is, if the solutions are initially segregated they remain segregated for all times. The second model (which we called the ESVM) uses a repulsion pressure which segregates the solution in finite time (except for a small interface) if initially mixed. We then linked these two models to their geometric descriptions through the incompressible limit and extracted meaningful biophysical properties. In what follows, we summarize the results obtained in Chapter 4.

7.1.2 Summary of the results

We confronted the VM (passive segregation) and the ESVM (active segregation) numerically, both of them endowed with the Brinkman law. We observed swirling motions in both models

within the PSM. However, only the ESVM was able to reproduce the anterior swirling motions in the PSM which displays anterior regions of alternating curls. We formally proved the strict segregation in the VM in the case the tissues' viscosities are equal and provided arguments for the more general case. We formally computed the incompressible limit of the two models and obtained their respective geometric descriptions. At the limit, we show that the L-ESVM yields full segregation of the solutions and that unintuitively the segregation pressure persists at the limit and still affects the dynamics. This is reminiscent of a *ghost effect*. We also prove (in the case the viscosities are equal) that the L-VM is endowed with passive segregation. We confront the models at the limit numerically. Here again, we observed that the correct swirling motions in the PSM are obtained only when the segregation pressure is present at the limit. We then studied the properties of the stationary L-ESVM which amounts to a velocity-pressure system. Posing the system in a bounded domain $\Theta \in \mathbb{R}^2$, we prove existence in H^1 and uniqueness of the velocity which solves a second-order elliptic system with discontinuous coefficients. We obtain regularity results on the velocity depending on the regularity of the segregation pressure. We show that if the segregation pressure is Hölder continuous in each subdomain of Θ occupied by the tissues, the velocity is in some Hölder space in each of these subdomains. If the segregation pressure is smooth ($\mathcal{C}^\infty$) then the velocity is also smooth in each subdomain. We derive a transmission problem which highlights the transmission conditions defined on each subdomain in Θ. Using this formulation, we prove the existence of pressure jumps on the subdomains' boundaries, by showing first that the velocity is not in H^2 on Θ.

To sum up, our results qualitatively show that the pressure (and the velocity gradient) exhibits jumps on the tissues' boundaries and nowhere else. The jumps on the exterior boundaries are linked to the use of the Brinkman law (viscosity-induced) whereas the jumps on the interface are linked to the difference in the viscosity coefficients of the tissues.

7.1.3 Discussion about our contribution and perspectives

Novelty of our models: viscosity and swirling motions. Passive segregation is a property commonly found in literature in models with contact inhibition or with volume exclusion. We used this property and coupled it to the Brinkman law to observe two distinctive embryonic phenomena. The novelty of our work is to consider this coupling in a bounded domain with suitable boundary conditions in dimension bigger than one, which allowed us to observe swirling motions. The second novelty is the study of the incompressible limit also considered in a bounded domain. In literature, the Brinkman law is commonly used in its gradient form, that is, the velocity is considered as the gradient of some potential. This form does not allow the appearance of swirling motions, but allows the use of famous techniques in elliptic theory when computing the incompressible limit. The Brinkman law we used (without considering the velocity as a gradient, and in

a bounded domain with boundary conditions) introduces new technical difficulties in the computations of the incompressible limit. For this reason, the incompressible limit in Chapter 4 is formal, and we leave the rigorous derivation of the corresponding free boundary problem for a future work.

Novelty of our approach: link between the hydrodynamic models for axis elongation and their free boundary descriptions. It is common in literature to develop free boundary problems to describe the embryonic tissues. Our approach shares this point of view via the incompressible limit. The novelty of our modelling approach compared to models for axis elongation in literature is that we find the corresponding geometric description of the hydrodynamic model we develop. This allows to maintain the link between the hydrodynamic description of the embryonic tissues and their free boundary description, via the computation of the incompressible limit. Furthermore, it allows us to choose the suitable tissue description depending on the biological data at hand, and depending on the regime in which we consider the tissues. If we are interested in describing the evolution of the tissues' boundaries, then the incompressible regime is the most suitable one. If we are interested in describing the density fluctuations and evolution, then we choose the hydrodynamic description. Another novel aspect is found in the obtained system at the incompressible limit. At the incompressible limit we achieved full segregation of the densities in the L-ESVM. Unintuitively, the segregation pressure does not vanish at the limit and still produces a finite effect on the solution behavior. We perceive the persistence of this pressure as a *ghost effect*, a terminology originating from kinetic theory. To our knowledge, such phenomena is novel to the literature of incompressible limits. In fact, we could not have phenomenologically predicted the appearance of this effect with a direct modeling at the geometrical scale, its appearance was the result of the computation of the incompressible limit and required technique and intuition.

Emergent biological hypothesis : an active force may be at play to segregate the embryonic tissues. We tested two types of segregations in the VM and in the ESVM, which could be responsible for the observed maintenance of segregation between the NT and the PSM. Our numerical simulations show that without the repulsion pressure, we cannot reproduce the correct swirling motions observed *in vivo*. This result strongly suggests that an active force may be at play to maintain the tissues segregated throughout axis elongation. This active force can take many forms in the vertebrate embryo. It can be a chemical repulsion which actively drives cells away from each other when they come in contact, or it can be an active mechanical force from cell surface tension. We propose to test this biological hypothesis by mixing PSM and NT cells and filming cell motion using live imaging. This experiment would validate the model hypothesis and give us more insight on the cell-cell interactions. Interestingly, this same experiment can be used to study the segregation of progenitors into the different tissues.

Emergent biological hypothesis : cohesion between cells of the same type. Introducing the repulsion pressure led to the introduction of the parameter α in the fourth order term in the PDEs for the densities. The parameter α is responsible for the cohesion of the species in the model and is necessary to prevent the formation of alternating densities (*bubble effect*). In theory, this parameter ensures the stability of the system. In practice, this parameter models a self-adhesion force, which promotes tissue segregation in the form of bulks of the same tissue type. We propose again the same biological experiment as before by mixing cells of different types and by studying the patterns they form when they segregate. If they segregate in the form of small patches, this suggests that the parameter α should be very small and that cohesion is weak. If they form bulks of densities of the same tissue type, then cohesion is strong between the cells and α should be taken large.

Emergent biological hypothesis : the *ghost effect*. The appearance of the *ghost effect* further advocates for the hypothesis that the segregation pressure cannot and should not be neglected when we describe the tissues in their incompressible regime as it plays an active role on the dynamics. It highlights the role of the segregation pressure as an active force segregating the tissues, maintaining their segregation, and giving rise to the swirling motions observed *in vivo* in the incompressible regime of the tissues.

Emergent biological hypothesis: a pressure jump at the tissues' boundaries. We have proved that the pressure in the tissues exhibits jumps at the tissues' interfaces and boundaries. The jump on the interface is due to the fact that the tissues do not share the same viscosity coefficient. This is the case in the vertebrate embryo between the NT and the PSM. We propose to test this hypothesis *in vivo*. As the pressure jump is expressed in terms of the growth functions, and as cell proliferation is known in the embryonic tissues thanks to [24], it would be interesting to see if this relation between the pressure and the growth at the tissues' boundaries holds *in vivo*. In our model, the interfaces on which discontinuities occur do not have any width. In the embryo, the interface between the tissues is made of extra-cellular matrix which has a certain thickness. This matrix can not only transmit forces from one tissue to another, but can also absorb pressure discontinuities. It is then difficult to measure *in vivo* the equivalent of a pressure discontinuity. This makes the comparison with biological experiments quite challenging.

Perspectives. As mentioned previously, the incompressible limit for two species with the Brinkman law in a bounded domain in 2D is very challenging. In an ongoing work with Sophie Hecht, we study a density-velocity system for a single tissue in a bounded domain with the Brinkman law. Our aim is two-fold: 1) prove the existence of the solution to the density-velocity coupled system 2)

compute the rigorous incompressible limit of the system. This work in the case of a single species will lay down the foundations of the computational techniques of the incompressible limit that may be reused for the multi-species case.

Furthermore, as we concluded in Chapter 4, an important modelling question to answer is whether there exists other forms of repulsion pressures which can reproduce the swirling motions observed *in vivo*. For that reason, we aim test in a future work other forms of active pressures promoting segregation (of linear type for example). The consequent swirling motions observed and other properties of the system could give us more insight on the type of active force we should be looking for in the vertebrate embryo.

7.2 Objective 2. Determine the share of each morphogenetic mechanism on axis elongation

7.2.1 Our strategy

Inspired by the models developed in Chapter 4, and as they do not allow, in their present form, to take into account cell injection from the PZ into the PSM and the NT, we developed a variant of the VM. This variant (which we called the VMI) incorporates an extra source term which accounts for new cells entering the tissues from their posterior tip. We calibrate this model with values taken from literature on vertebrate embryos. We developed a protocol to measure other parameters not present in literature. We compare this model to biological data and validate it. Finally, we ran multiple *in silico* experiments which led to many interesting biological hypotheses. We compared some of these emergent hypotheses with existing biological data. We also analyzed new biological results which confirmed the model hypotheses.

7.2.2 Summary of the results

After the calibration of the VMI, we ran a first simulation which corresponds to the WT embryo *in silico*. We found that the results quantitatively matched the measured densities and velocities in [24], and the elongation rate in [25]: the PSM velocities and densities exhibited an antero-posterior gradient. Our model shows that the cell velocity in the NT is also in a gradient pattern, which is in line with the analysis in [24]. Our model exhibited inter-tissue sliding in the anterior region of the tissues, with the NT sliding past the PSM. This was first hypothesized in [24] and our model confirms this hypothesis. We then tested the effect of differential proliferation and differential injection on axis elongation, tissue formation and inter-tissue sliding. We showed that when proliferation rates were equal to that of the NT, the sliding significantly decreased, as well the elongation rate, and that the NT became wider. When proliferation rates were taken equal to that of the PSM, the NT also widened, the elongation rate increased as well as the inter-tissue sliding. Differential cell

injection however had little effect on the tissues compared to cell proliferation. We then ran some extreme cases to test the contribution of each single phenomenon (proliferation and injection) on axis elongation. We found that inhibiting cell injection had no effect on tissue evolution whereas cell proliferation appeared to be crucial for long-term (12 hours) tissue formation and elongation. We compared some of these results to biological data by analyzing live movies of transgenic quail embryos from [25, 24] (WT and treated embryos with electroporated P27 in the PSM) and found that, as predicted by our model, the NT is wider in the P27 treated embryos. Finally, we tested our model with a different tissue couple: the PSM and the notochord. We changed the parameters of the model to fit the ones of the notochord and saw that the model reproduces very well the density and velocity profiles in the notochord as well as its shape. The model predicts a very high sliding between the PSM and the notochord and a graded cell motility in the notochord along the antero-posterior axis. The VMI proves to be a polyvalent and multi-functional model which can reproduce and predict interesting multi-tissue dynamics.

7.2.3 Discussion about our contribution and perspectives

Novelty of our approach. Although many models were proposed in literature to explain axis elongation, they did not account for cell proliferation coupled with cell injection as driving mechanisms of growth. This is due to the fact that studies in [25] showed no difference in elongation rates when embryos were treated with cell cycle inhibitors. The studies in [25] were however made for short times (6 hours). In our model, we introduce both phenomena as growth promoters. The VMI highlights the contribution of proliferation and of cell injection independently from one another, as well as the share of one with respect to the other on axis elongation. This approach allowed us to infer that cell proliferation explains long-term dynamics (as opposed to short time dynamics which can be explained by diffusion) of the elongation of the WT embryo and is essential for tissue formation and extension. Furthermore, literature models were most often PSM-based, meaning that they did not account for the axial tissues. The novelty of our model is that it is multi-tissue and in 2D. It considered the coupled dynamics of the PSM and the NT. And it does so, by maintaining tissue segregation and by allowing the appearance of swirling motions, both of which are observed in the vertebrate embryo. Finally, the study and quantification of inter-tissue sliding in different *in silico* treated embryos is a novel contribution to the literature on vertebrate embryos.

Benchmark. Our model highlights the importance of the PSM during axis elongation. We show that the PSM densification and growth pushes the NT laterally. This compression promotes the elongation of the NT (through a convergence-extension like behavior anteriorly) and the PSM's growth drives the posterior boundary. This is in accordance with a recent study in [160]. In [160], when authors ablated the posterior PSM, they observed a significant reduction in posterior move-

ment of the PZ. This observation suggested that the mechanism of convergence-extension of the axial tissues pushes the PZ towards the posterior. Furthermore, authors observed that this ablation led to a wider posterior NT. This confirmed that the PSM exerts lateral to medial compression on the axial tissues. This observation is also present in our numerical simulations, which we confirmed *in vivo* by comparing them to biological data on transgenic quails. Authors then propose an engine-like model of positive feedback: the PSM compresses latero-medially on the axial tissues, which pushes the PZ posteriorly, which in turn promotes the exit of cells from the PZ into the PSM, thus re-inducing compression. Our model confirms the role of the compression of the NT by the PSM which pushes the posterior boundary. The injection rate, in the present form of our model, is constant throughout axis elongation, then we cannot study the effect of axial compression and pushing forces on the addition of new cells as in [160]. However, the VMI proposes that cell injection has no effect on tissue nor on inter-tissue mechanics leading to axis elongation, which disproves the last step in the loop model of [160]. The VMI complements the study in [160] and confirms the hypothesis in [24] that inter-tissue sliding occurs between the PSM and the NT in the mid-anterior region of the tissues. Our preliminary analysis (data not shown here) of images of developing quail embryos confirms the inter-tissue sliding in the WT embryo.

To our knowledge, our work is the first to study and quantify the multi-tissue sliding in the vertebrate embryo. It predicts that inter-tissue sliding is governed by cell proliferation in each tissue, and that cell proliferation is behind long-term growth and elongation. In recent studies, we observe that short-term extension can be explained by other phenomena than cell proliferation. In a study on PSM cell motility [25], authors treat embryos with Aphidicolin, a cell cycle inhibitor (S-phase), and inhibit cell proliferation in the NT and in the PSM. Interestingly, and although the PSM and the NT are highly proliferative tissues, they noted no difference in the elongation rate of the embryos when analyzed for short times (6 hours). Authors explain this phenomenon by stating that random cell motility drives PSM extension. This result might seem contradictory to our findings where the VMI emphasizes on the importance of cell proliferation in the tissues for axis elongation. However, it is not. The discrepancy can be explained by the fact that the study in [25] was done on short times (up to 6 hours), and our simulations model 12 hours of biological time, which is enough time for the PSM to double its mass (proliferation rate of the PSM is approximately equal to 11 hours). Cell proliferation may then have no effect for short times, as the biological system can proceed its natural diffusion, but its long time effects translate onto axis elongation and tissue formation. This is in accordance with our simulations in Figure 7.1 which showed little difference between 0 hours and $3-4$ hours in posterior elongation between the WT case and the case where the proliferation rate of the PSM and of the NT are equal to zero. However between 4 and 12 hours, the elongation difference is radical. This suggests that tissues undergo a first phase where they diffuse, then go into the second phase where growth is necessary to sustain their elongation.

In addition, density measurements in [24] tell us that extension without proliferation is not

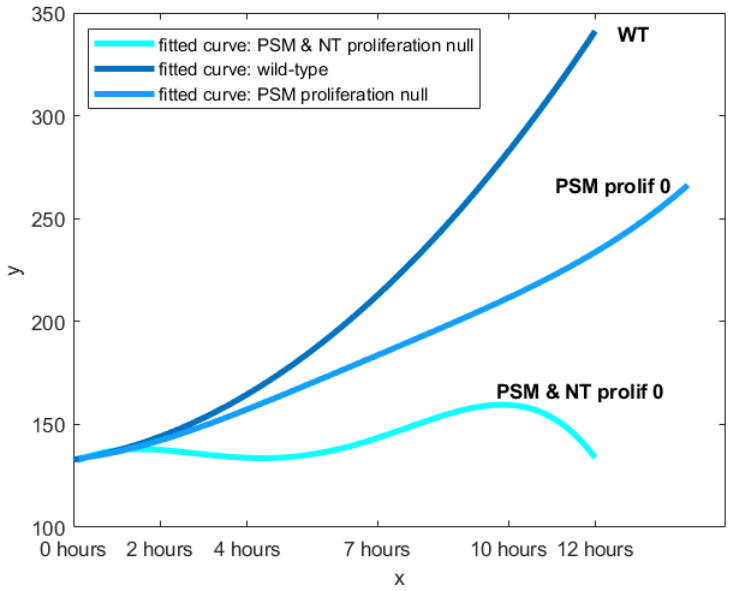

Figure 7.1 – Analysis of the numerical simulations: fitted curves of the elongation of the posterior tip (y-axis) with respect to time (x-axis) in three cases: wild-type case, when the PSM proliferation rate is null and when the proliferation of the PSM and the NT are null.

possible as the PSM density is rather constant. Therefore, diffusion (random cell motility) in the absence of mitosis (cell division into two daughter cells) is not enough to sustain long term tissue growth. Furthermore, using Aphidicolin prevents mitosis but it does not prevent cell growth (cell cycle progression to the other phases leading to cell size growth). Then the cell volume gain could actively promote tissue growth and extension during short times and could lead to short-term elongation. In fact, it was shown in Aphidicolin treated zebrafish embryos, that mitosis is not necessary for the somite segmentation clock to function [163]: somites formed normally without cell proliferation, but using only the cell volume growth. An interesting biological experiment would be to use cell cycle inhibitors that stop the production of mass inside the cell, which would block its gain in volume. In a very recent work [109], another interesting short-time phenomena was evoked that could explain the extension of the PSM, that is, the bloating of the extra-cellular matrix. Authors analyzed the elongation of PSM explants during 4 hours post Dextran treatment (a marker of the Hyaluronic Acid which is the most abundant component of the extra-cellular matrix). The analysis revealed that FGF signaling pathway regulates Hyaluronic Acid expression through glycolysis, the latter being a known regulator of cell motility in the PSM [118]. These results hold on explants analyzed for 4 hours but they cannot explain the formation and expansion of the PSM for longer times to maintain a constant PSM density. And as cell spacing in the absence of mass addition decreases the tissue density, we can safely deduce that for longer times proliferation must interfere and compensate the extra-cellular matrix bloating. To sum up, tissue extension led

by cell volume gain or by extra-cellular matrix bloating or cell diffusion can explain extension for only short times, and cell proliferation drives long-term elongation. This is in accordance with our simulations in Figure 7.1 which showed very little difference in posterior elongation for up to 4 hours between the WT case, the case where the proliferation rate of the PSM is zero, and the case where the proliferation of the PSM and of the NT are null. Tissues extended slightly in the absence of proliferation thanks to diffusion. When compared at larger times, we see that elongation drastically differs between the three cases and observe that the WT case has the fastest elongation. Interestingly, the VMI can also be applied to the case where the growth is led by matrix bloating for short times such as in [109]. Indeed, instead of considering the cell density as a variable, we can consider the volume (or area) of the cell and its surrounding Hyaluronic Acid (over the total volume in the PSM). This version of the model can complement the findings in [109] by giving us more insight as to the effective growth in the PSM. We note that many efforts in research were made to understand the involvement of the PSM in axis elongation, however very little is known about the NT's role during vertebrate extension. The VMI addresses this matter and further highlights the essential role of the NT and of its growth.

Our model further reveals the role of the differential growth between posterior tissues. Based on the model's results, we propose that differential cell proliferation in the posterior tissues plays a key role in sustaining long-term tissue formation and axis elongation and in creating inter-tissue sliding. Strikingly, it was shown that differential growth is also behind gut formation in chick embryo [132]. The gut is in fact composed of a gut tube attached to the mesentery along its entire length. In [132], authors show that the gut tube and the mesentery proliferate at different rates. The authors then develop a mathematical model based on two stitched rubbers: the first rubber (modelling the mesentery) is stretched and the second rubber (the gut tube) is unstretched. The different strains mimic the differential proliferation between the gut and the mesentery. Upon free relaxation, the rubbers deform into a looped structure very similar to the gut in chick embryos.

A mechanical model for axis elongation. In [108], the author proposes three possible models of axis elongation, see Figure 7.2. The first model, Figure 7.2 A, proposes that the PSM alone grows and pushes the PZ. This type of assumption was made for example in the mathematical 2D microscopic model in [129] (see Chapter 1). If this were the case, then the NT would only be a passive tissue, laterally pulled on and dragged by the PSM and inducing its elongation. We know that this is not the case as authors in [24] proved that the NT is a highly proliferative tissue with a tissue velocity higher than that of the PSM. One could even imagine the opposite scenario where the NT drags the PSM. But this is also not the case, as the NT is much shorter than the PSM, which means if the dragging force exists, it does not explain the posterior growth of the PSM. Our numerical simulations disprove the model A and show that in the absence of proliferation in the NT, see Figure 5.12c, some elongation can still occur thanks to lateral compression, but the NT cannot

form properly (density and shape wise). We now look at model B. The author proposes that axial

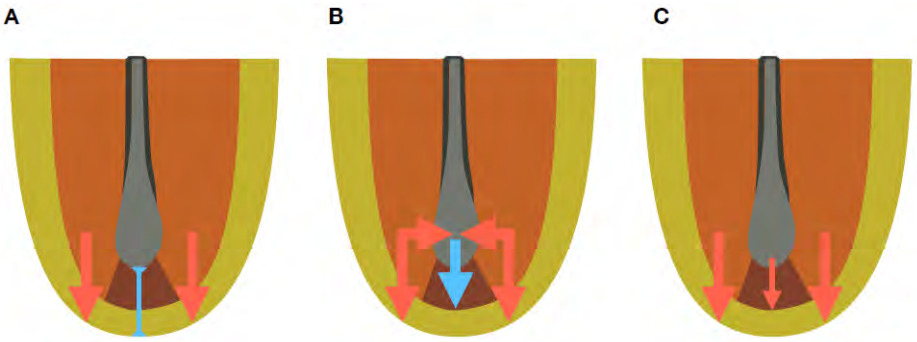

Figure 7.2 – Taken from [108]. Multi-tissue elongation models. A: PSM growth only model. The PSM is the only tissue growing and actively pushes the posterior boundary. B: PSM mediated convergent extension of the axial tissues model. The PSM is actively pushing the posterior boundary and compressing the axial tissues, which undergo convergent extension leading to their growth. C: Axial tissues independent growth model. Axial tissues push independently of the PSM activity but they generate a force too weak to displace the boundary in the absence of the PSM push. Red arrows: active forces, blue arrows: passive forces.

tissues undergo passive growth as a result of PSM lateral compression which also pushes the PZ posteriorly. Our numerical simulations show that this model does not sustain tissue formation. In the absence of NT proliferation, the NT indeed undergoes some convergence-extension like behavior which leads to its extension but not to its proper formation, see Figure 5.12c. In fact, due to the lack of growth, the NT cannot resist to the compression of the PSM and becomes very slim. This shows that axial tissues must also grow to properly form. This is further supported by the measured proliferation rate of the NT in [24] showing it is highly proliferative. Finally, we look at model C. In Figure 7.2 C, the author proposes a third model where the axial tissues and the PSM both grow, but the axial tissues cannot generate enough force to push the PZ downwards. The role of the PSM is then in the active pushing of the PZ boundary which leaves room for the axial tissues to grow. Our simulations are in accordance with this model. They reveal that when the axial tissues grow, in the absence of PSM growth, some elongation happens but it is not enough to drive the posterior tip downwards, see Figure 5.12c. This highlights the role of PSM growth in driving the PZ boundary towards the posterior and compressing the axial tissues. This leads us to propose a fourth model schematized in Figure 7.3, in the spirit of [24, 108] which accounts for the short-term and the long-term mechanisms of axis elongation.

In Figure 7.3, we propose that short-term dynamics (up to $T = 4$ hours) can be explained by PSM cell motility induced by the FGF8 gradient (represented by red arrows in three directions) and/or by matrix bloating which creates extra space between the cells (represented by the orthogonal red arrows). Diffusion and cell spacing can then induce posterior extension for short times. Lateral compression from the PSM on the NT can also contribute to the short-term extension of

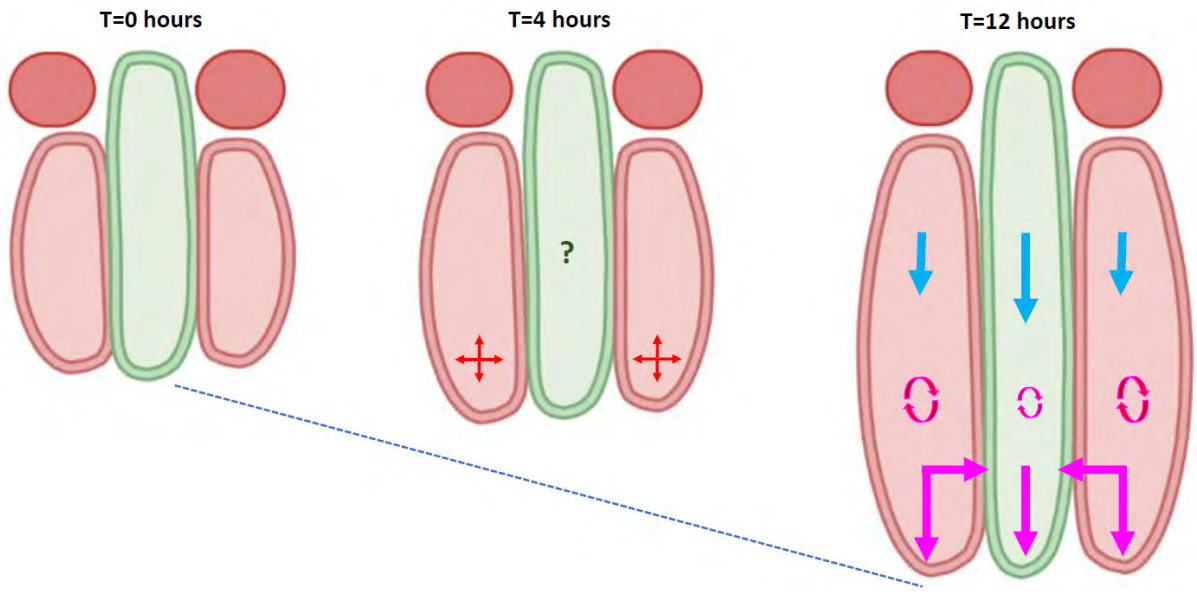

Figure 7.3 – Multi-tissue mechanics during axis elongation model. Short term dynamics ($T = 4$ hours): red arrows represent random cell motility in the PSM and matrix bloating. Long-term dynamics ($T = 12$ hours): purple arrows pointing towards the posterior in the PSM and in the NT represent the active growth of both tissues. Purple bent arrows in mid PSM (big arrows) and in mid NT (small arrows) represent cell proliferation (the size of the arrows represents the difference in the proliferation rates). Purple arrows pointing towards the NT represent lateral compression by the PSM on the NT. Blue arrows in both tissues in the mid-anterior region represent the inter-tissue sliding.

axial tissues. However, the involvement of the NT in these multi-tissue dynamics is still unknown on the short-term. On the other hand, the long-term dynamics (up to $T = 12$ hours) are driven by differential cell proliferation: the PSM and the NT actively grow which drives their posterior movement. This growth is mainly due to cell proliferation in each tissue. The PSM pushes the PZ boundary to make room for the axial tissues to extend posteriorly. While the NT grows, it is also compressed laterally by the PSM along the antero-posterior axis, which creates an additional displacement of the NT towards the posterior. In the mid-anterior region, differential proliferation creates the sliding between the two tissues. Random cell motility and matrix bloating in the PSM can also be contributing to the long-term to axis elongation.

Based on the results of the VMI, the proposed model in Figure 7.3 highlights the differences between the short and the long term mechanisms governing axis elongation and reveals the role of differential proliferation on axis extension and on inter-tissue sliding.

Parameter refinement. In a very recent study [11] which extends the work in [112], authors

develop a 2D free boundary problem to describe the elongation of the PSM. In this work, authors fit a space-dependent PSM viscosity function to account for its fluid-to-solid posterior-to-anterior transition. On a cellular level this transition is characterized by a MET transition. In their model, they consider only cell injection from the PZ as the driver of growth and not cell proliferation. This is a natural assumption as the biological model of interest in this work is the zebrafish, which indeed does not exhibit significant cell division in the posterior region but rather cell rearrangement. In this work, authors also fit a function modelling the cell injection rate from the PZ into the PSM which depends on the pressure at the posterior tip. Although the study was done on zebrafish embryos, we could imagine a similar type of function for the viscosity to fit in the VMI. In its present form, the viscosities in the VMI are tissue-dependent but not space-dependent. Then in practice refining the viscosity parameters would mean replacing β_1, β_2 by $\beta_1(x), \beta_2(x)$ in the elliptic equations for the velocities. We could also replace the source term in the VMI, which was until now taken as a constant, with the fitted pressure-dependent function of cell injection in [11]. However, this entails that cell injection indeed depends on the pressure at the posterior tip, in other words, if there is enough space cells are injected into the PSM. This is not proven in the case of the chick embryo which nevertheless exhibits different growth mechanisms than the zebrafish. This assumption might not even hold in the chick embryo, as we could imagine that cell injection is indeed constant and the accumulation of cells exerts a pressure which drives the PZ posteriorly. These possible model extensions can significantly complexify the theoretical study of the mathematical model.

The VMI: a multi-functional model. We tested the VMI with the PSM and the notochord. Interestingly, the results match very well the shape of the notochord as well as its velocity. The simulation in Figure 5.24a shows that the PSM pushes laterally on the notochord which drives it to the posterior very fast. This observation is in accordance with findings in [160], where authors replaced the posterior notochord with a gel and measured the gel deformation throughout the growth. The gel appeared thinner and longer, which confirmed that the posterior notochord is subjected to a passive convergence-extension process due to the compression from the posterior PSM. Our model compliments these findings and further predicts a very high sliding between the PSM and the notochord. These results show that the VMI is a polyvalent model that can be used to study the dynamics of most of the posterior embryonic tissues and is not limited to the PSM and NT.

Perspectives. The VMI reproduces very well tissue formation and the consequent elongation in the vertebrate embryo. We should keep in mind that we made several modelling assumptions during our modelling process. Indeed we considered the PZ to be a straight line (of width of one mesh size) at the posterior tip of the NT and of the PSM. We could imagine different forms of the PZ, e.g with varying width or round shaped or ellipsoid, which might affect the posterior shape of the tissues. This is yet to be explored numerically. We also assumed that the friction

coefficient of the NT is equal to that of the PSM. Using the measuring techniques in [108], this assumption can be verified or disproved. In either case, measuring the friction of the NT with its surroundings would refine the model parameters and give more accurate results. Finally, in our modelling assumptions we considered the embryo as a 2D structure and projected the tissues onto the 2D plane. In a future work, we aim to develop a 3D model of the embryonic tissues. This 3D version might give us more insight on the dorso-ventral dynamics in the posterior tissues. It would allow us to complexify the model and to consider three tissues in 3D: the PSM, the NT and the notochord which is located ventrally to the NT. This model might lead to interesting findings as to the 3D sliding between the tissues. In addition, we imposed homogeneous Dirichlet conditions on the velocity on all the numerical walls. On the lateral and upper walls, this condition is accurate as it models respectively the lateral plate and the last formed somite. On the lower wall, it might be less accurate. In our simulations, we see that the velocities decay when next to the lower wall which is due to these boundary conditions. In our future work, we aim to test different boundary conditions on the lower wall by first replacing them with Neumann conditions which model the outflow of the densities through this wall. On the lateral wall, we also could refine our choice of boundary conditions by using non-homogeneous Dirichlet conditions to account for the slip of the densities along the lateral plate.

Furthermore, in the present form of the VMI, we considered only the contribution of the PZ on the PSM and in the NT, that is, cell injection, and modeled it via a source term for simplicity. A natural extension of the model is to consider a third tissue as the PZ. This extension would make the theoretical study of the model more challenging. But from a biological point of view, it would be more accurate as the PZ plays a role in the posterior dynamics that cannot be ignored. For example, it could be resisting to the elongation.

In our modelling approach, we explain axis elongation from a mechanical point of view. As explained in Chapter 1, many models rely on the chemical point of view to explain PSM elongation as it was shown that it exhibits an FGF8 gradient [58]. A mechanico-chemical version of the VMI can be developed to account for the PSM's response to the antero-posterior FGF8 gradient.

Finally, the model entails many predictions pertaining to the tissues' densities, velocities, elongation rate, cell injection and inter-tissue siding. Our immediate perspective is to test these hypotheses in the vertebrate quail embryo. Our data at hand is of embryos with electroporated P27 in the PSM. We would need additional biological experiments on transgenic quails with P27 electroporated in the NT to validate all the model hypotheses.

Altogether, our modelling approach leading to the VMI gives us more insight on the mechanisms governing tissue formation and the consequent axis elongation. The VMI is a great model to study the sliding between the embryonic tissues and to test several *in silico* treated embryos. Interestingly, we could investigate whether this model applies for other vertebrates whose growth

is governed by cell division and/or cell injection. Even beyond the scope of developmental biology, ignoring cell injection, this multi-tissue model applies to cancer biology where a healthy tissue and a tumor cohabitate.

It remains to ask, can we explain morphogenesis with only a deterministic point of view ? And if we focus on the cellular level, what other properties can emerge ? This is the main topic of Objective 3 detailed below.

7.3 Objective 3. Investigate the role of the two proteins Sox2 and Bra on the population of progenitors

7.3.1 Our strategy

To study the effect of protein expression on cell differentiation and migration into the tissues, we studied in [130] a population of stem cells (progenitors) in the vertebrate embryos. We focused on two proteins, Sox2 and Bra, known to be involved in neural and mesodermal fates. By combining forced expression and down regulation experiments followed by live-imaging and image analysis, we were able to study the effect of each protein on the biological system. To study the effect of spatial cell distribution with respect to protein expression, we developed an agent-based model that links cell motility, protein regulation and progenitor differentiation. The model allows us to test different abnormal cell distributions, thus capturing the role of spatial cell distribution in the vertebrate embryo.

7.3.2 Summary of the results

By immunodetection technique on quail embryos, we discovered that progenitors display high spatial cell-to-cell heterogeneity of Sox2 and Bra expressions. Our study showed that this heterogeneity is coupled with an antero-posterior Sox2-to-Bra gradient of protein expression. Using electroporation technique to over-express and down-regulate either Sox2 or Bra in quail embryos, we concluded that Sox2 and Bra have a significant influence on cells' future tissue choice. Sox2 appears to favor cell exit from the PZ and entry into the NT and Bra favors cells exit from the PZ and entry into the PSM. Therefore, cell migration appeared to be an important factor which may be regulated by Sox2 and Bra. To confirm this, we first quantified cell motility in the WT embryo and found that cells in the PSM moved much faster than cells in the NT. We also discovered that progenitors are highly motile with a central velocity equal to that of the PSM, but with heterogeneous motilities inside the population. This finding reinforces the heterogeneous nature of the PZ. Cells in the PZ, PSM and NT exhibit random-like behavior, with cells in the PZ and in the PSM presenting very high diffusivity. Functional experiments followed by image analysis revealed that

Sox2 and Bra have antagonistic activities on cell motility: Sox2 inhibits it whereas Bra promotes it. We then developed an agent-based 2D model with three cell populations (the PSM, the NT and the PZ), where each cell is characterized by its position, protein level of Sox2 and Bra, and moves with a protein-dependent velocity. Our simulations show that the model reproduces tissue formation and axis elongation, as well as velocity profiles and replicates the results of the functional experiments. We used this model to test *in silico* different cell distribution in the PZ, namely graded and random distributions and a mix of both graded and random, to understand the role of spatial cell heterogeneity in this population. Our results suggest that cell heterogeneity promotes tissue elongation through posterior cell movement. Spatial heterogeneity also enhances diffusive cell behavior, promotes tissue shape conservation and tissue fluidity and facilitate self-correcting cell behaviors.

7.3.3 Discussion about our contribution and perspectives

The novelty of our contribution. It was known that progenitors differentiate and exit the PZ to colonize the posterior tissues and that a portion of these cells remains resident in the zone and self renew. To sustain the formation of the posterior tissues, the population of progenitors must maintain an appropriate balance between the two choices of staying in place and self-renew or exit the progenitor region to contribute to the formation of the NT and the PSM. How this balance is established and controlled over time was an open question. In Chapter 6, we answer this question by showing that variations of the Sox2-to-Bra ratio in progenitors of the PZ are critical to regulate progenitor motility and tissue destination. Furthermore, we showed that progenitors in quail embryos exhibit a high cell-to-cell heterogeneity in Sox2 and Bra protein expressions. Our work brings answers as to the relationships between the processes of cell specification and tissue morphogenesis as well as to the cellular mechanisms underlying the tightly regulated balance of progenitor choice. Finally, the mathematical agent-based model of this process highlights the role of the heterogeneous spatial distribution of Sox2/Bra within progenitors, a property that defies the french flag model. It suggests that chaos (cell heterogeneity) is an important factor sustaining an apparently very ordered process (morphogenesis).

Benchmark. Our study in [130] shows that Sox2 and Bra are co-expressed in progenitors in quail embryos. This co-expression proves to be conserved across vertebrate embryos as it has been reported in chick, zebrafish, mouse and also human embryos [119, 159]. Cell-to-cell heterogeneity was also reported in these vertebrates, with high Sox2 cells located in the anterior part of the PZ and NT fated and high Bra cells located in the posterior PZ and PSM fated [159]. The PZ in the quail embryos exhibits such a pattern. More so, we observe that neighboring cells expressed variable levels of Sox2 and Bra. The maintenance of these heterogeneous levels could be due to

the gradients of signaling pathways such as Wnt and FGF, which are involved in the regulation of Sox2 and Bra [161, 41, 75, 76, 43]. The creation of heterogeneity could also be explained by the Sox2-Bra cross-regulation activity [97]. This antagonistic activity between Sox2 and Bra has been put forward as a determinant of progenitor fate [97]. However, a recent study on mouse embryos defies this hypothesis as Bra did not directly repress Sox2's expression [79]. This is in line with our observations of Bra morpholinos which did not lead to the up regulation of Sox2 (see Chapter 6, Figure 2 and Supplementary Figure 2).

Our study proves that the antagonistic activity of Sox2 and Bra forms a more complex picture (Supplementary Figures) which makes it difficult to determine whether the Sox2-to-Bra ratio or their absolute value is the most determinant of their effect on progenitors.

Furthermore, their spatial heterogeneity suggests that their location does not systematically determine their destination tissue. We propose that neighboring progenitors could end up in different tissues. This is in accordance with prospective fate maps of the PZ [134, 156].

Our analysis of the WT embryo shows that progenitors are highly motile and without strong directionality. Interestingly, this seems to be a conserved property amongst vertebrates as studies on zebrafish showed that cells located axially also display highly disordered motility [56, 44].

When we performed functional experiments to elucidate the effect of Sox2 and Bra on cell motility, we observed an obvious inhibition of cell motility in Bra down-regulated and Sox2 over-expressed embryos. Results were less clear in Bra over-expression and Sox2 down-regulation where we saw only a slight increase in cell motility. This might be due to the fact that progenitors behave much more like PSM cells than NT cells, which explains why biasing progenitors towards a NT fate shows more drastic results. However, how local cell motility is regulated by Sox2/Bra activity remains an open question.

We make a first step at understanding this regulation in the agent-based model where we propose the hypothesis that this regulation is made through a Sox2-dependent adhesion between progenitors. We also introduce non-mixing rules which translate to cell displacement being redirected whenever in contact with a high density of foreign cells. These two properties could very well be behind progenitor segregation into different tissues. In the agent-based model, we unravel the role of spatial cell-to-cell heterogeneity in progenitors during morphogenesis. We propose that a random spatial pattern in cell distribution in the PZ promotes posterior movements, self-corrective behaviors and tissue fluidity of the PZ which helps conserve its shape. Fluidity in the PSM and disordered cell behavior proved to have an important role in zebrafish elongation [56, 112, 44]. The plasticity conferred to the PZ by random cell movement *in silico* supports the ablation of the PZ *in vivo* which regenerated after some time [90]. The model suggests that the self-corrective movements promoted by the random cell motion allows an easier auto-organization and re-organization of cells (in case of perturbation) than the graded pattern. The latter would be extremely affected by tissue ablation since the graded pattern is regulated by gradients of signaling pathways within

the tissues. The agent-based model highlights the role of spatial cell-to-cell heterogeneity within the population of progenitors. It also emphasizes on the properties it confers on the tissue and on the more global process of axis elongation. Stochasticity seems to sustain the robust and ordered process, that is morphogenesis. Cell-to-cell heterogeneity is also commonly found in cancer cells which makes them extremely resistant to treatments and drives the disease [128]. Stochasticity of agents extends beyond the scope of developmental biology, and could elucidate many underlying cell behaviors.

Multi-scale modelling. Interestingly in the microscopic model, cell injection appears to play a crucial role in tissue formation and PZ maintenance. Indeed we calibrated the model such that progenitor differentiation (thus consequent cell injection) balances cell production in the PZ as its density and volume were shown to be constant in [24]. When compared to the VMI in Chapter 5, this result might seem contradictory to our findings, as in the VMI, we observed that cell injection has no effect on tissue dynamics. These two point of views are actually complementary and not contradictory as it is a matter of modelling scale. On the cellular scale, our agent-based model reproduces local cell activities during short times. Cell injection is a local property, which gives it a paramount role in this model. On the macroscopic scale, cell injection being local, it is not sufficient to sustain a large scale process for long times as in the VMI. Cell proliferation on the other hand is non local in the sense that it is present in the entire tissue, and creates a driving pushing force towards the posterior due to the massive addition of mass. The reconciliation of these two point of views highlights the importance of the choice of scale in the modelling process which yields scale-dependent properties and conclusions.

Biological hypotheses: differential cell adhesion and non-mixing rules. In the agent-based model, we observed that to maintain tissue segregation and axis elongation, a Sox2-dependent adhesion as well as some non-mixing rules (cells move away from large densities of foreign type) were essential. Without them, cells mix extensively, and the PZ does not elongate as progenitors do not sense the pressure from NT cells anterior to them. These two phenomena could explain cell segregation in the PZ *in vivo* and cell segregation in the different tissues. Both of these model assumptions can be tested in the vertebrate embryo. A possible protocol would be to harvest PZ explants and look at how cells segregate over time. This can be done also *in silico* by simplifying the mixed agent-based model to the case of a PZ explant, see Figure 7.4. In Figure 7.4, we adapted the agent-based model for the case of PZ explants. We see that if progenitors are initially heterogeneously distributed (left), after some time, they segregate and form patterns (right). Cells with high Sox2 adhere and remain in the center, they are surrounded by a ring of progenitor cells and finally PSM cells form the last ring. It would be interesting to investigate *in vivo* the cell segregation patterns based on these *in silico* experiments. Furthermore, we aim to quantify the spatial

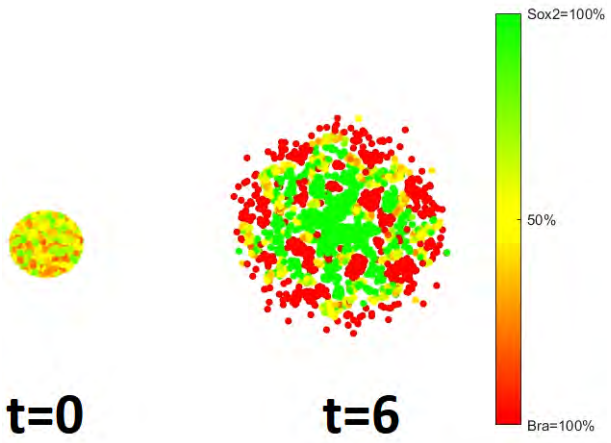

Figure 7.4 – The agent-based model in the case of a PZ explant. Left: initial condition: heterogeneous spatial distribution of cells in the PZ. Right: spatial distribution at $t = 6$ in the PZ explant. (red cells, yellow/orange cells, green cells)=(PSM cells, progenitors, NT cells).

heterogeneity in the embryo and *in silico*. On the mathematical side, this project was initiated during the internship of a master student (Gabrielle Roullet) where we studied the dependence of the average differentiation time on the intensity of the noise. Quantifying spatial heterogeneity is the subject of our future work.

Comparison of the mixed agent-based model and the ESVM: a micro-to-macro limit (perspective). We previously highlighted the similarities between the ESVM developed in Chapter 4 and the agent-based mixed model in Chapter 6. Namely, both models consider cell proliferation and the natural cell diffusion (one on the microscopic scale as a Brownian motion and the other on the macroscopic scale with the Laplacian term). The non-mixing property included in the mixed model plays the same role as the repulsion pressure q_m in the ESVM: it prevents tissue mixing and promotes segregation of different cell types. The mixed model and the ESVM in fact model the same phenomena and incorporate the same processes but on different scales. This motivates the computation of the micro-to-macro limit of the mixed model. Our future work consists in computing the micro-to-macro limit and comparing the resulting macroscopic description of the mixed model to the ESVM, while focusing on the different repulsions on the macroscopic scale.

Other perspectives. Our short term goal is to calibrate the agent-based model especially the noise intensity more accurately by quantitatively confronting the *in silico* results and the biological data. This project is ongoing, as we have started to understand the dependence of the average differentiation time of progenitors with respect to the noise intensity. The next step is to quantify cell spatial-heterogeneity depending on the noise intensity. We aim to use mathematical tools that

capture and give an accurate and interpretable quantification of heterogeneity. Furthermore, until now we have assumed in our model that cells regulate linearly their Sox2 and Bra expressions. That is, when cells increase their Sox2 expression they lower their Bra level accordingly. This assumption, although generally true (as we have proved in Chapter 6), is not systematic. Cells can vary their expression levels as a result of a non linear cross-regulation between Sox2 and Bra (see Chapter 6, Supplemental Figures). This could be a possible extension of the model to capture more precisely the temporal evolution of the Sox2 and Bra protein expression in progenitors.

Bibliography

[1] Abercrombie, M. Contact inhibition in tissue culture. *In Vitro 6*, 2 (1970), 128–142.

[2] Agosti, A., Antonietti, P. F., Ciarletta, P., Grasselli, M., and Verani, M. A cahn-hilliard–type equation with application to tumor growth dynamics. *Mathematical Methods in the Applied Sciences 40*, 18 (2017), 7598–7626.

[3] Agosti, A., Marchesi, S., Scita, G., and Ciarletta, P. The self-organised, non-equilibrium dynamics of spontaneous cancerous buds.

[4] Alikakos, N. D., Bates, P. W., and Chen, X. Convergence of the Cahn-Hilliard equation to the Hele-Shaw model. *Arch. Rational Mech. Anal. 128*, 2 (1994), 165–205.

[5] Amar, M. B., and Goriely, A. Growth and instability in elastic tissues. *Journal of the Mechanics and Physics of Solids 53*, 10 (2005), 2284–2319.

[6] Anderson, A., and Chaplain, M. Cheminform abstract: Continuous and discrete mathematical models of tumor-induced angiogenesis. *Cheminform 30* (03 2010).

[7] Aoki, K. The behavior of a vapor-gas mixture in the continuum limit: Asymptotic analysis based on the boltzmann equation. *AIP Conference Proceedings 585*, 1 (2001), 565–574.

[8] Aoki, K., Takata, S., and Kosuge, S. Vapor flows caused by evaporation and condensation on two parallel plane surfaces: Effect of the presence of a noncondensable gas. *Physics of Fluids 10*, 6 (1998), 1519–1533.

[9] Aoki, K., Takata, S., and Taguchi, S. *Vapor flows with evaporation and condensation in the continuum limit: effect of a trace of non condensable gas (2003). European Journal of Mechanics B/Fluids 22 (2003) 51–71*.

[10] Baker, R., and Maini, P. Travelling gradients in interacting morphogen systems. *Mathematical Biosciences 209*, 1 (2007), 30–50.

[11] Banavar, S. P., Carn, E. K., Rowghanian, P., Stooke-Vaughan, G., Kim, S., and Campàs, O. Mechanical control of tissue shape and morphogenetic flows during vertebrate body axis elongation. *Sci Rep 11, 8591.* (2021).

[12] Benazeraf, B. Dynamics and Mechanisms of Posterior Axis Elongation in the Vertebrate Embryo. *Cellular and Molecular Life Sciences* (Sept. 2018).

[13] Bentley, K., Gerhardt, H., and Bates, P. A. Agent-based simulation of notch-mediated tip cell selection in angiogenic sprout initialisation. *Journal of Theoretical Biology 250*, 1 (2008), 25–36.

[14] Benzekry, S. *Modeling, mathematical and numerical analysis of anti-cancerous therapies for metastatic cancers.* PhD thesis, 11 2011.

[15] Bergsland, M., Ramsköld, D., Zaouter, C., Klum, S., Sandberg, R., and Muhr, J. Sequentially acting sox transcription factors in neural lineage development. *Genes & development 25* (11 2011), 2453–64.

[16] Bertozzi, A. L., and Pugh, M. The lubrication approximation for thin viscous films: Regularity and long-time behavior of weak solutions. *Communications on Pure and Applied Mathematics 49*, 2 (1996), 85–123.

[17] Bertsch, M., Dal Passo, R., and Mimura, M. A free boundary problem arising in a simplified tumour growth model of contact inhibition. *Interfaces Free Bound. 12*, 2 (2010), 235–250.

[18] Bertsch, M., Gurtin, M. E., Hilhorst, D., and Peletier, L. A. On interacting populations that disperse to avoid crowding: preservation of segregation. *J. Math. Biol. 23*, 1 (1985), 1–13.

[19] Bouldin, C. M., Snelson, C. D., Farr, G. H., and Kimelman, D. Restricted expression of cdc25a in the tailbud is essential for formation of the zebrafish posterior body. *Genes & development 28*, 4 (2014), 384–395.

[20] Bragina, E., Vasiliev, J., and Gelfand, I. Formation of bundles of microfilaments during spreading of fibroblasts on the substrate. *Experimental Cell Research 97*, 2 (1976), 241–248.

[21] Brinkman, H. A calculation of the viscous force exerted by a flowing fluid on a dense swarm of particles. *Flow Turbulence and Combustion 1* (1949), 27–34.

[22] Burger, M., Capasso, V., and Morale, D. On an aggregation model with long and short range interactions. *Nonlinear Anal. Real World Appl. 8*, 3 (2007), 939–958.

[23] Burger, M., Di Francesco, M., Fagioli, S., and Stevens, A. Sorting phenomena in a mathematical model for two mutually attracting/repelling species. *SIAM J. Math. Anal. 50*, 3 (2018), 3210–3250.

[24] Bénazéraf, B., Beaupeux, M., Tchernookov, M., Wallingford, A., Salisbury, T., Shirtz, A., Shirtz, A., Huss, D., Pourquié, O., François, P., and Lansford, R. Multi-scale quantification of tissue behavior during amniote embryo axis elongation. *Development 144*, 23 (12 2017), 4462–4472.

[25] Bénazéraf, B., Francois, P., Baker, R. E., Denans, N., Little, C. D., , and Pourquié, O. A random cell motility gradient downstream of fgf controls elongation of an amniote embryo. *Nature 466*, 7303 (2010), 248.

[26] Bénazéraf, B., and Pourquié, O. Developmental biology: Cell intercalation one step beyond. *Current Biology 18*, 3 (2008), R119–R121.

[27] Bénilan, P., Boccardo, L., and Herrero, M. On the limit of solutions of $u_t = \delta u^m$ as $m \to \infty$. *Rend. Sem. Mat. Univ. Politec. Torino. Fascicolo Speciale, pp.1-13* (1989).

[28] Caffarelli, L., and Friedman, A. Asymptotic behavior of solutions of $u_t = \delta u^m$ as $m \to \infty$. *Indiana Univ. Math. J., pages 711–728* (1987).

[29] Cahn, J. W. On spinodal decomposition. *Acta Metallurgica 9*, 9 (1961), 795–801.

[30] Cahn, J. W., and Hilliard, J. E. Free energy of a nonuniform system. i. interfacial free energy. *The Journal of Chemical Physics 28*, 2 (1958), 258–267.

[31] Cahn, J. W., and Hilliard, J. E. Free energy of a nonuniform system. iii. nucleation in a two-component incompressible fluid. *The Journal of Chemical Physics 31*, 3 (1959), 688–699.

[32] Cambray, N., and Wilson, V. Axial progenitors with extensive potency are localised to the mouse chordoneural hinge. *Development 129*, 20 (10 2002), 4855–4866.

[33] Cambray, N., and Wilson, V. Two distinct sources for a population of maturing axial progenitors. *Development 134 (15): 2829–2840* (2007).

[34] Carrillo, J. A., Fagioli, S., Santambrogio, F., and Schmidtchen, M. Splitting schemes and segregation in reaction cross-diffusion systems. *SIAM J. Math. Anal. 50*, 5 (2018), 5695–5718.

[35] Carter, S. B. Haptotaxis and the mechanism of cell motility. *Nature 213* (1967), 256–260.

[36] Chaplain, M. A. J., and Lolas, G. Mathematical modelling of cancer cell invasion of tissue: the role of the urokinase plasminogen activation system. *Math. Models Methods Appl. Sci. 15*, 11 (2005), 1685–1734.

[37] Chatelain, C., Balois, T., Ciarletta, P., and Amar, M. B. Emergence of microstructural patterns in skin cancer: a phase separation analysis in a binary mixture. *New Journal of Physics 13*, 11 (nov 2011), 115013.

[38] Chatelain, C., Ciarletta, P., and Amar, M. B. Morphological changes in early melanoma development: Influence of nutrients, growth inhibitors and cell-adhesion mechanisms. *Journal of Theoretical Biology 290* (2011), 46–59.

[39] Chertock, A., Degond, P., Hecht, S., and Vincent, J.-P. Incompressible limit of a continuum model of tissue growth with segregation for two cell populations. *Math. Biosci. Eng. 16*, 5 (2019), 5804–5835.

[40] Ciarletta, P., Foret, L., and Ben Amar, M. The radial growth phase of malignant melanoma: multi-phase modelling, numerical simulations and linear stability analysis. *Journal of The Royal Society Interface 8*, 56 (2011), 345–368.

[41] Ciruna, B., and Rossant, J. Fgf signaling regulates mesoderm cell fate specification and morphogenetic movement at the primitive streak. *Developmental Cell 1*, 1 (2001), 37–49.

[42] Cristini, V. Nonlinear simulations of solid tumor growth using a mixture model: invasion and branching. *Journal of mathematical biology. 58*, 4-5 (2009).

[43] Cunningham, T. J., Colas, A., and Duester, G. Early molecular events during retinoic acid induced differentiation of neuromesodermal progenitors. *Biology Open 5*, 12 (10 2016), 1821–1833.

[44] Das, D., Chatti, V., Emonet, T., and Holley, S. A. Patterned disordered cell motion ensures vertebral column symmetry. *Developmental Cell 42*, 2 (2017), 170–180.e5.

[45] David, N., and Perthame, B. Free boundary limit of a tumor growth model with nutrient. *J. Math. Pures Appl. (9) 155* (2021), 62–82.

[46] David, N., and Schmidtchen, M. On the Incompressible Limit for a Tumour Growth Model incorporating Convective Effects. working paper or preprint, Mar. 2021.

[47] Debiec, T., Perthame, B., Schmidtchen, M., and Vauchelet, N. Incompressible limit for a two-species model with coupling through Brinkman's law in any dimension. *J. Math. Pures Appl. (9) 145* (2021), 204–239.

[48] Debiec, T., and Schmidtchen, M. Incompressible limit for a two-species tumour model with coupling through brinkman's law in one dimension (2020). *Acta Applicandae Mathematicae 169*, 1, 593–611.

[49] Degond, P., Hecht, S., Romanos, M., and Trescases, A. Multi-species viscous models for tissue growth: incompressible limit and qualitative behaviour. *J. Math. Biol. 85*, 2 (2022), Paper No. 16, 47.

[50] Degond, P., Hecht, S., and Vauchelet, N. Incompressible limit of a continuum model of tissue growth for two cell populations. *Netw. Heterog. Media 15*, 1 (2020), 57–85.

[51] Desvillettes, L., Lepoutre, T., Moussa, A., and Trescases, A. On the entropic structure of reaction-cross diffusion systems. *Comm. Partial Differential Equations 40*, 9 (2015), 1705–1747.

[52] Deutsch, A., and Dormann, S. *Mathematical modeling of biological pattern formation.* Springer, 2005.

[53] Ding, H., Spelt, P. D., and Shu, C. Diffuse interface model for incompressible two-phase flows with large density ratios. *Journal of Computational Physics 226*, 2 (2007), 2078–2095.

[54] Doumic, M., Hecht, S., and Peurichard, D. A purely mechanical model with asymmetric features for early morphogenesis of rod-shaped bacteria micro-colony. *Mathematical Biosciences and Engineering 17*, 6 (2020), 6873–6908.

[55] Drasdo, D., and Höhme, S. A single-cell-based model of tumor growth in vitro: monolayers and spheroids. *Physical biology 2*, 3 (2005), 133.

[56] Dray, N., Lawton, A., Nandi, A., Jülich, D., Emonet, T., and Holley, S. A. Cell-fibronectin interactions propel vertebrate trunk elongation via tissue mechanics. *Current Biology 23*, 14 (2013), 1335–1341.

[57] Duboule, D. Temporal colinearity and the phylotypic progression: a basis for the stability of a vertebrate bauplan and the evolution of morphologies through heterochrony. *Development (Cambridge, England). Supplement* (1994), 135–42.

[58] Dubrulle, J., and Pourquié, O. fgf8 mrna decay establishes a gradient that couples axial elongation to patterning in the vertebrate embryo. *Nature 427* (02 2004), 419–22.

[59] Duval, M. *De la formation du blastoderme: dans l'oeuf d'oiseau.* 1884.

[60] Ebenbeck, M., and Garcke, H. On a cahn-hilliard-brinkman model for tumor growth and its singular limits. *SIAM Journal on Mathematical Analysis 51*, 3 (2019), 1868–1912.

[61] Ebenbeck, M., Garcke, H., and Nürnberg, R. Cahn–hilliard–brinkman systems for tumour growth. *Discrete and Continuous Dynamical Systems - S 14*, 11 (2021), 3989–4033.

[62] Einstein, A. *Investigations on the theory of the Brownian movement.* Dover Publications, Inc., New York, 1956. Edited with notes by R. Fürth, Translated by A. D. Cowper.

[63] Elliott, C. M., and Songmu, Z. On the Cahn-Hilliard equation. *Arch. Rational Mech. Anal. 96*, 4 (1986), 339–357.

[64] Evans, L. C. *Partial differential equations.* American Mathematical Society, Providence, R.I., 2010.

[65] Eyles, J., King, J. R., and Styles, V. A tractable mathematical model for tissue growth. *Interfaces Free Bound. 21*, 4 (2019), 463–493.

[66] Fozard, J. A., Byrne, H. M., Jensen, O. E., and King, J. R. Continuum approximations of individual-based models for epithelial monolayers. *Mathematical Medicine and Biology: A Journal of the IMA 27*, 1 (07 2009), 39–74.

[67] Frieboes, H. B., Jin, F., Chuang, Y.-L., Wise, S. M., Lowengrub, J. S., and Cristini, V. Three-dimensional multispecies nonlinear tumor growth—ii: Tumor invasion and angiogenesis. *Journal of Theoretical Biology 264*, 4 (2010), 1254–1278.

[68] Frigeri, S., Lam, K. F., Rocca, E., and Schimperna, G. On a multi-species cahn-hilliard-darcy tumor growth model with singular potentials. *Commun. Math. Sci. 16*, 3 (2018), 821–856.

[69] Furter, J., and Grinfeld, M. Local vs. non-local interactions in population dynamics. *Journal of Mathematical Biology 27*, 1 (1989), 65–80.

[70] Galle, J., Loeffler, M., and Drasdo, D. Modeling the effect of deregulated proliferation and apoptosis on the growth dynamics of epithelial cell populations in vitro. *Biophysical Journal 88*, 1 (2005), 62–75.

[71] Garcke, H., Lam, K. F., Nurnberg, R., and Sitka, E. A multiphase cahn–hilliard–darcy model for tumour growth with necrosis. *Mathematical Models and Methods in Applied Sciences 28*, 03 (2018), 525–577.

[72] Garcke, H., Lam, K. F., Sitka, E., and Styles, V. A cahn-hilliard-darcy model for tumour growth with chemotaxis and active transport. *Math. Models Methods Appl. Sci. 26*, 6 (2016), 1095–1148.

[73] García, M. R., Vázquez, J. A., Teixeira, I. G., and Alonso, A. A. Stochastic individual-based modeling of bacterial growth and division using flow cytometry. *Frontiers in Microbiology 8* (2018).

[74] Gil, O., and Quirós, F. Convergence of the porous media equation to Hele-Shaw. *Nonlinear Anal. 44*, 8, Ser. A: Theory Methods (2001), 1111–1131.

[75] Goto, H., Kimmey, S. C., Row, R. H., Matus, D. Q., and Martin, B. L. FGF and canonical Wnt signaling cooperate to induce paraxial mesoderm from tailbud neuromesodermal progenitors through regulation of a two-step epithelial to mesenchymal transition. *Development 144*, 8 (04 2017), 1412–1424.

[76] Gouti, M., Delile, J., Stamataki, D., Wymeersch, F. J., Huang, Y., Kleinjung, J., Wilson, V., and Briscoe, J. A gene regulatory network balances neural and mesoderm specification during vertebrate trunk development. *Developmental Cell 41*, 3 (2017), 243–261.e7.

[77] Graner, F., and Glazier, J. A. Simulation of biological cell sorting using a two-dimensional extended potts model. *Physical review letters 69*, 13 (1992), 2013.

[78] Greenspan, H. P. On the motion of a small viscous droplet that wets a surface. *Journal of Fluid Mechanics 84*, 1 (1978), 125–143.

[79] Guibentif, C., Griffiths, J. A., Imaz-Rosshandler, I., Ghazanfar, S., Nichols, J., Wilson, V., Göttgens, B., and Marioni, J. C. Diverse routes toward early somites in the mouse embryo. *Developmental Cell 56*, 1 (2021), 141–153.e6.

[80] Gwiazda, P., Perthame, B., and Świerczewska Gwiazda, A. A two-species hyperbolic-parabolic model of tissue growth. *Comm. Partial Differential Equations 44*, 12 (2019), 1605–1618.

[81] Hamburger, V., and Hamilton, H. L. A series of normal stages in the development of the chick embryo. *Journal of morphology 88*, 1 (1951), 49–92.

[82] Harrison, N. C., Diez del Corral, R., and Vasiev, B. Coordination of cell differentiation and migration in mathematical models of caudal embryonic axis extension. *PLOS ONE 6*, 7 (07 2011), 1–18.

[83] Hawkins-Daarud, A., van der Zee, K. G., and Tinsley Oden, J. Numerical simulation of a thermodynamically consistent four-species tumor growth model. *International Journal for Numerical Methods in Biomedical Engineering 28*, 1 (2012), 3–24.

[84] Hecht, F. New development in freefem++. *J. Numer. Math. 20*, 3-4 (2012), 251–265.

[85] Hecht, S., and Vauchelet, N. Incompressible limit of a mechanical model for tissue growth with non-overlapping constraint. *Commun. Math. Sci. 15*, 7 (2017), 1913–1932.

[86] Helbing, D., Farkas, I., and Vicsek, T. Simulating dynamic features of escape panic. *Nature 407* (09 2000), 487–490.

[87] Herrmann, B. G. G. Cloning of the t gene required in mesoderm formation in the mouse. *Nature 343*, 6259 (1990-01-31).

[88] Huss, D., Benazeraf, B., Wallingford, A., Filla, M., Yang, J., Fraser, S. E., and Lansford, R. A transgenic quail model that enables dynamic imaging of amniote embryogenesis. *Development 142*, 16 (08 2015), 2850–2859.

[89] Jilkine, A., Marée, A., and Edelstein-Keshet, L. Mathematical model for spatial segregation of the rho-family gtpases based on inhibitory crosstalk. *Bulletin of mathematical biology 69* (09 2007), 1943–78.

[90] Joubin, K., and Stern, C. D. Molecular interactions continuously define the organizer during the cell movements of gastrulation. *Cell 98*, 5 (1999), 559–571.

[91] Julien, D., and Olivier, P. fgf8 mrna decay establishes a gradient that couples axial elongation to patterning in the vertebrate embryo. *Nature;427(6973):419-22. doi: 10.1038/nature02216* (2004).

[92] Keller, E., and Segel., L. *Model for chemotaxis (1971). J. Theor. Biol. 30, 225–234.*

[93] Keller, R. Cell migration during gastrulation. *Current opinion in cell biology 17*, 5 (2005), 533–541.

[94] Kim, I., and Požár, N. Porous medium equation to Hele-Shaw flow with general initial density. *Trans. Amer. Math. Soc. 370*, 2 (2018), 873–909.

[95] Kim, I., and Turanova, O. Uniform convergence for the incompressible limit of a tumor growth model. *Ann. Inst. H. Poincaré Anal. Non Linéaire 35*, 5 (2018), 1321–1354.

[96] Kim, I. C., Perthame, B., and Souganidis, P. E. Free boundary problems for tumor growth: a viscosity solutions approach. *Nonlinear Anal. 138* (2016), 207–228.

[97] Koch, F., Scholze, M., Wittler, L., Schifferl, D., Sudheer, S., Grote, P., Timmermann, B., Macura, K., and Herrmann, B. G. Antagonistic activities of sox2 and brachyury control the fate choice of neuro-mesodermal progenitors. *Developmental Cell 42*, 5 (2017), 514–526.e7.

[98] Kolmogoroff, A. N., Petrovsky, I. G., and Piscounoff, N. Study of the diffusion equation with growth of the quantity of matter and its application to a biology problem.

[99] Komarova, N. Mathematical modeling of tumorigenesis: Mission possible. *Current opinion in oncology 17* (02 2005), 39–43.

[100] Lawton, A. K., Nandi, A., Stulberg, M. J., Dray, N., Sneddon, M. W., Pontius, W., Emonet, T., and Holley, S. A. Regulated tissue fluidity steers zebrafish body elongation. *Development 140*, 3 (02 2013), 573–582.

[101] Lee, H. G., Park, J., Yoon, S., Lee, C., and Kim, J. Mathematical model and numerical simulation for tissue growth on bioscaffolds. *Applied Sciences 9*, 19 (2019).

[102] Li, Y., and Nirenberg, L. Estimates for elliptic systems from composite material. vol. 56. 2003, pp. 892–925. Dedicated to the memory of Jürgen K. Moser.

[103] Liu, J.-G., Tang, M., Wang, L., and Zhou, Z. Toward understanding the boundary propagation speeds in tumor growth models. *SIAM J. Appl. Math. 81*, 3 (2021), 1052–1076.

[104] Lotka, A. J. *Elements of mathematical biology. (formerly published under the title Elements of Physical Biology)*. Dover Publications, Inc., New York, N.Y., 1958.

[105] M. Bertsch, M. E. G., and Hilhorst, D. *On interacting populations that disperse to avoid crowding: the case of equal dispersal velocities (1987). Nonlinear Analysis: Theory, Methods and Applications, vol.11, pp.493-499*.

[106] Meineke, F., Potten, C., and Loeffler, M. Cell migration and organization in the intestinal crypt using a lattice-free model. *Cell proliferation 34* (09 2001), 253–66.

[107] Metzcar, J., Wang, Y., Heiland, R., and Macklin, P. A review of cell-based computational modeling in cancer biology. *JCO Clinical Cancer Informatics*, 3 (2019), 1–13. PMID: 30715927.

[108] Michaut, A. *Biomechanics of anteroposterior axis elongation in the chicken embryo*. Theses, Université de Strasbourg, Sept. 2018.

[109] Michaut, A., Mongera, A., Gupta, A., Serra, M., Rigoni, P., Lee, J. G., Duarte, F., Hall, A. R., Mahadevan, L., Guevorkian, K., and Pourquié, O. Activity-driven extracellular volume expansion drives vertebrate axis elongation.

[110] Miranville, A. The cahn–hilliard equation and some of its variants. *AIMS Mathematics 2*, 3 (2017), 479–544.

[111] Mongera, A., Michaut, A., Guillot, C., Xiong, F., and Pourquié, O. Mechanics of anteroposterior axis formation in vertebrates. *Annual Review of Cell and Developmental Biology 35*, 1 (2019), 259–283. PMID: 31412208.

[112] Mongera, A., Rowghanian, P., Gustafson, H., Shelton, E., Kealhofer, D., Carn, E., Serwane, F., Lucio, A., Giammona, J., and Campàs, O. A fluid-to-solid jamming transition underlies vertebrate body axis elongation. *Nature 561* (09 2018).

[113] M.R.S.E., R. B. F. H., and V.P.L.S., R. A. Xxvii. a brief account of microscopical observations made in the months of june, july and august 1827, on the particles contained in the pollen of plants; and on the general existence of active molecules in organic and inorganic bodies. *The Philosophical Magazine 4*, 21 (1828), 161–173.

[114] Murray, J. D. *Mathematical biology*, second ed., vol. 19 of *Biomathematics*. Springer-Verlag, Berlin, 1993.

[115] Murray, P. J., Edwards, C. M., Tindall, M. J., and Maini, P. K. From a discrete to a continuum model of cell dynamics in one dimension. *Phys. Rev. E 80* (Sep 2009), 031912.

[116] Newman, T. J. Modeling multicellular systems using subcellular elements. *Mathematical Biosciences and Engineering 2*, 3 (2005), 613–624.

[117] ODEN, J. T., HAWKINS, A., and PRUDHOMME, S. General diffuse-interface theories and an approach to predictive tumor growth modeling. *Mathematical Models and Methods in Applied Sciences 20*, 03 (2010), 477–517.

[118] Oginuma, M., Moncuquet, P., Xiong, F., Karoly, E., Chal, J., Guevorkian, K., and Pourquié, O. A gradient of glycolytic activity coordinates fgf and wnt signaling during elongation of the body axis in amniote embryos. *Developmental cell 40*, 4 (2017), 342–353.

[119] Olivera-Martinez, I., Harada, H., Halley, P. A., and Storey, K. G. Loss of fgf-dependent mesoderm identity and rise of endogenous retinoid signalling determine cessation of body axis elongation. *PLOS Biology 10*, 10 (10 2012), 1–17.

[120] Osborne, J., Fletcher, A., Pitt-Francis, J., Maini, P., and Gavaghan, D. Comparing individual-based approaches to modelling the self-organization of multicellular tissues.

[121] Osborne, J. M., Fletcher, A. G., Pitt-Francis, J. M., Maini, P. K., and Gavaghan, D. J. Comparing individual-based approaches to modelling the self-organization of multicellular tissues. *PLOS Computational Biology 13*, 2 (02 2017), 1–34.

[122] Palsson, E., and Othmer, H. G. A model for individual and collective cell movement in dictyostelium discoideum. *Proceedings of the National Academy of Sciences 97*, 19 (2000), 10448–10453.

[123] Pegrum, S. M., and Maroudas, N. Early events in fibroblast adhesion to glass: An electron microscopic study. *Experimental Cell Research 96*, 2 (1975), 416–422.

[124] Peirce, S. Computational and mathematical modeling of angiogenesis. *Microcirculation (New York, N.Y. : 1994) 15* (09 2008), 739–51.

[125] Perthame, B., Quirós, F., and Vázquez, J. L. The Hele-Shaw asymptotics for mechanical models of tumor growth. *Arch. Ration. Mech. Anal. 212*, 1 (2014), 93–127.

[126] Perthame, B., Tang, M., and Vauchelet, N. Traveling wave solution of the Hele-Shaw model of tumor growth with nutrient. *Math. Models Methods Appl. Sci. 24*, 13 (2014), 2601–2626.

[127] Perthame, B., and Vauchelet, N. Incompressible limit of a mechanical model of tumour growth with viscosity. *Philos. Trans. Roy. Soc. A 373*, 2050 (2015), 20140283, 16.

[128] Prasetyanti, P. R., and Medema, J. P. Intra-tumor heterogeneity from a cancer stem cell perspective. *Molecular Cancer 16* (2017).

[129] Regev, I., Guevorkian, K., Gupta, A., Pourquié, O., and Mahadevan, L. Rectified random cell motility as a mechanism for embryo elongation. *Development 149*, 6 (03 2022). dev199423.

[130] Romanos, M., Allio, G., Roussigné, M., Combres, L., Escalas, N., Soula, C., Médevielle, F., Steventon, B., Trescases, A., and Bénazéraf, B. Cell-to-cell heterogeneity in Sox2 and Bra expression guides progenitor motility and destiny. *eLife 10* (Oct. 2021).

[131] Sambasivan, R., and Steventon, B. Neuromesodermal progenitors: A basis for robust axial patterning in development and evolution. *Frontiers in Cell and Developmental Biology 8* (2021).

[132] Savin, T., Kurpios, N., Shyer, A., Florescu, P., Liang, H., Mahadevan, L., and Tabin, C. On the growth and form of the gut. *Nature 476* (08 2011), 57–62.

[133] Schaller, G., and Meyer-Hermann, M. Multicellular tumor spheroid in an off-lattice voronoi-delaunay cell model. *Physical Review E 71*, 5 (2005), 051910.

[134] Selleck, M., and Stern, C. Fate mapping and cell lineage analysis of Hensen's node in the chick embryo. *Development 112*, 2 (06 1991), 615–626.

[135] Shih, J., and Keller, R. Cell motility driving mediolateral intercalation in explants of Xenopus laevis. *Development 116*, 4 (12 1992), 901–914.

[136] Shih, J., and Keller, R. E. Patterns of cell motility in the organizer and dorsal mesoderm of xenopus laevis. *Development 116 4* (1992), 915–30.

[137] Sone, Y. Flows induced by temperature fields in a rarefied gas and their ghost effect on the behavior of a gas in the continuum limit. In *Annual review of fluid mechanics, Vol. 32*, vol. 32 of *Annu. Rev. Fluid Mech.* Annual Reviews, Palo Alto, CA, 2000, pp. 779–811.

[138] Sone, Y., Aoki, K., Takata, S., Sugimoto, H., and Bobylev, A. V. Inappropriateness of the heat-conduction equation for description of a temperature field of a stationary gas in the continuum limit: examination by asymptotic analysis and numerical computation of the Boltzmann equation. *Phys. Fluids 8*, 2 (1996), 628–638.

[139] Sone, Y., and Doi, T. Ghost effect of infinitesimal curvature in the plane Couette flow of a gas in the continuum limit. *Phys. Fluids 16*, 4 (2004), 952–971.

[140] Sone, Y., Takata, S., and Sugimoto, H. The behavior of a gas in the continuum limit in the light of kinetic theory: the case of cylindrical Couette flows with evaporation and condensation. No. 970. 1996, pp. 125–142. Mathematics of thermal convection (Japanese) (Kyoto, 1996).

[141] Steinberg, M. S. Reconstruction of tissues by dissociated cells. *Science 141*, 3579 (1963), 401–408.

[142] Steventon, B., Duarte, F., Lagadec, R., Mazan, S., Nicolas, J.-F., and Hirsinger, E. Species-specific contribution of volumetric growth and tissue convergence to posterior body elongation in vertebrates. *Development 143*, 10 (05 2016), 1732–1741.

[143] Steventon, B., and Martinez Arias, A. Evo-engineering and the cellular and molecular origins of the vertebrate spinal cord. *Developmental Biology 432*, 1 (2017), 3–13.

[144] T. Fulton, B. V., and Steventon, B. The unappreciated generative role of cell movements in pattern formation. *Royal Society Open Science vol. 9*, no. 4 (April 2022).

[145] Takata, S., and Aoki, K. The ghost effect in the continuum limit for a vapor-gas mixture around condensed phases: asymptotic analysis of the Boltzmann equation. vol. 30. 2001, pp. 205–237. The Sixteenth International Conference on Transport Theory, Part I (Atlanta, GA, 1999).

[146] Takemoto, T., Uchikawa, M., Yoshida, M., Bell, D., Lovell-Badge, R., Papaioannou, V., and Kondoh, H. Tbx6-dependent sox2 regulation determines neural or mesodermal fate in axial stem cells. *Nature 470* (02 2011), 394–8.

[147] Tzouanacou, E., Wegener, A., Wymeersch, F. J., Wilson, V., and Nicolas, J.-F. Redefining the progression of lineage segregations during mammalian embryogenesis by clonal analysis. *Developmental cell 17*, 3 (2009), 365–376.

[148] Vauchelet, N., and Zatorska, E. Incompressible limit of the Navier-Stokes model with a growth term. *Nonlinear Anal. 163* (2017), 34–59.

[149] Vázquez, J. L. *The porous medium equation.* Oxford Mathematical Monographs. The Clarendon Press, Oxford University Press, Oxford, 2007. Mathematical theory.

[150] Volterra, V. Variazioni e fluttuazioni del numero d"individui in specie animali conviventi. memoire della r. accademia nazionale dei lincei. *Nature, 118, 558-560* (1926).

[151] Waddington, C. H., et al. Organisers and genes. *Organisers and genes.* (1940).

[152] Wadkin, L., Orozco-Fuentes, S., Neganova, I., Lako, M., Shukurov, A., and Parker, N. The recent advances in the mathematical modelling of human pluripotent stem cells. *SN Applied Sciences 2* (01 2020).

[153] WARD, J. P., and KING, J. R. Mathematical modelling of avascular-tumour growth II: Modelling growth saturation. *Mathematical Medicine and Biology: A Journal of the IMA 16*, 2 (06 1999), 171–211.

[154] Warga, R., and Kimmel, C. Cell movements during epiboly and gastrulation in zebrafish. *Development 108*, 4 (04 1990), 569–580.

[155] Whitaker, S. Flow in porous media i: A theoretical derivation of darcy's law. *Transport in Porous Media 1* (03 1986), 3–25.

[156] Wilson, V., and Beddington, R. Cell fate and morphogenetic movement in the late mouse primitive streak. *Mechanisms of Development 55*, 1 (1996), 79–89.

[157] Wise, S., Lowengrub, J., Frieboes, H., and Cristini, V. Three-dimensional multispecies nonlinear tumor growth—i: Model and numerical method. *Journal of Theoretical Biology 253*, 3 (2008), 524–543.

[158] Woods, M. L., Carmona-Fontaine, C., Barnes, C. P., Couzin, I. D., Mayor, R., and Page, K. M. Directional collective cell migration emerges as a property of cell interactions. *PLOS ONE 9*, 9 (09 2014), 1–10.

[159] Wymeersch, F. J., Huang, Y., Blin, G., Cambray, N., Wilkie, R., Wong, F. C., and Wilson, V. Position-dependent plasticity of distinct progenitor types in the primitive streak. *eLife 5* (jan 2016), e10042.

[160] Xiong, F., Ma, W., Bénazéraf, B., Mahadevan, L., and Pourquié, O. Mechanical coupling coordinates the co-elongation of axial and paraxial tissues in avian embryos. *Developmental Cell 55*, 3 (2020), 354–366.e5.

[161] Yamaguchi, T. P., Takada, S., Yoshikawa, Y., Wu, N., and McMahon, A. P. T (brachyury) is a direct target of wnt3a during paraxial mesoderm specification. *Genes & development 13*, 24 (1999), 3185–3190.

[162] Yong, D., Levy, R., and Lape, N. Why no difference? a controlled flipped classroom study for an introductory differential equations course. *PRIMUS 25* (11 2015), 907–921.

[163] Zhang, L., Kendrick, C., Julich, D., and Holley, S. A. Cell cycle progression is required for zebrafish somite morphogenesis but not segmentation clock function. *Development 135*, 12 (06 2008), 2065–2070.

Mathematical modeling of vertebrate embryo axis elongation

Abstract: During vertebrate embryo development, thousands of cells self-organize in a very precise and complex choreography to form the tissues and organs of the future adult. The objective of this thesis is to understand the mechanisms orchestrating the morphogenesis of the tissues which form the caudal part of the embryo, by combining mathematical, numerical, and experimental approaches. In the first part, we develop hydrodynamic multi-species mathematical models based on partial differential equations, to understand how the neural and mesodermal tissues form during embryo elongation. These models consider biological properties observed in the embryo such as tissue growth and viscosity, and inter-tissue interaction. By deriving free boundary problems and transmission problems, we analyze tissue dynamics and obtain qualitative properties of the mathematical models: pressure jump, ghost effect. Biological hypotheses on the cellular and tissular mechanisms governing tissue dynamics emerge from our theoretical analysis of the models, which we then confirm experimentally by integrating the biological data to the mathematical models. In the second part, we take a closer look at the cell behaviour during the growth of bird embryos. We conduct biological experiments on stem-like cells to investigate the effect of two proteins in cell specification and migration. We discover a zone where cells are spatially heterogeneous in their protein expression. We then develop an agent-based model that considers cell specification and migration to understand the role of this heterogeneity. The model highlights a surprising paradox: chaos (heterogeneity) can sustain an apparently very ordered process (morphogenesis). Through an interdisciplinary approach, our multi-scale analysis of tissue growth reveals the underlying cellular mechanisms governing tissue formation. The results in this thesis rely on the development of adequate mathematical tools (incompressible limit, free boundary problems) which go beyond the scope of developmental biology (viscous fluid mechanics, tissue growth and oncology).

Keywords: Modelling, tissue growth, PDE, cross diffusion, incompressible limit, free boundary problems, transmission problems, morphogenesis, bird embryo, axis elongation.

Modélisation mathématique de l'allongement de l'axe antéro-postérieur de l'embryon vertébré

Résumé: Au cours du développement de l'embryon de vertébré, des milliers de cellules s'auto-organisent suivant une chorégraphie très précise et complexe pour former les tissus et les organes du futur adulte. L'objectif de cette thèse est de comprendre les mécanismes régissant la morphogenèse des tissus qui constituent la partie caudale de l'embryon, en combinant des approches mathématiques, numériques et expérimentales. Dans la première partie, nous développons des modèles mathématiques hydrodynamiques multi-espèces basés sur des équations aux dérivées partielles, pour comprendre comment les tissus neuraux et mésodermiques se forment pendant l'allongement de l'embryon. Ces modèles prennent en compte les propriétés biologiques observées dans l'embryon telles que la croissance et la viscosité des tissus, ainsi que l'interaction inter-tissulaire. En dérivant des problèmes à frontières libres et des problèmes de transmission, nous analysons la dynamique des tissus et obtenons des propriétés qualitatives des modèles mathématiques : saut de pression, effet fantôme. Il émerge de notre analyse théorique des modèles de nouvelles hypothèses biologiques sur les mécanismes cellulaires et tissulaires gouvernant la dynamique tissulaire, que nous confirmons ensuite expérimentalement en intégrant les données biologiques aux modèles mathématiques. Dans la deuxième partie, nous examinons de plus près le comportement des cellules pendant la croissance des embryons d'oiseau. Nous réalisons des expériences biologiques sur des cellules souches pour étudier l'effet de deux protéines dans la spécification et la migration cellulaire. Nous découvrons une zone où les cellules sont spatialement hétérogènes dans leur expression en protéines. Nous développons ensuite un modèle agent-centré qui prend en compte la spécification et la migration des cellules pour comprendre le rôle de cette hétérogénéité. Le modèle met en évidence un paradoxe surprenant : le chaos (l'hétérogénéité) peut soutenir un processus apparemment très ordonné (la morphogenèse). Grâce à une approche interdisciplinaire, notre analyse multi-échelle de la croissance des tissus révèle les mécanismes cellulaires sous-jacents qui régissent la formation des tissus. Les résultats de cette thèse reposent sur le développement d'outils mathématiques adéquats (limite incompressible, problèmes à frontières libres) qui dépassent le cadre de la biologie du développement (mécanique des fluides visqueux, croissance des tissus et oncologie).

Mots-clés: Modélisation, croissance tissulaire, EDP, diffusion croisée, limite incompressible, problèmes à frontière libre, problèmes de transmission, morphogenèse, embryon d'oiseau, allongement de l'axe.